Laser Induced Incandescence and High Speed Imaging in Hydra Optical Diesel Engine

Christopher K H Hong

LLB MEng

Department of Mechanical Engineering

Imperial College London

Submitted in partial fulfilment of the requirements for the degree of Doctor of Philosophy of Imperial College London.

This work, unless where it is referenced, is the result of the study carried out by Christopher K. H. Hong.

Christopher K. H. Hong

London, December, 2014

Abstract

The aim of this thesis is to investigate ways to reduce soot emission from compression ignition engines by investigating the combustion processes within the diesel engine. The approach is to include computational and experimental work. In order to investigate the trade-off between the amount and stratification of the premixing and the consequent rate of pressure rise, and in particular the effects of changing the autoignition properties of the fuel blend, a multizone code capable of representing the ignition of a premixed charge consequent on multiple injection of fuel is presented. As part of this investigation, this thesis began the process of looking into the potential of gasoline fuel.

Experimentally, investigations of soot distribution were carried out in an optically-accessed single cylinder “Hydra” engine. The soot was visualized using high speed imaging and laser induced incandescence in the optical engine to look at the effect of injection pressure on combustion luminosity and soot distribution. An extensive parametric study was carried out on the Hydra engine to look at the effect of engine load, injection timing and pressure, number of injections, intake temperature and combustion phasing. High speed imaging was carried out to measure injection tip penetration and soot luminosity as a function injection pressure. The combustion luminosity was studied, with proper orthogonal decomposition (POD) analysis, at different injection pressures. It was found that increase of injection pressure decreases combustion luminosity. The technique of laser induced incandescence (LII) was used to visualize the soot.

As a preliminary to the use of the LII in the engine, fundamental work on the technique itself was carried out at Heriot-Watt University to isolate the radiative emission component of heat loss from the soot and measure the complex refractive index of soot. Results on soot particle sizes were compared to scanning electron micrograph of the soot collected. The LII measurement was found to be much larger, due to the high signal to noise ratio and the bias towards detection of larger particles. The investigation also showed that the soot agglomerates could undergo micro-explosions on being exposed to laser irradiance. It is speculated that the soot molecules become ionized and mutually repel each other.

Contents

List of Figures

List of Tables

Nomenclature

A	Wall area (m^2)
A_0	Avogadro's number A_0=6.023x10^{23} molecules/mol,
B	Bore diameter (m)
C	Constant
C_{abs}	absorption cross section (cm^2)
c_0	speed of light (299792456ms^{-1})
c_p	specific heat capacity—constant pressure ($Jkg^{-1}K^{-1}$)
c_v	specific heat capacity—constant volume ($Jkg^{-1}K^{-1}$)
D	diameter
D_N	nozzle diameter of the injector (m)
f	Eucken correction to the thermal conductivity
f_h	empirical function correcting the Knudsen affected continuum heat flux
G	heat transfer factor
h	Planck constant (6.626196x10^{-34}Js)
h_c	heat transfer coefficient
h_i	specific enthalpy of species i
ΔH_v	heat of vaporization
I	Rayleigh signal
I_i	incidental laser intensity (W/cm^2)
k_B	Boltzmann constant (1.380662x$10^{-23}JK^{-1}$)
Kn	Knudsen number
l	conrod length (m)
m	complex refractive index
m_f	mass of fuel injected (kg)
m_g	molecular mass of the ambient gas (kg)
n_i	refractive index
N	total molecular density
N	engine speed (RPM)
N_0	number density at STP of 2.687x$10^{19}cm^{-3}$

N_k molecular flux of sublimated particles in the Knudsen regimes

Nu Nusselt number

N_v molecular flux of evaporated carbon (molecules/m^2s)

n_v molecular density of soot vapour

p_g pressure of the ambient gas (Pa)

p_m motored pressure (Pa)

P pressure (Pa)

P_v vapour pressure

$\dot{Q}$ heat flux (W)

Q_{abs} rate of laser energy absorbed by the particle

Q_{cond} rate of heat loss through conduction

Q_{int} internal rate of energy change of the particle

Q_{ht} heat loss

Q_n net heat release rate

Q_{rad} rate of heat loss through radiation

Q_{sub} rate of heat loss through sublimation

$q_{exp}(t)$ pulsed laser temporal power density normalised to its area over the heating pulse length

r_p particle radius (nm)

R/ R_m gas constant, 8.3143J/mol·K

Re Reynolds number

R_0 laser energy density (Jm^{-2})

R_s swirl ratio

S penetration length (m)

S stroke (m)

S LII signal

S_{bb} measured signal from black-body source during calibration (V)

S_p measured particle emission signal (V)

t time (s)

t_B breakup length of spray

T	temperature (K)
T_{bb}	temperature of black-body source during calibration (K)
T_g	temperature of gas (K)
T_{wall}	wall temperature
T_P^0	temperature of particle after heat up (K)
T_p	particle temperature (K)
u	turbulent velocity (m/s)
V	volume (m^3)
V_c	collection volume (cm^3)
V_d	displaced volume of the engine (m^3)
V_{fuel}	velocity at which the fuel is injected (m/s)
w	average cylinder gas velocity m/s
$\dot{w}_i$	chemical production rate
Y_i	mass fraction
Z_{surf}	collision rate (1/s cm^2)
α_T	translational energy accommodation coefficient
β	evaporation coefficient
β	scaling factor
Γ	diffusion coefficient of soot vapour (m^2/s)
γ	heat capacity ratio
ε	emissivity
η_c	the detection efficiency of the collection system
θ	scattering angle
κ_a	thermal conductivity
λ	wavelength (nm)
λ_{cond}	thermal conductivity of the gas ($Wm^{-1}K^{-1}$)
λ_g	mean free path of the gas molecules (nm)
μ	viscosity
ξ	scaling factor

ρ_g ambient air density (Kg/m^3)

ρ_m density of the fuel and air mixture in the cylinder (kg/m^3)

ρ_p density of particle material (kgm^{-3})

ρ_v depolarization ratio

σ_a mean molecule cross section

σ_i Rayleigh cross-section of the individual species in the gas mixture

$\partial\sigma/\partial\Omega$ Rayleigh cross section or differential cross section (cm^2/sr)

χ_i mole fraction of the species i in the mixture

ω_s swirl angular velocity (rad/s)

Ω solid angle of collection optics (sr)

Subscripts

abs absorption

bb black body

B Boltzmann

c continuum regime

c collection

d displacement

g gas

ht heat loss

i species designation

m motored

n net

N Nozzle

p particle

ref reference point/calibrated signal with a known temperature and Rayleigh cross-section

s swirl

tr transition regime

T traslantional

$_{w/wall}$ wall

λ wavelength

Abbreviations

2D	Two dimensional
ANHTR	Apparent net heat transfer rate
aTDC	After top dead centre
bTDC	Before top dead centre
BDC	Bottom dead centre
C/O	Carbon to oxygen
CAD	Crank angle degree
CCD	Charged coupled device
CFD	Computational fluid dynamics
CI	Compression ignition
DPF	Diesel particulate filter
EGR	Exhaust gas recirculation
ELS	Elastic light scattering
FMT	Friction modification technology
fps	Frames per second
FWHM	Full width half maximum
HC	Hydrocarbons
HCCI	Homogeneous charge compressing ignition
HRR	Heat release rate, an simplified term for ANHTR
iCCD	intensified charged coupled device
IMEP	Indicated mean effective pressure
LDV	Laser Doppler velocimetry
LIF	Laser induced fluorescence
LII	Laser induced incandescence
LSODE	Livermore solver for ordinary differential equations
LTC	Low temperature combustion

LTR	Low temperature reaction
MMT	Methylcyclopentadienyl manganese tricarbonyl
MON	Motored octane number
MK	Modular kinetics
Nd:YAG	Neodymium-doped yttrium aluminium garnet
PAH	Polycyclic aromatic hydrocarbons
PCCI	Premixed charge compression ignition
PDA	Phase Doppler Anemometry
PIV	Particle imaging velocimetry
PLIF	Planar laser induced fluorescence
POD	Proper orthogonal decomposition
PM	Particulate Matter
PMT	Photomultiplier Tube
PRF	Primary reference fuel
RON	Research octane number
RPM	Revolution per minute
SI	Spark ignition
SOI	Start of injection
STP	Standard temperature and pressure
SWP	Short wave pass
TC-TR	Two color time resolved
TDC	Top dead centre
TEM	Transmission electron microscope
UV	Ultraviolet
VIS	Visible

C_2H_2	Ethyne
CO	Carbon monoxide
CO_2	Carbon dioxide
HCHO*	Formaldehyde

HCO*	Aldehyde
H_2O	Water
MTBE	Methyl tert-butyl ether
N_2	Nitrogen
NO_x	Nitrous oxides
O_2	Oxygen

1 Introduction and Literature Review

1.1 Introduction

Diesel combustion or compression ignition engine for automotive application has the benefits of good fuel economy and produces higher torque compared to spark ignition engines using gasoline. As with the spark ignition engine, there are legislative limits on the pollutant emission levels of the compression ignition (CI) engine. The main pollutants from the CI engine are soot and nitrous oxides (NOx) and current legislation is met by a combination of the "design" of the combustion to reduce their production (or in the case of soot, promote their destruction) and hence the "engine out" emission. The "tailpipe out" emissions are further reduced by a combination of catalysts and filters. These latter two measures not only introduce a reduction in efficiency due to both pumping losses and to fuel spent in regeneration (particularly for the so-called diesel particulate filter, DPF) but also are both costly to install and need 'management' of the regeneration process which can be difficult to achieve - for example, in engines which run at modest powers in urban environments. There has always been a strong incentive to improve the design of the combustion and to reduce the stress placed on the catalysts to reduce these two emissions.

This trend can be expected to continue in the future as legislated limits to pollutants continue to become increasingly stringent: NOx emissions are estimated to account for about 25,00 premature deaths every year while particulate pollution is held to be responsible for about 250,000 premature deaths a year in the European Union alone (Urata & Taylor, Swaminathan and Bray (2011)). Much is known, at the level of engineering science, about the mechanism by which soot and particulates are generated. Technologically this knowledge, when applied to the current "design" of CI combustion, generally (not always) has the results that measures designed to reduce the one pollutant increase the other. This interdependency is generally referred to as the NOx-Soot trade-off.

This thesis is concerned with soot emissions: not only is soot the more dangerous of the two pollutants to human health, its generation and destruction is readily visualised in an engine which has optical access and this can provide useful insight into the design of combustion which is designed to reduce “engine out” soot emissions. A particular motivation has been the recent work of Aronsson, Chartier et al. (2009) which has suggested, through results from an investigation based on a ‘Design of experiments’, which the ‘engine out’ emissions depend most strongly on the extent of the soot oxidation in the later part of the cycle. The extent of the oxidation can be related to the strength of the rate of heat release in the latter part of the combustion of the fuel. Thus, it becomes interesting to investigate the soot present in the late combustion cycle as a function of the combustion design.

It is necessary to restrict soot emissions by vehicles and combustion in general into the atmosphere because of its potential danger to health. Its main threat is through the respiratory system causing irritation and other respiratory problems and even carcinogenic to humans and animals. It is also believed that particulates can cross blood vessels and can cause heart disease. At the other extreme of scale, carbon black particles have significant impact on climate change second only to carbon dioxide emission, with Bond (2011) showing various effects of black carbon in atmosphere and on artic snow/ice on climate forcing. From a legislative perspective, Figure 1-1 shows the gradual reduction in permissible level of particulate matter and NO_x by passenger diesel vehicles in Europe and there are similar legislations in countries around the world. This is one of the main technical challenges for the motor industry.

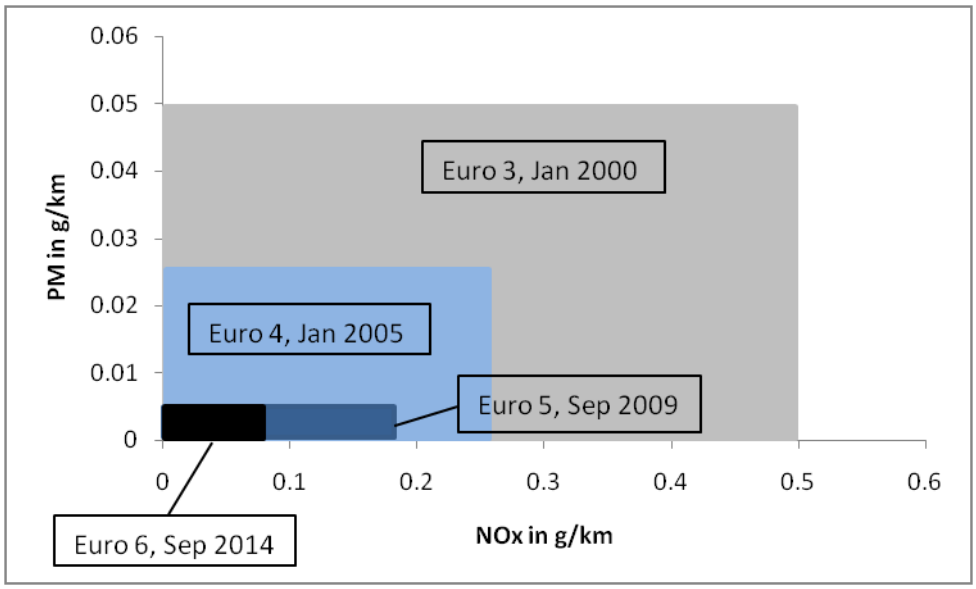

Figure 1-1: Tightening of European legislative restriction on diesel passenger vehicle emission of Particulate Matter (PM) and NO_x.

The nature of compression ignition combustion is such that there is a short time between injection of fuel into the combustion chamber and ignition of the fuel. This short period of time does not normally allow for complete mixing of air and fuel which produces regions of air fuel mixture which are both too lean and too rich. Combustion of these different lean and rich air-fuel mixtures produces nitric oxides, hydrogen carbons, carbon monoxide and carbon black (smoke/soot). In order to limit the emission of these into the atmosphere, one solution is to provide exhaust after-treatment devices. Alternatively, the production of smoke within the combustion chamber can be reduced by better understanding of the fuel spray dynamics, fuel air mixing processes, chemical kinetics and effects of injection schedule and combustion chamber, and in particular combustion bowl, design.

Altering these variables will change combustion processes and lead to different combustion regimes. These combustion regimes can collectively be called kinetically or mixing controlled CI combustion. At one extreme, conventional diesel combustion is at the mixing controlled end of the spectrum. This regime can be plagued by high emissions of both NOx and soot. Homogeneous charge compressing ignition (HCCI), which showed potential in the past decade in terms of low NOx and soot emissions

(primarily because the stoichiometry is kept lean or very lean), but ultimately, its limited load capability and if it is to avoid excessive noise, vibration harshness and the difficulty in controlling the time of ignition meant it has limited application. Low temperature combustion (LTC) and premixed charge compression ignition (PCCI) bridges the gap between HCCI and conventional diesel with the potential advantages of low emissions, while maintaining control over the time of ignition provided that the chemical kinetics - essentially the ignition delay - permit 'premixed enough' mixture preparation before ignition occurs. LTC or PCCI also has the practical advantage over HCCI in that it can be achieved by changing variables using current diesel combustion engine hardware. These include exhaust gas recirculation (EGR), turbocharger and common rail injection system, which all can contribute to improve efficiency and lower emission. These items allow for changing even the fuel type, as well as injection timing, strategy and pressure, EGR ratio, valve timing and amount of boost. More fundamental changes can be made to fuel injector design, compression ratio, and valve and combustion bowl geometry.

In order to evaluate these variables and how they affect the combustion processes and subsequently engine emission and performance, different techniques can be applied for measuring the effects of altering these variables. Computer simulation, based on computational fluid dynamics (CFD) to solve the equations for mass, momentum, energy and species, together with models for turbulence and combustion, the latter based on models of the chemical kinetics, and the engine performance and emission can be found by engine testing on a dynamometer. Additional experimental investigations can be based on optical diagnostics techniques can be applied to evaluate spray dynamics, mixing processes, species formation and oxidation and other in-cylinder processes. Although optical engines have their limitations in exactly replicating a metal engine due not only to their limited load and speed, difficulty in estimating blow by losses and usually fail to maintain the proper compression ratio but also the heat losses are not the same as in a metal engine. Nevertheless, optical investigations of diesel combustion and optical engines have proved useful to provide information on the fundamental combustion processes that takes place in a metal engine.

Although the focus of the past decade or so, legislation and hence engine research and development has expanded to include carbon dioxide emission due to the adequate effectiveness of the current generation of diesel particulate filter (DPF), current engine out emission are met. However, current DPF operation still have a cost penalty and, due to the need to regenerate the PDF in order to burn off the soot, has an impact on the overall fuel economy of the vehicle. Hence reduction in engine out soot may also reduce carbon dioxide emission. A reduction of engine out soot remains an important goal with respect to imminent legislation and given increased concern with particulate emissions. Such developments will imply the need for greater emphasis on the efficiency of the DPF and 'in cylinder' measures to lighten the task of the DPF will remain a worthwhile research goal.

With this in mind, the focus of this research is on soot formation and oxidation within the combustion chamber and this is to be investigated by using laser induced incandescence in the combustion chamber of an optical diesel engine. It is important to have an understanding of the different variables which affect smoke generation within the combustion chamber so a review of all the variables is required.

1.1.1 Thesis Outline

The aim of this thesis is to look at the generation and destruction of soot, by investigating the combustion processes within an optical diesel engine. The approach to this was multifaceted. In the belief that LTC and PCCI are likely to represent and important development in the next decade, that the parameter space of investigation is likely to be large (extending to fuel type, as well as more traditional variables such as EGR level, boost level, injection schedule and so on) but that the rate of pressure rise - as a proxy for the noise emitted by the engine - is likely to be an important limiting value, a Multi-Zone, Multiple Injection Simulation was begun. The main part of the thesis involved the visualisation of soot generation (through natural luminescence, CH chemiluminescence, as well as spray visualisation based on single and double injection schedules) and the remnant after the completion of oxidation by laser induced incandescence.

In greater detail, soot formation rate was changed by going from the diesel combustion regime to a more premixed one by increasing mixing of air and fuel, achieved by increasing the injection pressure and advancing the injection timing. And experiments were carried out, using high speed imaging (Chapter 7) and laser induced incandescence (Chapter 8) in the optical engine to look at the effect of injection pressure on combustion luminosity and soot distribution.

In the context of pursuing the above aims, other investigations were pursued. In the context of technique of laser induced incandescence, an attempt to quantify at a fundamental level the component of heat loss by radiative heat transfer was investigated by conducting LII in a vacuum work was carried out in Herriot-Watt University (Chapter 2). A promising possibility of reducing emission from compression ignition engines is to use a gasoline type fuel. This thesis began the process of looking into the potential of such fuels by describing the chemical and physical properties of gasoline fuel (Chapter 4).

In view of the aims of the thesis, the remainder of this chapter is set out as follows. Soot and its generation is a central theme and section 1.2 provides a literature review and this is followed in section 1.3 by a review of combustion regimes in compression ignition engines. This thesis is in large part based on an optical engine and hence section 1.4 reviews the relevant optical diagnostic techniques applicable to optical engines. Laser induced incandescence (LII) is an important technique used in this thesis and thus section 1.5 is dedicated to this experimental technique.

1.2 Soot

The nature of diesel combustion makes the fundamental study of in-cylinder soot formation difficult because of its environment of high gas temperature and pressure and complex fuel composition. Soot formation is dominated by the turbulence mixing process and the unsteady nature of mixing and the 3-D geometry of the combustion chamber (Heywood (1988)).

1.2.1 Soot Formation

Carbonaceous particles are produced during incomplete combustion of fuel. Equation (1-1) from Heywood (1988) suggests that soot formation occurs when *m* becomes larger than *2y*. In other words, soot forms when there is insufficient oxygen, i.e. when carbon to oxygen (C/O) is larger than unity. If C/O is less than 1, the oxygen is sufficient produce CO and CO_2. In reality, soot forms even when C/O is less than 1 and soot has been observed to form at C/O ratio even as low as 0.5 (Wagner (1981)).

$$\boldsymbol{C_m H_n + yO_2 \rightarrow 2_y CO + \frac{n}{2} H_2 + (m - 2y) C_s} \qquad (1\text{-}1)$$

The exact detail of the chemistry involved in soot formation is not clear even after years of study. Below is a summary of description of soot formation from Heywood (1988), Bockhorn (1994), Seinfeld and Pandis (2006) and Mollenhauer and Tschoeke (2010) and is partly illustrated in Figure 1-2.

The initial nucleation of soot can be described by one of two theories. The first is the polycyclic hypothesis when hydrocarbon fuel degrades during oxidation and/or pyrolysis in a fuel rich environment and the oxidation of unsaturated hydrocarbons leads to the formation of ethyne (C_2H_2, also known as acetylene). These form the building blocks to grow into aromatics. These larger aromatic structures coagulate forming primary carbonaceous particles which continue to pick up aromatics for surface growth.

The second theory is the elementary carbon hypothesis where fuel is broken down into basic elements of carbon and hydrogen. These carbon atoms form clusters of hexagonal and pentagonal structures and grow to form primary carbon particles.

Particles also grow by coagulation which occurs as smaller particles collide and coalesce. Collision of two spherical particles may result in their coagulation into single spheroid and rapid surface growth will restore them to their original shape. Surface growth contributes to the final soot volume fraction whereas coagulation determines the final size of the soot particles. Once the spherules have solidified

and surface growth diminished, these primary particles have sizes around 10nm to 30nm. These small, roughly spherical primary particles are subsequently cluster together to form aggregates. These chains agglomerate can be straight or branched and vary widely in size and morphology and can grow up to a few micrometres.

Further described in Heywood (1988), in the combustion chamber of a diesel engine, soot evolution continues with soot oxidation. This can happen at any stage of the soot formation process and fortunately a large fraction of soot formed within the cylinder is oxidized before being exhausted. Oxidation rate can depend on kinetics of the reaction, morphology of the aggregates and the diffusion of reactant to, and product from, the surface. The formation of soot increases and the amount of soot peaks and subsequently gradually oxidises and reduces to the level which is ultimately the amount of soot in the exhaust gas. Any soot not oxidised will be exhausted out and filtered out by the diesel particulate filter (DPF).

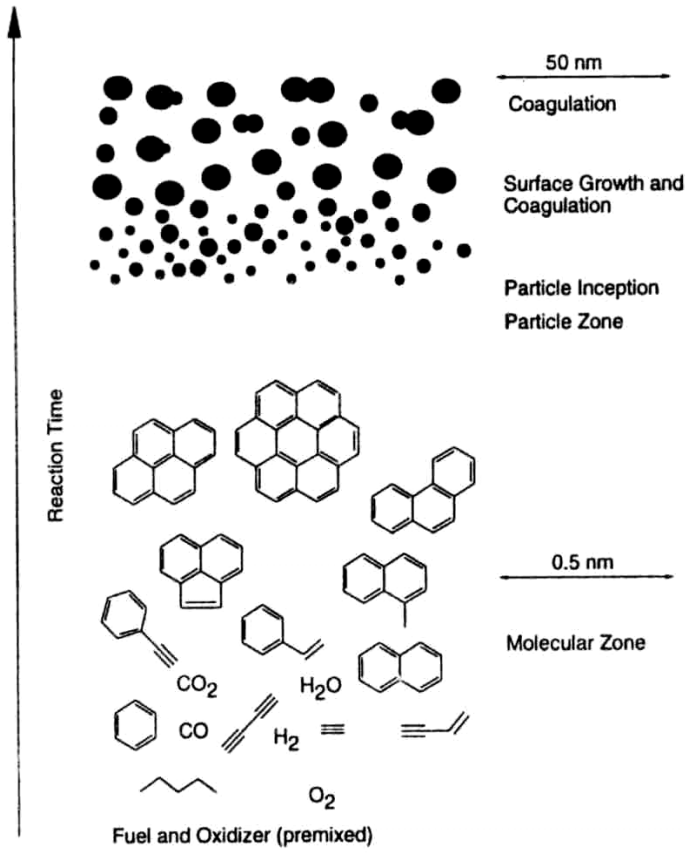

Figure 1-2: Representation of soot formation in premixed flames (Bockhorn (1994)).

1.3 Compression Ignition Engines

Internal combustion engines are widely used throughout the world for transport and power generation. One of the challenges for engine manufacturers is to lower NO_x and particulate matter (PM) or soot emissions in order to comply with the ever restrictive emissions standards. However, this must be achieved while CO_2 emissions are reduced as well, which means operating with high thermodynamic cycle efficiency. Low temperature combustion provides a possible future combustion regime as an alternative to the conventional diesel compression ignition combustion. Low temperature combustion offers the potential for lowering both NO_x, by having a lower combustion temperature, and soot emission, by increasing the local air/fuel ratio.

1.3.1 Conventional Diesel Compression Ignition Combustion

Compression ignition (CI) engines operate by compressing air, fuel is then introduced and mixed with the air close to top dead centre and parts of the mixture are ignited. The air and fuel mixture continues to burn by a combination of premixed and non-premixed combustion and flame propagation. CI engines operate at compression ratios of 12-24, with higher values having the potential to deliver higher thermal efficiency. The load of the engine is controlled by the amount of fuel injected into the combustion chamber.

One of the major benefits of CI engines is the higher efficiency compared with spark ignition engines, both in terms of pumping loss and thermal efficiency because of its higher compression ratio. There are however the disadvantages of its high NOx and high soot emissions. Advances have been made in the past 20 years with the development of common-rail injection system, exhaust gas recirculation (EGR) and variable turbine geometry in turbochargers which all help to address the problem of emission.

There are various variables that can be changed for altering the performance and emissions of the engine. Here is a list of some of the main variables.

1. Compression ratio

2. Injection nozzle design, timing and strategy and injection pressure
3. EGR rate
4. Pressure in (amount of boost/turbo charging)
5. Temperature in (related to EGR)
6. Valve opening/closing timing
7. Turbulence and mixing within the combustion chamber (combustion bowl and intake geometry)

The main output variables to be observed are:

1. Specific fuel consumption and efficiency
2. Emission (unburned hydrocarbons (HC), particulate matter (PM), NO_x, CO and CO_2)
3. Power output
4. Noise, vibration harshness

There are also a set of intermediate variables that can be measured in order to provide valuable information on the performance of the engine. These variables include the local and global equivalence ratio, in cylinder pressure, heat release rate, pressure rise rate, ignition delay, combustion duration and location of species and particles within the cylinder during combustion.

The process of diesel engine combustion can be broken down into three stages: an initial premixed burn with cool flame/low temperature reaction (LTR) and then the main mixing controlled burn phase and a late mixing controlled combustion phase. This is illustrated in the heat release chart in Figure 1-3. Studies have shown that an increase in injection pressure increases the magnitude of the LTR phase (Martin, Mueller et al. (2008)). For more detailed description of the two stage ignition process, along with supporting literature from chemical kinetics and optical diagnostics, see Musculus, Miles et al. (2013).

The detailed operation of a conventional diesel engine can be found in textbooks such as Heywood (1988) and Mollenhauer and Tschoeke (2010). Some correlations illustrating how the variables affects the output variables can be found in various

publications (Heywood (1988), Kook, Bae et al. (2005), Pickett, Siebers et al. (2005), Komninos, Hountalas et al. (2007), Manente, Tunestal et al. (2007)).

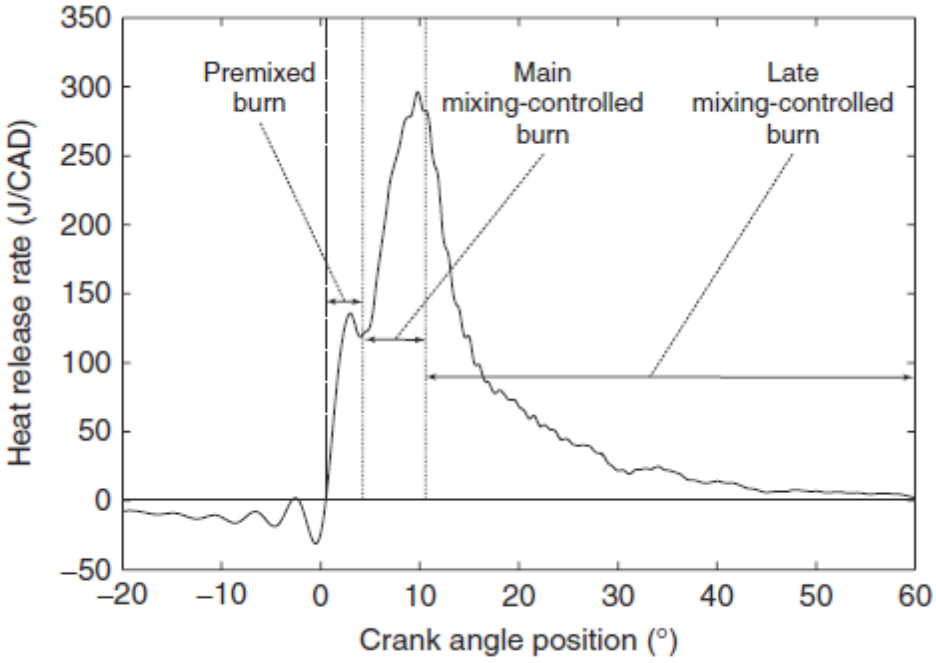

Figure 1-3: Different combustion phasing from a heat release rate of a 13L heavy duty diesel engine operated at 50% load.Andersson and Miles (2014).

1.3.2 Alternative Diesel Combustion Regimes

Current diesel technology suffers from the NO_x -soot trade-off phenomenon. This means steps taken to reduce NO_x usually increase soot emission and vice-versa. The reasoning for this is because soot formation in diesel engines generally occurs at 1000-2800K and at pressure between 50 and 100 atmosphere (Heywood (1988)). The majority of soot formation starts at 1500K and terminates at 2300K where NO_x formation occurs at 2000K and above. Ordinary diesel combustion occurs between 2000K-3000K and therefore within the operating region where soot and NO_x formation is high. Other than temperature, NO_x and soot formation also depends on local equivalence ratio. Generally, locally rich mixture generates soot and locally lean mixture produces NO_x (Kamimoto and Bae (1988)). Because conventional diesel is mainly non-premixed combustion in a non-homogeneous fuel and air mixture, the area of rich mixture produces soot whereas the lean area produces NO_x.

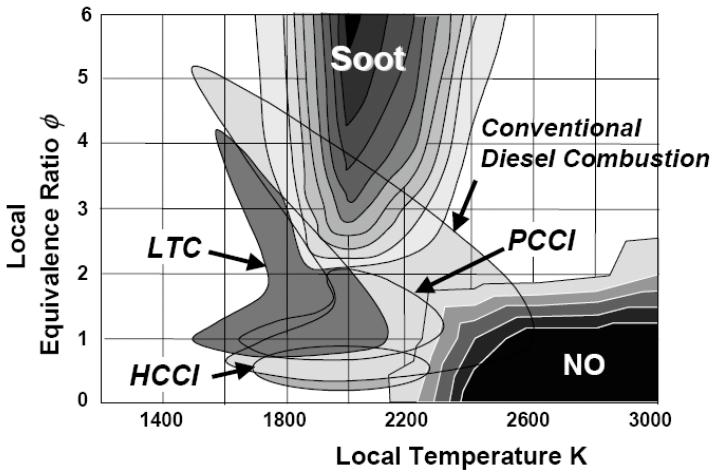

Figure 1-4: Modern diesel combustion strategies plotted in Φ–T space Koci, Ra et al. (2009)

Figure 1-4 shows the region where soot and NOx are produced, assuming premixed combustion, as a function of temperature and local equivalence ratio. As shown in the figure, there are possible combustion regimes which have low soot and NOx production, mainly in the area of low local temperature. The shaded areas in Figure 1-4 show the operating region for conventional diesel combustion, premixed charge compression ignition (PCCI), low temperature combustion (LTC) and homogeneous charge compression ignition (HCCI).

One way to reduce soot and NOx emission is to lower the temperature of combustion within the combustion chamber. Low temperature diesel combustion can be achieved by injecting fuel near top dead centre (TDC), delaying ignition by using high EGR allowing the fuel and air to become a more homogeneous mixture than would otherwise be the case. It can also be achieved by early injection (Iwabuchi, Kawai et al. (1999)) and by using a large amount of EGR and higher fuel injection pressure. Another method is to use a high level of cooled EGR, a lower compression ratio and use of retarded injection timing. Low temperature combustion is a mixing control combustion process in contrast to HCCI combustion where the combustion process is a more or less global autoignition. Combustion in HCCI mode is premixed because of the long pre-mixing time leading to mainly lean combustion and reducing the production of soot and NOx.

One of the main challenges to the use of LTC, HCCI and PCCI combustion is ignition control. In contrast to spark ignition engines which use spark to control timing, conventional diesel compression ignition engines inject fuel when combustion is required. Ignition in compression ignition alternative combustion regimes require a delay between the start and end of injection and ignition, and the longer the delay, the greater the reliance on chemical kinetics to determine the time at which ignition arises, governed mainly by temperature, pressure and species concentration. These factors cannot be directly controlled and require adjusting and coordinating various other variables. There is also the problem of limited load capacity as they do not cover the whole operational range of conventional diesel engines. Studies of this limit have been made (Knafl, Jacobs et al. (2006), Ishibashi and Morikawa (2007), Ishibashi and Morikawa (2008)). Higher load will lead to higher combustion temperature which then produces higher NOx and soot emissions, because of the increased amount of fuel to be burnt and hence lower global A/F ratio. Excessive ignition delay will cause an excessive amount of premixing which, once autoignition happens, usually results in a sharp rise in pressure which may exceed the generally acceptable level of combustion noise at $dP/d\theta$=300kPa/CAD (Tufail (2015)). There is also relatively higher emission of HC and CO (Jacobs and Assanis (2007)) which may not be as effectively oxidised in the vehicle's after treatment processes as the exhaust gas is not as hot as conventional diesel. There may thus be an increase in fuel consumption with the use of these alternative combustion regimes (Jacobs and Assanis (2007)).

There remains much work that can be done on looking at the more pre-mixed type combustion with the aim to primarily reduce soot and NOx, but attention needs to be paid to load capacity, pressure rise rate, HC and CO emissions due to early injections.

1.3.3 Low Temperature Combustion

There are different ways to reduce combustion temperature and soot and NO_x emission and this section outline the effects of different strategies. For example, the

increase of boost pressure advances autoignition timing and reduces pressure rise rate (Hasegawa and Yanagihara (2003)). Reduction of inlet air temperature first decreases then increases NO_x (Akagawa, Miyamoto et al. (1999), Musculus (2004)). For valve opening and closing timing, late intake valve closing has the equivalent effect of reducing compression ratio and can help with ignition control for early injection regimes (Duffy, Faulkner et al. (2004), He, Durrett et al. (2008), Murata, Kusaka et al. (2008)). Lowering compression ratio (Laguitton, Crua et al. (2007)), coupled with increased EGR (Noehre, Andersson et al. (2006)), reduces NO_x and soot emission. Parametric sweeps of engine variables have been carried out to find regimes which reduce soot, if not to provide a completely soot free combustion (Polonowski, Mueller et al. (2011)). All these enable combustion to operate in the LTC region and a conceptual model for partially premixed low-temperature diesel combustion has been developed in Musculus, Miles et al. (2013) and an overview can be found in Andersson and Miles (2014). The following variables have greater scope of reducing soot and NO_x emission.

1.3.3.1 Injection

Injection variables affecting combustion in a compression ignition engine include injection pressure, duration, timing, number of injections and injector design. Increased injection pressure has been shown to reduce smoke (see Table 1-1) as it increases mixing rate (Pickett, Caton et al. (2006)). Effects of nozzle design, configuration and size of injector orifice (see Table 1-1), injection rate shape (see Table 1-1), injection duration (Wang, Han et al. (1999)) have also been investigated.

Injection timing has an effect on combustion temperature because it changes ignition delay and mixing time affecting NO_x production (Iwabuchi, Kawai et al. (1999), Kook, Bae et al. (2005), Fang, Coverdill et al. (2009)). Effects of injection timing on auto-ignition have been studied (Kashdan and Papagni (2005)). Early, or retarded, injection also reduces soot as premixing is increased (Iwabuchi, Kawai et al. (1999), Kook, Bae et al. (2005), Musculus (2007), Fang, Coverdill et al. (2009)).

Variable	References
Increase of injection pressure reduces smoke	Badami, Nuccio et al. (1999), Inagaki, Takasu et al. (1999), Wang, Han et al. (1999), Dodge, Simescu et al. (2002), Hountalas, Kouremenos et al. (2003), Morgan, Gold et al. (2003), Okude, Mori et al. (2004), Atzler, Weigand et al. (2007), Karra and Kong (2008), Weigand, Atzler et al. (2008), Fang, Lee et al. (2010), Horibe, Tanaka et al. (2011)
Nozzle design, configuration and size of injector orifice	(Harada, Shimazaki et al. (1998), Akagawa, Miyamoto et al. (1999), Wang, Han et al. (1999), Dodge, Simescu et al. (2002), Okude, Mori et al. (2004), Lechner, Jacobs et al. (2005), Pickett, Caton et al. (2006)
Injection rate shape	Wang, Han et al. (1999), Juneja, Ra et al. (2004), Tanabe, Kohketsu et al. (2005), Kastner, Atzler et al. (2006), Kastner, Atzler et al. (2008), Pickett, Manin et al. (2013)
Narrow spray angle and retarded injection timing reduces NO_x and Soot	(Kimura, Aoki et al. (1999), Kimura, Aoki et al. (2001), Kimura (2002), Lee and Reitz (2003), Okude, Mori et al. (2004), Choi, Miles et al. (2005), Kook, Bae et al. (2005), Fang, Coverdill et al. (2009))

Table 1-1: Summary of references relating to studies conducted on different injection variables.

There are some disadvantages of using early injection which causes fuel to stick to the wall, reduces efficiency and causes oil dilution. Early injection may form rich mixture in the squish volume, increasing HC and CO emission (Kim, Ekoto et al. (2008)). The disadvantages of early injection may be minimised by using some of the following strategies. Lower pressure and more disperse spray angle helps with mixing and reduced wall wetting (Akagawa, Miyamoto et al. (1999), Iwabuchi, Kawai et al. (1999), Yanagihara (2001)) but a narrow spray cone for early injection was found to reduce soot and NO_x emission for low flow rate injector along with optimized EGR rate and split injection strategy (Lechner, Jacobs et al. (2005)). Cylinder liner impingement is a problem for early injection but can be adjusted

with a narrower spray direction (Walter and Gatellier (2002)) or employ the lower pressure early injection (Duffy, Faulkner et al. (2004), Sun and Reitz (2008)). Lowering of compression ratio helps with controlling ignition timing when early injection is used (Walter and Gatellier (2002), de Ojeda, Zoldak et al. (2008)). The effect of compression ratio on ignition delay has been investigated (Akagawa, Miyamoto et al. (1999)).

For injection closer to TDC, narrower spray angle together with high pressure and high mixing rate reduces smoke and NO_x. Retarded injection timing or near TDC injection reduces smoke and NO_x due to low temperature combustion (see Table 1-1), although there is an increase of HC emission (Musculus, Lachaux et al. (2007), de Ojeda, Zoldak et al. (2008)). Retarded injection forms over-lean regions in the squish volume and increase HC in that region (Kim, Ekoto et al. (2008)). The so-called Modulated kinetics (MK) mode employs retarded injection so mixing occurs during the expansion stroke, thereby delaying ignition (Kimura, Aoki et al. (2001)). Although another study found that retarded injection timing reduces soot and increases NO_x emission and it was possibly caused by reduced heat transfer through soot's radiative properties and increases temperature for NO_x production (Musculus (2004)).

Application of dual injection helps to reduce combustion temperature and reduce smoke and NO_x such as those used in UNIBUS (Hasegawa and Yanagihara (2003)) and other systems (Yokota, Kudo et al. (1997), Yanagihara (2001), Mueller, Martin et al. (2004)). Multiple injections and their effect on pollutant formation, has also been investigated (Kastner, Atzler et al. (2006), Kastner, Atzler et al. (2008)). The importance of post injections and its mechanism of pollutant reduction has been studied (Bobba, Musculus et al. (2010), Chartier, Andersson et al. (2011), O'Connor and Musculus (2013), O'Connor and Musculus (2014)). Even multiple injection using differently orientated injections has been tried (Akagawa, Miyamoto et al. (1999)).

Apart from soot and NO_x emissions, unburned hydrocarbons emission is also affected by injection timing (Harada, Shimazaki et al. (1998), Iwabuchi, Kawai et al. (1999), Kashdan, Mendez et al. (2007), Dec, Davisson et al. (2008), Ekoto, Colban et al. (2008)). Early injection increases HC emission because longer ignition delay produces lean mixtures near the injector which is too lean to combust (Lachaux and Musculus (2007)). This may be caused by the transient ramp-down at the end of injection which has a low momentum producing the excessively lean mixture which is exhausted as unburned hydrocarbons (Musculus, Lachaux et al. (2007)). Another study found the sources of unburned hydrocarbons comes from nozzle dribble and incomplete reactions within the cylinder core and side wall above the crevice region (Ekoto, Colban et al. (2008)).

There are gaps within the literature which can be investigated. Variation of injection pressure and advanced timing, coupled with multiple injections with a post injection to identify the effects of these on in-cylinder combustion processes and soot and emissions will be useful, with specific attention paid to HC and CO productions and load limitation.

1.3.3.2 EGR Rate

EGR rate affects the amount of soot and NO_x in the cylinder (see Table 1-2). The influence of EGR on auto-ignition generally has been investigated (see Table 1-2). EGR and its effect on auto ignition and soot formation was investigated in detail in Idicheria and Pickett (2011). High level of cooled EGR controls the ignition process and prevents premature ignition when early injection is used (see Table 1-2). The modular kinetics (MK) system also employs high EGR rate to delay auto ignition. Increased EGR rate has been shown to reduce NO_x by suppressing peak combustion temperature to accommodate early or retarded injection timing (Kook, Bae et al. (2005)). There is however the problem of high CO emission for high EGR rate with retarded injection or high EGR rate in general (see Table 1-2).

As EGR is increased, soot first increases and then decreases (Akihama, Takatori et al. (2001), Idicheria and Pickett (2005), Huestis, Erickson et al. (2007)). The initial

increase is aided by longer soot residence time in the reacting fuel jet for moderate EGR (Idicheria and Pickett (2005)) and lower soot oxidation due to lower oxygen level (Huestis, Erickson et al. (2007)). For higher EGR, the combustion temperature is reduced so soot formation is limited (Akihama, Takatori et al. (2001), Idicheria and Pickett (2005), Huestis, Erickson et al. (2007)). Within a diesel spray, higher EGR causes soot to form in regions further away from the injector in the radial and axial direction (Idicheria and Pickett (2005)).

Variable	References
EGR rate on soot	Baert, Beckman et al. (1996), Akihama, Takatori et al. (2001), Idicheria and Pickett (2005), Atzler, Weigand et al. (2007), Huestis, Erickson et al. (2007), Jacobs and Assanis (2007), Weigand, Atzler et al. (2008), Aronsson, Sjöholm et al. (2010)
EGR rate on NOx	Atzler, Weigand et al. (2007), Jacobs and Assanis (2007), Weigand, Atzler et al. (2008), Sjoberg and Dec (2009)
EGR on autoignition	Akagawa, Miyamoto et al. (1999), Per Risberg (2004), Kashdan and Papagni (2005), Kalghatgi, Risberg et al. (2007)
EGR to prevent premature ignition	Akagawa, Miyamoto et al. (1999), Walter and Gatellier (2002), Okude, Mori et al. (2004), Sjoberg, Dec et al. (2007)
High CO emission for high EGR rate	Akihama, Takatori et al. (2001), Kook, Bae et al. (2005), Noehre, Andersson et al. (2006), Atzler, Weigand et al. (2007), Kim, Ekoto et al. (2008)) and HC emission (Noehre, Andersson et al. (2006), Atzler, Weigand et al. (2007), Kim, Ekoto et al. (2008)

Table 1-2: Summary of references relating to studies conducted on different EGR variables.

Conventional EGR operates by inducting cooled exhaust gas into the intake manifold from the exhaust. EGR can also be supercharged into the cylinder by opening of exhaust gas valve during the intake stroke utilising the exhaust blow-down pressure wave from other cylinders (Kuboyama, Moriyoshi et al. (2009)). This creates a large thermal stratification, reduces pressure rise rate and extends

load range in gasoline HCCI. Simulating the effect of increase EGR has been shown to reduce soot precursor formation rate but increased the residence time for soot precursor formation (Pickett, Caton et al. (2006)). The effect of the quality of EGR has on combustion has also been investigated (Sjoberg and Dec (2009)). It was found that maximum indicated mean effective pressure (IMEP) using simulated EGR in HCCI combustion is limited by the amount of oxygen. Whereas maximum IMEP using real EGR is limited by EGR, NOx and wall heating induced run-away.

More fundamental research on EGR's effect on combustion has been done regarding low temperature diesel combustion (Kook, Bae et al. (2005), Pickett (2005)). Studies have been done to look at the effect of different oxygen contents (Pickett (2005)) and also combined with fuel injection timing variation (Kook, Bae et al. (2005)) on combustion phasing and emission. Distinctions have been made between phases of premixed and mixing-controlled combustion at these different settings.

The use of EGR in engine is important for the reduction of smoke and NO_x and the understanding of the effects of EGR on spray and droplet formation, affected by injection parameters such as injection pressure, will provide information on the fundamental mechanism of emission formation.

1.3.3.3 Lean/Rich Mixture Combustion

Lean and rich combustion can be achieved by varying EGR, injection pressure and timing to reduce NO_x and soot (Okude, Mori et al. (2004), Jacobs and Assanis (2007)) but this also changes the fuel consumption (Jacobs, Bohac et al. (2005)). Mixture stoichiometry can also be altered by changing the amount of fuel injected which affects auto ignition timing (Akagawa, Miyamoto et al. (1999)). Retarded injection near top dead centre reduces mixing and prevents over rich zone to form and reduces NO_x and soot (Okude, Mori et al. (2004)). Rich diesel combustion can be achieved by increased level of EGR and reduced combustion temperature to limit soot and NO_x formation (Akihama, Takatori et al. (2001), Jacobs, Bohac et al.

(2005)) but this increased fuel consumption (Jacobs, Bohac et al. (2005), Jacobs and Assanis (2007)).

It was found that soot formation in low temperature combustion is relatively insensitive to air/fuel ratio (Jacobs and Assanis (2007)). Similarly, lean diesel combustion also reduces NO_x and soot emission but also increases fuel consumption, carbon monoxide and hydrocarbons emission (Akagawa, Miyamoto et al. (1999), Jacobs, Bohac et al. (2005)). Near stoichiometric operation along with high EGR and low compression ratio also lowers NO_x and soot (Noehre, Andersson et al. (2006)). But over-mixed and over lean fuel/air mixtures were found to be the main source of HC and CO emissions (Petersen, Miles et al. (2012)), so a balance will need to be achieved. More studies are required to find ways to maintain the reduction of soot and NO_x and attempt to reduce HC and CO emission.

1.3.3.4 Bowl Shape and Geometry

Bowl shape and geometry has an impact on diesel engine combustion as these affect spray dynamics, mixing and mixture formation. Bowl shape and different injection pattern from different injectors were investigated for mixing and spray wall interaction (Harada, Shimazaki et al. (1998), Akagawa, Miyamoto et al. (1999), Kashdan, Docquier et al. (2004)). A larger bowl diameter reduces impingement and provides a leaner jet but a higher proportion of the jet becomes too lean to combust with soot forming in the centre of the jets (Genzale, Reitz et al. (2008)). A smaller bowl encourages more mixing and provides a generally leaner mixture with soot forming between the jets (Genzale, Reitz et al. (2008)). Turbulence and mixing within the combustion chamber is also affected by combustion bowl design and intake geometry. Swirl affects combustion processes such as ignition delay, rate of heat release and peak heat release (Miles (2000)).

Wall temperature will have an influence on the combustion of diesel fuel in the cylinder as it provides a thermal stratification forming a boundary layer near the wall. Increased wall quenching by changing the distance between the top ring and top surface of the piston was shown to reduce CO and HC emission (Akagawa,

Miyamoto et al. (1999)). Changing the injection timing in a wall guided diesel combustion chamber showed large variation of HC emission. This was caused by mixing induced bulk quenching and temperature stratification within the bowl (Kashdan, Mendez et al. (2007)). Bowl geometry played a significant part in combustion and emission for late injection HCCI mode when two bowl shapes were compared (Kashdan, Docquier et al. (2004)).

Variation of bowl shape and geometry is limited in its application as usually one shape is used for all load and speed of an engine and it is difficult for it to be optimised for all conditions. Further work can be done on the variation of injection pressure and combination of bowl shape and dimension to better understand the optimal combination of the two in terms of wall wetting and HC and CO emission. The increase in turbulence by swirl and bowl design can also be included for further study.

1.3.3.5 Fuel Properties

Research into properties of diesel and other fuels has been investigated extensively for the purpose of diesel combustion control (Siebers (1985), Kalghatgi, Risberg et al. (2003), Kalghatgi and Head (2004), Per Risberg (2005), Pickett and Hoogterp (2008)). Computer simulation which makes use of detailed or global chemical kinetics is useful because modern fuels are blended with a large number of different hydrocarbons. Simplification made to the chemistry is necessary in order to produce a model which is close to the properties of the fuel being simulated, while retaining a necessary level of complexity to reproduce the underlying chemistry is sufficient detail..

Investigation of the auto-ignition properties of fuel is useful because auto-ignition is important for HCCI/low temperature combustion operations so the combustion can be controlled adequately. Changes to the fuel used will have an effect on auto ignition consequent on changes to the chemical kinetics (Hwang, Dec et al. (2008), Morgan, Smallbone et al. (2010)) and experiments on autoignition of different fuels have been carried out (Akagawa, Miyamoto et al. (1999), Kalghatgi, Risberg

et al. (2007), Kalghatgi, Risberg et al. (2007), Fikri, Herzler et al. (2008), Kalghatgi, Hildingsson et al. (2009)). The effect of fuel chemistry on combustion phasing has been investigated as a way to control ignition using fuel stratification (Dec and Sjoberg (2004), Kokjohn, Reitz et al. (2012)).

Blends of primary reference fuels (PRF) are a useful way, and perhaps the only way, to simplify the chemical kinetics involved in commercial fuel blends. The balance to be struck is to avoid the number of species and reactions becoming too numerous and computationally expensive but detailed enough to represent the fuel adequately. Also, application to internal combustion engines requires a more specific approach than general chemical kinetics. Specific models matching the range of conditions expected in an engine will be more productive. In addition, chemical kinetics provides information as to whether a particular reaction takes place under certain conditions (Andrae, Johansson et al. (2005), Naik, Pitz et al. (2005), Andrae, Bjornbom et al. (2007), Andrae, Brinck et al. (2008), Smallbone, Morgan et al. (2010)).

Investigation of fuel properties is important to understand their effect on autoignition and combustion. But given commercially available fuels are generally manufactured to a specific standard and composition, its application to engine design is limited unless a major stakeholder, such as a large oil company, is involved to provide the infrastructure of a new fuel product. Nonetheless, this can be further developed and it will be discussed in more detail in Section 1.3.5 on gasoline compression ignition engine.

1.3.4 Homogeneous Charge Compression Ignition (HCCI)

Homogeneous charge compression ignition (HCCI) has the advantage of low NO_x and soot emission, because he global equivalence ratio is limited to values below about 0.5, which inevitably results in relatively small operating load, with similar efficiency to diesel combustion in part load because of low pumping loss. HCCI operates by having a more or less homogenous mix of fuel and air within the combustion chamber and the whole charge auto ignites when the pressure and temperature

necessary for autoignition is reached. One challenge for HCCI combustion is controlling the autoignition timing. The small operating load limit restricts the application of HCCI but some of the principles of HCCI can be applied to partially premixed diesel and low temperature combustion.

Controlling methods for HCCI combustion include altering inlet temperature and/or pressure, fuel injection strategies, EGR rate, compression ratio, timing for valves closing and opening and equivalence ratio. Autoignition quality of the fuel, EGR quality, EGR unmixedness and pressure rise rate affect the high-load limit of HCCI combustion (Sjoberg and Dec (2009)). Study of the effect of boost pressure in HCCI condition has been conducted from a chemical kinetics point of view (Silke, Pitz et al. (2008)). Modelling with CFD on a range of equivalence ratios was conducted to compare with research engine data (Hessel, Foster et al. (2008)).

Thermal stratification affects combustion in HCCI operation which is caused by wall heat transfer and large scale turbulence transport. Simulations have been used to investigate the thermal stratification effect on HCCI combustion (Aceves, Flowers et al. (2002), Aceves, Flowers et al. (2004)) and compared with experiments in engines (Sjoberg, Dec et al. (2005)). The main objective in studying thermal stratification is to understand how thermal stratification controls ignition and combustion phasing. It is also used for increasing high and low load limits and decreasing pressure rise rate. Development of thermal stratification during the compression and expansion stroke was investigated and the thickness of the thermal boundary layer was identified (Dec and Hwang (2009)). Effects of thermal and compositional stratification on HCCI combustion have been investigated in a test engine and found competing stratification effects makes technological application difficult (Herold, Krasselt et al. (2009)).

Fuel stratification controlled by fuel injection strategy can be used to control combustion phasing and reduce pressure rise rate. It can also extend the limit of high and low load HCCI operation. Dual injection consisting of one injection in the intake stroke and one in the compression stroke was found to reduce pressure rise rate and

heat release rate as well as increase IMEP (Sjoberg and Dec (2006)). However, it was noted that injection penetration may have to be altered as early injection can lead to wall wetting and increased NO_x emission (Sjoberg and Dec (2006)). Retarded injection timing changes stratification and improves combustion efficiency. It also reduces penetration of fuel towards the wall and crevice while creating a rich fuel zone for complete combustion (Dec, Davisson et al. (2008)). Leaner mixture increases hydrocarbons and oxygenated hydrocarbon emissions (Dec, Davisson et al. (2008)) and injection timing also affects unburned hydrocarbons emissions (Dec, Davisson et al. (2008)).

The effect of the autoignition quality of a fuel and load limit in HCCI has been explored and fuel with medium reactivity was found to produce the highest IMEP (Sjoberg and Dec (2008)). Comparison of gasoline and diesel fuel has been done for HCCI and MK system and higher resistance to autoignition is more advantageous by encouraging premixing (Kalghatgi, Risberg et al. (2007), Kalghatgi, Risberg et al. (2007)). The effect of fuel volatility on HCCI combustion has been investigated (Collin, Nygren et al. (2004)) and effects of oxygenates on soot formation processes has been researched (Mueller, Pitz et al. (2003)). Spectroscopy and chemical kinetics of HCCI combustion of single and two stage ignition fuels has been conducted and stages of ignition and combustion have been identified (Hwang, Dec et al. (2008)). The combustion stability of single and two stage ignition fuel in HCCI combustion has also been studied (Sjöberg and Dec (2007)). In addition, the use of blends of Diesel with biofuels may also modify the ignition delay in an advantageous way.

The limitation of HCCI has been discussed with its limited practical application. However, insofar as PCCI and LTC have aspects of combustion which are similar to HCCI, understanding the effects of changing operation strategy and of variables leads to useful guidelines, at least in the initial stages of research, for the operation of HCCI and LTC regimes.

1.3.5 Gasoline Compression Ignition

Another way to reduce emission of the diesel engine combustion is to utilise fuel chemistry and properties to overcome the problems of LTC and HCCI. The concept of using gasoline like fuel in a compression ignition has been tested to provide diesel like efficiency with reduced NOx and PM emission (Kalghatgi, Risberg et al. (2006), Kalghatgi, Risberg et al. (2007), Sellnau, Sinnamon et al. (2011)). There has been report of peak gross indicated efficiency of 57% (48.47% brake efficiency) in heavy duty engines showing the promising potential of this combustion system (Manente, Johansson et al. (2009), Splitter, Hanson et al. (2011)). The mechanism behind this concept is the auto ignition resistance quality of gasoline which means that the fuel injection can take place earlier than would have been the case with diesel fuel allowing for more premixing and hence producing less NOx and soot. The longer mixing time also means fuel can be injected at lower injection pressure to prevent wall impingement/wetting. This also brings the possibility of lower injection equipment cost and parasitic losses because of the lower injection pressure required. There is yet further reduction in cost because there is no need of after treatment for NOx and soot.

However, conventional gasoline fuel is not the ideal fuel for this mode of combustion as its high resistance to auto ignition means there is the possibility of misfiring and lack of ignition reliability. In contrast to conventional diesel fuel and its propensity for auto ignition, early injection and long mixing time creates early combustion phasing and limited load capacity. Fuels with different octane number (Hildingsson, Kalghatgi et al. (2009)) and fuel type such as naphtha (Viollet, Chang et al. (2014)) have been tested. There is a need for lower octane gasoline for this type of combustion system which will not only benefit the vehicle emission, it will result in lower energy cost in producing a less volatile fuel than current gasoline from the refinery perspective.

Various aspects of gasoline compression ignition have been investigated such as the lower load limit (Weall and Collings (2009), Borgqvist, Tunestal et al. (2012),

Kolodziej, Ciatti et al. (2014)), various injector designs and compression ratios (Won, Peters et al. (2013)) and injection pressures (Kolodziej, Ciatti et al. (2014)) to compensate for the lower load.

In addition to challenges at low and high load, other obstacles such as cold start and idle, hardware optimisation and fuel quality will need to be resolved. For this study, the investigation of the viability of using gasoline in a compression ignition engine begins in Chapter 4 of this thesis. The composition, properties and blending of gasoline will be described in order to understand the fuel chemistry which may assist in designing a better fuel blend for gasoline compression ignition. This is a starting point in the application of gasoline compression ignition engine.

1.3.6 Diesel Spray Dynamics

One of the important aspects in diesel combustion is diesel spray dynamics. The understanding of the physics behind spray behaviour may allow for future improvement in injector design and injection strategy and minimise emissions and improve efficiency.

An overview of diesel spray combustion in general has been produced (Flynn, Durrett et al. (1999)). Study has been done on the liquid and vapour spray structure for diesel injection (Bruneaux (2001), Pickett, Manin et al. (2011)). High speed imaging and multiple optical diagnostics have been applied to further understand spray dynamics with regard to liquid and vapour phase location, penetration length, soot formation locations and low and high temperature reactions (Pickett, Kook et al. (2009)).

Study of diesel jet combustion in a constant volume combustion vessel has been conducted to understand how the change of ambient temperature and oxygen concentration affects variables such as the location of species formation, lift-off, soot and the dynamics of diesel jet combustion (Idicheria and Pickett (2007)). A conceptual model for reacting diesel jet has been developed (Idicheria and Pickett

(2007)) which was compared with a two-stage Lagrangian model of a reacting jet (Pickett, Caton et al. (2006)).

Some of the features of spray dynamics are presented below and firstly, the Dec (1997) conceptual model of soot formation in diesel spray gives an overview of the mechanism involved, at least for heavy duty diesel operation.

1.3.6.1 Dec's Conceptual Model of Soot Formation in Diesel Spray

The idealised model of diesel jet combustion begins with the premixed burn phase. As the diesel jet is injected into the cylinder, the liquid phase of the jet grows and vaporizes as hot air is entrained into the jet to form an air-vapour mixture at the end of the liquid phase. The air-vapour mixture continues to grow and is then ignited to form polycyclic aromatic hydrocarbons (PAH). This produces natural soot luminosity, which gradually grows to cover the whole area of the air-vapour mixture. There is also soot particle formation around the periphery of the plume by means of a non-premixed flame. This then progresses towards the second phase of the jet combustion, namely mixing-controlled combustion (Eastwood (2008)).

Dec's conceptual model of mixing-controlled combustion of diesel spray provides an overview of the general combustion zones within the plume as shown in Figure 1-5 (Dec (1997)). Soot formation begins in the premixed flame area and grows in size and concentration while travelling down the plume towards the head vortex. Particle size is the largest and with the highest concentration at the head vortex. There is also a second soot formation zone in the area of the non-premixed flame on the plume periphery. The particle size in the plume periphery is larger than in the plume stem but smaller than those in the head vortex. The concentration is similar between the head vortex and the plume periphery (Eastwood (2008)). This soot conceptual model of diesel spray has been experimentally investigated and compared with operating at no engine-out smoke operating point (Chartier, Aronsson et al. (2009)).

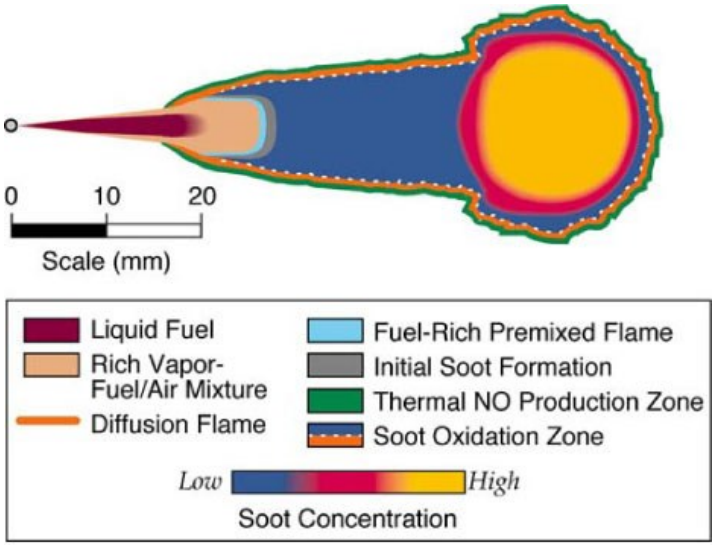

Figure 1-5: Dec conceptual model of soot formation within diesel spray (Dec (1997)).

1.3.6.2 Liquid Length, Penetration and Flame Lift Off

The liquid length of the spray affects penetration and mixing in the combustion chamber. For low temperature combustion, liquid fuel penetrates further before vaporizing than in conventional diesel combustion (Musculus (2007)). There is greater pre-combustion mixing forming leaner mixture and soot is formed further downstream than conventional diesel combustion (Musculus (2007)).

Models for diesel injection length tip penetration has been presented in Hiroyasu and Arai (1990) and Yule and Filipovic (1992) which can be used to compare fuel injection spray penetration measurements. Siebers (1998) provided a scaling law gives the liquid length of a fully developed diesel spray as opposed to a transient liquid penetration distance. Desantes, Payri et al. (2006) also developed a model for diesel spray tip penetration based on momentum flux conservation. And liquid length at various conditions such as injection pressure and ambient density have been investigated (Kennaird, Crua et al. (2002), Abdelghaffar, Karimi et al. (2007), Genzale, Pickett et al. (2010)).

Flame lift off length is another important variable as it affects air entrainment and soot formation. This is the distance between the injector hole and the start of combustion and this determines how much air is entrained, hence mixing

before premixed combustion. Siebers and Higgins (2001), Siebers, Higgins et al. (2002) and Pickett, Siebers et al. (2005) showed lift-off length decreases when ambient gas temperature, density and oxygen concentration increases and its effect on soot concentration.

Fuel injector design will have an effect on liquid penetration as penetration length decreases linearly with smaller injector orifice (Siebers (1998), Pickett, Kook et al. (2009)). Single and multiple orifice injectors on rate of penetration (Abdelghaffar, Karimi et al. (2007)) and pressure fluctuation at injector nozzle has been compared (Kennaird, Crua et al. (2002)). Increasing Injection pressure increases spray penetration length (Abdelghaffar, Karimi et al. (2007)) and has no significant effect on liquid length (Siebers (1998)) and increase of temperature and pressure decreases liquid penetration length (Siebers (1998), Pickett, Kook et al. (2009)). But there is a trade-off between temperature and pressure as an increase in pressure raises the boiling point temperature of the fuel and increases air entrainment. Both of these factors affect liquid penetration length (Pickett, Kook et al. (2009)).

Multiple injections significantly reduce liquid penetration compared to single long steady injection (Pickett, Kook et al. (2009)). The increase of EGR lengthens the lift-off length of diesel spray and pushes the soot formation region downstream and stretches it out (Siebers, Higgins et al. (2002)). There is an effect on interaction due to change in inter-jet spacing and jet length and evaporative cooling (Lequien, Berrocal et al. (2013)). CFD on diesel sprays has provided some understanding as to the mechanism of mixing and lift off (Campbell, Gosman et al. (2008)).

With regard to fuel properties, decreasing fuel volatility or fuel temperature increase the liquid length (Siebers (1998)). Evaporation in a diesel spray happens with higher volatility components and liquid length is controlled by the lower volatility components (Siebers (1998)). Fuel with a lower boiling point was shown to have less liquid penetration (Pickett, Kook et al. (2009)). The Injection duration

must be shorter than the time taken for the spray to reach steady state in order to reduce maximum liquid penetration compared with the quasi-steady liquid length (Pickett, Kook et al. (2009)).

Understanding the physics behind spray dynamics is important to the mixing with air and has a significant effect on emissions. More work can be done on the transient injection with regard to penetration, liquid length and its influence on multiple injections. Spray to spray variations and their effect on combustion will be another interesting variable to study.

1.3.6.3 Entrainment

As described in the diesel spray combustion model, the mixing of air and fuel within the fuel jet involves air entrainment as the jet propagates away from the injector. Air entrainment is fundamental to mixing of fuel and air which determines the fuel air ratio and hence product formation. The vaporization of diesel spray is governed by air entrainment and is not limited by atomization and local interphase transport processes (Siebers (1998)). The effect of air density on air entrainment showed that higher ambient gas density caused more air entrainment in the spray and led to higher spray dispersion but reduced spray penetration (Naber and Siebers (1996)). Air entrainment in a diesel like gas jet was visualised in Bruneaux, Causse et al. (2011) where the effect of wall impingement and aerodynamic structures were analysed. More study can be done at investigating injector design and injection pressure on various variables such as the mechanism of air entrainment.

1.3.6.4 End-of-Injection

End-of-injection dynamics are affected by injection pressure, nozzle size, ramp down rate, fuel volatility and ambient temperature (Kook, Pickett et al. (2009), Musculus and Kattke (2009)). The start of injection spray dynamics has also been investigated (Crua, Shoba et al. (2010)). Spray dynamics relating to end-of-injection has shown maximum liquid penetration length to recede towards the

injector after end-of-injection. This is because fuel flow rate decreases during ramp down of the rate of injection (Kook, Pickett et al. (2008)). The end-of-injection event increases the rate of air entrainment into the jet which begins at the injector nozzle and travels downstream as an entrainment wave (Kook, Pickett et al. (2008)). This entrainment causes over lean mixture leading to incomplete combustion and produces HC emission. A model of entrainment wave in diesel jets has been developed to better understand the physical to investigate how various variables such as injector design and injection pressure affect the mechanism of end of injection.

1.3.6.5 Wall Interaction

Wall and spray interaction is important as this is related to bowl geometry for in-cylinder application. Research into droplet sizes in a spray against a wall has been investigated (Park and Lee (2004)). Diesel jet impingement on a wall was shown to have less mixing in the centre part of the jet before impact (Bruneaux (2005)). The wall vortex increase the mixing rate at the jet tip because more air was being entrained compared to a free jet (Bruneaux (2005)). From Bruneaux (2008), the presence of a wall at an angle to the jet was found to significantly affect the mixing structure in the spray confining the jet to the wall upstream. It also changed the fuel concentration upstream significantly and increased ignition delay. A small incident jet-wall angle reduced soot formation because of improved mixing. Whereas higher incident angle reduced mixing and increased soot formation due to confinement of the jet to the wall. The effect of injection pressure and bowl wall on fuel/air ratio was investigated in Chartier, Sjoholm et al. (2012). Variation of injection pressure and the interaction of bowl wall with the jet was investigated (Rusly, Le et al. (2013)). More work can be done on the combined effect of the interaction of various jets at the wall instead of individual spray.

1.3.6.6 Double Injection

Study of double injection has been shown to increase mixing at the head of the second jet but the effect diminished as dwell time (time between the two injections) was increased in Bruneaux and Maligne (2009). Soot and PAH were formed in the second jet due to combustion at a higher temperature as hot air from the combustion of the first injection was entrained into the second jet; no soot and PAH were found in the combustion of the first jet. Also, longer dwell time created intermediates which promoted the early ignition and combustion closer to the injection nozzle, leading to fuel rich combustion producing soot and PAH. Studies of double injection using multiple diagnostic techniques and high speed imaging provided further understanding of the dynamics of two injections (Pickett, Kook et al. (2009), Pickett, Kook et al. (2009)). Closely spaced double injection generally reduces liquid and vapour penetration (Parrish, Zhang et al. (2012)). More work can be done on closely coupled injection and the effect of the first injection has on speed and penetration of the second. The pressure wave effect in the high pressure fuel line during multiple injections should also be further examined.

1.3.7 Summary

This set of literature provides a background on how different variables affect emissions and other engine output regarding diesel combustion, HCCI, PCCI and low temperature diesel combustion. The work on spray dynamics provide an overview of the physics in diesel spray and how it may be applied in an engine.

Comparing different combustion regimes, PCCI/low temperature combustion seems to have the benefit of the range of loads and control over HCCI. HCCI shows what compression ignition combustion can achieve in terms of low emissions but low temperature combustion has the potential to be fully implemented in production engines.

There are gaps within the literature where individual or a combination of the following variables can be investigated. These variables include variation of injection pressure and advanced injection timing, coupled with multiple injections with a post injection, the use of EGR, change of bowl shape and dimension, increase in turbulence and swirl. Further understanding of the effect of spray to spray variations and injection will also be useful. The questions to be answered are what effects of these variables have on in-cylinder combustion processes and soot and NOx emissions, with specific attention paid to HC and CO productions and load limitation. Their effects on spray and droplet formation, air entrainment, end of injection, pressure wave effect in high pressure fuel lines provide ample opportunities for further work.

The aim of this research is to use low temperature combustion in a diesel engine to reduce soot and NO_x output without increasing HC and CO emission which reaches high load and produces low noise, vibration and harshness. Simulations are useful for looking at possible combination of settings which may then be applied to real engine combustion testing. In general, using the information outline in this section, early and high pressure injection into combustion chamber with high EGR looks to achieve low soot and NO_x. Combined with using different fuels, dual or multiple injections and comparing different bowl geometries, this provides a useful set of variables to find how soot production and emissions are affected.

1.4 Optical Diagnostic Techniques

This section gives an overview of the widely used optical techniques that can be applied in combustion studies relating to internal combustion engines. Most of the information comes from Chapter 16 of Zhao (2010). The problems associated with working with lasers and optical equipment in optical vessels and engines have been discussed (Musculus and Pickett (2005)). Some of these techniques include:

1) Laser Induced Fluorescence (LIF)
2) Particle Imaging Velocimetry (PIV)

3) Laser Doppler Velocimetry (LDV)
4) Phase Doppler Anemometry (PDA)
5) Spontaneous Raman Scattering
6) Shadowgraph
7) Schlieren Imaging
8) Light Extinction Method

Other techniques that were used in for the thesis are described in more detail below.

1.4.1 Chemiluminescence

Chemiluminescence is the imaging of the light emitting from combustion by filtering at a certain wavelength. This allows detection of the locations of combustion zones (Herold, Krasselt et al. (2009)) and can lead to analysis of cycle-to-cycle variations (Hultqvist, Christensen et al. (1999)), through identification of specific species such as CH, C_2 and OH (Idicheria and Pickett (2007), Chartier, Andersson et al. (2011), Kokjohn, Reitz et al. (2012)) and flame lift-off by OH chemiluminescence (Aronsson, Chartier et al. (2009), Kook and Pickett (2012), Rusly, Le et al. (2013), Manin, Skeen et al. (2014)). Flame front structures can be visualised by CH and C_2 signals and air/fuel ratio can be estimated using intensity ratios of these signals (Ikeda, Kaneko et al. (2001)). The requirement for applying this technique is optical access to combustion and the image can be acquired using an intensified charged coupled device (iCCD) camera or high speed camera.

For visualisation of the pre-ignition cool flame in the low temperature reaction, formaldehyde (HCHO*) and aldehyde (HCO*) chemiluminescence can imaged (Idicheria and Pickett (2011)) as low temperature reaction is characterised by formaldehyde chemiluminescence (Sheinson and Williams (1975)). A spectrometer can be used to analyse the species involved as different species give out a different wavelengths of light during combustion (Hultqvist, Christensen et al. (1999), Kashdan, Docquier et al. (2004)). A streak camera can also be used to take consecutive images on the progression of combustion (Hultqvist, Christensen et al. (1999)).

1.4.2 Mie Scattering

Mie scattering applies to light scattering from droplets when the droplets are larger than the wavelength. Mie scattering can be used for spray visualisation giving the spray penetration and spray angle (Munch (1992), Higgins, Siebers et al. (1998), Siebers (1998), Bruneaux, Verhoeven et al. (1999), Park and Lee (2004), Musculus (2007), Kook, Pickett et al. (2008), Chartier, Aronsson et al. (2009), Pickett, Kook et al. (2009), Fang, Lee et al. (2010), Pickett, Manin et al. (2011), Parrish, Zhang et al. (2012), Lequien, Berrocal et al. (2013)). Mie scattering operates by recording the elastically scattered light off liquid phase droplets. The light recorded will be of the same wavelength as the light source. Mie scattering is potentially difficult to employ in an engine because of strong reflection from the surrounding walls.

1.4.3 Rayleigh Scattering

The principle of Rayleigh temperature measurement is the scattering of radiation energy by molecules in a gas mixture of the incident the radiation source wavelength. It can be understood by photons from radiation source colliding with particles in the gas mixture. If this collision is perfectly elastic, the photons deflected will remain unchanged in wavelength and this is Rayleigh scattering. More on this subject can be found in a review by Zhao and Hiroyasu (1993). Work carried out on temperature measurement of a flame on a McKenna burner is described in Appendix B of this thesis.

The main uses of Rayleigh scattering are measurement of concentration, density and temperature of the gas in various combustion regimes such as open flames and internal combustion engines. It can also be used to measure flame thickness in flow fields, hot and cold jets, boundary layers, confined vessels and reciprocating engines. This can also be combined with other methods for simultaneous measurements (Zhao and Hiroyasu (1993)). It has been used in engine for temperature measurement (Schulz, Sick et al. (1996)), fuel/air ratio (Espey, Dec et al. (1994), Espey, Dec et al. (1997)), and fuel vapour density (Espey, Dec et al. (1997), Schulz, Gronki et al. (2004), Vogel, Hasse et al. (2005), Idicheria and Pickett (2007),

Musculus, Lachaux et al. (2007)). Application of Rayleigh imaging to quantitative mixing measurement of an evaporating diesel spray in combustion vessel has been extensively discussed (Idicheria and Pickett (2007), Pickett, Manin et al. (2011)). The effect of EGR on equivalence ratio and ignition delay has been studied using time resolved Rayleigh scattering measurement and found that EGR increases ignition delay, average flame lift off distance and gives a spatial distribution of equivalence ratio at different EGR input for diesel injected into a pressurised combustion chamber (Idicheria and Pickett (2007)).

The Rayleigh signal is directly proportional to the laser intensity, density and Rayleigh cross section. The intensity of Rayleigh scattering signal, I_{Ray} is given by Equation (1-2).

$$I_{Ray} = \eta_c I_i \Omega V_c N \sum_{i=1}^{j} \chi_i \sigma_i \qquad (1\text{-}2)$$

where η_c is the detection efficiency of the collection system, I_i is the incidental laser intensity (W/cm^2), V_c is the collection volume (cm^3), Ω is the solid angle of collection optics (sr), χ_i is the mole fraction of the species i in the mixture and σ_i is the Rayleigh cross-section of the individual species in the gas mixture.

N is the total molecular density and is defined by Equation (1-3).

$$N = \frac{P A_0}{R T} \qquad (1\text{-}3)$$

where P is the pressure, A_0 is Avogadro's number, A_0=6.023x10^{23} molecules/mol, T is the temperature and R is the gas constant, 8.3143J/mol·K. By using this relationship, Rayleigh scattering can be used to measure concentration or temperature given the appropriate calibration. One issue with applying Rayleigh is to match the fuel to the combustion products so the measurement across the flame does not vary, apart from temperature and density as the signals depend on specific species.

The Rayleigh cross section is a function of refractive index, depolarization ratio, excitation wavelength and total molecule number density and independent of

temperature (Espey, Dec et al. (1997)). The cross section of different species can be found (Vogel (1946), Veazey, Company et al. (1964), Gardiner, Hidaka et al. (1981), Espey, Dec et al. (1997), Fielding, Frank et al. (2002), Sutton and Driscoll (2004)). The scattering cross section is defined as the ratio of the power of the scattered beam to the power of the incident beam and is given by Equation (1-4).

$$(\frac{\partial \sigma}{\partial \Omega})_{Ray} = \frac{4\pi^2 (n_i - 1)^2}{N_0^2 \lambda^4} \sin^2 \theta \frac{3}{3 - 4\rho_v} \tag{1-4}$$

where $\partial\sigma/\partial\Omega$ is the differential cross section (cm^2/sr), n_i is the refractive index, λ is the wavelength, N_0 is the number density at STP which has a value of 2.687×10^{19} cm^{-3}, θ is the scattering angle and ρ_v is the depolarization ratio. The depolarization ratio (Fielding, Frank et al. (2002), Sutton and Driscoll (2004)) is related to the molecule anisotropy and can generally be ignored and assumed to be zero for most of the combustion process involved (Zhao and Hiroyasu (1993)).

For temperature measurement, the equations can be simplified if a reference temperature, signal intensity and Rayleigh cross-section can be found. The relationship between the signal measured on the test subject and the temperature is given by Equation (1-5).

$$T = \frac{\left(\frac{\partial \sigma}{\partial \Omega}\right)}{\left(\frac{\partial \sigma}{\partial \Omega}\right)_{ref}} \frac{I_{ref}}{I} T_{ref} \tag{1-5}$$

where T is the temperature, I is the Rayleigh signal, $\partial\sigma/\partial\Omega$ is the Rayleigh cross section and the subscript 'ref' is for a calibrated signal with a known temperature and Rayleigh cross-section.

One of the disadvantages of Rayleigh scattering is its relatively low signal strength, combined with the fact that, as an elastic scattering process, it is hard to distinguish from background flare from the same radiation source. Other advantages include the ease of implementation and its ability to provide real-time spatially resolved measurements. A challenge is to overcome the interference from scatterers other

than the measured variable. One source of that is from Mie scattering caused by larger particles (i.e. dust or soot) rather than Rayleigh range molecules which are much smaller. However, the Mie scattering signal is much stronger and can be differentiated from the Rayleigh signal. The practical way to minimise this interference is to reduce the number of these particles by filtering and other methods (Zhao and Hiroyasu (1993)). Soot also interferes with the Rayleigh signal by absorbing and scattering the incident laser light and reducing the Rayleigh signal strength.

For Rayleigh, the signal and the incident laser beam are at the same wavelength, which means that any light that does not originate from the target molecules will affect the resulting image. This will have to be minimised in order to avoid interference by this noise. These interferences can arise from optics, viewing windows, reflections and other surfaces. Practical measures have to be taken to minimise these noises contributions, such as by enclosing the viewing area, using black non-reflective surfaces, etc. Rayleigh scattering is easier to apply in constant volume combustion chambers than optical engines because of the geometry which provides lower background reflection. In the engine, background reflection is strong and increases the interference. Strategies for minimising other scattering within an engine have been developed (Espey, Dec et al. (1997), Idicheria and Pickett (2007)).

Application to combustion of Rayleigh technique is potentially problematic as the Rayleigh cross section is unknown during high temperature pyrolysis and combustion (Idicheria and Pickett (2007)), although the equivalence ratio can be estimated by comparing to non-reacting experiments. In simple hydrocarbon systems, the variation of the Rayleigh cross section between reactants and combustion products is in the order of 10% (Kohse-Hoinghaus and Jeffries (2002)). It is applied to homogeneous mixtures more effectively which have spatially similar elastic light scattering effective cross section (Dibble and Hollenbach (1981)). However, correction factors derived by Namer and Schefer (1985) can be calculated to account

for the variation and the factors are as a function of degree of reaction, fuel and equivalence ratio.

1.4.4 Soot Luminosity

Light emitted from diesel combustion mainly includes contributions from soot luminescence and incandescence. Natural soot luminosity can be imaged during the combustion process without the need of lasers. An iCCD camera or high speed camera which collects natural luminosity from the diesel combustion suffices for the study of soot luminosity. The relative intensity of the signal depends on temperature, concentration and optical properties of the soot particle but the system needs to be calibrated against known results (Mueller and Martin (2002)).

Soot distribution in cylinder or combustion vessels can be obtained by visualising soot luminosity (Mueller, Pitz et al. (2003), Musculus (2004), Musculus (2007), Pickett, Kook et al. (2009), Manin, Skeen et al. (2014), O'Connor and Musculus (2014)). The effect of increase injection pressure on soot luminosity was investigated by Fang, Lee et al. (2010). Similarly, soot pyrometry was used for in-cylinder soot measurement (Bakenhus and Reitz (1999), Huestis, Erickson et al. (2007), Bobba, Musculus et al. (2010)). This technique measures the temperature by taking the ratio of intensities of the light from soot at two different wavelengths. Also, flame-spray dynamics, such effect of EGR on flame lift off length from the atomiser exit (Siebers, Higgins et al. (2002)), has been studied using soot incandescence.

Analysis of the combustion luminosity can be made by applying proper orthogonal decomposition (POD) (Chen, Reuss et al. (2013)). POD extracts dominant features, coherent and incoherent fluctuations and cycle variability from an ensemble dataset, especially in CFD (Liu and Haworth (2011)) and PIV data for turbulence flows. This method can be applied to knock and cycle-to-cycle variation (Fontanesi, D'Adamo et al. (2013)) in SI engines and both optically accessible spark ignition and compression ignition engines (Bizon, Continillo et al. (2009), Bizon, Continillo et al. (2010)).

1.4.5 High Speed Imaging

Line-of-sight high speed imaging of injection spray penetration has been conducted in combustion vessel (Pickett, Kook et al. (2009), Pickett, Manin et al. (2013)) and a rapid compression machine (Kennaird, Crua et al. (2002), Abdelghaffar, Karimi et al. (2007)). And application of high speed imaging on chemiluminescence and combustion luminosity has been described in the relevant section above. High speed microscopic imaging of the start of injection of a diesel spray has also been applied (Crua, Shoba et al. (2010)).

1.4.6 Laser Induced Incandescence (LII)

Laser induced incandescence (LII) is the measurement of the non-black body radiation emitted by the soot particles when heated up by a laser. A more detailed description of its method and application is presented in the next section.

1.4.7 Summary

The techniques described are useful tools for measuring and visualising different aspects of combustions, spray dynamics and flow. Techniques which can be applied for quantitative measurements in engines are limited due to optical access and conditions inside the combustion chamber. In order to focus on emission control, soot and HC, and with more difficulty, NO_x and CO, can be measured using techniques described here and one which provides a quantitative and useful tool is to apply LII for soot measurements in an optical engine. This will be discussed in more details in the next section.

1.5 Laser Induced Incandescence

Laser induced incandescence (LII) is the measurement of the non-black body radiation emitted by the soot particles when heated up by a laser. LII signal is due to the blue-shifted light from soot particles as they are heated up to a temperature much higher than surrounding gas. LII is a way to measure soot primary particle sizes and soot volume fraction. Soot volume fraction is approximately proportional to both the

integrated signal and peak signal level (Melton (1984), Bladh, Johnsson et al. (2007)). The decay rate of the LII signal will give the size of the primary particle.

An overview of research performed in the area of LII was described by Tropea, Yarin et al. (2007), Zhao (2010). Weeks and Duley (1974) first observed the heating up of soot particle using a CO_2 laser. It has since been applied to soot volume fraction measurements in laminar diffusion flames (Quay, Lee et al. (1994), Ni, Pinson et al. (1995), Shaddix and Smyth (1996), Bryce, Ladommatos et al. (2000), Witze, Hochgreb et al. (2001)), laminar premixed flames (Vander Wal (1994), Appel, Jungfleisch et al. (1996), Zhao and Ladommatos (1998), Axelsson, Collin et al. (2000), Axelsson, Collin et al. (2001)), turbulent flames (Ni, Pinson et al. (1995), Geitlinger, Streibel et al. (1998), Bockhorn, Geitlinger et al. (2002), Meyer, Roy et al. (2005)), combustion vessels (Idicheria and Pickett (2005), Idicheria and Pickett (2007), Vogel, Riess et al. (2013)), in-cylinder measurements (Dec and Espey (1992), Dec, Zur Loye et al. (1992), Kock, Eckhardt et al. (2002), Bougie, Ganippa et al. (2006), Kock, Tribalet et al. (2006), Boiarciuc, Foucher et al. (2007), Bougie, Ganippa et al. (2007), Miles, Collin et al. (2007), Musculus (2007), Singh, Reitz et al. (2007), Chartier, Aronsson et al. (2009), Aronsson, Sjöholm et al. (2010), Menkiel, Donkerbroek et al. (2012)) and exhaust gases (Schraml, Will et al. (2000), Snelling, Smallwood et al. (2000), Viskup, Stanger et al. (2013)).

1.5.1 LII Technique

There are several approaches to apply LII for soot measurements in optical engines. The main ones are the planar 2D LII method and the two-color time-resolved (TC-TR) method. Alternatively, both can be simultaneous applied. These approaches are described below.

1.5.1.1 Two-Color Time-Resolved LII(TC-TR)

Soot particles emit light as these are heated up by laser due to the high temperature. By assuming grey body radiation, the light emitted varies with temperature and particle size according to Plank's law. The two-color time resolved LII detects the LII signal using two photomultipliers tubes (PMT) and the

LII signal is filtered at two different wavelengths for each of the PMTs. The ratio between the two signals gives the temperature of soot within the probe volume measured and the size of the primary soot particle can be calculated. This operates by the shift of light spectrum emitted by radiation as temperature changes. The change of temperature will give a change in ratio at two wavelengths. Time resolved LII can be achieved by either taking the entire duration of the signal decay (Vander Wal, Ticich et al. (1999), Axelsson, Collin et al. (2000), Woiki, Giesen et al. (2000), Kock, Eckhardt et al. (2002), Lehre, Jungfleisch et al. (2003), Menkiel, Donkerbroek et al. (2012)) or by taking two different points of time at both wavelengths after the signal peak to find the ratio as applied in Will, Schraml et al. (1996), Will, Schraml et al. (1998). Particle sizes can be calculated by assuming either a monodisperse (Vander Wal, Ticich et al. (1999), Axelsson, Collin et al. (2000), Woiki, Giesen et al. (2000), Menkiel, Donkerbroek et al. (2012)) or a poly-disperse lognormal particle size distribution (Kock, Eckhardt et al. (2002), Lehre, Jungfleisch et al. (2003)).

The benefit of the two color time resolved (TC-TR) method is it is self-calibrating without the need to calibrate against a known source, unlike in the planar LII case. It also gives the temperature of the probe volume. The disadvantage is that the probe volume is small and unable to give a full picture of soot distribution in the combustion chamber, in the region of 0.07-0.2cm^3 in the case of Bougie, Ganippa et al. (2006), Bougie, Ganippa et al. (2007) and 0.15 cm^3 in the case of Kock, Tribalet et al. (2006). The specification from a number of publications is described below.

In Bougie, Ganippa et al. (2006), Bougie, Ganippa et al. (2007), a six cylinder, heavy duty engine was converted into an optical engine by having a valve and piston replaced and the laser beam was passed top-down through the cylinder head. The LII signal was acquired through the sidewall of the combustion chamber. The earlier paper (Bougie, Ganippa et al. (2006)) provided an analysis of the experimental techniques employed. In the second paper (Bougie, Ganippa

et al. (2007)), two locations within the combustion chamber were investigated: in one case, the laser passed through the injected diesel spray and the other was in between the sprays. However, the data presented did not provide any information on the difference between the two locations.

Kock, Tribalet et al. (2006) used a laser beam across the centre of combustion chamber of a single cylinder optical compression ignition engine and the signal was recorded through the window from the top through the cylinder head. The fuel was injected directly into the centre of the combustion chamber and adjusted so the centre line of the spray intersected with the centre of the laser and detection axis.

Menkiel, Donkerbroek et al. (2012) used a laser beam across the combustion chamber side windows of a Ricardo Hydra optical engine and the LII signal was recorded perpendicular to the laser beam which was approximately 10mm from the tip of the injector towards the piston and 11mm towards the side window.

This method is useful for acquiring temperature and particle sizes without the need for calibration. This technique measures a small area and the ability to measure individual soot particle but application to engine is restricted as it does not give a full picture of soot distribution within the combustion chamber. It will be useful to use in conjunction with the planar LII method described below.

1.5.1.2 Planar LII

Planar LII uses a laser sheet to illuminate a measuring plane and the LII signal is recorded by an iCCD camera. The advantage of the planar method is that the two-dimensional imaging provides measurement on the soot spatial distribution and soot volume fraction within an area of interest. This method was used in Dec and Espey (1992), Dec, Zur Loye et al. (1992), Singh, Reitz et al. (2007), Idicheria and Pickett (2011), Kook and Pickett (2012) Cenker, Bruneaux et al. (2013) Morgan, Gold et al. (2003), Menkiel and Ganippa (2012), O'Connor and Musculus (2014) and specifically for analysing different injection pressure in

Crua, Kennaird et al. (2003). For Dec and Espey (1992), Dec, Zur Loye et al. (1992), an additional camera was used to record the elastic light scattering image. Planar LII was used to analyse different injection pressure.

Consideration has to be given to the choice of planar LII filter as the excitation of species such as OH and C_2 can interfere with the LII signal. For example, Boiarciuc, Foucher et al. (2007) used a short pass filter of 400 to 450 nm was used against a Nd:YAG laser at 532nm. The rest of the setup are described below.

In Dec and Espey (1992), Dec, Zur Loye et al. (1992), a laser sheet at 532nm wavelength was horizontally directed across the combustion chamber from the side wall and an optical window allowed partial view through the cylinder head into the combustion chamber. LII signal was collected through a 450nm short-wave-pass (SWP) edge filter; a further 450nm SWP interference filter and a BG39 Schott-glass SWP filter. A 532nm laser mirror was used to minimise interference from visible light. The elastic light scattering signal was filtered using a 532nm band-pass filter (10nm FWHM) and neutral density filter.

In Singh, Reitz et al. (2007), a laser sheet was directed across the combustion chamber at 14° to the horizontal, aimed towards the injector hole parallel to the axis of one of the fuel jets. This provided the visualisation across the middle of the fuel spray. The detection system used was an iCCD camera, which had a 450-nm short wave pass filter to reject natural luminosity of soot and a 532nm notch filter to reject elastically scattered laser light. Soot luminosity was also recorded.

Miles, Collin et al. (2007) used a vertical laser sheet from the sidewall of the combustion chamber and the LII signal was collected at 90 degrees to the laser sheet. The laser sheet was aligned with the axis of one of the fuel jets. The detection system was an iCCD camera, which integrated the emitted light for 100ns, beginning 10ns before the start of laser pulse. A total of 50 images were acquired for each crank angle.

Aronsson, Sjöholm et al. (2010) used a flat laser sheet entering from the side at an angle to the horizontal through the axis of the diesel spray for visualisation of in-cylinder soot. Multiple lasers were used to allow recordings of up to an image for each of 8 consecutive CAD. A specialized high speed framing camera, SIM 8, with a fast image intensifier (300ns decay time) was used for imaging. The intensified signal was then split using seven 50-50 beam splitters and directed into 8 ICCD cameras. An optical filter with transmittance of around 50% between 372nm and 427nm was used to block out laser light and combustion processes. Also, a heat absorbing KG3 filter was used for infrared filtering.

Menkiel and Ganippa (2012) used a flat laser sheet across the combustion chamber and recorded the LII signal using CCD camera through the 45 degree mirror through the window in the piston. The signal was filtered using a beam splitter and recorded the reflected signal between 400nm to 700nm from a 1064 nm Nd:YAG laser.

Planar LII is useful for spatial distribution of soot in the measured volume. It does not give an absolute value of the amount of soot measured but a relative value which can be compared or calibrated. The ideal solution for both spatial distribution and particle sizes and temperature is to combine the use of planar LII and two color LII.

1.5.1.3 Simultaneous TC-TR LII and planar LII

By simultaneously using 2-color time-resolved LII and planar LII, the advantage of both can be utilised. The two-color pyrometry provides the local soot volume fraction and this can be extrapolated from that single point to the entire measurement in the two dimensional planar image. The 2D image can then be used to give the spatial soot volume fraction distribution. The 2-color pyrometry also gives the equivalent soot temperature. One of the disadvantages of this method is that if there is no signal received by the PMTs used in the TC-TR method because of the lack of signal in the probe volume, the 2D image will have to be discarded or calibrated otherwise.

This method was used in experiments conducted by Boiarciuc (2006), Boiarciuc, Foucher et al. (2007). A horizontal laser sheet was projected across the combustion chamber using the side window of an optical single cylinder engine. The LII signal was detected from below through the optical piston using two PMTs for the two color time resolved LII system and an iCCD for the planar LII. The technique was optimized using an isooctane-air diffusion flame before being applied to in-cylinder work.

1.5.2 LII Theoretical Model

Melton (1984) first set up the mass and energy balance equation for quantitative measurement of soot. Two sources of model from Schulz, Kock et al. (2006), who reviewed LII techniques, and models and Michelsen, Liu et al. (2007) reviewed and compared LII models. Will, Schraml et al. (1998), Snelling, Liu et al. (2000), Hofeldt (1993), Bladh and Bengtsson (2004), Michelsen (2003), Dreier, Bougie et al. (2006) and Vander Wal (1994) are other modelling and theory sources. Dreier, Bougie et al. (2006) reviewed models which are more specifically on LII in a high pressure spray combustion environment with time-resolved LII technique. The model described below is based on Kock, Tribalet et al. (2006) model as it applies to high pressure environment and his model is based on the work of Williams and Loyalka (1991). For other in-cylinder modelling, Boiarciuc, Foucher et al. (2007) used the high pressure LII model as proposed by Kock, Tribalet et al. (2006).

The basic equation for the rate of change in energy of a carbon particle undergoing laser heat up is shown in equation (1-6).

$$\dot{Q}_{int} = \dot{Q}_{abs} - \dot{Q}_{sub} - \dot{Q}_{cond} - \dot{Q}_{rad} \quad (1\text{-}6)$$

In equation (1-6), $\dot{Q}_{int}$ is the rate of internal rate of energy change of the particle; $\dot{Q}_{abs}$ is the rate of laser energy absorbed by the particle; $\dot{Q}_{cond}$ is the rate of heat loss through conduction; $\dot{Q}_{sub}$ is the rate of heat loss through sublimation; $\dot{Q}_{rad}$ is the rate of heat loss through radiation. Other heat loss mechanisms such as annealing and oxidation are omitted here. Annealing is when carbon particles melt

and re-crystallise producing an annealed particle and oxidation of the carbon particle produces a compound such as carbon monoxide. More information about these heat loss mechanisms can be found in Michelsen (2003).

Absorption accounts for the temperature of the particle reaches after laser heating according to Mie theory. The maximum temperature reached is independent of particle size as the temperature of the particle in the Rayleigh limit is proportional to the particle volume.

$$T_P^0 = T_g - \frac{6\pi R_0}{\rho_p c_p \lambda_{Laser}} Im\left(\frac{m^2-1}{m^2+2}\right) \quad (1\text{-}7)$$

Equation (1-7) shows the particle temperature, T_P^0, after being heated up by the laser. R_0 is the laser energy density, T_g is the gas temperature, ρ_p is the particle density, c_p is the particle heat capacity and λ_{laser} is the wavelength of the laser. m is the complex refractive index and Smyth and Shaddix (1996) has a review of soot refractive index. Sorensen (2001) reviewed the scattering and absorption of light by fractal aggregates which included different complex refractive indexes from a physical point of view. For LII application, Schulz, Kock et al. (2006) and Dreier, Bougie et al. (2006) included the complex refractive index in the models reviewed. There is an issue with smaller particles as they have larger surface to volume ratio than larger particles and hence cool faster (Tropea, Yarin et al. (2007)). This has implication on detection gate setting as the longer or delayed detection gate produces an integrated signal which underestimates particle sizes (Ni, Pinson et al. (1995), Vander Wal (1996)).

In order to avoid using m, the alternative is to apply two-color pyrometry to determine the particle temperature. The use of the two-color pyrometry allows the LII signal to be detected at two different wavelengths and the temperature can be calculated from the following equation (1-8).

$$T_P = \frac{hc_0}{k_B}\left(\frac{1}{\lambda_2}-\frac{1}{\lambda_1}\right)\times\left\{ln\left[\frac{S_p(\lambda_1,T_p)}{S_p(\lambda_2,T_p)}\frac{S_{bb}(\lambda_2,T_{bb})}{S_{bb}(\lambda_1,T_{bb})}\frac{\varepsilon_p(\lambda_2)}{\varepsilon_p(\lambda_1)}\right]+\frac{hc_0}{k_B T_{bb}}\left(\frac{1}{\lambda_2}-\frac{1}{\lambda_1}\right)\right\}^{-1} \quad (1\text{-}8)$$

In equation (1-8), h is the Planck constant, c_0 is the speed of light, k_B is the Boltzmann constant, λ is the detection wavelength, S_p and T_p are the measured particle emission signal and temperature, S_{bb} and T_{bb} are the measured signal and temperature from black-body source during calibration and ε_p is the particle spectral emissivity. For small particles in the Rayleigh limit, the equation can be simplified as follows:

$$\frac{\varepsilon_p(\lambda_2)}{\varepsilon_p(\lambda_1)} \approx \frac{\lambda_1}{\lambda_2} \quad (1\text{-}9)$$

The rest of the energy equation relates to the heat loss through radiation and conduction. The cooling rate can be classified by the Knudsen number, Kn, which is the ratio of the particle radius, r_p to the mean free path of the gas molecules, λ_g, in which the particle is suspended. For diesel engine conditions, it was shown that the Knudsen numbers are around 1, meaning that the radius of the particles and the mean free path of the gas molecules are about the same (Kock, Eckhardt et al. (2002)). This means the system is in the transition regime. The conduction term can be expressed in equation (1-10) as:

$$\dot{Q}_{cond,tr} = \dot{Q}_{cond,c} f_h(Kn_h) = 2\pi d_p \lambda_{cond}(T_p - T_g) f_h(Kn_h) \quad (1\text{-}10)$$

$\dot{Q}_{cond}$ is the conduction heat flux, subscript tr is for transition regime and c is the continuum regime, f_h is an empirical function correcting the Knudsen affected continuum heat flux as defined in equation (1-11) and Kn_h is defined in equation (1-12).

$$f_h(Kn_h) = \left[1 + Kn_h \frac{1.9234A+1.3026}{1.9234Kn_h+1}\right]^{-1} \text{ with } A = \frac{\dot{Q}_{cond,c}}{\dot{Q}_{cond,fm}} = {5\sqrt{\pi}}/{\alpha_T}\left(\frac{\gamma-1}{\gamma+1}\right)Kn_h \quad (1\text{-}11)$$

γ is the heat capacity ratio and α_T is the translational energy accommodation coefficient which describes the efficiency of the energy transfer in molecular collision. The translational energy is in the range of 0.07 and 1.00 Kock (2005).

$$Kn_h = \frac{4\lambda_{cond}T_g}{5r_p p_g}\left(\frac{m_g}{2k_B T_g}\right)^{1/2} \quad (1\text{-}12)$$

p_g and m_g are the pressure and molecular mass of the ambient gas, λ_{cond} is the thermal conductivity of the gas. The high pressure environment has the effect of increasing the cooling by conduction, producing a shorter signal Hofmann, Bessler et al. (2003) and, conversely, a low pressure environment or a vacuum will reduce conduction and produce a longer signal (Beyer and Greenhalgh (2006), Liu, Daun et al. (2006)).

The sublimation heat loss is given by equation (1-13). This occurs as the carbon particle is heated up to above 2800 K causing the carbon to sublime into gas-phase carbon atom clusters (Michelsen (2003)).

$$\dot{Q}_{sub} = \dot{U}_{sub}\Delta h_v \quad (1\text{-}13)$$

Δh_v is the evaporation/sublimation enthalpy of the particle material, using the Clausius-Clapeyron equation, was found to be 21,946kJkg^{-1} and $\dot{U}_{sub}$ in transient condition can be expressed by equation (1-14).

$$\dot{U}_{sub,tr} = \dot{U}_{sub,c} f_c(Kn_c) = 2\pi d_p D(\rho_s - \rho_\infty) f_c(Kn_c) \quad (1\text{-}14)$$

D is the diffusion coefficient of the vapour into the gas in m^{2}s^{-1}, ρ_s and ρ_∞ are the vapour density of the carbon at the particle surface and infinity respectively and ρ_∞ is assumed to be negligible. ρ_s can be approximated to carbon vapour pressure p_s using the Clausius-Clapeyron equation as shown in equation (1-15).

$$p_s = p^* exp\left(-\Delta h_v M_v / R_m \left({}^1/_{T_p} - {}^1/_{T^*}\right)\right) \quad (1\text{-}15)$$

M_v is the molar mass of the vapour, R_m is the molar mass constant. p* and T* are referenced to the appropriate points on the vapour pressure curve taken at 61.5 Pa at 3000 K Leider, Krikorian et al. (1973).

The empirical function correcting the Knudsen affected continuum evaporation/ sublimation rate is defined in equation (1-16).

$$f_c(Kn_c) = \left[1 + Kn_c \frac{1.3333B + 1.0161}{1.3333Kn_c + 1}\right]^{-1} \text{ with } B = \frac{\dot{U}_{sub,c}}{\dot{U}_{sub,fm}} = {}^{Kn_c\sqrt{\pi}}/_{\alpha_v} \quad (1\text{-}16)$$

f_c is the empirical function, α_v is the accommodation coefficient for sublimation for non-equilibrium sublimation kinetics and real gas effects. This can be simplified to 1. The empirical function of the Knudsen number, Kn_c is given in equation (1-17).

$$Kn_c = \frac{2D}{r_p}\left(\frac{m_v}{2k_B T_v}\right)^{1/2} \quad (1\text{-}17)$$

The heat flux due to radiation is given in equation (1-18) where ε_{pt} is the total emissivity of the particle which can be assumed to be 1 and σ is the Stefan-Boltzmann constant. Radiation heat loss is comparatively minor compared to conduction and sublimation heat loss.

$$\dot{Q}_{rad} = \pi d_p^2 \epsilon_{pt} \sigma\left(T_p^4 - T_g^4\right) \quad (1\text{-}18)$$

The LII signal generated by each particle in the detection volume is given by equation (1-19). Using this equation, the signal can be found to be solved by integrating along the range of wavelength for a range of temperature from 1000K to 6000K for every 5K.

$$S = \Omega \pi D^2 \int_\lambda \varepsilon_\lambda \frac{2\pi hc^2}{\lambda'^5\left[\exp\left(hc / \lambda' k_B T\right) - 1\right]} \sum_\lambda (\lambda') d\lambda' \quad (1\text{-}19)$$

In equation (1-19), S is the LII signal, Ω is a normalization constant relating to the solid angle, D is diameter of the particle, ε_λ is the emissivity which is given in equation (1-20) and related to the absorption cross section, C_{abs} , h is the Planck

constant, c is the speed of light, λ is the wavelength of light, k_B is the Boltzmann constant and T is the temperature. Spectral intensity is the radiation in the interval dλ around a single wavelength and total intensity is the integral over all wavelengths.

$$\varepsilon_\lambda = \frac{4C_{abs}}{\pi D^2} \tag{1-20}$$

The energy balance equation (1-6) can be used to calculate the theoretical temperature of the soot particle at any point of time after being energised by the laser. It also calculates the theoretical rate of temperature change and the contribution from each of the heat loss mechanisms and allows for the soot particle diameter to be calculated using the measured temperature and rate of temperature change.

Using equation (1-19), the LII signal can be calculated. The theoretical signal can be calculated for a range of temperatures using two set ranges of wavelengths. A ratio of the theoretical signal between the two wavelengths at a given temperature can be found and used with the measured signal to find the temperature in the measured volume. The LII signal equation can also be used to calculate the size of the particles as the diameter term in the equation cancels out when calculating the emissivity. Using the theoretical signal at a given temperature at either sets of wavelength, the emitting surface of the soot particle, and hence the size of the particle, can be calculated using the measured signal. Because this is a ratio of signals, the absolute value of the calculated signal and the measured signal is not important.

1.5.3 Laser

Most of the LII work done in engines, such as Miles, Collin et al. (2007), Boiarciuc (2006), Boiarciuc, Foucher et al. (2007) and Kock, Tribalet et al. (2006), Menkiel, Donkerbroek et al. (2012), used a Nd:YAG laser with the wavelength of 1064nm. Boiarciuc (2006), Boiarciuc, Foucher et al. (2007) gave the reason for choosing 1064nm as being the avoidance of possible broadband PAH fluorescence interference and electronically excited C_2 emission at 532nm or lower wavelength.

This is a view supported by others (Vander Wal (1994), Bengtsson and Aldén (1995), Schoemaecker Moreau, Therssen et al. (2004)). Dec and Espey (1992), Dec, Zur Loye et al. (1992), Singh, Reitz et al. (2007) and Bougie, Ganippa et al. (2006), Bougie, Ganippa et al. (2007) used Nd:YAG lasers with the wavelength of 532nm. Aronsson, Sjöholm et al. (2010) used 4 double-pulse Nd:YAG lasers cluster for multiple measurements within 1 cycle. The laser was setup with a wavelength of 532nm and capable of 8 pulses per cycle with time separation between 5-440µs and up to 1.4J/pulse. A top-hat profile was used in Boiarciuc (2006), Boiarciuc, Foucher et al. (2007), Aronsson, Sjöholm et al. (2010) and Kock, Tribalet et al. (2006) Menkiel, Donkerbroek et al. (2012) and one of the methods to generate this is by filtering the laser beam geometrically. Table 1-1 shows the collated information on laser used.

Author	Laser	Wave-length	Profile	Energy	Pulse width/ Frequency
Dec and Espey (1992), Dec, Zur Loye et al. (1992)	Nd:YAG	532nm	Not specified	1.2J/cm^2	8ns
Bougie, Ganippa et al. (2006), Bougie, Ganippa et al. (2007)	Nd:YAG	532nm	Not specified	0.25 J/cm^2	10ns (FWHM)
Boiarciuc (2006), Boiarciuc, Foucher et al. (2007)	Nd:YAG	1064nm	Top-hat	0.15 J/cm^2	10ns
Kock, Tribalet et al. (2006)	Nd:YAG	1064nm	Top-hat	0.1 J/cm^2	8ns
Singh, Reitz et al. (2007)	Nd:YAG	532nm	Not specified	0.2 J/cm^2 35mJ/pulse 25mm by 1mm sheet	10ns
Miles, Collin et al. (2007)	Nd:YAG	1064nm	Not specified	0.6 J/cm^2	Not specified
Aronsson, Sjöholm et al. (2010)	4 Nd:YAG	532nm	Top-hat	0.2J/cm^2	Not specified
Menkiel, Donkerbroek et al. (2012)	Nd:YAG	1064nm	Top-hat	0.21 J/cm^2	8ns

Table 1-3: Laser, laser power and profile used in various literature

1.5.4 Engine Set-Up

This section describes the various engine settings used in the literature here such as the use of skip firing and type of fuel.

Exhaust gas recirculation (EGR), as used in modern diesel engines, was used in Boiarciuc, Foucher et al. (2007), Miles, Collin et al. (2007), Singh, Reitz et al. (2007), Aronsson, Sjöholm et al. (2010). The increase of EGR rate causes an increase in soot because of a decrease in air/fuel ratio given the same amount of fuel injected. However, Miles, Choi et al. (2004) demonstrated that higher EGR together with late injection could decrease the emission of NO_x and soot. In Boiarciuc, Foucher et al. (2007), EGR was simulated by adding N_2 and CO_2 to the air. Singh, Reitz et al. (2007) employed cooled EGR by diluting the intake air with nitrogen to an oxygen concentration of 12.7%, which equates to about 60% EGR. To account for different specific heat capacity and specific heat ratios compared to exhaust gases, intake temperature and pressure were adjusted. Miles, Collin et al. (2007) used exhaust from an industrial fuel-oil burner as a source of EGR as the engine was skipped-fired. The EGR level in this case was set to 56%, equivalent to 12% volume of oxygen. Intake air pressure was also increased in the case of Bougie, Ganippa et al. (2006), Bougie, Ganippa et al. (2007). For Aronsson, Sjöholm et al. (2010), the injection timing was changed along with EGR to match combustion phasing of 27 CAD injection duration. Simulated EGR produced by a diesel fired domestic heater was used. It was then cooled and mixed with inlet air and conditioned by another (electrical) heater and a mechanical compressor.

Skip firing was employed in Singh, Reitz et al. (2007), Bougie, Ganippa et al. (2006), Bougie, Ganippa et al. (2007) and Miles, Collin et al. (2007). Miles, Collin et al. (2007) injected fuel once every fifth cycle to synchronize with the PIV system and the intake air temperature was increased to 125°C in order to compensate for the lower wall temperature due to skip firing. Firing pattern was also used to maintain wall temperature and residual effects Dec and Sjoberg (2004). In Singh, Reitz et al. (2007), fuel was injected once every 10 cycles and engine speed was maintained by dynamometer. Bougie, Ganippa et al. (2006), Bougie, Ganippa et al. (2007) injected fuel into the combustion chamber once every 35 cycles at 1430rpm to avoid overheating the non-lubricated cylinder. Aronsson, Sjöholm et al. (2010) skip-fired

every 60th cycle for 4 fired cycles for imaging due to slow acquisition of the camera system.

Simulated diesel was used in some experiments. Commercial diesel fuel was used in Bougie, Ganippa et al. (2006), Kock, Tribalet et al. (2006), Bougie, Ganippa et al. (2007), Singh, Reitz et al. (2007), Menkiel, Donkerbroek et al. (2012). Miles, Collin et al. (2007) used a mixture of 70% n-heptane and 30% iso-octane, which has the same ignition delay and heat release characteristics as standard diesel fuel. Boiarciuc (2006), Boiarciuc, Foucher et al. (2007) used 95% n-heptane with 5% of alpha-methyl-naphthalene. Dec and Espey (1992), Dec, Zur Loye et al. (1992) used a low-sooting fuel with a blend of 80% 2,ethoxyethyl ether and 20% hexadecane (n-cetane) as it has similar vaporization and ignition characteristics to diesel fuel. Aronsson, Sjöholm et al. (2010) used 99% n-heptane with 1% lubricant to minimise laser induced fluorescence interference from unknown species and allow longer life of components.

This shows what can be done in relation to EGR and fuel used regarding soot and LII and their outcome. There are benefits using simulated EGR given optical engines usually employ skip firing which makes real EGR difficult. Skip firing is useful but the problems of low wall temperature and unrealistic residual gas need to be addressed. Simulated fuel gives the benefit of consistency due to the varied nature of different batches of commercial diesel fuel although the question of how close a simulated fuel represents the real fuel needs consideration.

1.5.5 Variable Investigated and Outcome

Some general observations regarding soot formation and oxidation were made in the engine studies reviewed. Boiarciuc, Foucher et al. (2007) found that soot appears predominantly in the spray direction towards the extremity of the bowl on the basis of 2D LII images. Another observation was that soot particles initially increased in size and decreased later on during the combustion cycle. The same observation was made by Bougie, Ganippa et al. (2006), Bougie, Ganippa et al. (2007), Kock, Tribalet et al. (2006) and Boiarciuc (2006). The reasoning behind this is that soot particles

form and grow at the beginning of the combustion cycle until oxidation reduces the size of the soot particles. This is discussed further in Heywood (1988).

Dec and Espey (1992), Dec, Zur Loye et al. (1992) applied LII in combination with other optical techniques in an engine. Elastic light scattering was applied in one (Dec, Zur Loye et al. (1992)) and elastic light scattering and laser-induced fluorescence (LIF) were applied in another for characterisation of liquid fuel distribution (Dec and Espey (1992)). In Dec, Zur Loye et al. (1992), the purpose of the investigation was to verify LII and its application for in-cylinder measurement and compared with the elastic light measurements. In Dec, Zur Loye et al. (1992), the engine speed and injection pressure were varied and soot concentration was found to decrease with increased engine speed and injection pressure. Also, soot was found further upstream in the spray at lower engine speed compared with higher engine speed.

In Miles, Collin et al. (2007), LII measurements of the evolution of soot distribution during a combustion cycle was investigated together with particle image velocimetry and LIF for partially oxidised fuel. The operating condition was a low temperature, highly dilute, direct injection diesel engine. Fuel was injected at -12° CAD aTDC for the duration of 4° CAD with the engine running at 1200RPM. Soot was first observed using LII at 10-11° CAD aTDC near the cylinder centreline and some near the bowl rim. Also, soot concentrated in the central region of the cylinder later in the cycle and little soot was found in the squish volume.

1.5.5.1 Engine Load

Engine load was changed along with boost pressure in Bougie, Ganippa et al. (2007) and two cases were tested. However, the author did not distinguish the specific effect of boost pressure increase on soot compared to engine load. This may due to the need to keep the air-fuel ratio the same for both engine loads as more fuel was required for the higher load. It was found in both cases that primary particle size grows to 40nm and then decreases in the combustion cycle. The higher load case had increased scatter in the data. However, this may be due to the increased attenuation caused by signal-to-noise ratio problems rather than

any difference in soot formation and oxidation process for the two load cases. In an earlier work Bougie, Ganippa et al. (2006), the authors found the same trend of soot growing and subsequently decreasing in size as the combustion cycle progressed. The earliest sign of soot was found at 14 CAD aTDC when fuel was injected between 5 CAD before and after TDC.

Kock, Tribalet et al. (2006) varied the engine load by altering the amount of fuel injected and increasing the injection duration. It was found that increased engine load (increase of fuel equivalence ratio) increased the size of soot primary particle. The varying of engine load translated into varying the fuel/air equivalence ratio while increased richness in the combustion chamber resulted in increased soot volume fraction. This was confirmed by LII, calibrated by the line-of-sight laser extinction technique.

Menkiel, Donkerbroek et al. (2012) investigated the change in engine load and its effect on soot particle sizes by altering the amount of fuel injected in each cycle, injecting 20 mg/stroke, 15.4 mg/stroke and 11.6 mg/stroke and the corresponding IMEP were 3.42, 2.46 and 1.5 bar respectively. Larger particles were found for higher load, caused by the richer fuel air mixture, and there was less oxygen available for soot oxidation. The soot volume fraction was derived from the TC-TR LII data, extracting the data from a small region and inferred to the rest of the combustion chamber. This followed the same trend of increase in soot volume fraction for increase load.

1.5.5.2 Injection Timing

Multiple injection was investigated in Singh, Reitz et al. (2007) and a total of 65mg of fuel was injected per cycle, of which 31.5mg was injected at -22° CAD aTDC and 33.5mg was injected starting at +15° CAD aTDC. The evolution of LII signal from soot was described. One of the main observations was the high variability of soot distribution from cycle to cycle. Soot was generally found near the bowl edge. In the first injection, small pockets of soot were formed near the bowl edge late in the combustion process about 15° CAD after start of injection.

For the second injection, the fuel jet penetration was shorter and soot formed about 7° CAD after start of injection, again near the bowl edge and continued to form until about 20° CAD after start of injection. The small amount of soot formed during the first injection showed the engine was operating in low temperature combustion and the area within the fuel jet was below the sooting limits. In the second injection, there was less mixing causing more soot to form compared to the first injection.

Injection timing was varied in Boiarciuc, Foucher et al. (2007). Early injection was used to compensate for the ignition delay in cases of higher EGR. Early injection was found to raise global temperature in combustion chamber. The same EGR rate of 30% and with earlier injection timing produced higher maximum pressure with the same ignition delay and shorter cold flame duration. Earlier injection at 30% EGR produced higher amount of soot and larger soot particles.

In Menkiel, Donkerbroek et al. (2012), the injection timing was varied between 10˚bTDC, 5˚bTDC, TDC and 2˚aTDC. It was found the injection timing had little effect on measured primary particle size. A link was found between larger amount of soot produced for shorter ignition delay cases for injection timing of 10˚bTDC and 5˚bTDC compared to longer ignition delay for injection at TDC and 2˚aTDC.

1.5.5.3 EGR

Boiarciuc, Foucher et al. (2007) varied the EGR amount from 0% to 40% to find the effect of EGR on soot. By varying EGR, a decrease of maximum pressure was found as EGR increased. There was also an increase of ignition delay and cold flame duration. Increasing maxima of soot concentration inside combustion chamber and exhaust were found for higher EGR because there was less oxidation. However, soot particle diameter decreased with increased EGR. Also, soot evolution throughout the combustion cycle did not appear to vary with different EGR rate.

Meyer, Roy et al. (2005) varied EGR amount by altering O_2 content between 9% and 21%. It was found that engine smoke out initially increased with decreasing O_2 mole fraction then drastically decreases below a certain O_2 level. Soot formed as soon as pre-mixed combustion ceased and this was assumed to be delayed because of the slower soot formation chemistry of n-heptane compared to normal diesel. For high O_2 fractions, soot formed in the jet free path before hitting the combustion chamber wall. Soot appeared along the wall for lower O_2 fraction and for the lowest, only appeared in the recirculation zone between the jets. Soot growth rate increased rapidly as O_2 fraction decreased and peaked at 13% oxygen content, and then the growth rate decreased below 13% oxygen content. But the measurement of soot growth rate might have been affected by signal trapping. Soot lift-off length, which is the distance between fuel nozzle and first soot occurrence in the combusting fuel jet, generally moved upstream as injection progressed. Finally, soot front position correlated well for cases between 10-16% O_2 content, following a logarithmic curve for soot front position and CAD after SOI. This meant soot oxidation does not play a part in these settings, as it will affect the position of the soot front with different oxygen content.

1.5.6 Experimental Issues

Bougie, Ganippa et al. (2007) commented on how the LII theory may affect the outcome of LII experiments. It was speculated that LII is more sensitive to larger particles because the LII signal scales with the square of particle radius. The size of the soot aggregate found in the experiment could be skewed towards larger particles. Secondly, although the LII signal is supposed to give information about the individual primary soot particle, the shapes of the aggregates may affect the result and this was raised by Liu, Smallwood et al. (2005) previously. Aggregates that are long and with a chain-like structure are more likely to be more accurately represented than compact, ball-like aggregates. Therefore, decline in primary particle size, as found in the latter part of the combustion cycle, may be due to soot

aggregates being broken up into smaller, less compact fragments rather than changes in the primary particle size. Finally, on the practicalities of the experiment, no lubrication was used to prevent fouling of the window of the optical engine.

Kock, Tribalet et al. (2006) raised the same issue with the LII measurement of the size of primary particle affected by the aggregate structure. The LII signal gives an equivalent “heat-transfer diameter” rather than actual size because of the touching surfaces between each primary particle. This leads to misrepresentation of the size based on how tightly packed the aggregates are. The temperature given by TR-LII signal was found to be about 200K higher than the calculated value using pressure data. The averaged value of the two was used, but it was reasoned that the dependency of particle size on gas temperature was not high after sensitivity analysis. An error margin of 200K was taken into account in the result. Analysis of the gas in the combustion cylinder was assumed to contain only nitrogen.

In Boiarciuc (2006), the process of calibrating the PMT and using a diffusion flame for calibrating the system was described. The issue of uncertainty on soot volume fraction found by LII due to its dependence to temperature was raised. It was not possible to find the in-cylinder temperature, which is necessary for the accurate application of LII. This was partly solved by finding the temperature using 2-color LII detection system before initiating the laser illumination. In Boiarciuc later paper (Boiarciuc, Foucher et al. (2007)), the processing of the LII images was discussed, including elimination of CCD background noise, laser induced noise and natural emission intensity. Corrections were also made for attenuation due to soot deposit.

In Singh, Reitz et al. (2007), a set of 20 images was taken from 20 different engine cycles for each crank angle investigated. A representative image was then selected to be presented as the result. Another problem was, as the laser sheet struck the tip of the fuel jet, strong reflection and broadband flare ‘leaks’ through the optical filters and became visible in the image under some conditions. In Miles, Collin et al. (2007), bowl distortion was corrected to eliminate effects of the curvature of the bowl distorting the acquired image. It was corrected by fitting a two-dimensional cubic

polynomial to describe the distortion of a matrix of points on a target placed inside the combustion chamber.

In Aronsson, Sjöholm et al. (2010), it was noted that the LII signals are very short at elevated pressure (10ns at 60bar) (Hofmann, Bessler et al. (2003), Dreier, Bougie et al. (2006)). Laser fluence level had to be checked against signal level because of domination of sublimation at higher fluence level. Background chemiluminescence and Plank radiation from combustion needed to be suppressed by spectral filters and a gated iCCD both spectrally and temporally. The effect of consecutive laser pulses on diminishing the number density of soot due to sublimation of particles was discussed. Results were qualitative only. This was because of laser excitation and signal trapping due to varying oxygen fraction and high turbulence in the combustion chamber. This was compounded by problems of window fouling, beam steering and combustion luminosity. Also, since there is no complete agreement on modelling the LII signal, a qualitative result was more appropriate. There were some LII measurement problems with the extinction of laser sheet by soot particles and trapping (attenuation) of the signal from measurement area to detector and they both affected the result. These are both spatially inhomogeneous, requiring time consuming 3D measurements to compensate (Inagaki, Miura et al. (1998), Bruneaux (2001), Talley, McDonell et al. (2001)). However, laser extinction can be minimised by carefully selecting the laser profile and fluence (Bladh and Bengtsson (2004)).

Further consideration and analysis of high speed two dimensional LII measurements was presented in Sjöholm, Wellander et al. (2011). They presented the change in LII signal as separation between two laser pulses changes and found signal from the first laser pulse was still being detected in the second pulse for pulses separation under 5µs. The possible destruction of soot by sublimation by the earlier laser pulse and affecting the subsequent pulse was discussed. The issues of signal trapping and laser attenuation were also analysed. This highlights the challenges of high speed, closed coupled planar LII.

Menkiel, Donkerbroek et al. (2012) described experimental signal fitting issues due to noise and problems with selecting the initial condition for determining soot particle size. A least square method was applied in an attempt to minimise the problem. It highlighted the dependence on assumption of uncertain optical properties of soot, in-cylinder pressure, gas temperature and initial soot temperature for the purpose of determining soot particle size. Other variables such as the choice of thermal accommodation coefficient also affected the accuracy of the result.

1.5.7 Result Verification

One of the ways to verify LII soot volume fraction measurement in an engine is to analyse the particulates at the exhaust, which was applied in Boiarciuc (2006), Boiarciuc, Foucher et al. (2007) and Aronsson, Sjöholm et al. (2010). Boiarciuc, Foucher et al. (2007) found, as EGR increased, stronger increase of soot concentration when analysing exhaust gas compared to in-cylinder measurement. It was suggested that this might have been due to less oxidation as dilution increased.

In Kock, Tribalet et al. (2006), the soot particle size measurement was verified by collecting the soot and analysing it using a transmission electron microscope (TEM). TEM analysis was also used in Boiarciuc (2006) and it showed good agreement between the size obtained by LII and TEM by modifying the accommodation coefficient and refractive index used in the calculation for modelling and simulating the LII processes. However, the uncertainty in sampling through TEM has be raised (Kondo, Aizawa et al. (2013)).

1.5.8 Summary

This section has shown the different LII techniques which can be applied to measurement of soot in an optical engine. Different engine setting has been used to measure soot formation and distribution within the combustion chamber and have identified experimental issues encountered.

The ideal LII setup is to use simultaneous 2-color LII and planar LII which gives a quantitative value to soot distribution in the combustion chamber. Criteria for selecting the laser will be the wavelength which has less interference from the combustion processes and also enough power to energise the soot particles but not so much so that sublimation dominates. It is also appropriate to use simulated EGR and skip-firing due to the limitation of the optical engines. Combined with the variables which can be varied in Section 1.3, soot measurement can be made for low temperature combustion of diesel in an optical engine.

1.6 Chapter Conclusion

This chapter laid out the various diesel engine combustion strategies and the underlying variables and their effects on efficiency and emission. This provides the theoretical basis for the experimental work carried out. Different optical diagnostic techniques were reviewed and specifically the LII of soot in optical engines was described.

LII measurement provides the ability to visualise soot formation and oxidation within the engine. The best approach is to apply 2-color time-resolved LII together with planar LII which will provide spatial information on in-cylinder soot without the need for calibration. Another plan will be to employ 4 double pulsed lasers and find the soot development within one engine cycle.

Soot visualisation combined with the ability to control injection timing, injection pressure, and EGR, the use of multiple injections and skip firing, variation of bowl design and optical access from below and sides of the combustion chamber will allow for different variables and their effects to be tested. The research opportunity lies in the ability to simulate low temperature combustion as described in the literature found in Section 1.3 and apply LII to measure soot in an optical engine. This will enable a comprehensive study of in-cylinder soot using low temperature diesel combustion.

This experimental study is supported by the use of a multi zone calculation of PCCI based on chemical kinetics. The understanding of combustion based on chemical kinetics is important for low temperature combustion as ignition is chemically and mixing

controlled. Using the calculation enables study of the low temperature combustion, or PCCI combustion, in conjunction for time consuming experiments. The calculation may bring in new information which may be possible to replicate in the experiment.

2. Laser Induced Incandescence (LII) in Vacuum

2.1. Introduction

This work was carried out at Herriot-Watt University Physics Departement along with Vivien Beyer and Douglas Greenhalgh and was used as a basis for understanding the theory, technique and potential issues of the LII work that was subsequently carried out in the Hydra optical engine in Imperial. There is significant difference in operating condition between the low pressure condition used in this chapter and the condition to be expected in the combustion chamber of an engine. At pressure of 10^{-6} bar as applied in this chapter, conduction heat loss equation is intentionally hugely reduced, whereas in the combustion chamber of the engine, at around 10^{2} bar, the conduction term dominates and will lead to significantly shorter LII signal duration. Despite this, the theoretical basis, calibration procedure and the challenges of applying LII to study soot particles for both conditions remain the same and it was valuable to gain experience using this technique.

Laser induced incandescence (LII) is an optical method of studying nanoparticles such as soot and carbon black. The technique involves detecting the heating of the particles by laser and its subsequent cooling. The cooling is predominately due to radiation, conduction, sublimation, along with other heat loss mechanisms that may include oxidation and annealing. By applying LII to soot particles in a vacuum eliminates the conduction term of the heat loss calculation and the LII signal itself is increased and prolonged. This also reduces the signal to noise ratio and the lower detection limit for small particles. By eliminating the conduction term and maintaining the soot particle to below soot sublimation temperature, or identifying where sublimation subsides and radiation dominates, the modelling of radiation heat loss can be investigated more thoroughly. The modelling of radiation relies on knowledge of the emissivity and of the complex refractive index of the soot particle and these values suggested from various sources in the literature (Schulz, Kock et al. (2006) and Dreier, Bougie et al. (2006)) can be evaluated using this experiment.

2.2. LII Model

This section presents a modelling investigation to find the condition at which sublimation occurs as a function of particle size, ambient pressure and laser fluence. This sections starts in section 2.2.1 by describing the model and in section 2.2.2. and 2.2.3 which describes the application of the model with different conditions and particle sizes to look at the theoretical heat loss by different mechanism. Laser induced incandescence (LII) involves the measurement of the non-black body radiation emitted by the soot particles when heated up by a laser. The LII signal comes from blue-shifted light from soot particles as they absorb the incident laser radiation and hence are heated to a temperature much higher than surrounding gas. LII is a way to measure soot primary particle sizes and soot volume fraction. Soot volume fraction is approximately proportional to both the integrated signal and peak signal level (Melton (1984), Bladh, Johnsson et al. (2008)). The decay rate of the LII signal is related to the size of the primary particle.

An overview of research done in the area of LII was described by Schulz, Kock et al. (2006), Tropea, Yarin et al. (2007), Zhao (2010). Weeks and Duley (1974) first observed the heating up of soot particle using a CO_2 laser. It has since been applied to soot volume fraction measurements in laminar diffusional flames (Quay, Lee et al. (1994), Ni, Pinson et al. (1995), Shaddix and Smyth (1996), Bryce, Ladommatos et al. (2000), Witze, Hochgreb et al. (2001)), laminar premixed flames (Vander Wal (1994), Appel, Jungfleisch et al. (1996), Zhao and Ladommatos (1998), Axelsson, Collin et al. (2000), Axelsson, Collin et al. (2001)), turbulent flames (Ni, Pinson et al. (1995), Geitlinger, Streibel et al. (1998), Bockhorn, Geitlinger et al. (2002), Meyer, Roy et al. (2005)), combustion vessels (Idicheria and Pickett (2005), Idicheria and Pickett (2007), in-cylinder measurements (Dec and Espey (1992), Dec, Zur Loye et al. (1992), Kock, Eckhardt et al. (2002), Bougie, Ganippa et al. (2006), Kock, Tribalet et al. (2006), Boiarciuc, Foucher et al. (2007), Bougie, Ganippa et al. (2007), Miles, Collin et al. (2007), Musculus (2007), Singh, Reitz et al. (2007), Chartier, Aronsson et al. (2009), Aronsson, Sjöholm et al. (2010)) and exhaust gases (Schraml, Will et al. (2000), Snelling, Smallwood et al. (2000)).

2.2.1. LII Model Description

Melton (1984) first setup the mass and energy balance equation for quantitative measurement of soot. A summary of subsequently developed models are available: from Schulz, Kock et al. (2006), who reviewed LII techniques and models, and Michelsen, Liu et al. (2007) who reviewed and compared LII models. Will, Schraml et al. (1998), Snelling, Liu et al. (2000), Hofeldt (1993), Bladh and Bengtsson (2004), Michelsen (2003), Dreier, Bougie et al. (2006) and Vander Wal (1994) are other modelling and theory sources. The model used here for LII in vacuum work is based on the work of Michelsen (2003).

The basic energy equation of a carbon particle undergoing laser heat up is shown in equation (2-1).

$$\dot{Q}_{int} = \dot{Q}_{abs} - \dot{Q}_{sub} - \dot{Q}_{cond} - \dot{Q}_{rad} \quad (2\text{-}1)$$

In equation (2-1), $\dot{Q}_{int}$ is the internal rate of energy change of the particle; $\dot{Q}_{abs}$ is the rate of laser energy absorbed by the particle; $\dot{Q}_{cond}$ is the rate of heat loss through conduction; $\dot{Q}_{sub}$ is the rate of heat loss through sublimation; $\dot{Q}_{rad}$ is the rate of heat loss through radiation. Other heat loss mechanism such as annealing and oxidation are omitted here. Annealing is when carbon particles melt and re-crystallise producing an annealed particle and oxidation of the carbon particle produces gases including carbon monoxide. More information about these heat loss mechanisms can be found in Michelsen (2003).

$\dot{Q}_{int}$ is the rate of internal energy change of the particle and it depends on specific heat capacity c_s, density ρ_s, diameter d_p (implicitly assuming that a suitable equivalent spherical particle diameter can be defined or otherwise found) and rate of change of temperature of the particle, $\frac{dT}{dt}$. This is shown in equation (2-2)

$$\dot{Q}_{int} = \frac{\pi d_p^3 \rho_a c_s}{6} \frac{dT}{dt} \quad (2\text{-}2)$$

The rate of absorption of laser light energy, $\dot{Q}_{abs}$, shown in equation (2-3) depends on laser fluence F [J.cm^2]. $q_{exp}(t)$ is the pulsed laser temporal power density

normalised by the particle area over the heating pulse duration, for example, 60ns (Snelling, Liu et al. (2004)).

$$\dot{Q}_{abs} = C_{abs} \frac{F q_{exp}(t)}{\int_0^{60ns} q_{exp}(t)\, dt} \tag{2-3}$$

The absorption cross section C_{abs} can be expressed as in equation (2-4) where λ is the wavelength of light.

$$C_{abs} = \frac{\pi^2 d_p^3 E(m)}{\lambda} \tag{2-4}$$

E(m) is a function of the complex refractive index and can be expressed by equation (2-5).

$$E(m) = -Im\left(\frac{m^2 - 1}{m^2 + 2}\right) = \frac{6 n_m k_m}{(n_m^2 - k_m^2 + 2)^2 + 4 n_m^2 k_m^2} \tag{2-5}$$

Where m is the complex refractive index and $m=n_m-k_m i$. Smyth and Shaddix (1996) review values of soot refractive index and suggested the complex refractive index is 1.57-0.56i. Sorensen (2001) reviewed the scattering and absorption of light by fractal aggregates which included different complex refractive indexes from a physical point of view. For LII application, Schulz, Kock et al. (2006) and Dreier, Bougie et al. (2006) included the complex refractive index used in the models reviewed.

There is an issue with smaller particles as they have larger surface to volume ratio than larger particles and hence cool faster (Tropea, Yarin et al. (2007)). This has implication for detection gate setting as a longer or delayed detection gate produces an integrated signal which underestimates particle sizes (Ni, Pinson et al. (1995), Vander Wal (1996)). A further discussion of this can be found in Snelling, Liu et al. (2000).

The radiation heat loss, $\dot{Q}_{rad}$ is the energy loss from the soot particle derived from non-black body emission after heating by the laser and is the source of LII signal. It is derived from integration of the Planck function and can be expressed by equation (2-6) where ε_λ is the emissivity which is related to the absorption cross section, k_B is

the Boltzmann constant (1.381×10^{-23} J/K), T is the particle temperature, h is the Planck constant (6.626×10^{-34} Js) and c is the speed of light (2.998×10^{10} cm/s).

$$\dot{Q}_{rad} = \pi {d_p}^2 \int_0^\infty \varepsilon_\lambda \frac{2\pi hc^2}{\lambda'^5 [exp(hc/\lambda' k_B T)]} d\lambda' \tag{2-6}$$

The emissivity is given in equation (2-7) and this value is a matter of much discussion as it relates directly to the accuracy of both energy balance equation and signal calculation. As the emissivity is dependent upon E(m), in addition to the short discussion above, this is investigated further in Section 2.3.3.1.

$$\varepsilon_\lambda = \frac{4C_{abs}}{\pi d_p^2} = \frac{4\pi d_p E(m)}{\lambda} \tag{2-7}$$

Heat conduction from the soot particle to the surroundings is carried out as gas molecules collide with the surface of the soot particle. The first variable to define is the mean free path of the gas molecule in cm, λ_g for the surrounding gas with a mean molecule cross section, σ_a in cm^2 given in equation (2-8). The medium is assumed to be air and the Boltzmann constant, k_B is 1.381×10^{-23} J/K.

$$\lambda_g = \frac{k_B T_0}{\sqrt{2}\sigma_a P_0} \tag{2-8}$$

The cooling rate can be classified by the Knudsen number, Kn, which is the ratio of the particle radius, r_p to the mean free path of the gas molecules, λ_g in which the particle is suspended. When Kn is around 0, this is in the familiar continuum regime where the mean free paths of the gas molecules are very much smaller as compared to the particle radius. For Kn approximately equals to 1, this is the transition regime where the mean free paths of gas molecules are about the same as the particle radius. For mean free path larger than the particle radius, this is the free molecule (kinetic) regime and Kn approaches infinity. If the mean free path greatly exceeds the radius of the particle, heat and mass transfer is in the free molecule regime and conduction is given by equation (2-9). α_T is the thermal accommodation coefficient for rotational and translational degrees of freedom and assumed to be 0.3 but a range between 0.2-1 has been found in various studies. A_0 is Avogadro's number 6.023×10^{23} molecules/mol.

$$\dot{Q}_{cond} = \frac{\pi {d_p}^2 \alpha_T Z_{surf}}{A_0}\left(C_p - \frac{R}{2}\right)(T - T_0) \tag{2-9}$$

Z_{surf} is the collision rate (1/s cm^2) of ambient gas molecules with the particle surfaces per unit surface area and is given in equation (2-10). R_m is the universal gas constant in effective pressure units (82.058 atm cm^3/mol K) and W_a is the average molecular weight of air with the value of 28.74 g/mole.

$$Z_{surf} = \frac{P_0}{k_B T_0}\sqrt{\frac{R_m T_0}{2\pi W_a}} \tag{2-10}$$

If the condition of equation (2-11) is satisfied where the flow is in the transition regime between Knudsen and continuum flow, the heat loss through conduction is given by equation (2-12). In equation (2-11), γ is the heat capacity ratio for the gas surrounding the particles and is 1.4 for air at 300K and 1.3 for air at 1500K.

$$K_n = \frac{\lambda_g}{d_p} < 5\sqrt{\frac{\gamma\pi}{2}} \tag{2-11}$$

For the heat loss by conduction, given in equation (2-12), κ_a is the thermal conductivity of the surrounding gas and this is given by equation (2-13). The heat transfer factor, G, is given by equation (2-14).

$$\dot{Q}_{cond} = \frac{2\kappa_a \pi D^2}{\left(D + G\lambda_g\right)}(T - T_0) \tag{2-12}$$

In equation (2-13), A_0 and A_1 for air are given as 1.0811×10^{-4} W/cm K^2 and 5.1519×10^{-7} W/cm K^2 respectively.

$$\kappa_a = A_0 + A_1 T_0 \tag{2-13}$$

In equation (2-14), f is the Eucken correction to the thermal conductivity given in equation (1-19).

$$G = \frac{8f}{\alpha_T(\gamma + 1)} \tag{2-14}$$

$$f = \frac{9\gamma - 5}{4} \tag{2-15}$$

Sublimation heat loss come from sublimation and breaking up of carbon atoms into vapour. This process begins at 1800K and contributes significantly to heat loss around 2500-2600K. There are different ways to calculate the sublimation heat loss and the one used is from Snelling, Liu et al. (2000) which was derived from Eckbreth (1977), Melton (1984), Hofeldt (1993). $\dot{Q}_{sub}$ is given in equation (2-16) where ΔH_v is the heat of vaporization of graphite in J/mole and M_v is the molecular weight of soot vapour in g/mole.

$$\dot{Q}_{sub} = \frac{\Delta H_v}{M_v}\frac{dM}{dt} \tag{2-16}$$

$\frac{dM}{dt}$ can be expressed in a mass conservation equation shown in equation (2-17) where $\frac{dd_p}{dt}$ is the change of particle diameter with respect to time, N_v is the molecular flux of evaporated carbon in molecules/m^2s as defined in equation (2-18).

$$\frac{dM}{dt} = 2\rho_s \pi {d_p}^2 \frac{dd_p}{dt} = -4\pi {d_p}^2 N_v \frac{M_v}{A_0} \tag{2-17}$$

$$\frac{1}{N_v} = \frac{1}{N_c} + \frac{1}{N_k} \tag{2-18}$$

In equation (2-18), N_c is the molecular flux of sublimated particles in the continuum regime given in equation (2-19) where n_v is the molecular density of soot vapour given in equation (2-20) and Γ is the diffusion coefficient of soot vapour in m^2/s.

$$N_c = 2n_v \frac{\Gamma}{d_p} \tag{2-19}$$

In equation (2-20), P_v is the vapour pressure of soot in Pa and R is the universal gas constant which is 8.313J/mole K.

$$n_v = \frac{P_v A_0}{RT} \tag{2-20}$$

N_k is the molecular flux of sublimated particles in the Knudsen regimes (free molecules) given in equation (2-21) and β is the evaporation coefficient of about 0.8. ΔH_v, M_v and P_v are all function of temperature.

$$N_k = \beta n_v \sqrt{\frac{\mathrm{RT}}{2\pi M_V}} \tag{2-21}$$

The LII signal generated through radiation from each particle in the detection volume is given by equation (2-22). Using this equation, the signal can be found by integrating over the range of wavelength for a range of temperature.

$$S = \Omega \pi D^2 \int_\lambda \varepsilon_\lambda \frac{2\pi hc^2}{\lambda'^5 \left[\exp\left(hc / \lambda' k_B T\right) - 1\right]} \sum_\lambda (\lambda') d\lambda' \tag{2-22}$$

In equation (2-22), S is the LII signal, Ω is a normalization constant relating to the solid angle (2 dimensional detection angle of a 3 dimensional object from a distance), D is diameter of the particle, ε_λ is the emissivity which is related to the absorption cross section, h is the Planck constant, c is the speed of light and λ is the wavelength of light.

2.2.2. Application of the Model

The modelling applied here was based on Michelsen (2003) as shown in the previous section. The benefit of low pressure environment is to minimise the heat loss through conduction and hence simplifying the energy balance equation. This extends the signal time providing a potentially more detailed analysis on other heat loss mechanism such as radiation and sublimation. As some of the values, such as emissivity, used in the model are not reliably known, the reduction of pressure will enable better accuracy in their determination. This extension of signal duration is shown as a function of pressure and the variation of temperature through the time in Figure 2-1, calculated from modelling as shown in Beyer (2006) . This extension of signal in the reduced pressure environment is due to the reduction of conduction as

a heat loss mechanism, so that the soot particles remain at a higher temperature for longer.

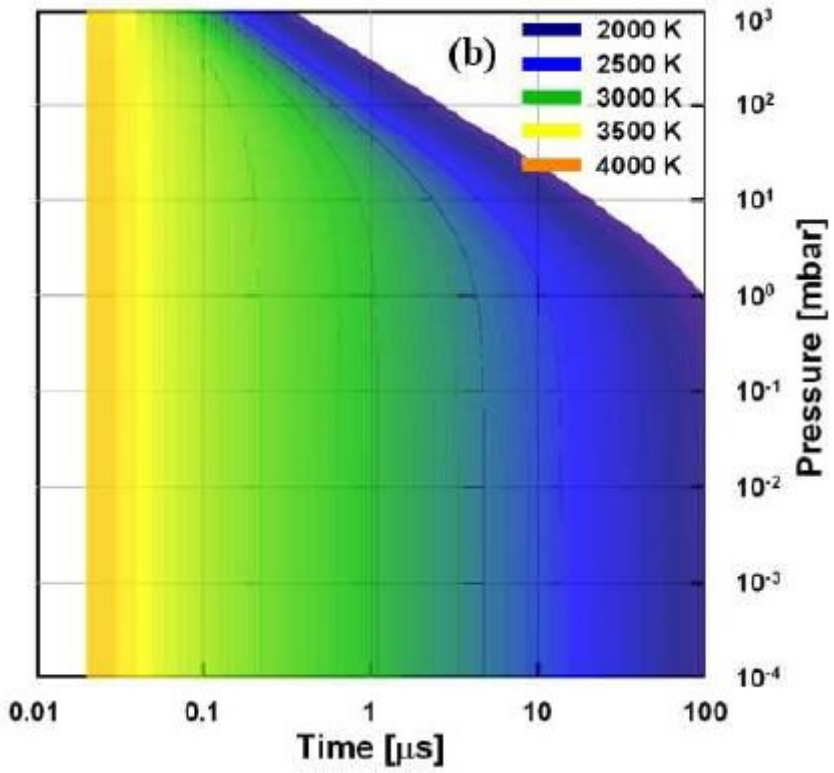

Figure 2-1: Modelling result showing LII signal duration as a function of pressure with temperature as a parameter for a 5nm diameter primary particle subjected to 0.06J/cm^2 of laser fluence in a gas at 300K (Beyer (2006)).

For the investigation in this thesis, laser irradiance, atmospheric pressure and particle size was varied. Sublimation of carbon particles is expected to dominate above 2800K and this can be reached by using higher laser fluence if sublimation is a mechanism of interest. The effect of sublimation will be more prominent at lower pressure as heat loss through conduction will be lower. Larger particles have a higher sublimation heat loss compared to conduction because the surface to volume ratio is smaller.

The experiment here made use of the so-called aerodynamic lens, which creates an aligned stream of particle from the particle source (described below) forming a molecular beam in the experiment which ejected different sized particles at different speed. Therefore, changing the particle size affects the two factors, time exposed to

the laser and area for laser absorption, which change the maximum temperature reached. One important point regarding particle diameter is that it is usually correlated with the particle velocity across the laser beam. This means, specifically, that smaller particles have a higher velocity across the laser beam and a shorter amount of time available for laser absorption. The variation of velocity is due to the use of the mode of operation of the aerodynamic lens.

2.2.3. Modelling Results

2.2.3.1. Factors Influencing the Heat Loss Contribution

The results presented belowe shows the contribution of conduction, radiation and sublimation as a percentage of total energy loss. A few variables were modified and compared to see how the various heat loss mechanisms were affected. The model was run with laser irradiance of 10% (7.56 $x10^4 W/cm^2$), 50% ($3.78x10^5 W/cm^2$) and 100% ($7.56x10^5 W/cm^2$) based on the laser used, described in section 2.3.2, in the experiment. Different particle diameters of 10nm, 30nm and 60nm at pressures of 10^{-6} bar, 10^{-5} bar, 10^{-4} bar, 10^{-3} bar and 10^{-1} bar were also compared.

Figure 2-2 to Figure 2-4 show energy loss through conduction as a percentage of the total energy loss as a function of time as a function of laser power with ambient pressure as a parameter for particles sized 10, 30 and 60 nm. The sharp initial rise of conduction loss is due to the absorption of the laser energy and increase in internal energy of the soot particle. This is true for all cases. As pressure increases, conduction increasingly becomes the major contribution of energy loss as the absolute radiation energy loss remains constant- as it is not pressure dependent. Generally, particle size affects the surface to volume ratio which dictates the rate of heat loss, which is particularly apparent between 30nm and 60nm particle.

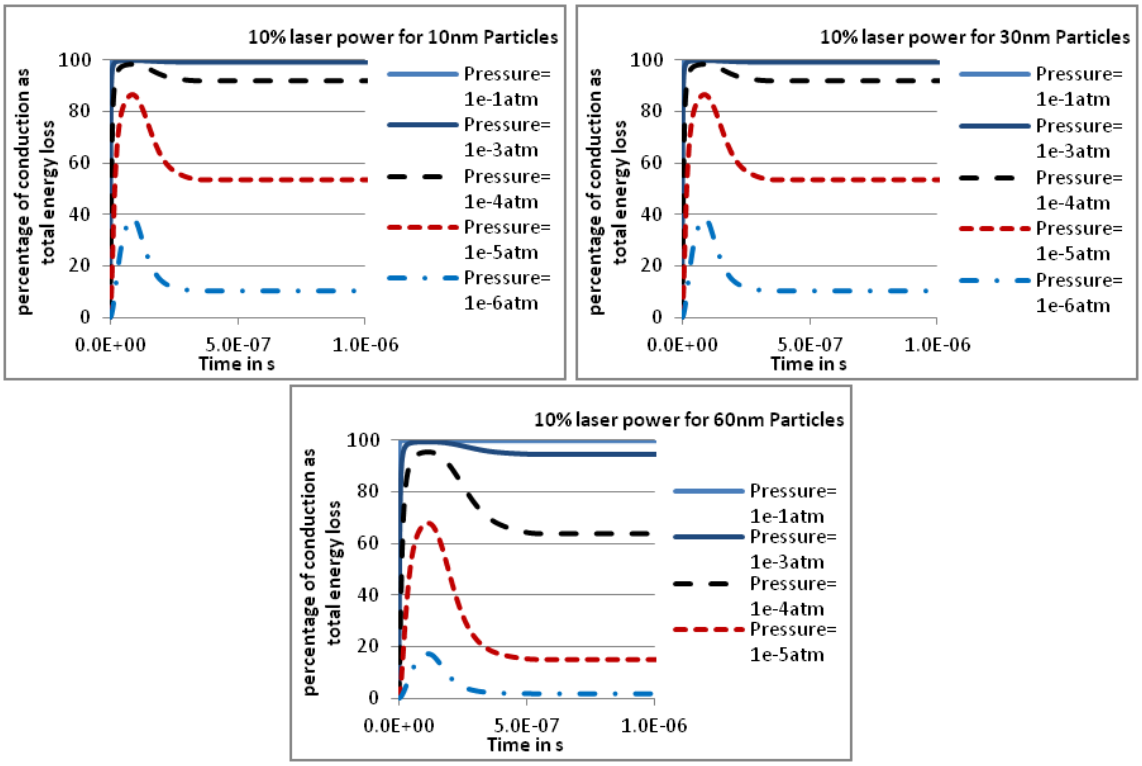

Figure 2-2: Heat loss through conduction, as a percentage of total energy loss , as a function of time through time at 10% laser irradiance with pressure as parameter for three diameters (10,30 and 60nm).

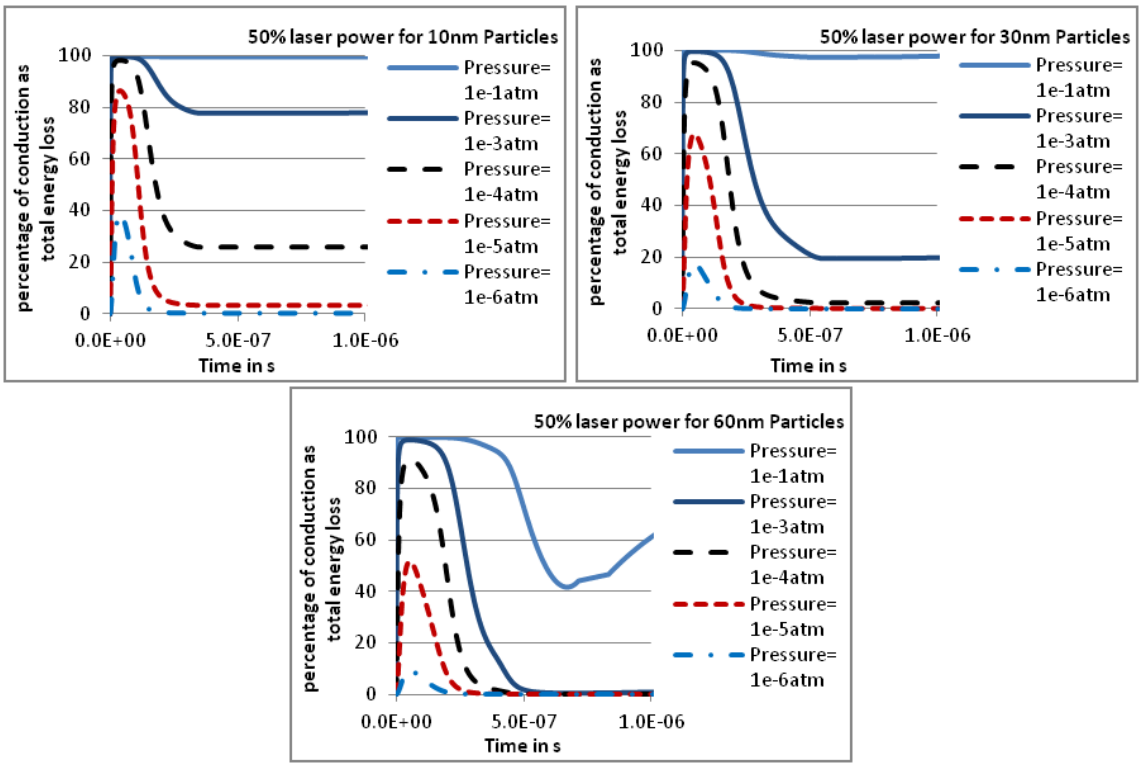

Figure 2-3: Heat loss through conduction, as a percentage of total energy loss , as a function of time through time at 50% laser irradiance with pressure as parameter for three diameters (10,30 and 60nm).

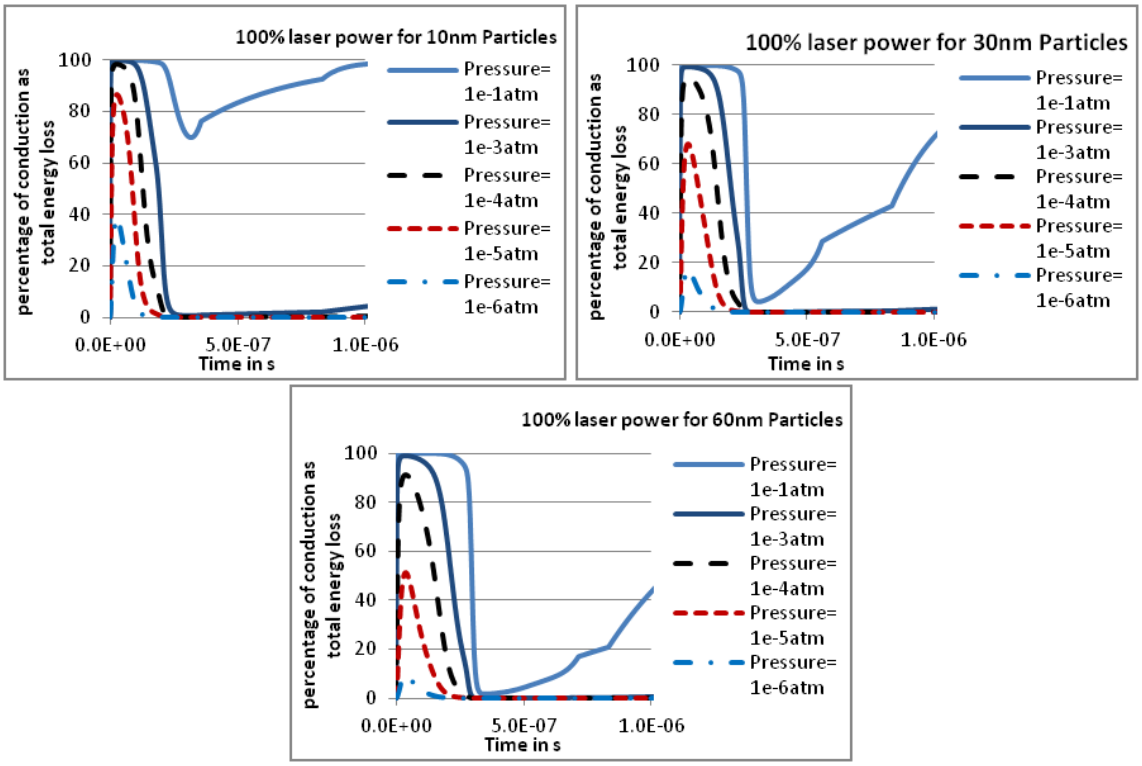

Figure 2-4: Heat loss through conduction, as a percentage of total energy loss , as a function of time through time at 100% laser irradiance with pressure as parameter for three diameters (10,30 and 60nm).

The general trend shows increase contribution to total energy loss by conduction as the pressure increase. Larger particles have lower contribution of heat loss from conduction than smaller particles and duration of conduction heat loss decreases as particle size decreases. Notably, the small particles at higher pressure and lower laser irradiance have smaller proportions of radiation heat loss as conduction dominates. For the 30 and 60 nm particles, below 10^{-1} atmosphere pressure, and for 10 nm particles at 10% laser irradiances at 10^{-3} atmosphere, conduction has a reduced part in the heat loss after the initial warm up period. This shows the benefit of conducting LII in a low pressure environment for isolating the effect of conduction.

As an example of the contribution from the different heat loss mechanisms, the heat loss is shown as a percentage of total heat loss as a function of time. Figure 2-5 shows two examples of a 10 nm particle with 10% laser irradiance at pressure of 10^{-3} and 10^{-6} atmosphere. It can be seen that sublimation does not occur for 10% laser irradiance setting and heat loss is a trade-off between

conduction and radiation. Conduction dominates at the higher pressure while radiation dominates at the lower pressure, noting that radiation heat loss remains the same for both conditions so the change is brought on by the difference in conduction heat loss.

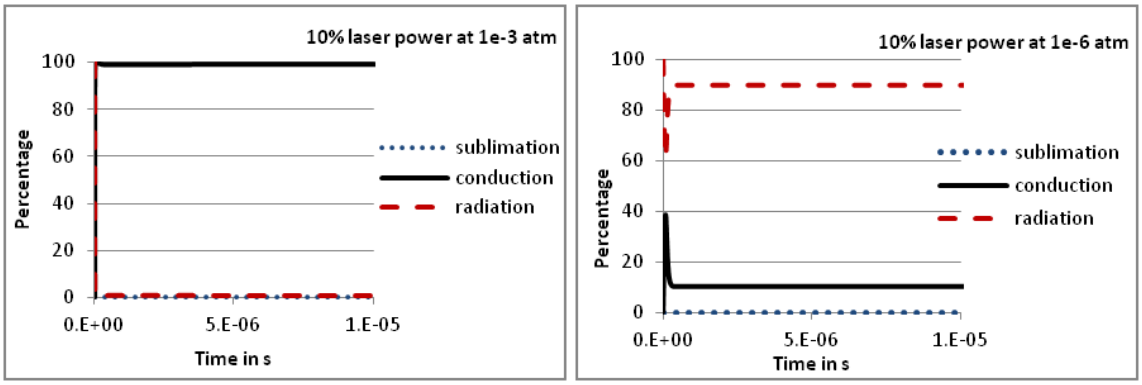

Figure 2-5: Percentage of each heat loss mechanism as a function of time at 10% laser irradiance for a particle diameter of 10nm for two different pressures.

For 50% laser irradiance, not shown here, sublimation depends on particle size, or rather, residence time in the laser. For 10nm particles, sublimation represents a much smaller proportion of the total heat loss and similar to that at the lower, 10%, laser irradiance. For 30nm particles, as shown in Figure 2-6, sublimation makes up at the start of the irradiation a maximum of about 20% of the energy loss at all pressures and thereafter heat loss is a trade-off between radiation and conduction where conduction dominates at higher pressure and radiation dominates for lower pressure. Figure 2-7 shows that, for the 60nm particle, sublimation dominates after 0.7 micro seconds making up to 95% of energy loss and decreases after that. In the case of 100% laser irradiance, very rapidly after the initial period of energy loss through radiation and conduction, sublimation dominates thereafter but declines over time, as shown in Figure 2-8, being balanced by radiation once more.

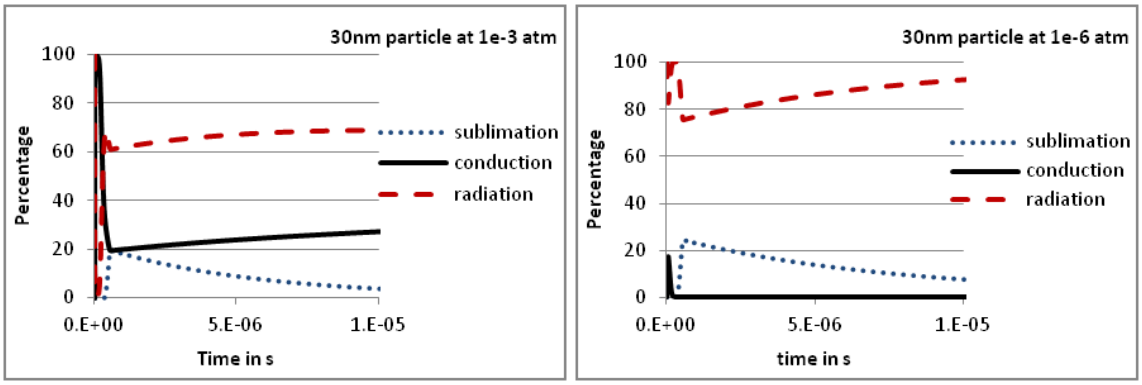

Figure 2-6: Percentage of each heat loss mechanism as a function of time at 50% laser irradiance for a particle diameter of 30nm for two different pressures.

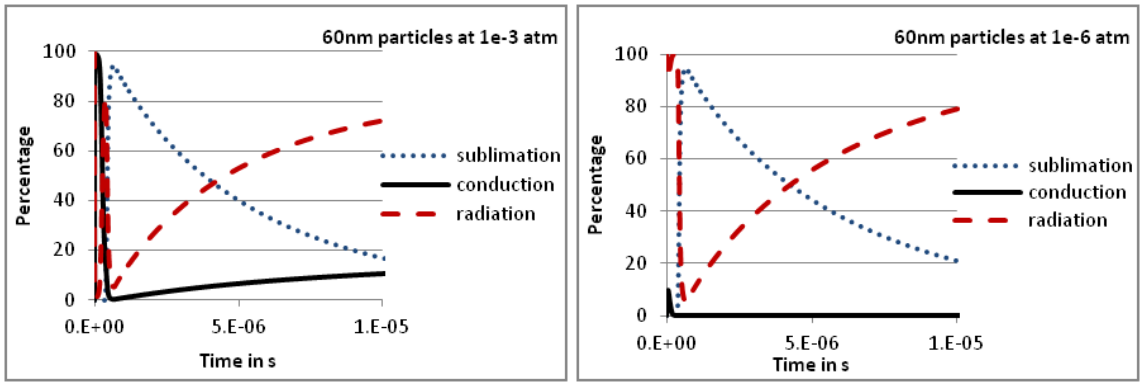

Figure 2-7: Percentage of each heat loss mechanism as a function of time at 50% laser irradiance for a particle diameter of 60nm for two different pressures.

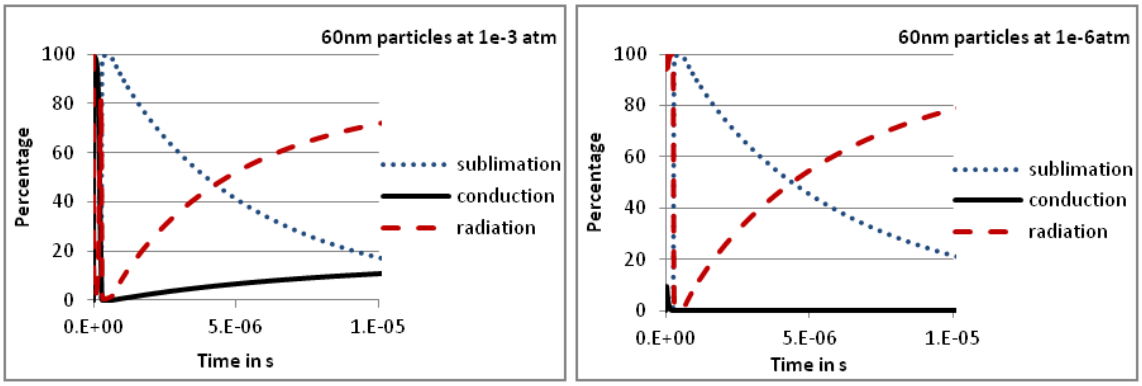

Figure 2-8: Percentage of each heat loss mechanism as a function of time at 100% laser irradiance for a particle diameter of 60nm for two different pressures.

Combining these data, comparisons can be made of the effect of residence time in laser beam (as a consequence of being ejected out of the aerodynamic lens and traversing across the laser) and pressure. Thus, the conduction contribution, at 550ns is shown as a function of particle diameterin Figure 2-9. The sublimation

heat loss as a percentage of total heat loss at 550ns as a function of particle diameter after initial heating is shown in Figure 2-10. The lower laser fluence has been omitted as sublimation does not occur for the lower laser fluence. These two figures complement each other: the balance comes from radiation loss.

At 550ns after start of laser heating, conduction is prominent for lower laser fluence and smaller particle sizes at higher pressure. As pressure decreases, the conduction mechanism for heat loss diminishes. There is a significant drop off for the case of 60nm particle at 3.78 $x10^5 W/cm^2$ laser fluence at a pressure of 10^{-1} atmosphere which indicates the shift to the sublimation regime for larger particles. This can be seen in Figure 2-10 which shows the contribution from sublimation heat loss from the particle. The plot for 10% laser irradiance is omitted here because sublimation does not occur in the model at this power. For the higher laser irradiance setting, conduction is minimal until the pressure reaches 10^{-1} atmosphere. For the 50% laser fluence setting, conduction starts to become important at a lower pressure, namely about 10^{-3} atmosphere which is a function however of particle size at this setting.

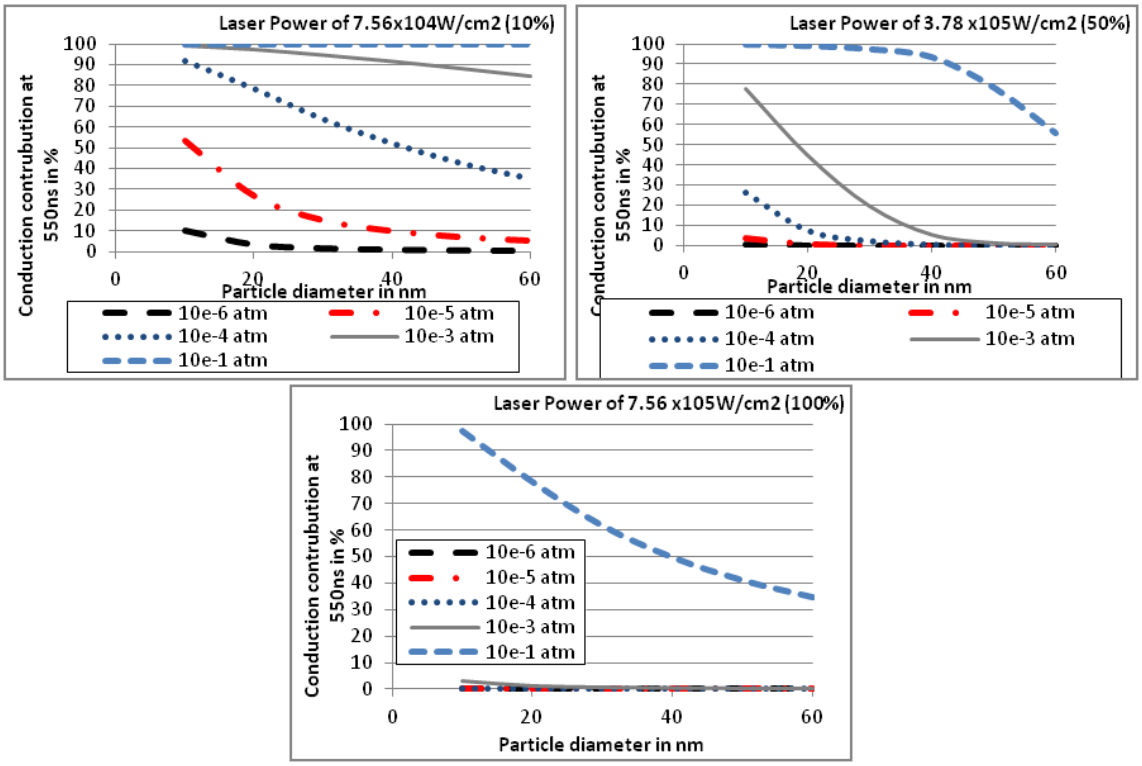

Figure 2-9: Conduction contribution to total heat loss at 550ns for the three laser irradiance values as a function of particle diameter with pressure as a parameter.

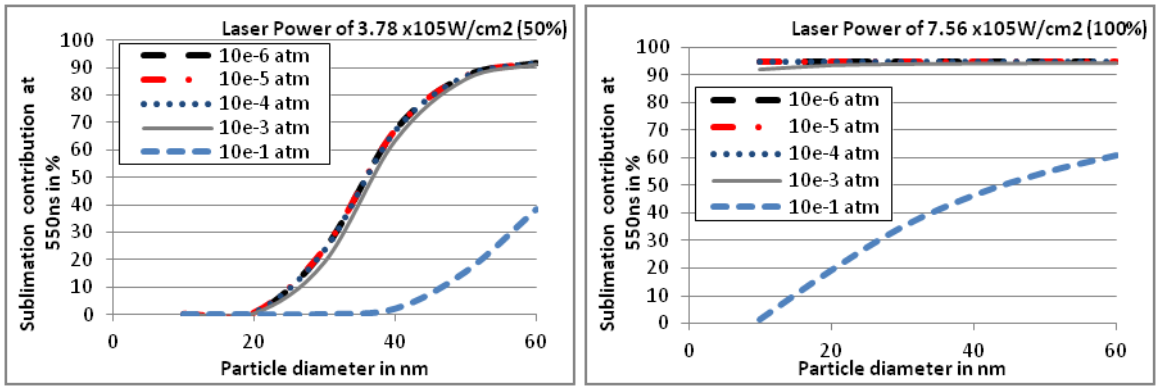

Figure 2-10: Sublimation contribution to total heat loss at 550ns for the two higher laser irradiance values as a function of particle diameter with pressure as a parameter.

2.2.3.2. Particle Temperature

Looking at the same set of variables with laser fluence, pressure and particle size, we can compare the peak temperature and temperature change against time at different conditions. The peak temperature for different particle sizes (and residence time) in laser beam and laser fluence is shown in Table 2-1. The peak temperatures at different pressure are the same hence this is omitted. The

obvious trend is that the higher the laser fluence, the higher the peak temperature which is to be expected. Secondly, the larger the particle size (which implies the longer residence time in the laser), the higher the peak temperature it reaches.

particle diameter	laser irradiance in W/cm2		
	7.56E+04	**3.78E+05**	**7.56E+05**
10nm	759K	1973K	3209K
30nm	949K	2764K	3556K
60nm	1088K	3295K	3710K

Table 2-1: Peak temperature in K of particles at different conditions

In Figure 2-11, temperature as a function of the carbon particle diameter at 550ns after being heated up by the laser is shown, with pressure as parameter. Generally, larger particles reach a higher temperature and higher laser irradiance will produce a higher temperature in a carbon particle. The trend is the same throughout the entire heating and cooling duration. The interesting feature here is that for a particle of 10nm in a pressure of 10^{-1} atmosphere with laser irradiance of $7.56x10^{5}W/cm^{2}$, the temperature is lower than trend shown on the graph compared to the larger particles. This is because, at this pressure and for this particle size, sublimation does not take place which limits the temperature which the particle will achieve.

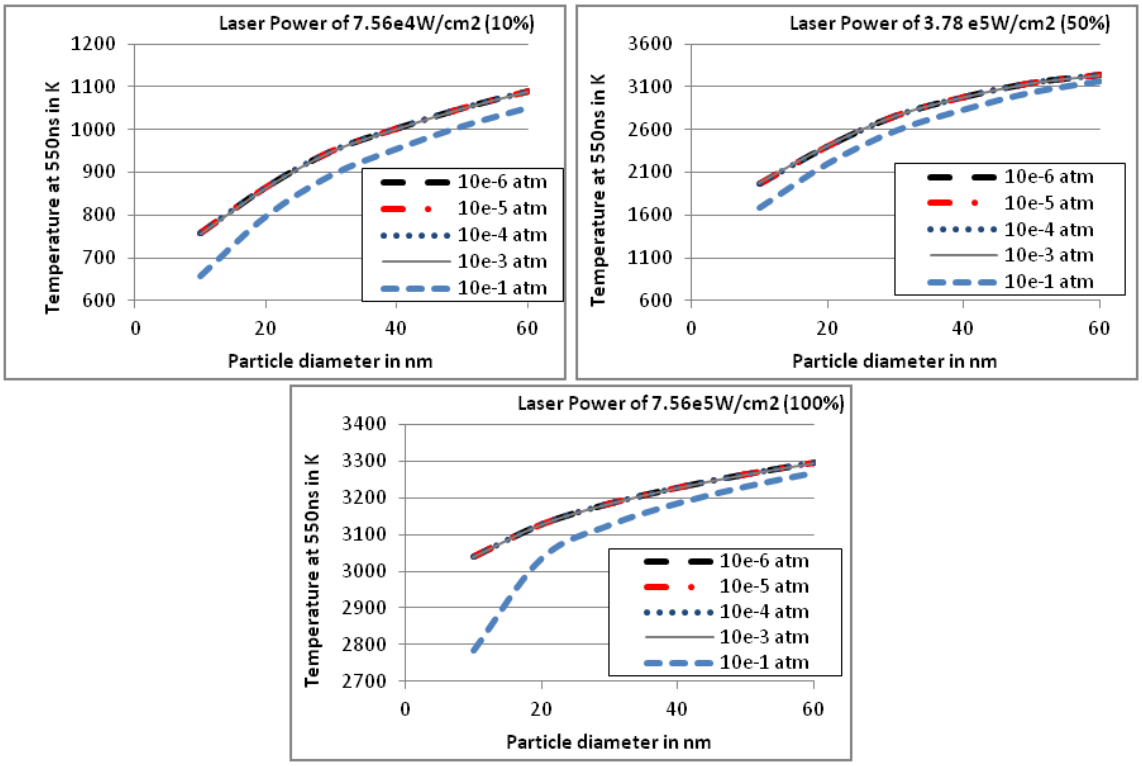

Figure 2-11: Particle temperature at 550ns for the three laser irradiance as a function of particle diameter with pressure as a parameter.

Figure 2-12 shows the temperature evolution of particles with 20nm, 40nm and 60nm diameter at different pressure and laser irradiance. As expected, the rate of decay of temperature is faster at higher pressure. The difference between the laser irradiance of 50% and 100% are not great but there is a difference for laser irradiance of 10% with much lower temperature and smaller decrease of temperature initially. This is because the lack of sublimation heat loss mechanism.

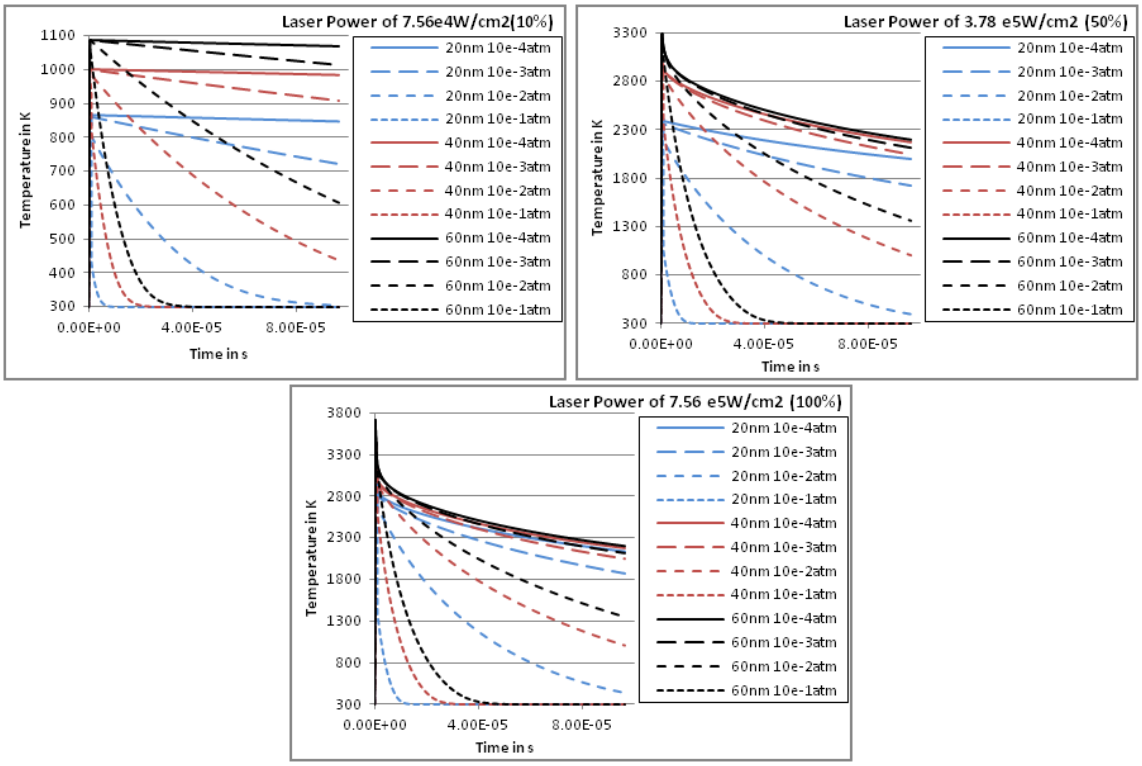

Figure 2-12: Temperature evolution of 20nm, 40nm and 60nm particles at high pressure with various laser irradiances

Peak temperature is an indication of whether sublimation takes place and plotting it against peak sublimation contribution to heat loss will be useful to find its onset. Figure 2-13 shows the relationship (in terms of a scatter plot) between the peak temperature and peak sublimation contribution: there is a change of sublimation contribution at around 2800K. From the previous figures, it can be deduced that the beginning of sublimation occurs for laser irradiance of $3.78 \times 10^5 W/cm^2$ and above for particles larger than 30nm and pressure below 10^{-3} atmosphere.

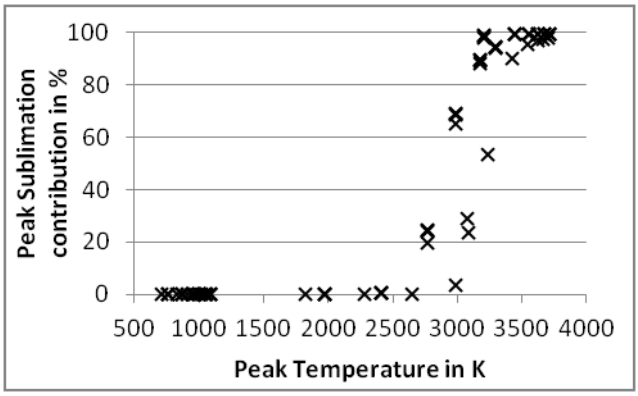

Figure 2-13: Scatter plot of peak sublimation contribution with peak temperature for all values of laser irradiance, pressure and particle sizes

2.2.4. Modelling Conclusion

This modelling investigation has quantified the conditions under which sublimation occurs as a function of particle sizes, ambient pressure and laser irradiance. There is a transition point when the peak temperature reaches 2800K which represents a laser irradiance of $3.78 \times 10^5 W/cm^2$ for pressure lower than 10^{-3} atmosphere. Further investigation can be carried out to look at the exact transition point of which sublimation occurs for smaller increment of laser fluence level. This provides useful information for comparison with the experimental result.

2.3. Experiment

The experiment can be summarised as follows: carbon particles were introduced into a vacuum chamber at a pressure of 10^{-3} mbar through an "aerodynamic lens" (described in greater detailed below) so a focused stream of carbon particles was aligned with the laser beam at a velocity determined by particle size. The laser source was a continuous wave laser operating at 400W, 1070nm fibre laser and optically manipulated to provide a top-hat profile. The LII signal was collected using a two color LII system giving the temperature and particle sizes. Elastic light scattering signal was also collected to determine the particle velocity. With the reduction of pressure, the conduction heat loss was minimised and the LII signal was thereby prolonged and one benefit of which is the better detection of smaller particles.

2.3.1. Equipment

2.3.1.1. Aerosol Generator

Carbon particles were produced by an aerosol generator containing black photocopier toner mixed with water which was driven by compressed air. Carbon particles suspended in the water were passed through an approximately monodisperse micro droplet generator. This was then heated and dried through the heater module and ejected near the inlet to the aerodynamic lens. The concentration of the toner particle in water was 2% by mass. The generator is shown in Figure 2-14 with the heater in the top orange half and tubing connected to the air supply.

Figure 2-14: Aerosol generator with heater (orange part).

2.3.1.2. Aerodynamic Lens

The carbon particles were introduced into the vacuum chamber through the aerodynamic lens creating an aligned stream of particles from the final outlet orifice forming a molecular beam. The principle of the aerodynamic lens is based

on free expansion of the aerosol into a vacuum. Other designs are possible in order to create a molecular beam such as a single orifice or capillary and a pulsed nozzle. However, the single orifice design requires high pumping rate and the pulsed nozzle will create difficulties with synchronising with the laser. An aerodynamic lens allows for wide range of particle diameters and has high transmission efficiency. It also provides a continuous stream of particles into the measurement volume. The beam was focused at 20 mm from the choked nozzle for the particle size range between 10 nm to 10 micrometres.

An aerodynamic lens consists of a series of orifices with decreasing diameter from the inlet to the outlet. The decreasing diameter allows the molecular beam to focus particles of different sizes to pass through the final orifice. Figure 2-15 shows the path of particles of different sizes passing through the aerodynamic lens. More detail of the operation and principles behind the aerodynamic lens can be found in Zhang, Smith et al. (2004) and Zhang, Smith et al. (2002).

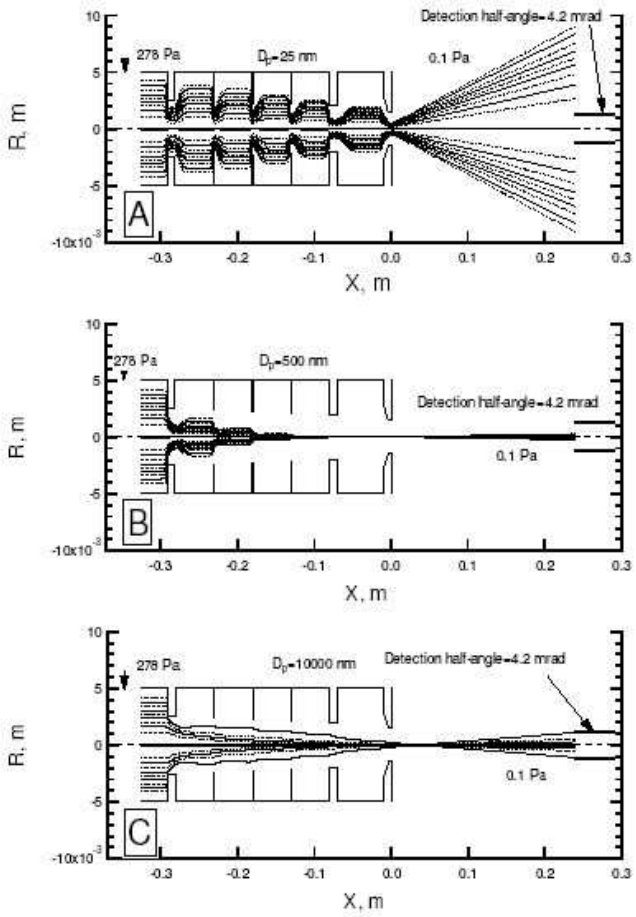

Figure 2-15: Model of the operation of the aerodynamic lens with particles sizes as parameter 25nm diameter particles in A, 500nm particles in B, 10 micrometer diameter particles in C. R,m is the relative distance from the centre of the cylindrical lens and X,m is the distance from the lens inlet. Figure from Zhang, Smith et al. (2004)

Another advantage of the aerodynamic lens is the correlation between particle velocity and particle size because the velocity with which the particles travel through the aerodynamic lens depends on their aerodynamic size. This correlation was measured in the experiment using elastic light scattering to compare with the LII result. The measured relationship between particle velocity and particle diameter can be found in Figure 2-16.

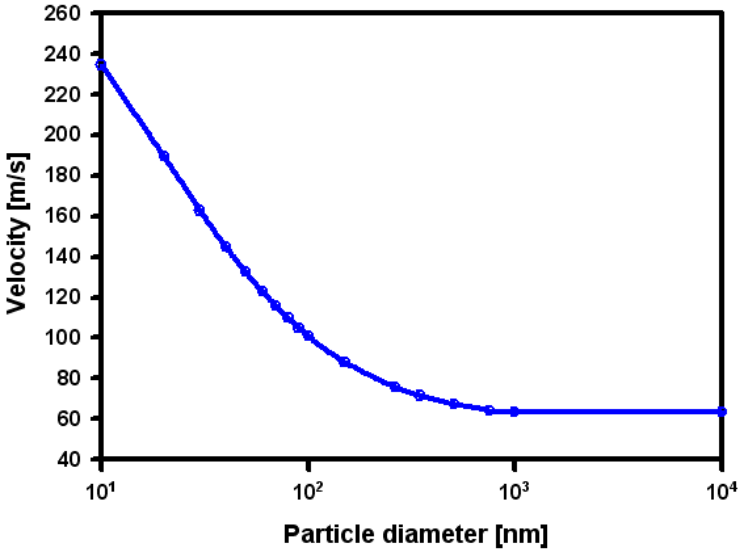

Figure 2-16: Carbon particle velocity variation with particle diameter through the aerodynamic lens.

2.3.1.3. Vacuum Chamber

The vacuum chamber used had windows on three sides to allow for the laser to pass through opposing sides with imaging of the signal from the third, at the top, perpendicular to the other two. One side of the vacuum chamber was connected to the aerodynamic lens for the introduction of particles which passed through the laser beam. The bottom of the vacuum chamber was connected to two pumps to reduce the pressure of the chamber to 10^{-3} mbar. The aerodynamic lens, vacuum chamber and one side of the vacuum chamber are shown in Figure 2-17.

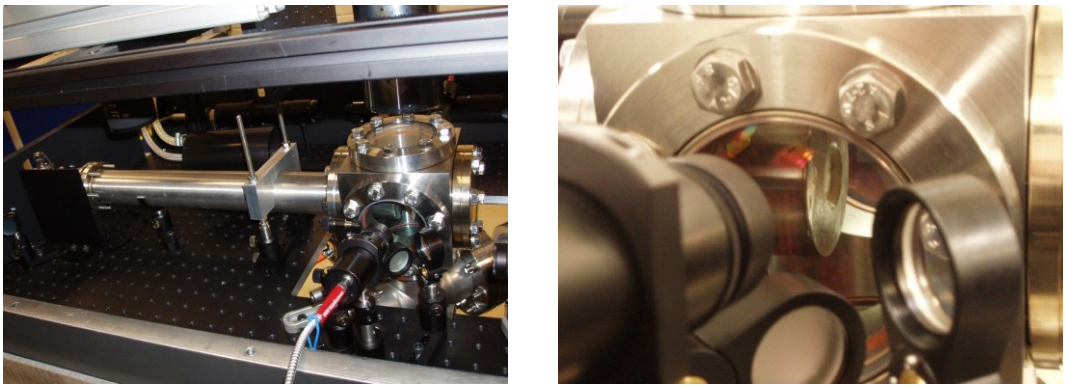

Figure 2-17: Aerodynamic lens and vacuum chamber (left) and a side view of the vacuum chamber (right).

2.3.2. Laser and Optical Setup

The laser and optical setup began with a R4-25 400W continuous wave fibre laser at 1070nm and this was connected to a beam expander, taking the laser beam to 12mm in diameter. The expander required adjustment to its lens separation for the beam to be properly collimated. The complete optical setup is shown in Figure 2-18.

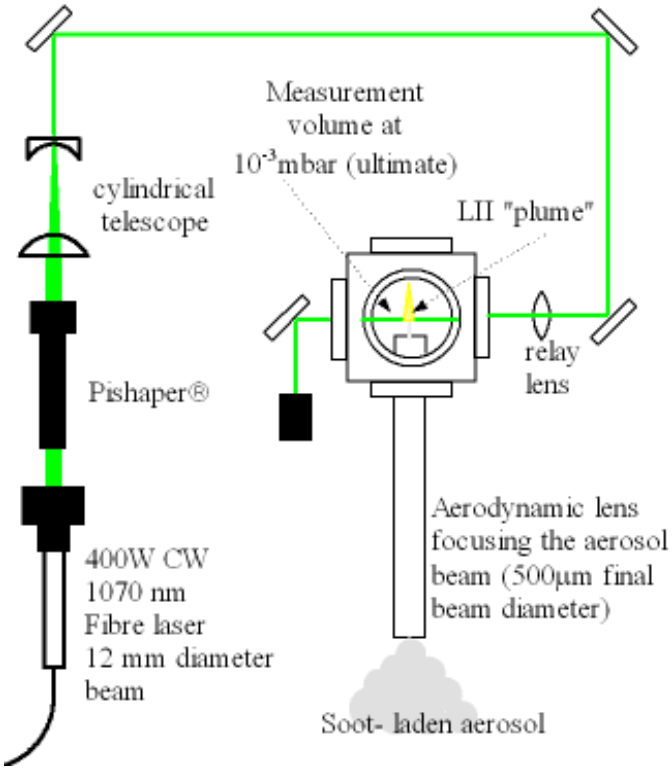

Figure 2-18: Optical setup of the experiment

In order to produce a top hat laser profile, a MolTech GmbH πShaper 12_12_1064 Pi-shaper was used to transform the laser beam from a Gaussian spatial profile. It required the perfect alignment in order for the pi-shaper to convert the profile from Gaussian to top-hat. The alignment had to be precise as the pi-shaper was designed specifically to work with a narrow range of laser diameter and, in this case, it only had the tolerance between 11.9mm-12.1mm. The main tool for alignment was a profile camera which gave the spatial profile of the laser beam. The alignment involved shifting the laser entrance to the pi-shaper towards the location where power was distributed in the output and matching the output end to reform the

profile of the laser beam to the most uniform distribution possible. This iteration continued until the profile was relatively uniform. There was also a need to ensure the laser beam remained collimated after exiting the pi-shaper by changing the distance between the two lenses inside the pi-shaper and this could only be assessed by measuring, in the far field, the laser profile of the beam.

A set of cylindrical lens were used as a telescope to form the beam into a thin sheet and an air gap provided the separation for the focusing lens to focus the 12mm diameter beam into the thickness of 800µm with a negative magnification of 15. Therefore, an air gap of 2.4 meters was required before the lens and 0.16m after the lens to produce the desired laser beam size at the site of observation. However, with this sharp and short focusing distance, there was a possibility that an optical tweezers is created. This is caused by a sharply focused laser beam creating a sufficiently strong electric field gradient at the beam waist to apply a force on sub-micron dielectric particles. A way to reduce this problem is to have a longer focusing distance and lessen the rate of focus over a longer distance. The final laser profile can be seen in Figure 2-19.

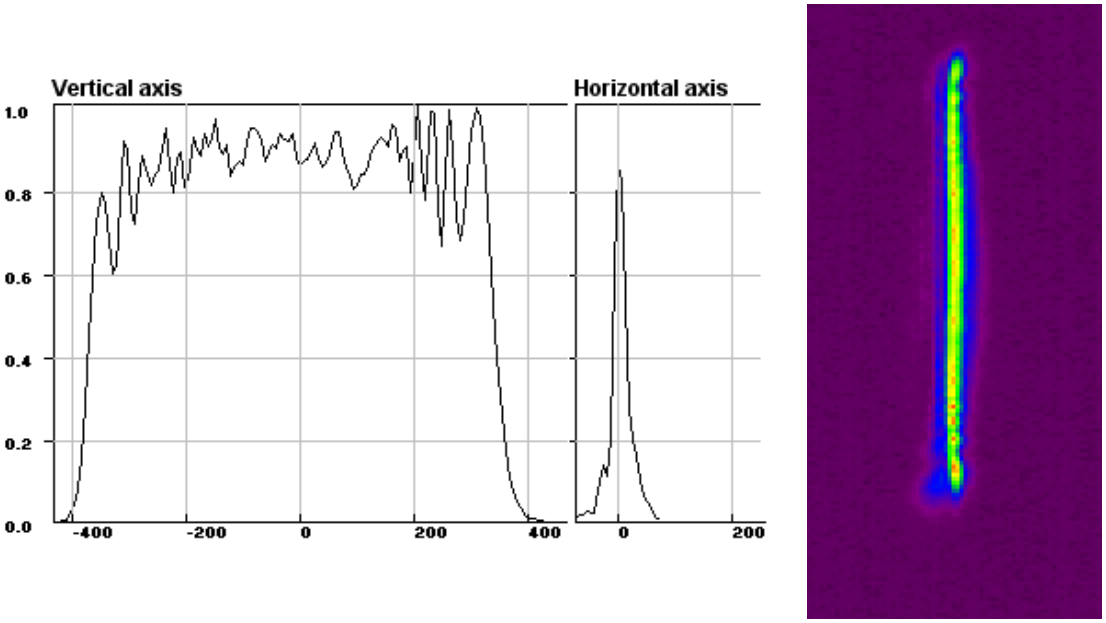

Figure 2-19: Final laser profile

2.3.2.1. Signal Acquisition System

The signal acquisition system used was a two-color time-resolved LII detection system and a forward and backward scattering elastic light scattering (ELS) system. Additionally, an intensified CCD camera was used in place of the two color LII detection system for a 2D view of the LII signal. The two-color time-resolved system used two photomultiplier tubes which detected the LII signal at two different ranges of wavelengths. The intensity of the signal gave the soot particle diameter and the ratio of the signals gave the temperature of the particle. The forward and backward ELS enabled the measurement of the particle velocities. Figure 2-20 shows the two-color LII signal detection system and a diagram of its associated optics.

Photomultiplier tubes (PMTs) detect non-black body emission from the incandescence of the heated soot particles. This provided the self-calibrating red and blue filtered PMT the signal which gave the temperature of the particle in the measuring volume. The PMT detecting the blue signal was a Hamamatsu R7600-200 SEL and a Hamamatsu R5700U-20 detected the red signal. The centre detecting wavelengths for the two PMTs were 443.6 nm (113 nm) and 759.4 nm (97.3 nm).

The Elastic light scattering PMTs detected the elastic light scattered in the infra-red spectrum, registering photons that have collided with the particles and deflected from the measurement volume. The duration of the signal provided the residence time of the soot particles within the measuring volume and the signal intensities provided information on the size of the particle. The PMTs used for this experiment were Hamamatsu R5108 and the signal was collected by a set of lenses and transferred through a fibre optic cable to the PMTs in order to reduce the amount of equipment around the pressure vessel. This also enabled the signal collecting lens to be adjusted easily through the flexible cable connection. This is shown in Figure 2-21.

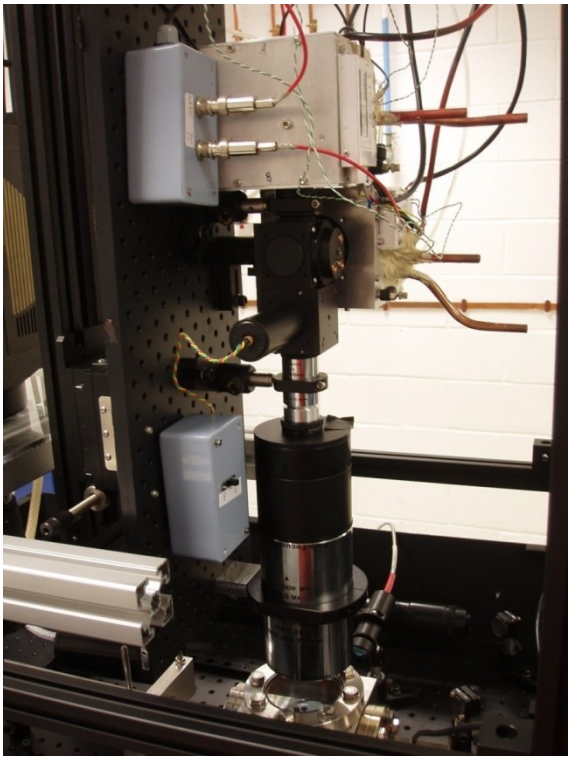

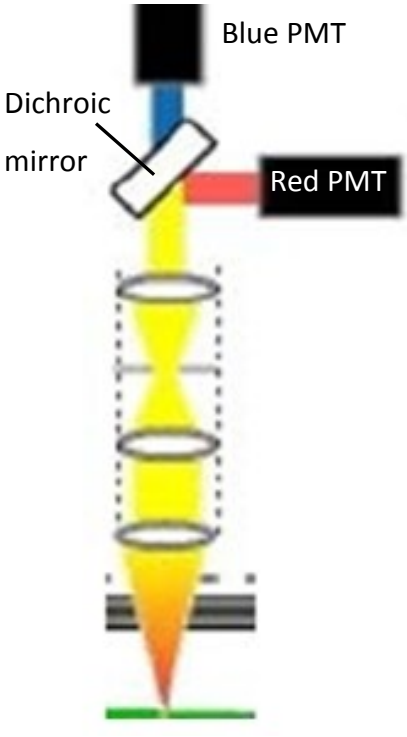

Figure 2-20 The two color LII signal detection system and a diagram showing the optical setup.

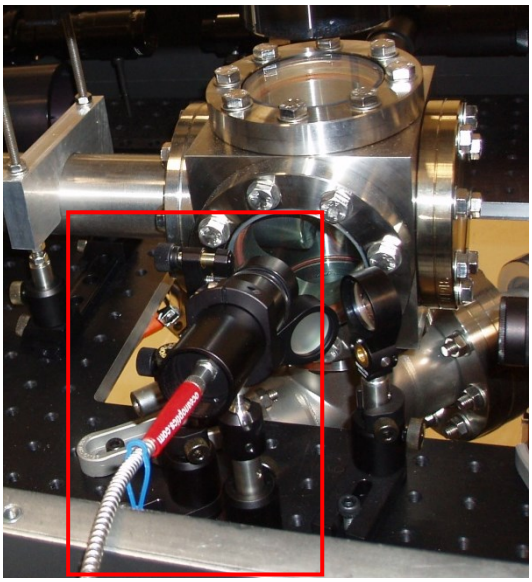

Figure 2-21: Area marked shows the ELS signal collection optics and fibre optic cable connecting to the PMT

2.3.3. Signal Modelling

The LII signal generated by each particle in the detection volume is given by equation (2-23) and the signal can be found integrating over the range of wavelengths for a range of temperature from 1000K to 6000K for every 5K.

$$S = \Omega \pi D^2 \int_\lambda \varepsilon_\lambda \frac{2\pi hc^2}{\lambda'^5 \left[\exp\left(hc / \lambda' k_B T\right) - 1\right]} \sum_\lambda (\lambda') d\lambda' \quad (2\text{-}23)$$

In equation (2-23), S is the LII signal, Ω is a normalization constant relating to the solid angle, D is diameter of the particle, ε_λ is the emissivity which is related to the absorption cross section, h is the Planck constant, c is the speed of light, lambda is the wavelength of light, k_B is the Boltzmann constant and T is the temperature.

Once the signal has been calculated across the range of temperatures, interpolation was needed to match the values given by the transmissivity of the filters and detectors combined, and multiplied by the corresponding red and blue filter and lens transfer function. Note that the values of emissivity (if it has a constant value with respect to wavelength) and the diameter of the particle in this equation do not affect the signal ratio. This reduces the number of dependencies of the red/blue ratio of the signal to only the temperature and wavelength.

Having taken into account the filters and the transfer function, the signal at a given temperature was integrated to give the corresponding red and blue signal. The ratio of these two signals as a function of temperature is shown in Figure 2-22. Having found the temperature calibration, the signal ratio from the experiment can be interpreted as a temperature and find the corresponding signal per area. From this, the emitting area can then be found.

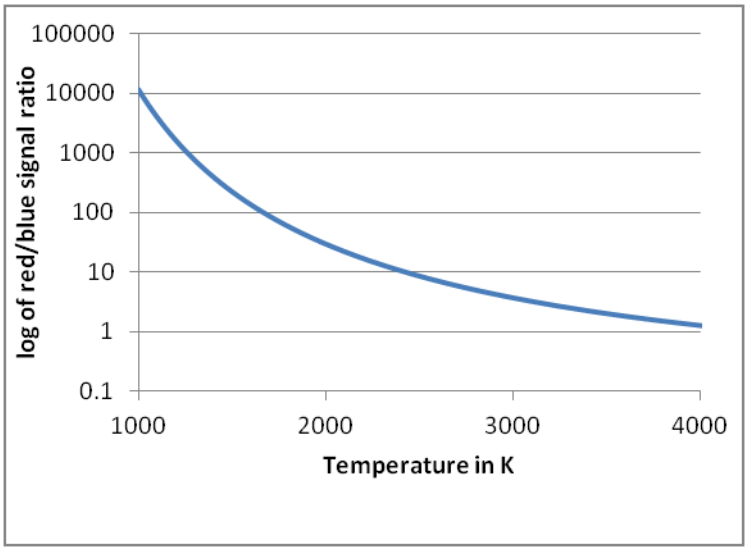

Figure 2-22: Red and blue signal ratio as a function of the corresponding temperature

2.3.3.1. Emissivity Variation

The determination of the Emissivity and E(m), equation (2-5), was important as this was one of the variables for calculating the temperature of the soot particle using two-color LII. To demonstrate the effect that different E(m) values have on the evaluation of temperature of the soot particles, the following calculations have been done.

For calculating the signal ratio between blue and red according to equation (2-23), the variables include the particle diameter, emissivity and temperature. The temperature is the value to be found in the experiment so the particle diameter and emissivity are the other two that need to be determined. Part of the reason for using two-color LII is because the temperature is found using a ratio rather than an absolute value of the signal and also when the ratio is calculated, the particle diameter value cancels out meaning that only emissivity is left.

There is plentiful literature on the value of emissivity as shown in the earlier section. Spectral emissivity is calculated using equation (2-7) and depends on E(m): the general consensus for the value of E(m) is around 0.3±0.06 (Schulz, Kock et al. (2006)). A value can also be derived from equation (2-5), using the

value of m=1.57-0.56i (Smyth and Shaddix (1996)) which gives a value of E(m) of 0.26. Yet another estimate of the emissivity is based on wavelength and, using Rayleigh-Debye-Gans theory to account for particle aggregation, can be calculated using equation (2-24). Quoting from two literature sources, the scaling factor β=28.72 and ξ=0.83 (Koylu and Faeth (1996), Köylü (1997)) can be used. To illustrate how the choice of emissivity affects the result of this experiment, these three different values of emissivity shall be. These values are E(m)=0.3 (Schulz), E(m)=0.26 (Smyth) and wavelength dependent one using equation (2-24) (Koylu):

$$E(m) = \frac{\lambda^{1-\xi}\beta}{6\pi} \tag{2-24}$$

The different E(m) values from Schultz, Koylu and Smyth and their corresponding spectral emissivity values are plotted in Figure 2-23 over the visible spectrum and near IR region. The E(m) value for Smyth and Schultz is constant with wavelength while the Koylu's value changes with wavelength. Their respective emissivity values are also shown in Figure 2-23. The resulting red/blue ratio and temperature curves using these emissivity values in the signal calculation showed that Smyth and Schultz both resulted in the same red/blue ratio curve because the emissivity term cancelled out in the ratio. In contrast, this does not happen when using the emissivity given in Koylu but this resulted in only a slightly different calibration curve. These two curves are plotted in Figure 2-24.

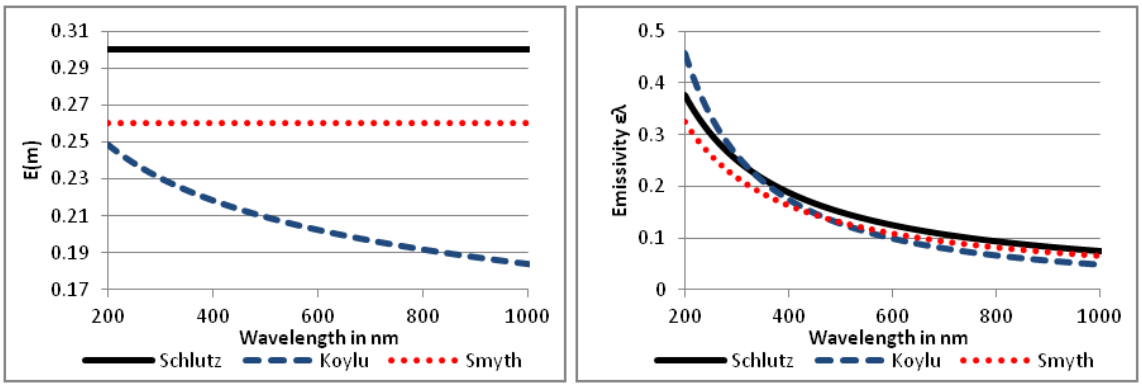

Figure 2-23: Variation of E(m) (left) and spectral emissivity (right) with wavelength

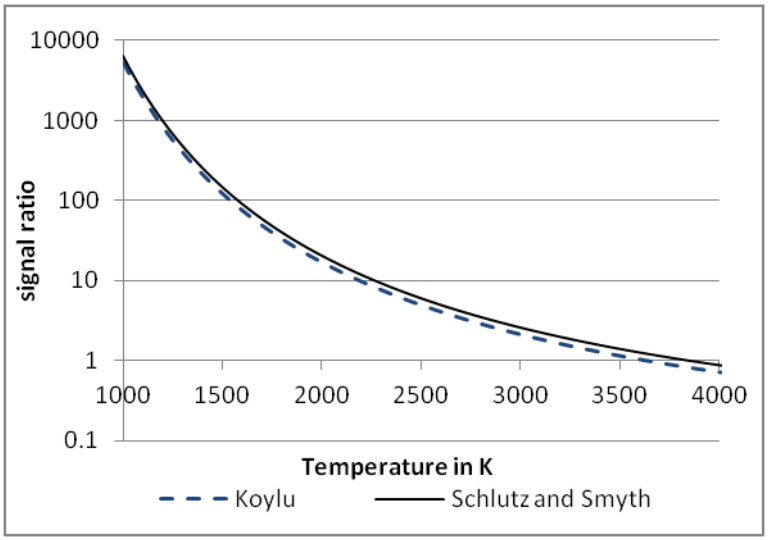

Figure 2-24: Red/blue ratio with the different E(m) values

It is useful to find out the effect on the experiment if different value of emissivity is used. A different signal ratio calibration means that a different temperature is attributed to a given signal ratio. Figure 2-25 shows the temperature difference for a given signal ratio plotted against the equivalent temperature found using Schlutz/Smyth against Koylu. The difference ranges between 2% to 7% at a given temperature and an average difference of 4%. This will have to be taken into account when interpreting the results of the experiment.

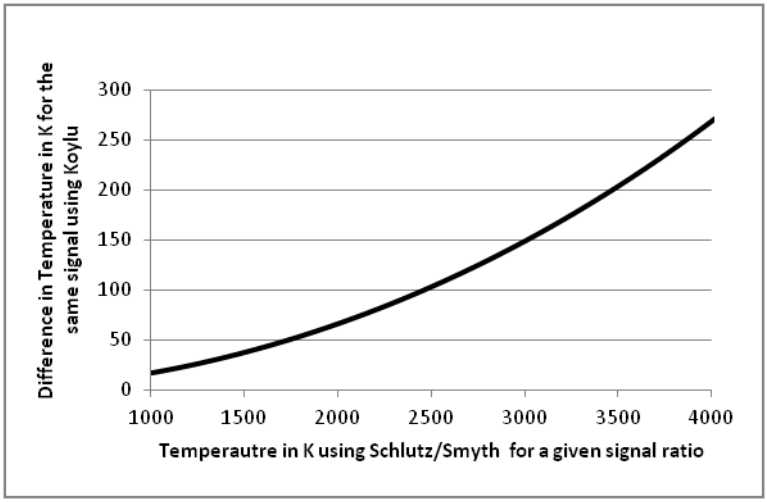

Figure 2-25: Temperature difference between the Koylu E(m) values and Shlutz/Smyth E(m) values at a temperature for a given signal ratio

2.3.4. Equipment Calibration

The signal emitted from soot particle incandescence had to be transferred through the intermediate mediums before being interpreted as a signal on the oscilloscope. This transfer of signal has to be taken into account. The non-black body radiation from laser heated soot needed to pass through the windows of the vacuum chamber, the lens of signal detection system, the aperture, the dichroic mirror and the filters. The quantum efficiency of the detectors will also have to be included. The transmissivity of all this train of equipment must be multiplied together across the wavelength of the visible light spectrum. The transmissivity can be found by using a light source of a known radiance (watt per steradian per square meter). This light source is projected into an integrating sphere and it has a given radiance for a given amount of power input. The spectrum is measured at one of the output of the integrating sphere and the spectrum at the output of the tested optics is also measured. The ratio of these two values is the transmissivity of the equipment tested. By multiplying the transmissivity of all the optics, the total transmissivity of the system can be found. This value is the response of the detection system based on a known irradiance in the form of the lamp. Also, the reference spectrum of the calibration lamp is taken every time it is used so that changes in the lamp incandescence can be charted throughout its use.

2.3.4.1. Window Transmissivity

The window of the pressure vessel was calibrated for its transmissivity of light at different wavelengths and this was done by measuring the spectrum of the light source without the window and afterwards finding the percentage of light transmitted through with the window as shown in Figure 2-26.

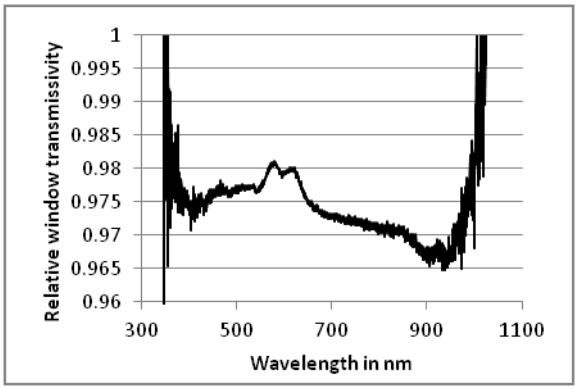

Figure 2-26: Relative transmissivity of the vacuum vessel window across the spectrum

2.3.4.2. Red and Blue Filter and Dichroic Mirror Transmissivity

The rest of the signal acquisition system was calibrated so the transmissivity of the lens, dichroic mirror and the red and blue filter could be found. This was done by measuring the spectrum of the light source and comparing the spectrum at the other end of the signal acquisition system, i.e. after the blue and red filter. This was then combined with the window transmissivity to get an overall signal transfer function across the wavelength spectrum for both the blue and red signal. The final transfer function is shown in Figure 2-27.

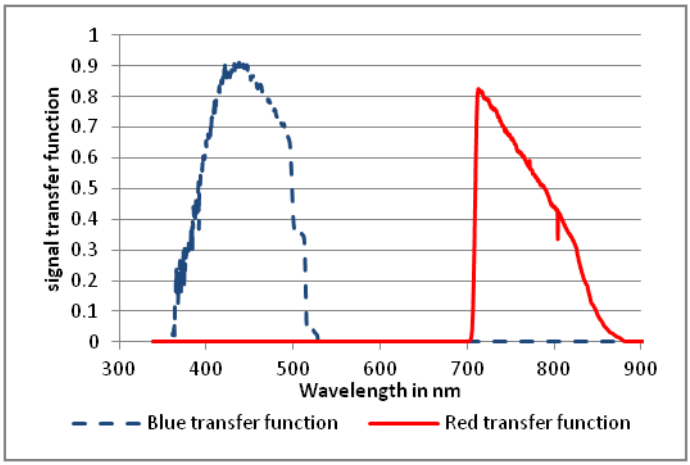

Figure 2-27: Red and Blue signal transfer function through vessel window, lens and filters

2.3.4.3. Aperture Setting and Measurement Volume

The aperture of the red/blue detection system was calibrated to find the detection volume of each of the aperture settings. This was done by setting the

aperture and adjusting the iris of the integrating sphere until the signal received by the red and blue PMTs decreased. The iris diameter was then recorded to give the measurement volume diameter. The depth of this detection volume can be assumed to be approximately the diameter of this measurement volume. Figure 2-28 shows the variation of the aperture setting and the cross sectional diameter of the measurement volume.

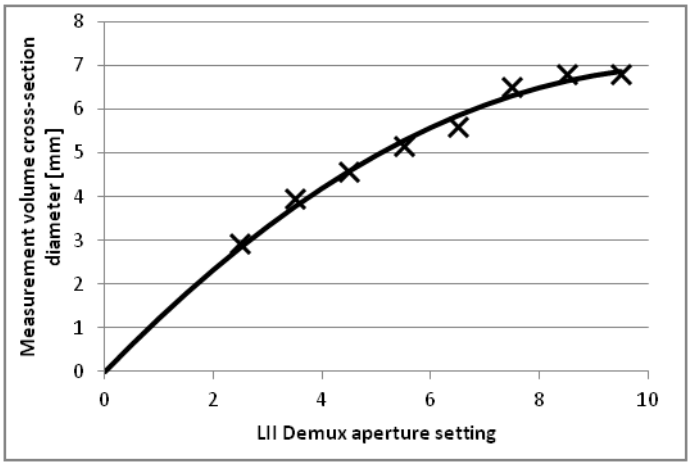

Figure 2-28: Aperture setting of the detection system against the cross-sectional diameter of the measurement volume

2.3.4.4. Gains Calibration

The PMT gain control setting had an output ranging from 6V-10V which translated to up to 1000V being applied to the dynode stages of the photo-multiplying tubes. This voltage was controlled using a Labview interface. The gain curve of the PMT had to be calibrated in order to normalise the result of gain setting during experiments. The gain curve was calculated by using the full range of gain settings and plotting against the normalised value of the average amplitude of the signal at each gain setting (in μA by dividing the voltage by 50Ω) dividing the normalised integral of the spectrum intensity ((spectrum-background)/(reference spectrum-reference background). This results in a qualitatively exponential/power relationship which can then be used to find the gain level. The gain calibration was done with the ELS PMTs for the range of 7-10V and the result of which is shown in Figure 2-29.

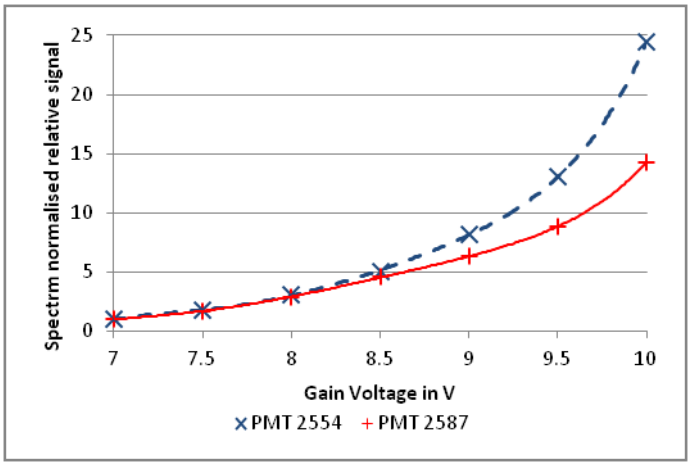

Figure 2-29: ELS PMT gain calibration curves

For the red and blue PMT gain calibration, the same procedure was followed with the signal processing but there was the additional step of converting the spectrum signal to include the filters and lens in front of the PMTs. This was done by measuring the spectrum at the light entrance to the PMT and dividing it by the lamp light spectrum at the integrating sphere. This gave a transfer function which, when multiplied by the measured spectrum at the sphere, produced the gain curves for the red and blue PMT. The red and blue PMT also had 3 sets of reading at different iris setting which was matched by the iris on the integrating sphere. The iris was set to 1, 6 and 12 which was the maximum in order to see the response of the PMT at these different settings. Figure 2-30 shows the gain calibration for the red and blue PMTs at difference gain level voltages.

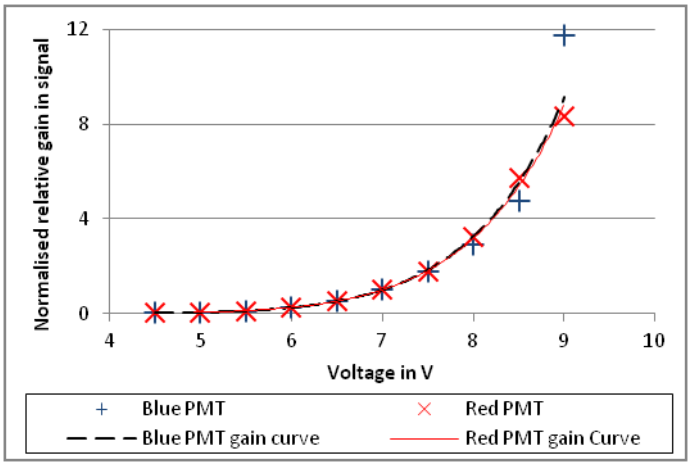

Figure 2-30: Red and blue PMT gain calibration curves

2.3.4.5. PMT Noise Level and Potential Cooling

There are two types of PMT noises: shot noise and dark current. Shot noise occurs as the photon is collected, the conversion into a signal causes fluctuation and potentially generate noise in the output. PMT operates by producing electrons as a photon strikes the photocathode and the electrons are multiplied by secondary emission to produce a signal. Dark current happens as the thermal excitation alone within the PMT creates electrons which produce a current even in the absence of a light source. This is why cooling the PMT will reduce the dark noise of the PMT to improve the signal to noise ratio and hence also the sensitivity. This cooling is achieved by the use of Peltier coolers which are capable to cooling the PMT down to -20°C. The noise of the system can be found by finding the variation of signal acquired by the signal acquisition system at a given setting.

2.3.4.6. Spectrum Shift

The repeatability of the spectra from the detector was checked for consistency because it is possible for the spectrum to shift during the calibration process. Figure 2-31 shows a set of 11 readings of the calibration lamp light inside the integrating sphere to determine whether there was a wavelength shift for the different readings. The signal is normalised for comparison. It shows there was no shift that required correction.

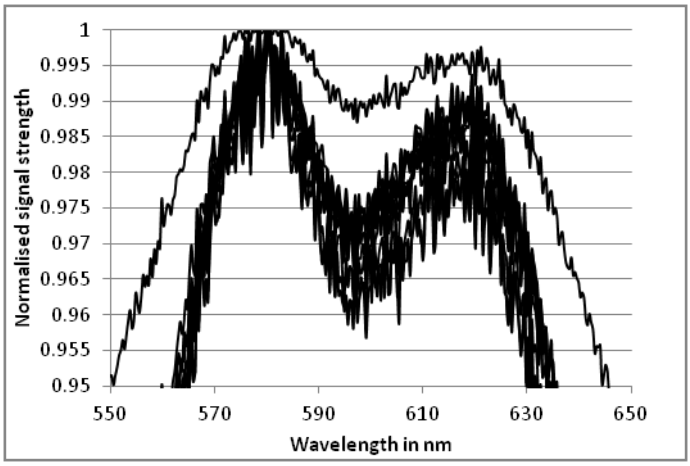

Figure 2-31 Normalised spectra distribution from different sets of reading

2.3.5. Experimental Conditions

The experiment was carried out at a pressure of 10^{-3} mbar in the vacuum chamber at various laser irradiances. The gain levels on the PMTs were set to the maximum gain possible without saturating the signal amplitude and this was laser irradiance dependent. A series of data consisted of single shot signals from individual soot particles acquired by collecting the signal continuously. Additionally, a series of multiple averages was taken triggered by the presence of the soot particle signal using the oscilloscope.

2.4. Results and Discussions

The results from the experiment comprise several different stages. Firstly, soot particles were collected from inside the vacuum chamber and visualised using a Transmission Electron Micrograph (TEM). This gave information about the sizes of the soot agglomerates and primary particles as well as on the morphology of the soot particles. Then the experiment was carried out in the vacuum chamber with LII to give the temperature profile of individual soot particles as there were heated by the laser. This gave the soot particle size, temperature information and, using the ELS signal, the speed of the particle. With the knowledge of the size and the speed of the particle, this can be correlated with the information from the aerodynamic lens, as a given size will have a specific speed. The result was compared with modelling data.

2.4.1. Transmission Electron Micrograph (TEM)

Soot particles samples were collected from inside the vacuum chamber and sent for analysis. Figure 2-32 shows images from TEM of three examples of the agglomerates of soot particle from the vacuum chamber. Individual primary particle can be seen as part of the agglomerates.

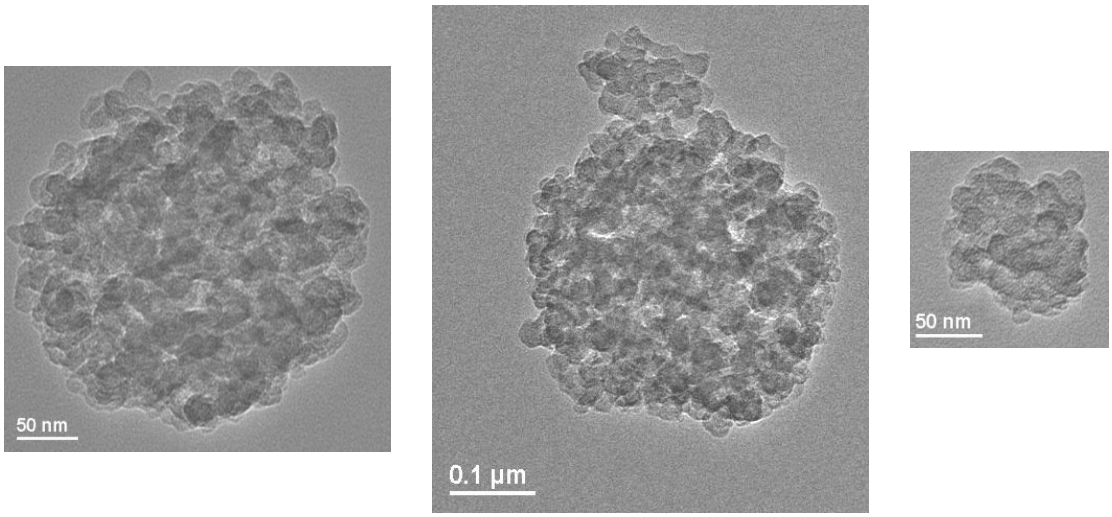

Figure 2-32: TEM of soot particles collected inside the vacuum chamber

The structure and morphology of these soot particles are less similar to freshly produced soot particle found in combustion but more similar to those that have been exposed to atmospheric aging. Freshly produced soot particles have a chain like structure whereas aged soot particles, subjected to absorption and condensation of other atmospheric species, are more densely packed and have a circular form. TEM results from Zhang, 2008, shown in Figure 2-33, demonstrated this change in morphology after the soot agglomerate was exposed to sulphuric acid.

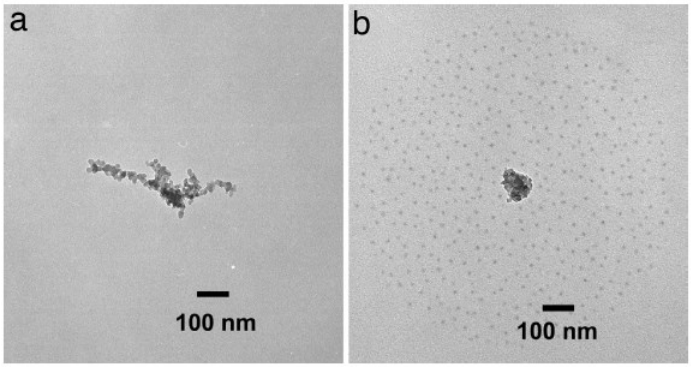

Figure 2-33: Comparison of soot from a flame and soot similar to those found in this experiment. Soot aggregate before (a) and after (b) exposure to Sulphuric Acid Vapour and 5% relative humidity (Zhang et al, 2008)

Further analysis of the soot particle size and distribution shows that the median primary particle size was 18.6nm and the median agglomerate diameter was 180nm. The population density of the diameter of the primary particle and the agglomerate were measured from the TEM samples and this is shown in Figure 2-34. The population density of the number of particles within individual agglomerates was also measured from the TEM and shown in Figure 2-35. The data shows that the agglomerates have mostly between 100 and 1000 primary particles per agglomerate.

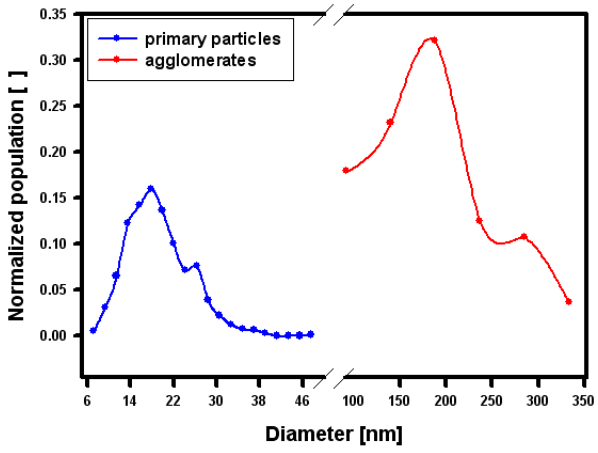

Figure 2-34: Population density of the diameter of primary particles and agglomerates from TEM analysis

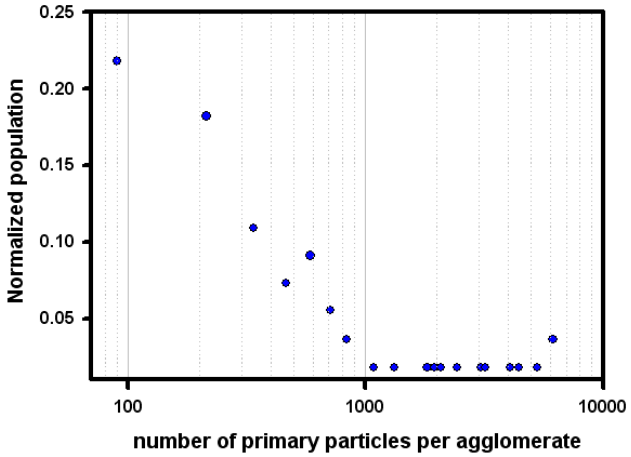

Figure 2-35: Population density of the number of primary particles per agglomerate from TEM analysis

2.4.2. iCCD Images of the LII Signal

An iCCD camera was used to image the signal perpendicular to the laser beam at a high laser irradiance of 200W and four of these images are shown in Figure 2-36. These images are dominated by large agglomerates which can be seen travelling from the right side coming out from the aerodynamic lens, across the laser beam and with the LII signal on the left edge of the laser beam shown in images a) and b). It can be seen that at the start of lasing, starting from the image a), there are soot agglomerates which appears to explode with a trail of debris. Image b) follows with more intense signal near the centre and progressed to image c) where only small particles are getting through. Finally, image d) shows that many of the particles are travelling in the different directions. Image d) was taken within 3 seconds after image a) and the start of lasing. These images are normalised to the maximum of each image itself. This explains why there are particles which were smaller and were deflected by other particles, seen especially in image d). The maximum absolute signal in image d) is much lower than the maximum absolute signal in image a).

The first observation can be made is that there was no signal coming out from the beam itself which means there was high light absorption within the beam. Also, by the progressive reduction of signal intensity by the time of image c) and d), it can be deduced that there was a build-up of particles in the beam itself and only small particles were deflected by other particles inside the beam or passed through the

beam. This is the characteristic shown that optical tweezing has taken place. Optical tweezing occurs when there is an axial intensity gradient, as in this case with the focussing beam, providing a radiative pressure within the beam which affects the dielectric properties of the soot particles (Ashkin, Dziedzic et al. (1986)). As the particles pass through the beam, this radiative pressure traps the particles inside and retains them. This explains the high absorption of light within the beam. And as larger particles inside the beam built up, the smaller particles were being deflected and escape the force provided by the optical tweezing.

It has to be noted that the laser irradiance used here was high and it was a continuous wave laser. This effect can be eliminated by using a pulsed laser and at a lower level of laser irradiance. Although even at low irradiance, the signal diminished over time because the number of particle within the beam led to high absorption of the LII signal.

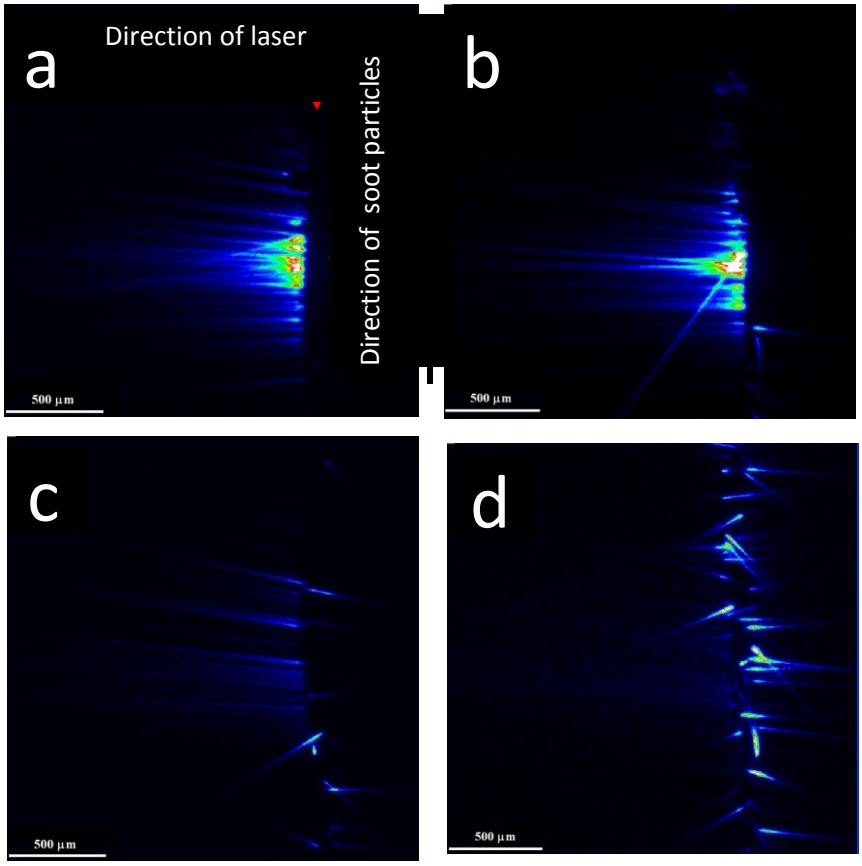

Figure 2-36: 2D images of the LII signal at a laser irradiance of 200W using an iCCD camera showing a) soon after the start of lasing, follow by b), c) and d), 3 seconds after start of lasing.

2.4.3. Single Shot Two-Color LII and ELS signal

Signals were acquired through the two-color LII system along with the ELS signal. A sample of the signals is produced in Figure 2-37. Various laser irradiance settings were used to collect a range of maximum soot temperature and these settings were between 20W to 100W. These settings meant that the soot particles should not undergo sublimation at the lower power setting and but at the higher power level of the laser.

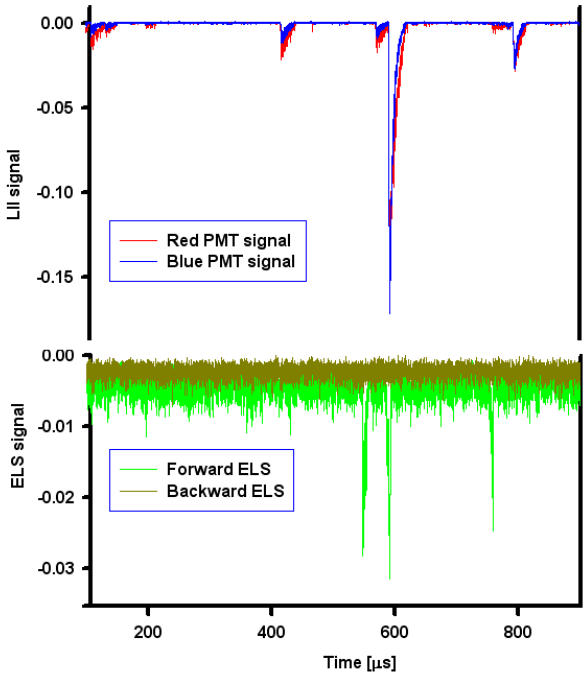

Figure 2-37: a set of LII and ELS signal showing the intensities relative to baseline.

These signals were then processed so the temperature, particle size and velocity could be found. The temperature was found using the ratio of red and blue signal as deduced from the calibration. The particle size is the ratio of the red or blue signal from the experiment and the calculated theoretical red or blue signal at a given temperature. The velocity was calculated using the duration of the ELS signal divided by the measuring volume of the laser, assuming the particle travel in a straight line through the measuring volume. Data processing of the signal involved filtering the red and blue signals that reached a certain threshold and ensured there was a

discernible signal in both channels. These signals were then processed further so that those that were too short, too low or saturated were discarded.

Figure 2-38 shows the normalised population density of soot agglomerate size based on 5470 samples. The size distribution is approximately an order of magnitude larger than the measurement shown by TEM analysis in Figure 2-34. This is because the LII system used in the experiment had a high detection threshold due to the uncooled system with high background noise which could not detect smaller particles. A way to improve this system would be to activate the Peltiers cooling system. This was not used in this first step of investigation.

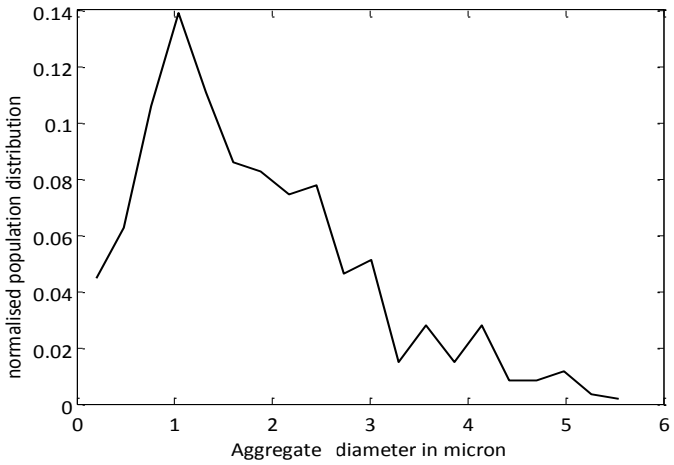

Figure 2-38: Normalised population density of soot aggregate size measured based on 5470 samples

Figure 2-39 shows the normalised population density of the maximum and final temperature of the soot particles sampled at 20% (80W) laser irradiance. This gives the range of maximum temperature reached at a given laser irradiance and showed that the maximum temperature is around 2500K to 3000K with an end temperature between 2000K-2500K.

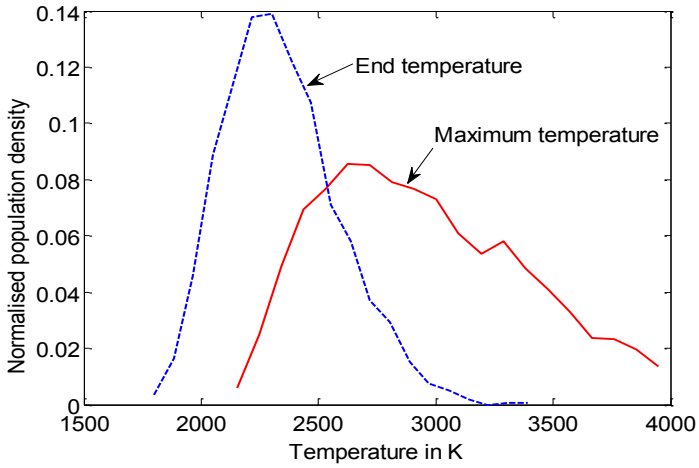

Figure 2-39: Normalised population density of the maximum and end temperature from the detected LII signal.

Figure 2-40 shows the relative population density of the soot particle velocity measured by forward ELS signal. There is a scatter in the data and it doesn't replicate the particle size function shown above, as shown in Figure 2-38 from the LII measurement. Although the aerodynamic lens was supposed to deliver given particle size at a given speed, there were a few factors affecting this. The speed with which particles exit the aerodynamic lens is based on their aerodynamic size, not actual size. So there can be a difference in aerodynamic size and the actual size of the soot particles. Another factor was that, as particles were trapped inside the beam and collided with other particles, this caused the soot particle to deviate from a straight line direction of travel and change the residence time inside the beam. These all affected the result obtained by ELS signal.

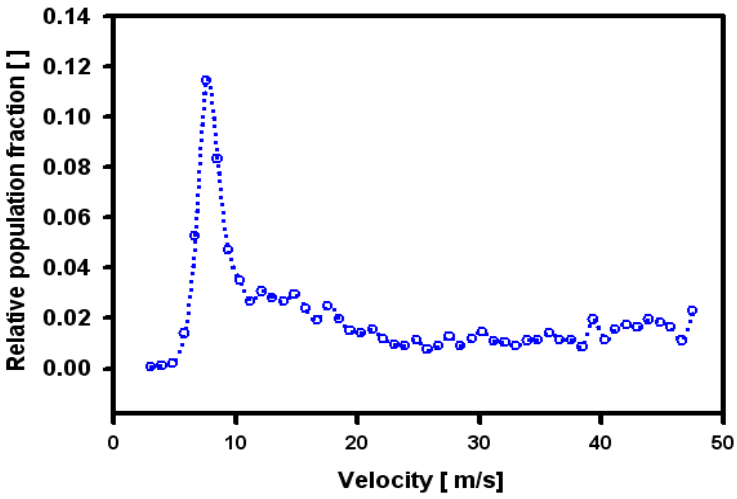

Figure 2-40: Relative population density of the soot particle velocity.

2.4.4. Multiple Shot Averaged LII Signal

Multiple shots averaged LII signal was also taken. This was done by recording the signals using the oscilloscope's own trigger and averaged using a built in function of the oscilloscope whilst the signal was acquired. This was done for a period of time and the output at the end was one set of red and blue signal which gave the average of the soot particles that passed through the laser beam set at 20% or 80W laser irradiance. Figure 2-41 shows the red and blue signal against time and the corresponding temperature. This shows a maximum temperature of 3061K and gives the average soot agglomerate diameter at 1.18 micron which is consistent with the result found by the single shot set of data. The average maximum temperature from the single shot data at the same laser irradiance was 2919K which is a similar temperature to the multiple shot data. The difference can be explained by the different signal filtering method employed in the single shot created in MATLAB as part of data processing while the multiple shot was averaged using a built in function of the oscilloscope.

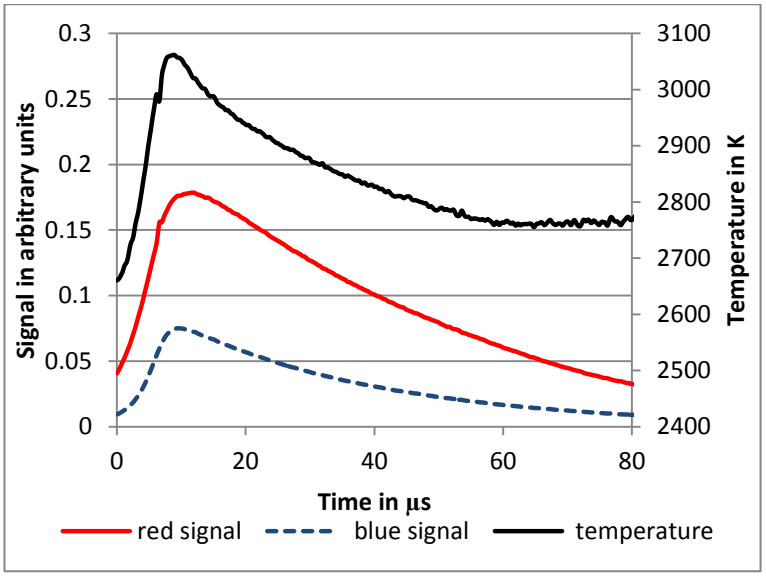

Figure 2-41: Multiple shot averaged LII signal and the corresponding temperature of the soot particles sampled at 20% laser irradiance (80W). Blue and red signal correspond to the left axis and the temperature correspond to the right axis.

2.4.5. Comparison with Modelling Results

The model can be checked against the experimental conditions by using the temperature profile of the multiple averaged results, as shown in Figure 2-41, the temperature profile using the model described in Chapter 2.2. The condition used for the modelling is 20% laser power giving an irradiance of151180W/cm^2 at 1e-6 atm for a particle with the diameter of 10 nm. The other variable was the speed with which the particle travelled and, given that the residence time in measuring volume was not as expected due to collision with other particles trapped inside the beam, it was not possible to give it an accurate value. Also, the value of E(m) can vary, as discussed earlier, which affects the prediction of the absorption of laser and radiative properties of the particle. Conversely, by varying the speed of the particle and the value of E(m) change the maximum temperature predicted by the model and so the maximum temperature is matched to that achieved in the experiment. The resulting comparison is therefore not on laser absorption but mainly on the heat loss mechanisms and this is shown in Figure 2-42.

There is a good match for the initial temperature decay once the maximum temperature is reached after about 10μs. The temperature in the model then deviates from the experiment because heat loss is at a higher rate than in the experiment. This must be due to overestimation of heat loss through radiation as sublimation and conduction only accounts for less than 1% at this pressure and laser irradiance level. This, of course, is a function of the accuracy of the value of E(m).

This preliminary study indicates how this experiment can be used to improve the model once the problems with the experiment have been resolved. More variables can be tested which allow the model to be further developed. This includes looking at the radiative heat loss at the conditions used in this example and the rate of heat loss by sublimation by using higher laser irradiance. Finally, conduction heat loss can be further investigated after a more robust model has been developed for radiative and sublimation heat loss model.

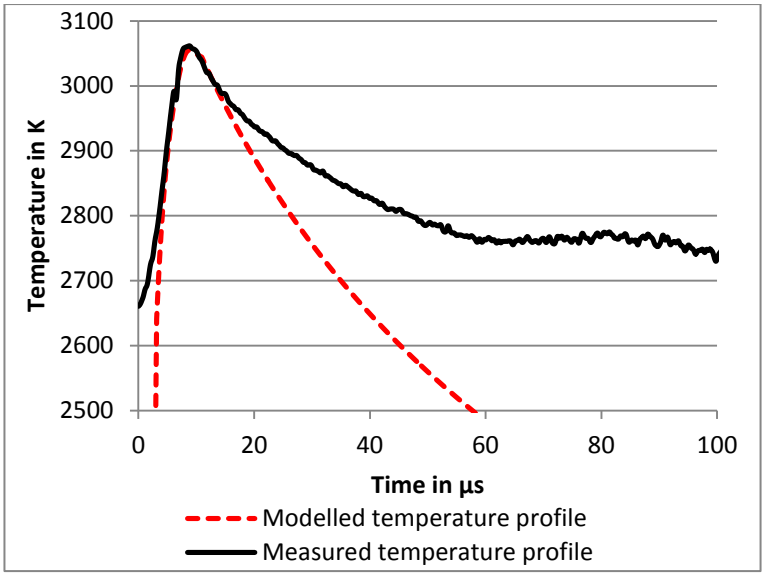

Figure 2-42: Temperature profile of the multiple shot averages measured in the experiment and modelled using the Michelsen model

2.4.6. Ionisation of Soot Aggregates and Primary Particles

This section of work was presented as a poster at the 10th International Conference Series on Laser-Light and Interactions with Particles 2014 (LIP2014) in Marseille, August 2014 Beyer, Greenhalgh et al. (2014).

When carbon aggregates are heated up to a suitably high temperature, it was observed that these fragment and appear to "explode", and breaking up into smaller particles (Beyer and Greenhalgh (2006)). It is now speculated that the increase in temperature and hence energy of the carbon aggregates may cause the electrons in the primary particles to escape and the resulting positively charged carbon primaries then repel each other and move in opposing directions, hence appearing to "explode" (Figure 2-43). The ionisation of clusters (matter which lies between the atomic and solid state (Castleman and Keesee (1988))) in a laser field (Joachain and Potvliege. (2011)) and carbon atoms has been demonstrated to characterise their ionization potentials (Jaroń-Becker, Becker et al. (2004)). Studies have also been conducted on larger carbon-fullerene molecules (Johansson, Fedor et al. (2012)). The ionisation of soot has been shown to be important in the process of soot formation (Smyth and Gary Mallard (1981)) and study of ionisation directly contributes to the

modelling of soot formation (Balthasar, Mauss et al. (2002)). The phenomenon of soot ionisation has also been applied to soot detection (Manzello, Lee et al. (2005)).

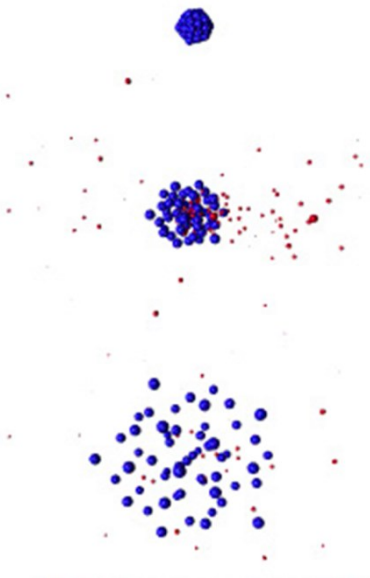

Figure 2-43: Simulation of an exploding argon cluster irradiated by a fs laser pulse at three points in time Greenhalgh (2014).

Soot, when promptly abstracted from flames, is made up of large chains of primary particles bound by tens to hundreds of carbon atoms across graphite like planes. 'Bound' primary particles have bond strengths of order of 35meV per atom, much higher than a typical C-C bond strength in a graphene-like layer which is of order of 1.5 eV (Benedict, Chopra et al. (1998)), because hundreds of carbon atoms constitute the fusion points on the primary particles (Vander Wal (2005)). These atoms are likely to be held by a strength of order 3-30 eV. Chains of primary particles may then condense or aggregate in the post flame or exhaust as aggregates, weakly bound by van der Waals forces. Understanding the binding forces between primary particles and soot aggregates will lead to better understanding of the morphology of soot aggregates and primary particles.

During LII of carbon particles, it was found that soot aggregates under high intensity laser pulses undergo a two stage "explosion", the first of which is presumed to be the rupture of the weaker force holding the aggregates together (up to 10 μs in

Figure 2-44) and the second is the fracturing of the individual, tightly packed graphite layers of the primary particles (between 20 and 30 µs in Figure 2-44). This fragmentation of the particles may be caused by the ionisation of carbon under the laser field with the ejection of electrons, causing the positively charged carbon molecules to repel each other and fragment. For a large particle subjected to the laser field, this produces many electrons locally and, effectively, a weak plasma which interacts with, and absorbs, incident laser light. A continuous wave laser and the continued energising of carbon particles eventually blocks any signal being detectable by the ICCD camera.

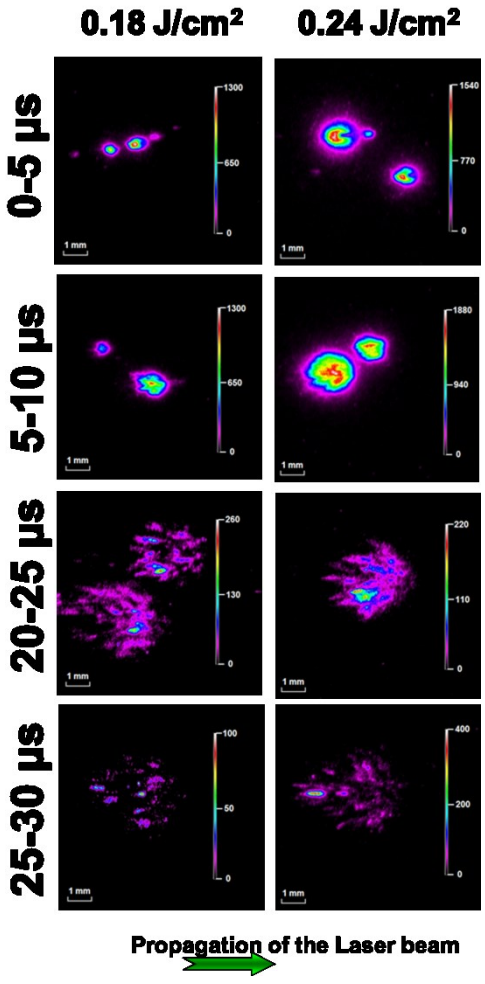

Figure 2-44: Timed images of two stage "explosion" of carbon particles under two different laser irradiance.

Further work can be done on the study of carbon particles in a laser field to record the trajectory of fragments. This can then compared with a second set of trajectories

when the fragments are subjected to the electric field. Difference between these trajectories, along with the known strength of the electric field, can be used to determine the Coulombic forces in the soot aggregates and primary particles, the temperature threshold for the ionisation and the mass/charge ratio for the particles. A model of this laser induced soot aggregate ionisation can be devised.

2.5. Chapter Conclusion

The work done at Heriot Watt of LII in a vacuum provided useful experience on the technique of LII which was then applied to the Hydra engine at Imperial. This chapter showed the general setup and processes used in applying LII in a low pressure environment. The laser beam was set up using a 5mm diameter TEM_{00} CW laser and converted into a top-hat 60x760 micron profile using a pi-shaper and relay imaging. A two color LII signal acquisition system was set up. The PMTs used could have been cooled by Peltiers which were electronically controlled and cooled by a water jacket. Although it was not used for the data presented here, it is a feature which could be used in the future. The ELS signal collection system was assembled along with the fibre optics cable delivering the signal to the PMTs. The signal acquisition system was calibrated correcting for the transmissivity of the filters, windows and lenses. The PMT gains, spectra and apertures were also calibrated.

The LII signal was modelled so the ratio of red and blue signal could be converted into temperature. The heat loss mechanism was also modelled using various particle sizes, pressure and laser irradiance. For the experiment, soot samples were collected for TEM analysis and results showed the morphology, size distribution and number of primary particles present in the aggregates. Time resolved, two color LII and ELS signals were collect at 10^{-3} bar for agglomerates at various laser power or equivalent irradiances, ranging from 5% (20W) to 30% (120W). These data were collated giving maximum temperature, agglomerates sizes and velocity. This was compared to the TEM analysis and found that the particle sizes were larger than those found on the TEM samples. This was because the signal to noise level was high without the use of the PMT cooling system, preventing the detection of the smaller particles.

Also, the effect of optical tweezing was found to exist due to the high beam waist gradient formed due to the use of a continuous wave laser causing particles to be trapped inside the beam and thereby affecting the measurements. This was confirmed by iCCD images of the measurement volume. The result was an increased residence time in laser beam which also affected the velocity measurement caused by particles collision and deflection away from the intended particle trajectory. A comparison between the experimental result with the model has been carried out which illustrated the potential for improving the model used to explain LII heat loss mechanism.

The experiment can be improved by changing the laser to a high duty cycle semi-CW regime in order to permit particles trapped inside the beam to be released. This will eliminate the signalling problem with iCCD camera, LII signal and ELS signal. However, there is then the problem of synchronising the generation of the soot particles with the laser pulse. The PMTs can be cooled to lower the baseline noise in order to detect smaller particles. Different types of soot can be used so different soot morphologies can be assessed for their effect on the experiment and result. This can be done with an inverted burner where the soot is quenched and more carefully generated soot rather than that found in this experiment. More experimental time can be devoted to see the effect of pressure to isolate the different effects of heat loss mechanisms such as sublimation, conduction and radiation.

3. Imperial College Ricardo Consulting Engineers Hydra Engine and Instrumentation

To apply the LII technique in an engine, the optical engine that is to be used is described in this chapter. The engine used for this work was based on the single cylinder Ricardo Hydra optical diesel engine available in the Thermofluids Section of the Mechanical Engineering Department at Imperial College since the 1980s. The Hydra model was originally designed for the Ford "York" engine, 93.672 x 90.55 for the 2½ litre 4 cylinder engine. However, the aspects of the associated hardware were either refurbished, or radically upgraded or replaced during the course of this thesis. These aspects will be described, as relevant, during the course of this chapter. The major replacement was with respect to the engine head, which was a standard Ford Puma 2.0L Euro V diesel engine which had been modified by Colin Hall to fit onto single cylinder, with the remainder of the head corresponding to the remaining cylinders removed. An image and the specifications of the engine are provided in Figure 3-1. The combustion chamber consisted of a metal piston with an optical window at the bottom and , in the liner, a metal module which accommodated insets for four optical windows or metal blanks. The engine was upgraded to have a hydraulic platform which allowed the liner to be dropped (and raised) quickly and conveniently to thereby provide access to the optical parts of the combustion chamber for the requisite regular cleaning every 5 minutes of running. This replaced the original specification laborious method of lifting the engine head completely which involved a much longer turnaround time. The engine was coupled with a refurbished Cussons 30kW dynamometer sitting on a seismic block and was controlled through a re-built control unit designed and supplied by Cussons. The engine was located in a newly refurbished cell, with appropriate LEV, sound proofing and other services.

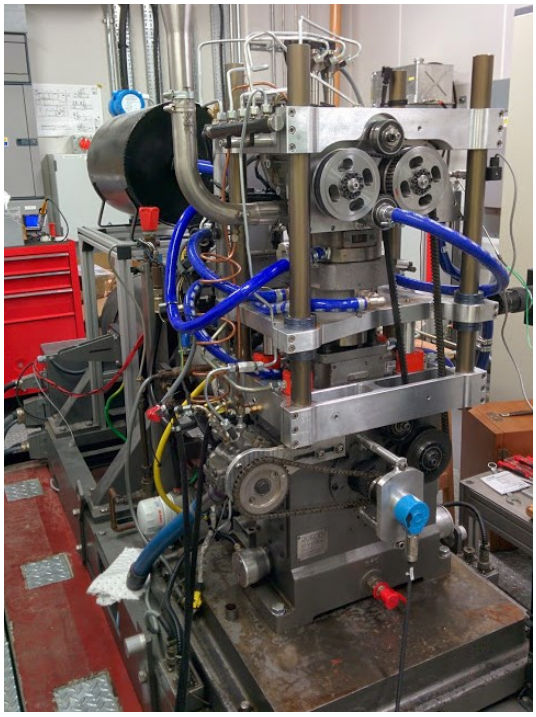

Engine stroke	90.55 mm
Engine Bore	93.62 mm
Combustion bowl diameter	46.5 mm
Combustion bowl depth	14.2 mm
Con rod length	154 mm
Squish	0.8 mm
Piston diameter	92.8 mm
Bowl volume	24000 mm^3
Displacement	623 cm^3
Compression ratio	16.9

Figure 3-1: An image of the Ricardo Hydra optical diesel engine and its specifications.

3.1. Hydraulic Platform

The original Hydra was modified to be fitted with a hydraulic system which allowed for the liner to be lowered allowing the window carrier/combustion annulus to be removed quickly for cleaning. Figure 3-2 shows the Hydra before and after the hydraulic system was fitted. The hydraulic system consisted of a free moving platform which supported the remained of the liner (which was water cooled) of the engine below the window carrier/combustion chamber annulus which was supported by four hydraulic jacks. The platform carrying the liner and the window carrier/combustion chamber annulus, cylinder head and the Hydra crankcase were all connected and located radially by four

pillars which were fixed to the crankcase bellhousing: the cylinder head was fixed, at the appropriate axial distance from the top surface of the crankcase, towards the upper (free) ends of the four pillars. The free moving platform carrying the liner and the window carrier was hence free to move up and down the pillars. A seal was established between the window carrier and the cylinder head by application of a pre-set hydraulic pressure.

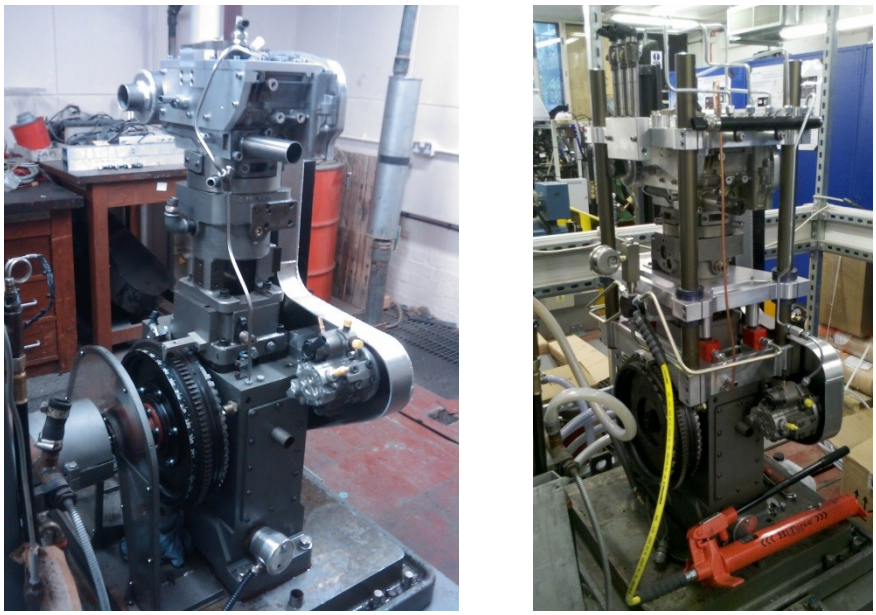

Figure 3-2: Hydra engine before (left) and after (right) modification

The free moving platform sat on top of four hydraulic jacks which were connected to a hydraulic hand pump. When the pressure was released, the platform dropped and allowed the combustion annulus to be removed. After cleaning of the windows, the combustion chamber annulus was placed back on the platform and, the hand pump was operated so the pressure from the hydraulic jacks pushed against the free moving platform and the combustion chamber annulus and was secured and sealed against the engine head by the pressure.

The hydraulic hand pump was fitted with a pressure gauge to show the pressure applied and it was sufficient for the engine to run when the system was pressurised to 10 bar. As the engine warmed up, and parts expanded, the pressure could reach 100 bar. The top face between the combustion annulus and the cylinder head could seal without any

gasket material. The surface between the combustion annulus and the platform was sealed with an O-ring (102mm ID x 3mm CS Nitrile (NBR) 70 ShA from Polymax).

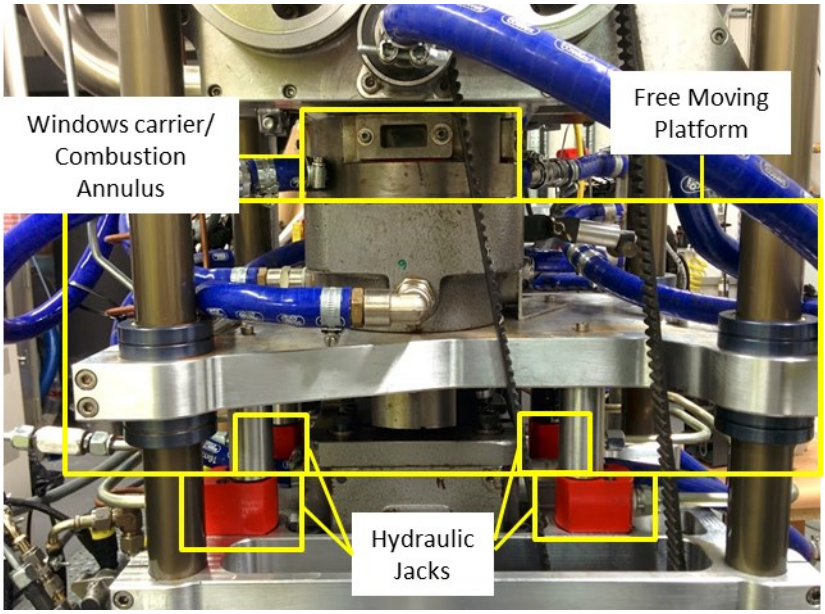

Figure 3-3: The hydraulic jacks, free moving platform and the window carrier/combustion annulus.

3.2. Engine Bowl

The engine bowl was a metal piston with a quartz bottom for optical access. The piston featured a simple cylindrical bowl as shown in Figure 3-4. The bowl depth could be altered by replacing the top piston plate in order to alter the compression ratio. Such change was made as the bowl depth was changed from 16.23mm to 14.23mm and with the cylinder head height adjusted accordingly with the squish set with a 0.8mm shim. This gave the geometric compression ratio of 16.9 and an effective compression ratio of 13.9 with the polytropic coefficient of the motored cycle of 1.27.

This was close to the lowest the cylinder head could go before the gap between the lowered free moving platform and the engine head would be too small for the window carrier to get into. The length of support pillars for the free moving platform over the hydraulic jacks was reduced accordingly but any further reduction would mean the piston ring would pop from either above (easily resolved) or below (difficult, and might require destroying the ring to get it out) the free moving platform. This meant care had to be taken when changing the height of the free moving platform.

Figure 3-4: Image of the piston showing a cylindrical piston bowl and a quartz window at the bottom of the bowl.

3.3. Piston Rings

The piston rings arrangement was important to the sealing of the combustion chamber and the maintaining of compression ratio. Also, considerations had to be made to the lubrication of the rings. There were two pistons in the engine; the bottom piston was connected to the crank and con rod in the crank case. The top piston was the extended Bowditch optical piston which allowed for a mirror and its platform to be installed for optical access.

For the optical top piston, the piston rings and their drawings are shown in Figure 3-5. The top piston ring used was for a Ford Transit York 1984-1988 (Part number R39920, with a displacement of 2496cm3 and producing 50kW) and it sat in an adaptor ring. The dimension was 93.648mm (3.6869") in diameter and 2 mm thick. Due to lack of oil lubrication from the crank case, the piston ring was lubricated by molly paste. The lower piston ring riders were made according to the original Ricardo Consulting Engineers drawings and manufactured by Mersen graphite grade JP900 according to Hydra drawing number 4029-314 (middle ring) and 4029-315 (bottom ring). They were made in two halves and slotted into the groove.

For the bottom piston in the crankcase, the major issue was the sealing to prevent the oil mist coming from the crank case that had a major effect on the optical work as the

optical mirror sat directly on top of this bottom piston. At one point during the course of this work, oil was being ejected out through the bottom piston which made optical work using the mirror impossible. This effect is shown in Figure 3-6 where oil can be seen ejected onto the protective cage after only a minimal amount of operation.

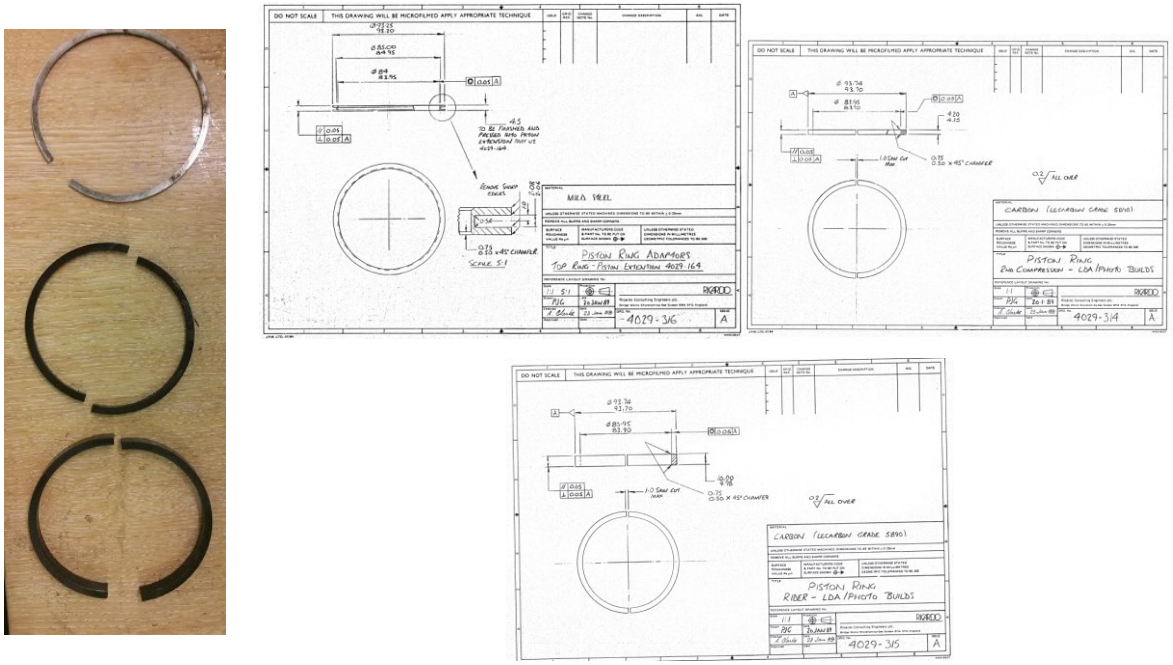

Figure 3-5: Piston rings of the top optical piston. The top one was a metal Ford York ring which sat in an adaptor, second and third were carbon rings.

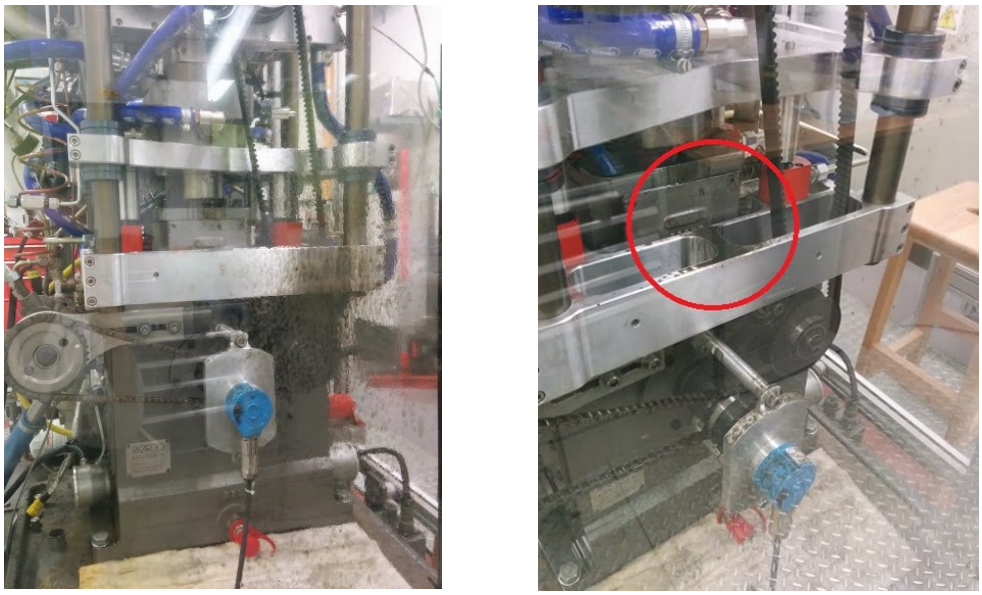

Figure 3-6: Effect of the bottom piston seal failing with oil being ejected through the seal.

Upon investigation, which involved completely dismantling the engine (shown in Figure 3-7), it was found that the plate joining the Bowditch extension and the bottom piston had a faulty seal. It was also found that the piston seal/ring for the bottom piston was missing altogether. A new sealing plate fitted with an O-ring was manufactured and this is shown in Figure 3-8. A bottom piston seal/ring was also ordered from Eriks K8SPEC with dimension of 93.67X84.96X6.58-M 5. It had a Moly Glass (PTFE) outer surface with 2 Viton X rings for elasticity.

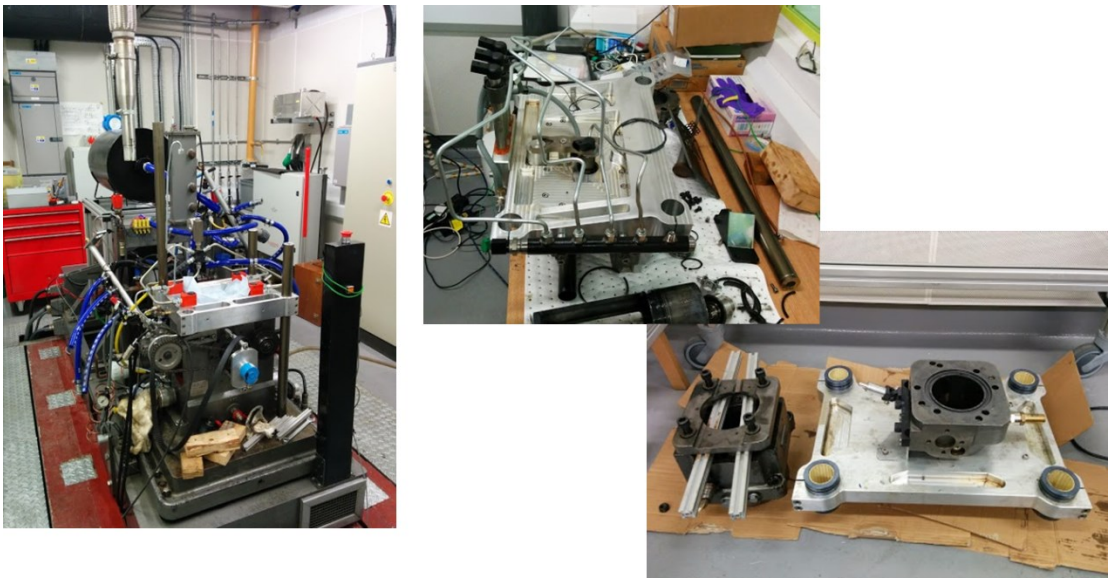

Figure 3-7: Complete dismantling of the Hydra engine for the oil leak problem from the bottom piston.

Figure 3-8: New sealing plate with O-ring connecting the Bowditch extended optical piston to the bottom piston.

3.4. Crank and Cam Drive, Belt and Their Timing

The original setup for the crank and cam timing consisted of a belt connecting the crank shaft to the cam shaft pulley which drove the two cam shafts connected through a chain drive behind the front cover of the engine head. The configuration is shown in Figure 3-9. Various components had been modified since for different reasons.

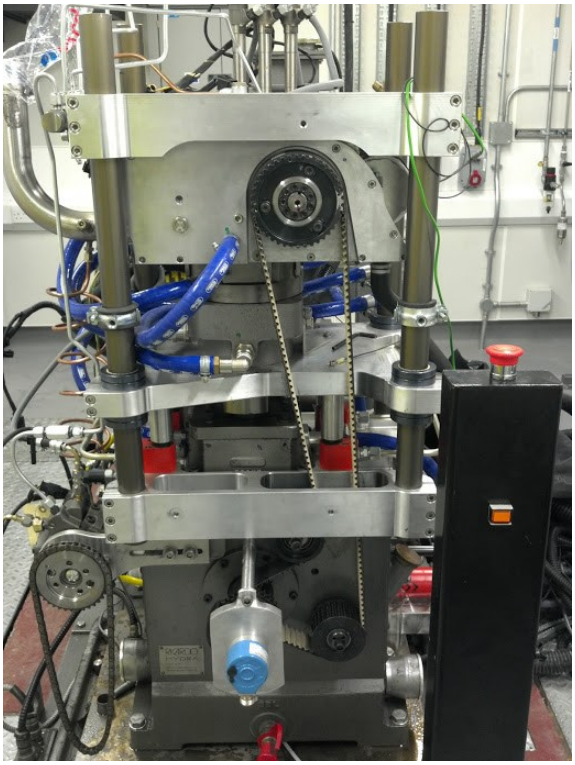

Figure 3-9: Original belt setup for the crank and cam drive (with the new cam drive and cam connector installed)

The first item modified was the cam drive pulley connection to the cam shaft as it started to slip. It was originally connected by a key which was damaged and this was replaced by a Ringfeder RfN 7012 25 x 50 locking assembly which expanded when the screws were tightened, connecting the pulley and the shaft. The assembly, before and after the modification, is shown in Figure 3-10.

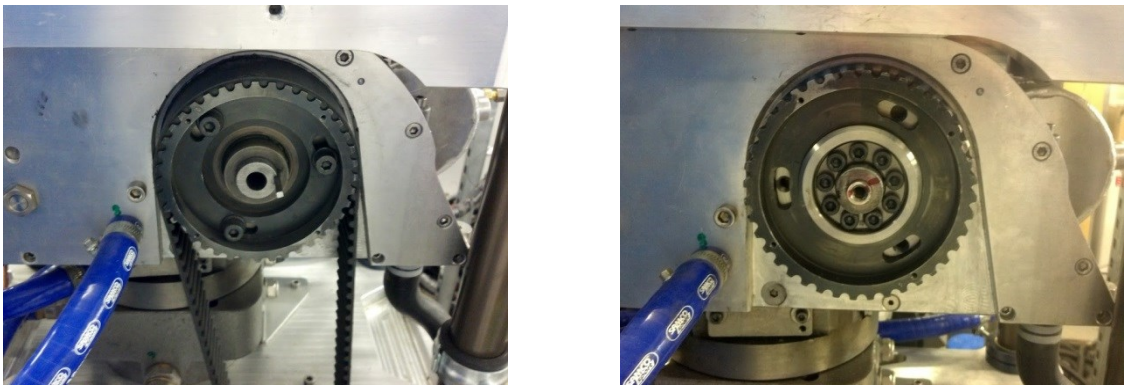

Figure 3-10: Cam drive before (left) and after modification (right)

Subsequently, it was found that the cause of the cam pulley slip was because the cam shaft chain drive had stopped rotating. Further investigation found the plastic roller

which diverted the chain around an oil drainage hole has been worn down by the chain and snapped. An image of the old cam shaft chain drive system behind the front cover of the engine head and the damaged plastic roller is shown in Figure 3-11.

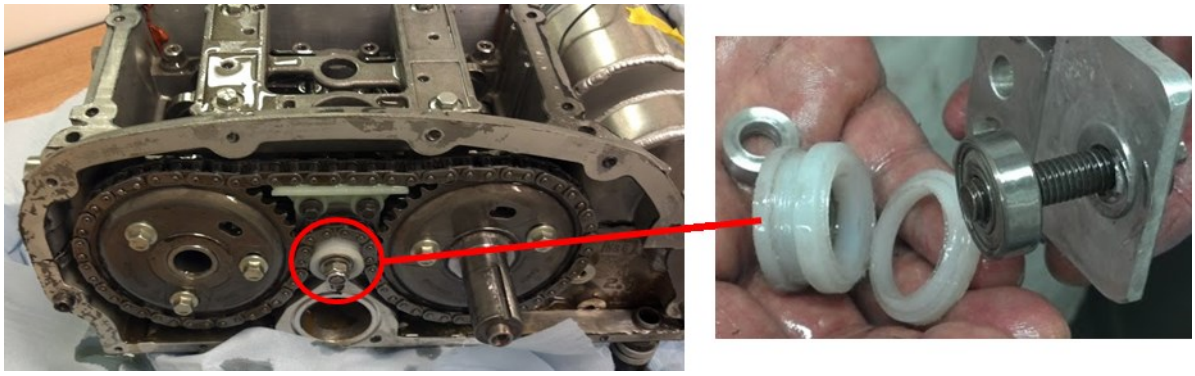

Figure 3-11: Previous design of the cam drive (left) and the damaged plastic roller (right)

The modification for this was to externalise the cam shaft drive system with two pulleys connected with a belt. In the modified design, the two cam shafts both had an external pulley, one of which had another pulley connecting it to the crank shaft via a belt. The modification was carried out by Harris Performance Products Ltd and the pulleys were manufactured by Alan Young Engineering. The crank shaft pulley and other tensioners were also replaced in order to match the teeth profile of the new cam shaft pulley. The new belt was a Gates Synch Belt 1800-8M GT3, 1800mm pitch, 225 teeth and 20mm wide and the modified cam shaft drive system can be seen in Figure 3-12.

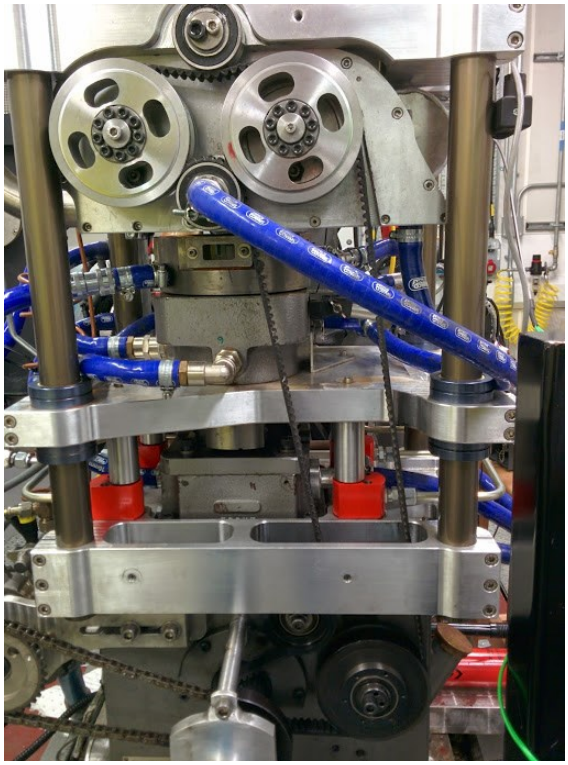

Figure 3-12: Modified cam shaft drive system.

3.4.1. Crank and Cam Timing Synchronisation

In order to synchronise the cam and crank shaft timing, there were pegging points on the crank flywheel and both cam shafts. Though the crank and cam timing synchronisation was highly dependent on the belt tension which meant that even with the cam and crank set at the right location, the belt tension could shift the timing out of synchronisation. In order to check the timing, the crank angle at which maximum valve lift occurred had to be checked. The following procedure was followed in order to set the correct crank and cam timing.

With the belt unhooked, the crank flywheel had to be set at 307CAD and locked with a metal peg on the crank position sensor slot. The two cam shafts also needed to be pegged by unscrewing an access hole through the two cam shaft pulleys using specially made pegging tools. The belt was then fitted and the two tensioners tightened. The pegging tools for the crank and the cam shaft could then be removed.

The correct timing setting between the crank and the cam should give a maximum inlet valve lift at 104CAD. To check whether the timing was correct, a dial indicator was set against the valve and set the crank to 80CAD, the crank flywheel was rotated past maximum valve lift and note was made of the CAD when the dial indicator returned to its original position. If the CAD was not at 128CAD, the process would have to be repeated. This was a trial and error process

3.5. Instrumentation on the Cussons Control Unit and Operation

The control system was refurbished by Cussons Technology Ltd. in 2010. The Cussons control unit had an integrated system of measuring and controlling the various engine and dynamometer operations. The front panel of the main control unit is shown in the left side of Figure 3-13. The following were measured, controlled and displayed on the main control unit.

Displayed and controlled by Cussons control unit:

- Oil temperature
- Fuel temperature
- Coolant temperature
- Engine speed
- Engine torque

Displayed only by Cussons control unit:

- Intake air temperature
- Ambient air temperature
- Fuel flow

The oil, fuel and coolant temperature were controlled by their own dedicated digital controllers and a set point could be entered so the fluid could be heated up by their dedicated heaters. The fluids were cooled by the cooling water circuit, controlled by Sarco valves.

A remote control unit (shown in the right side of Figure 3-13) was located outside the test cell and provided the ability to stop, start, and control the engine speed, dynomometer run mode (Auto, Absorb or Motor) and was equipped with an emergency stop button. This was connected in a way which meant the equivalent buttons on the main control unit did not work and could only be controlled by the remote control unit.

Figure 3-13: Front panel of the Cussons main control unit (left) and the remote control outside the test cell (right).

3.5.1. Fuel Conditioning Unit

Another main component of the Cussons dynamometer setup was the Cussons Fuel Conditioning Unit and this was an integrated unit which measured the fuel flow. The fuel flow measurement was displayed on the Cussons main control unit and it also output a signal that was acquired by the data acquisition system. The fuel temperature was controlled by the Cussons main controller by setting the desired temperature which was conditioned by the Fuel Conditioning Unit.

3.6. Data Acquisition and Control through LabVIEW

Apart from the control provided by the Cussons Control Unit, additional control and data acquisition were provided by a National Instrument CRIO Real-Time PowerPC with an embedded FPGA and through the LabVIEW software. The benefit of the FPGA was that it

gave a fast response time and a deterministic operation which did not depend on resources of other components, such as a host computer. Data acquisition was at 80MHz and automatic control would not be slowed by other processes.

The main hardware was a National Instrument CRIO-9022, Real-Time PowerPC embedded controller for CompactRIO, together with a cRIO-9114 8-slot reconfigurable chassis. There was an on-board FPGA, a programmable hardware chip with a high acquisition rate. The Real-Time embedded controller allowed for deterministic operation. This was important for synchronising the engine and the laser and other imaging equipment. Modules were installed onto the chassis for different control and data acquisition, such as reading thermal couples, digital and analogue input and output.

The chassis and modules were controlled through three levels of LabVIEW VI. The FPGA VI collected the data and executed controls such as air heater and laser/image acquisition synchronisation. It also carried out some basic processing. The Real-Time VI was on-board of the CRIO which dealt with collecting the data from the FPGA to prevent the buffer on the FPGA overflowing and stored it temporarily on the chassis which had a larger memory than the FPGA. Then a window host PC based VI contained the main user interface which collected the data from the Real Time VI and performed most of the post processing such as pressure display, heat release calculation, temperature conversion and data saving. A representation of the hierarchy of the three levels of LabVIEW programes is shown in Figure 3-14.

Figure 3-14: Hierarchy of control and data transfer of the three levels of LabVIEW VIs.

3.6.1. Modules and Their Applications on the National Instrument Control Unit

The CRIO had different modules connected to it for different data logging and control functions. The NI9213 16-channel thermocouple module was connected to

thermo couples measuring ambient air temperature (TC1), coolant temperature (TC8), oil temperature (TC7), inlet air temperature (TC0) and fuel temperature (TC9).

An 8-channel +/-10VDC analogue input (NI9201) read the speed (AI0, where 0-10V equals 0-6000rpm), torque (AI1, where 0-10V equals -50 to 50Nm) and air flow rate (AI3, reading multiplied by 10). It also measured the in-cylinder pressure (AI2) and the current clamp reading for injection timing (AI4).

The 8-channel TLL digital input/output module (NI9401) read the crank angle signal from the shaft encoder (DI00 for the signal at every 0.2 CAD and DI01 for the signal at every revolution). It also output a TTL signal for triggering laser or imaging devices (DI04) at desired crank angle degree and another output to control the air heater setting (DI05).

The NI9203 8-channel +/- 20mA current analogue input read the intake pressure through the Druck XT1570 pressure transducer. And finally the NI9421 8-channel 24V sinking digital input module measured the fuel flow which recorded at 1627.9 pulses per cc of fuel flow.

3.6.2. User Interface of the LabVIEW Vi

The top level of the user interface (on host PC) is shown in Figure 3-15 and contained display of various temperature, pressure, indicators and control. Starting from the top left corner going clockwise, the “Charge Amp Range Setting” corresponded to the setting on the charge amplifier so the correct multiplication factor could be applied for the pressure reading. The “Delay between readings FPGA” was the time between measuring variables such as temperatures, engine speed, torque, intake pressure and air flow rate. “Time to wait (Win)” was the looping time for the windows host interface that balanced resources, speed and the ability to relieve the buffers in the RT host.

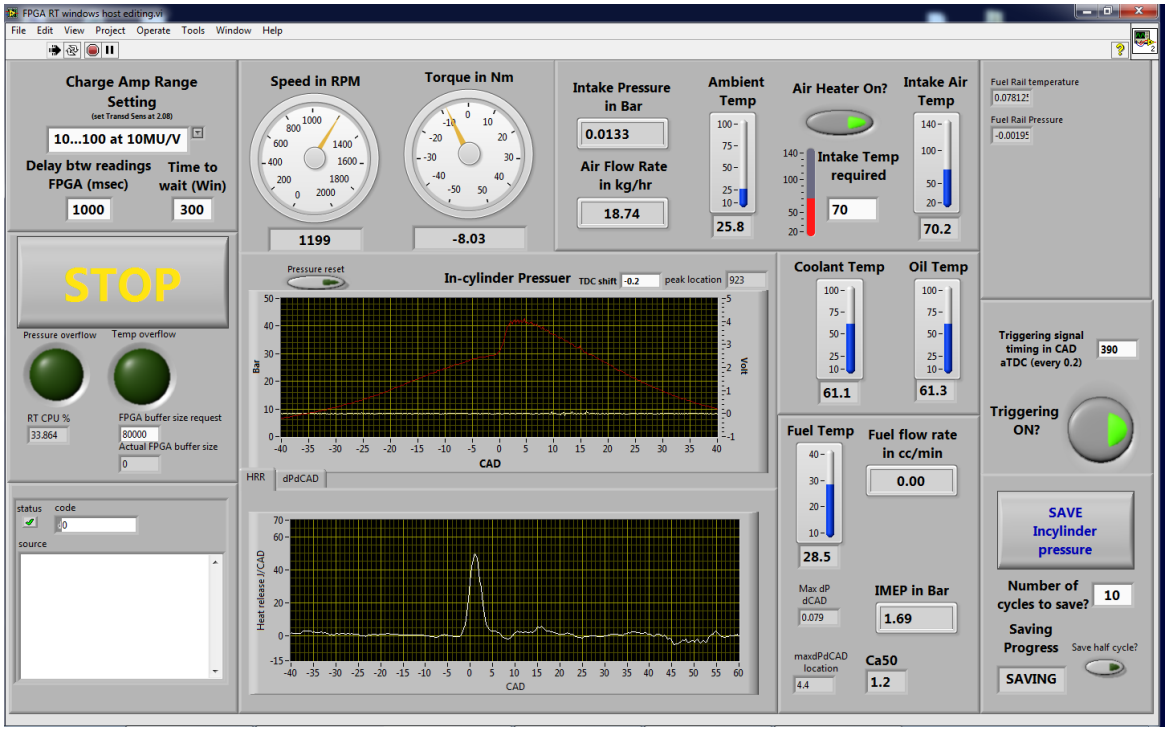

Figure 3-15: Top level LabVIEW user interface on the host PC

The next frame to the right had the speed in RPM and torque registered in Nm. Another frame displayed all the intake air information and control which included the intake pressure, air flow rate, ambient air temperature and the intake air temperature. There was the control for the air heater with a button for on/off and the input for intake temperature required.

On the top right corner, there were two readings for the future if a fuel rail pressure and temperature sensor is installed. Below it was the triggering control for imaging and laser, with an on/off switch, and the timing at which the trigger was applied. Bottom right corner contained the save in-cylinder pressure button and the choice to save different number of cycles. There was also an option to either save half cycles or full cycles and an indicator showing whether saving was in progress.

The column to the left had the coolant and oil temperature. Below it had the fuel temperature, fuel flow rate, IMEP, CA50, maximum change in pressure (Max dpdCAD) and the location of it (MaxdPdCAD location).

The main chart in the middle showed the in-cylinder pressure and current clamp reading at the top and the ability to adjust TDC with a maximum pressure called "Peak location" indicator. Also, due to the occasional errant shaft encoder signal, the acquisition of pressure could be reset by the "pressure reset" button so the pressure readings corresponded to the correct CAD. Below were the heat release rate and the change of pressure charts which could be toggled using the tabs above.

In the bottom left corner was the error message display. Above it was the stop button for the Vi and display whether there was an overflow of the pressure data or the temperature data in the buffer from the FPGA. Finally, there was a request for the FPGA buffer size and the actual buffer size returned from the FPGA and an indicator of the Real Time CPU usage rate.

3.6.2.1. Apparent Net Heat Transfer Rate (ANHTR) (Heat Release) Calculations

An apparent net heat transfer rate (ANHTR) (or otherwise less accurately described as heat release rate (HRR) elsewhere in this thesis) programme was embedded into the LabVIEW user interface and it calculated the heat release rate with a heat loss mechanism and pressure rise rate in real time. The net heat release rate (dQ_n/dt) in J per CAD was calculated by using equation (3-1). γ was the ratio of specific heats taken as a constant 1.35, commonly used for unburned gas in a diesel combustion chamber (Heywood (1988)) or it can be calculated using equation (3-2) where c_p, in J/kgK is the specific heat at constant pressure calculated using equation (3-3), where T is temperature in K, and R, in J/kgK is the gas constant.

$$\frac{dQ_n}{dt} = \frac{\gamma}{\gamma - 1} p \frac{dV}{dt} + \frac{1}{\gamma - 1} V \frac{dp}{dt} - Q_{ht} \tag{3-1}$$

$$\gamma = \frac{c_p}{c_p - R} \tag{3-2}$$

$$c_p = \frac{1000}{28.97}(28.11 + 1.967 \times 10^{-3} T + 4.802 \times 10^{-6} T^2 - 1.966 \times 10^{-9} T^3) \tag{3-3}$$

For equation (3-1), p was the pressure inside the cylinder in Pa, dV/dt was the rate of change in volume in the engine in m^3, V was the volume of the cylinder in m^3, dP/dt was the change in pressure in Pa. Q_{ht} was the heat loss to the wall calculated using equation (3-4) where A_w was the wall area in m^3, h_c was the heat transfer coefficient defined in equation (3-5), T_g was the gas temperature in K and T_w is the wall temperature in K.

$$Q_{ht} = A_w h_c (T_g - T_w) \tag{3-4}$$

$$\frac{dQ_n}{dt} = \frac{\gamma}{\gamma - 1} p \frac{dV}{dt} + \frac{1}{\gamma - 1} V \frac{dp}{dt} - Q_{ht}$$

The heat transfer coefficient was calculated using the Woschni correlation shown in equation (3-5) where B was bore diameter in m, p was pressure in kPa, T_g was gas temperature and w was the average cylinder gas velocity in m/s.

$$h_c = 3.26\, B^{-0.2} p^{0.8} {T_g}^{-0.55} w^{0.8} \tag{3-5}$$

The average cylinder gas velocity could be calculated using equation (3-6) where C_1 is 2.28, N was the engine speed in rmp, C_2 used is 0.000324, V_d was the displaced volume of the engine in m^3, T_{ref} was the temperature of the gas at BDC in K, p_{ref} was the gas pressure at BDC in Pa, V_{ref} was the volume at BDC in m^3, p was the pressure at the current crank angle in Pa and p_m was the motored pressure at the same point in Pa.

$$w = C_1 N + C_2 \frac{V_d T_{in}}{p_{in} V_{in}} (p - p_m) \tag{3-6}$$

3.7. Other Instrumentations

3.7.1. Cylinder Pressure Transducer and Shaft Encoder

The in-cylinder pressure was measured by a Kistler type 6056A41 Quartz Pressure Sensor, M5x0,5, for combustion engines pressure transducer, mounted in a type 6542Q313 glow plug adaptor. The pressure transducer gave 20.87pC/bar which was connected to a Kistler Type 5001 charge amplifier.

The cylinder pressure was recorded using the LabVIEW software and the pressure was logged at every 0.2CAD through the programmable shaft encoder (Sick DRS61). The encoder also gave a signal every revolution which helped towards error checking in case of any missed shaft encoder signal.

There were issues with the disturbance to the pressure reading and it was found that the charge amplifier should not be mounted on the dynamometer frame as the vibrations from the engine were transferred to the pressure reading.

3.7.2. Air Flow Meter

The air flow meter was a Valumass 500 Series in-line thermal mass flow meter. It was installed upstream of a plenum chamber which smoothed the pulsating airflow from the single cylinder engine so the air flow meter would see a steady flow. The setup is shown in Figure 3-16. The data was output to the National Instrument data acquisition system. The reading was also used to control the air heater to prevent damage to the heater when air flow was low.

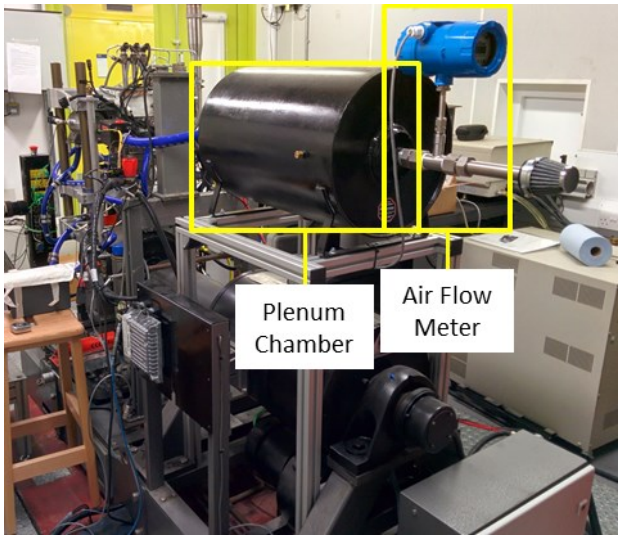

Figure 3-16: Airflow meter and plenum chamber on the Hydra engine.

3.7.3. Intake Air Heater

The intake air could be heated up by the air heater installed. The air heater was a Leister LHS System 41S producing 3.6kW and it was connected directly upstream of the inlet manifold of the engine. The air heater had a minimum air flow requirement

of 240l/min (17.7kg/hr) which was monitored and controlled by the FPGA on board as a safety feature. The measured air flow rate from the air flow meter was directly linked so the air heater would only operate if the air flow had reached a certain level.

The air heater itself was controlled by the duty cycle of a square wave due to the presence of a temperature controller within the air heater. The duty cycle (between 0 and 1) corresponded to a temperature setting and its relationship was found to be duty cycle = (Temperature + 24.762)/585.71. The user input was compared with the intake temperature measurement, and an output was computed by using a PID Vi in LabVIEW. The PID worked best with Kc value of 0.5, Ti value of 0.7 and Td of 0.5, with dt set to 3s. Also, the output range was set to the value input with a maximum of an additional 0.02 to avoid runaway.

3.7.4. Current Clamp for Injection Signal

The fuel injection signal was recorded using a Fluke i30s Current clamp that was attached to the injector signal cable from the ECU. This gave the timing at which the injection took place in addition to the information given by the injection system control through ATI. This was displayed through the LabVIEW control software together with the cylinder pressure trace and recorded.

3.8. Injection System and Control

The fuel injection system was from a production Ford Puma 2.2L engine featuring common rail technology. The different parts of the injection system are shown in Figure 3-17 . The fuel pump was a Siemens/Continental K10_16 and used in conjunction with a Siemens VDO K10_14 common Rail with four 8-holes Siemens injectors, with 140° cone angle, nominal spray hole diameter of 0.12mm and a static flow rate of 350cm^3/30” at 100 bar. One of the four injectors injected into the engine while the other three injected into a collection volume so the pressure wave effect of injections in the high pressure lines can be simulated. The collected fuel could be returned and measured.

The injection was controlled by a custom made ECU and its own calibration software through the calibration interface ATI Vision 3.5.1 (Accurate Technologies Inc). This

injection system was capable of up to six injections per cycle, skip firing and up to 1600bar of injection pressure. Rail pressure, injection timing and injected fuel amount were fully adjustable. The ECU had most of its input requirement disabled due to the lack of standard sensors associated with an engine installed on a vehicle. All it required was a power supply, cam and crank sensors' signal so the engine speed could be determined. Also the injectors, common rail and the fuel pump were connected to the ECU so they could be controlled. The user interface is shown in Figure 3-18.

The ECU was connected to an ATI network hub located on the Cussons Main Control Unit, together with the power supply to the ECU. The ATI network hub was connected through an USB cable to the controlling computer.

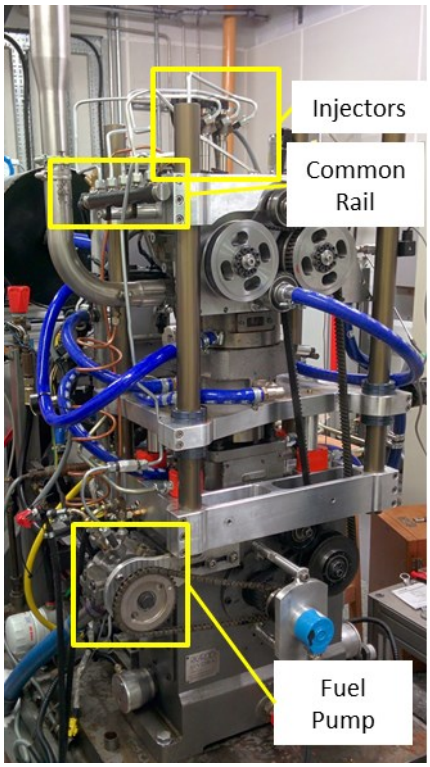

Figure 3-17: Injection system on the Hydra

The setup process included issue with the ECU having problem registering the engine speed. This was resolved by redesigning the cam sensor location and extending the cam shaft with an additional cam lobe to replicate the metal engine. There was also the issue with the fuel pressure not registering which was solved by replacing the fuel pump with

one which was compatible with for the ECU and other injection equipment installed. This also meant a new sprocket and chain drive was installed.

3.8.1. The ATI Vision ECU Interface

A brief description of the user interface, shown in Figure 3-18, is as follows. Starting from the top left frame, there were the on/off switches for the individual injection, with the possibilities in any combination of having two pre injections, two main injections and two post injections. The panel to the right had the rail pressure information with “c_fup_sp_man” for the user input to the required injection pressure, while “fup” was the actual injection pressure, “fup_sp” was the set point which should match the user input. “lc_fup_sp_man” was the manual input on/off which was set to 1 if manual input was required.

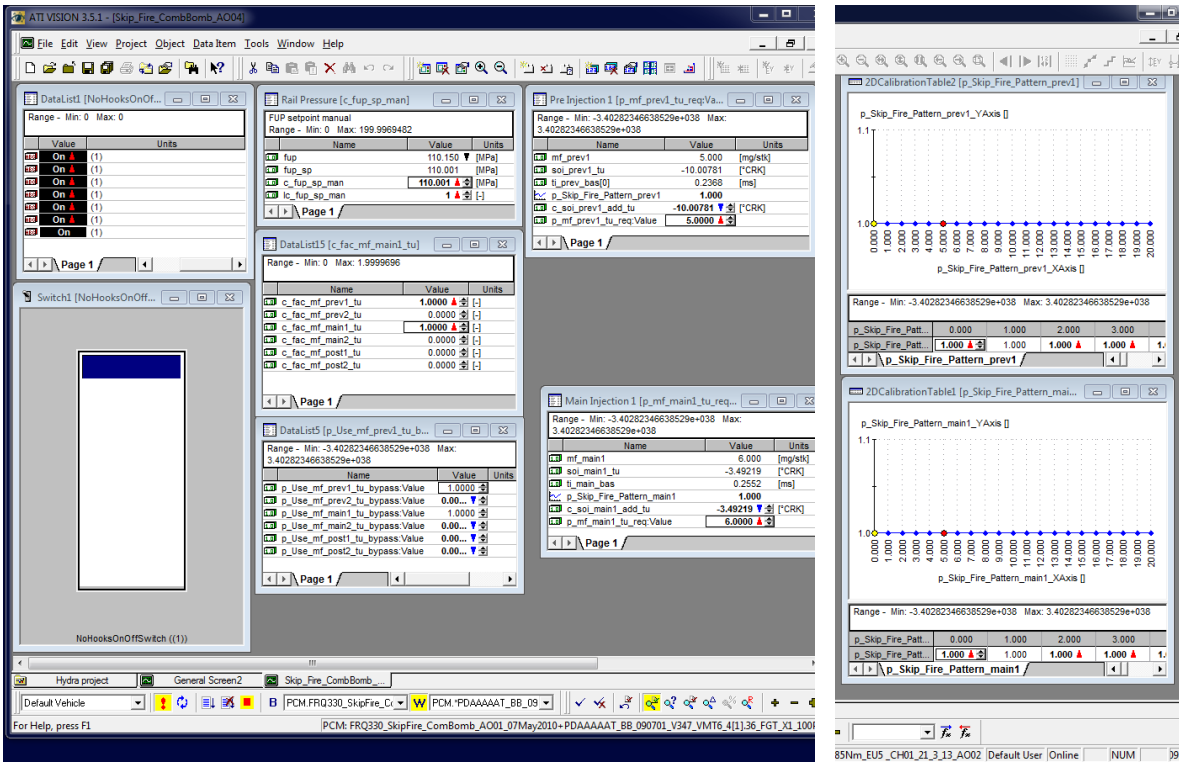

Figure 3-18: User interface of the ECU control through ATI, with the right panel showing the skip firing control

The frame to the right was the pre injection setup box with the first three values as “mf_prev1” showing the input fuel injection amount, “soi_prev1_tu” was the start of injection timing and “ti_prev_bas[0]” was the injection duration.

“p_Skip_Fire_Pattern_prev1” brought up the chart on the right which gave control to skip firing cycle which could be varied in any combination within a 20 cycles period and where “1” was on and “0” was off. “c_soi_prev1_add_tu” was the user input of injection timing and the “p_mf_prev1_tu_req:Value” was the injection fuel amount. The same panel was available for the other five injections labelled “prev1”, “prev2”, “main1”, “main2”, “post1”, “post2”.

The bottom two panels in the middle column controlled the on/off for each injection, with a value of 1 being on and 0 off. Finally, the bottom left panel was the overall on/off switch for all the injections.

There was a quirk in the ATI control that if the main injection on/off switch was set to “off” with fuel injection fuel demand more than zero in any injection there would be an injection when the engine started and stopped. This could lead to a combustion event which could have been violent. So care had to be taken to change all fuel injection quantity to zero and switching the on/off switch to “On” before engine start up and shut down.

3.9. Optical Equipment and Setup

The window carrier/ combustion chamber annulus of the Hydra had four openings on the sides for either window inserts or blanks to be installed. The drawing for the window carrier is shown in Figure 3-19. The windows were made from quartz obtained from Knight Optical (drawing 4029-182). They sat in a metal frame which secured the windows in place and they were sealed with Locktite 5920 silicon. The existence of a window frame and the non-optical metal piston meant visualisation and laser access to the combustion chamber could only be made before 30CAD bTDC and after 30CAD aTDC.

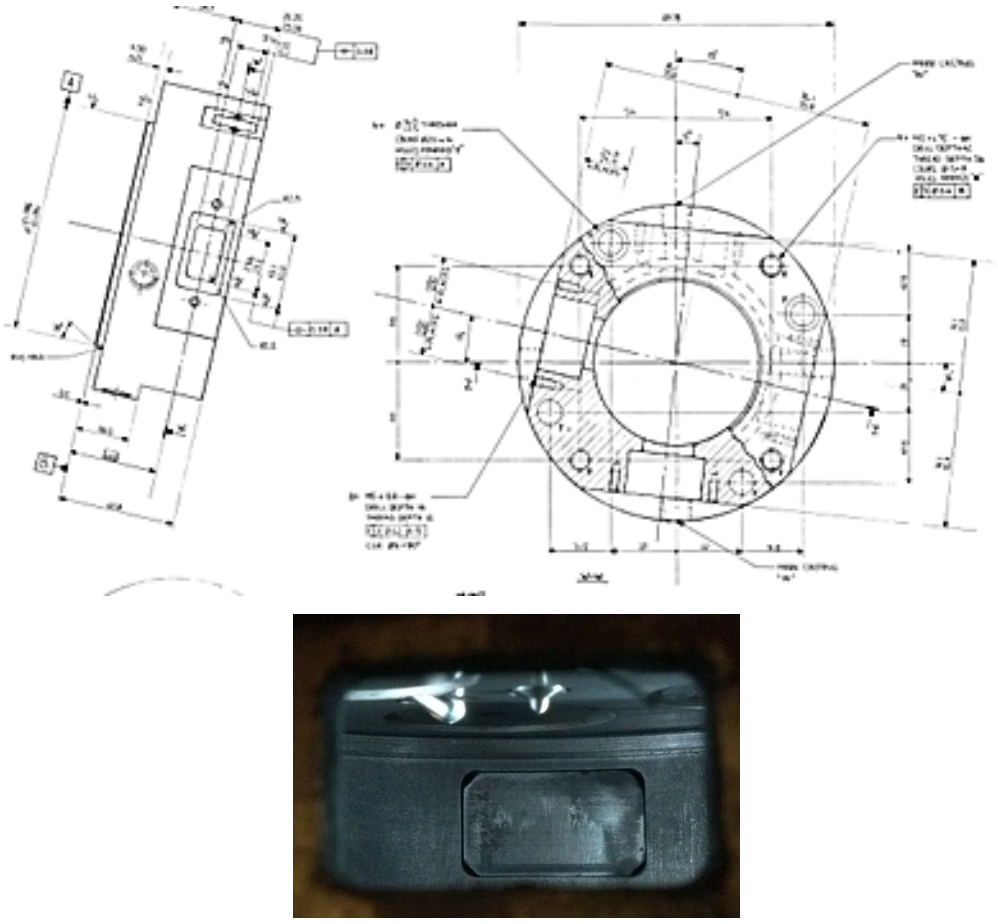

Figure 3-19: Drawing of the windows carrier (combustion chamber annulus) for the Hydra and a view into the combustion chamber through the side window. A metal blank can be seen through the window on the opposite side of the bore.

The bottom of the piston was also made of quartz obtained from Knight Optical (drawing 4029-307). It provided optical access to the combustion chamber via a 45 degree mirror mounted under the piston. Through that, imaging could be carried out with a camera and also provided the possibility of introducing a light source through the mirror. The mirror installed was an Edmund optics enhanced aluminium 4-6 Wave Mirror. A view of the combustion chamber through the optical piston and the 45 degrees mirror is shown in Figure 3-20.

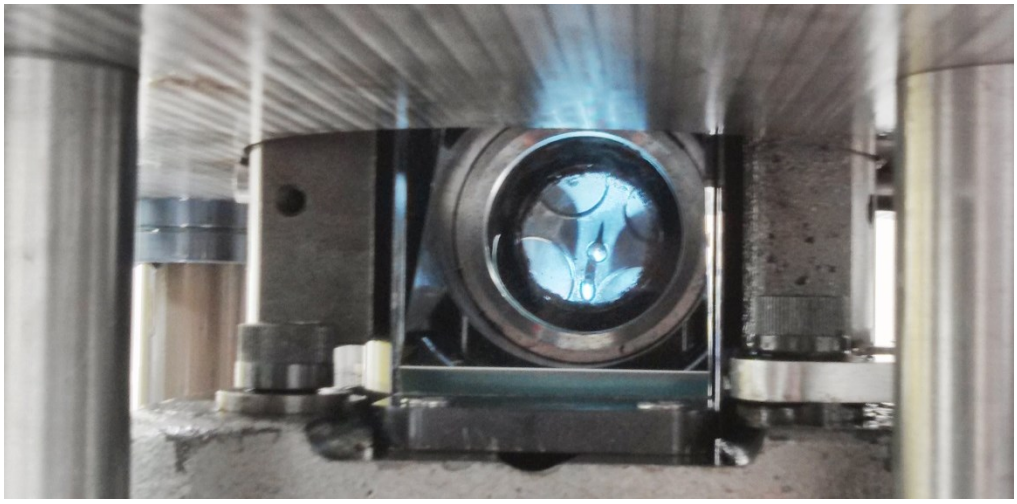

Figure 3-20: View of the combustion chamber through the optical piston and the 45 degrees mirror.

3.9.1. Engine Monitoring During Laser Use

For any laser use in the test cell, the curtains and cell door had to be closed. In order to monitor the engine operation from outside the cell, a camera with microphone was installed inside the cell and both sound and vision could be relayed to the control computer outside the cell.

3.10. Engine Start-up Procedures and Operation.

The start-up procedure began by turning on the main switch on the Cussons main power unit. With the alarm sounding, a sequence of accept, reset and accept, reset was required to be pressed on the Cussons Main Control Unit. The coolant and oil pumps and their heater could be turned on through the main control unit. The fuel pump could be turned on by pressing the “Injection I/O” button. The intake air heater could also be activated by pressing the Air Heater button. The ATI network hub and power to the ECU had to be switched on through the Cussons Main Control Unit. The valves of the cooling water and drain to the engine could be switched on from the side of the test cell.

The window carrier/combustion chamber annulus on the engine had to be checked for secure placement and the hydraulic pump was pressurized to a minimum of 10 bar. The engine was then rotated by hand to check for any abnormality and obstructions to the rotating parts. The ATI ECU interface and the LabVIEW software on the main controlling

computer was then started and connected, as was also the camera and sound monitoring if required.

Checks had to be made to ensure that all the injection fuel quantities in the ATI ECU interface had been set to 0 and the main on/off button set to On before starting. To start the engine, the start button was pressed on the Cussons remote control unit. Real time display of pressure and heat release rate would be displayed on the LabVIEW interface and ATI ECU interface registered engine speed and fuel rail pressure. Tests could then be performed and before stopping the engine, once again, it was necessary to ensure that all the injection fuel quantities were set to 0 in ATI ECU interface and main on/off button is set to ”On”.

The start-up procedure was reversed when finished. It was important to note that before releasing the hydraulic platform pressure, it was important to check that the piston was not between ±30 CAD around TDC as this would expose the top piston ring while the free moving platform was lowered.

3.10.1. Piston and Mirror Cleaning Between Measurements

The procedure for effectively and efficiently cleaning the piston bottom window and the 45 degree mirror was as follow. Firstly, it was necessary to switch off air heater, oil pump, fuel pump and coolant heater, leaving the coolant pump on. The cooling water circuit was open and the coolant Serco (near the intake air heater) valve was turned down to 40C. This would activate the cooling water circuit. Once the coolant water was below 40C, the cooling water supply was switched off and Serco valve was turned up to 90C or any desired temperature.

To clean the 45 degree mirror, the mirror platform and mirror had to be removed. The mirror was cleaned with isopropanol and lens tissue, with a gentle, slow motion and not rubbing or polishing. Protective gloves were necessary and up to 3 lens tissues were consumed in the process. Oil had to be wiped around the mirror mounting point in the Hydra, the extended piston shaft and its base and the bottom of the optical piston using oil absorbent pad.

While making sure the piston was not between 330CAD-30CAD (near TDC) on the crank to avoid popping the piston ring, the hydraulics were released, quick release pipes were disconnected and the window carrier/combustion chamber annulus were removed. The piston glass was cleaned with baking soda mixed with a drop of water using a toothbrush. Then any residual was wiped clean and dried and blown off using the compressed air.

To clean the underside of the piston window, the RS optical instrument cleaner was used and blue tissue paper was used to wipe the piston optics underside dry, and then repeated with isopropanol. The combustion chamber annulus was installed and the pipes were connected and the hydraulics jacked up. Switch on the coolant pump and heater to start heating the water. Install the cleaned mirror and switch on oil pump, air heater and Injection I/O and wait for the engine to heat up to the desired temperature.

3.11. Future Modifications

There are numerous improvements that could be made to the engine to improve the capability and testing range of the engine, both for the mechanical setup and the optical setup of the Hydra.

3.11.1. Engine Components Modifications

A different combustion bowl design can be implemented to closer replicate a production engine. But there are considerations required for the design of the optical access and any change to geometry and its associated optical distortion. It may be more productive to change the whole piston to an optical piston but the option is available.

An important addition to the engine would be the addition of exhaust gas recirculation simulation, either using a burner or reduced oxygen content by a controlled gas supply from gas bottles. The burner option is a simpler system but the associated fouling of pipes and windows may be problematic. Simulated EGR using

gas bottles will be a cleaner option in terms of fouling but it is a more complex system to control.

The Hydra can also be adapted for new injection equipment to be installed if different injection system is required. But this will require an associated change in the control software for the new system. This flexibility also extends to the possibility of installing a new engine head.

3.11.2. Optical Components Modifications

The major hindrance to the optical access was primarily the metal piston as it did not allow optical access from the side around TDC. An improvement can be made by machining an indent onto the optical piston with windows to be secured into the slot. An illustration for such an arrangement can be seen in Figure 3-21. There are technical challenges for securing the widows onto the piston with considerations on its ability to withstand the pressure and heat during combustion. The way the widows are attached and bonded to the metal is also important as it will be catastrophic if the windows were to come loose during engine operation. Consideration will also be required on whether the inserts will have flat sides for minimal optical distortion or curved sides in order to maintain the shape of the combustion chamber, to maintain the compression ratio and minimising the crevice volumes on the side of the piston.

A more radical step from the optical insert into the metal piston is the option of a full optical piston. This will eliminate the issue of attaching the metal inserts onto the metal piston but it will be a less robust component as a whole. This, however, will also enable different bowl geometries to be tested and utilise one which is similar to a production engine. But distortion of laser light entering and scattered light exiting the curved bowl geometry will provide challenges for image processing. And the same consideration of curved side walls and optical distortion will need to be addressed.

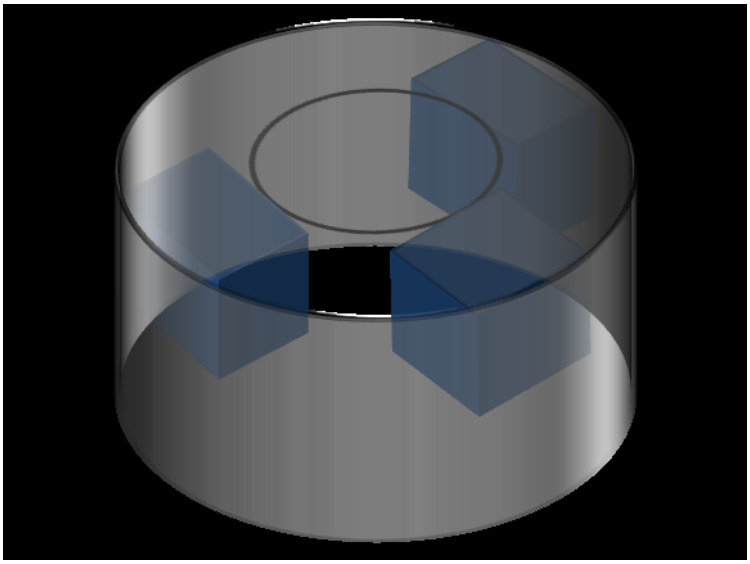

Figure 3-21: Illustration for optical inserts into piston to allow optical access near TDC.

Finally, the entire metal window carrier can be replaced by a full optical annulus for full, all round optical access to the combustion chamber. This will give further access from the side towards TDC and will provide better flexibility for optical access. But again, this will further reduce the robustness of the engine and care will be needed for the engine operation.

3.12. Chapter Conclusion

The physical setup of the engine was described along with the installed instrumentation, data acquisition and control. Details of the injection equipment and the LabVIEW acquisition programme are recorded. Modifications to the engine components throughout the period of the work, such as belt drive, piston rings and hydraulic platform have been described. Possible future modifications to the engine have been discussed. The start-up procedure and engine window cleaning process is set out for reference.

4. Fuel Properties of Gasoline for Use in Gasoline Compression Ignition Engine

4.1. Introduction

To begin the process of studying using gasoline in a compression ignition engine, the physical and chemical properties of gasoline should be studied. As different kinds of hydrocarbon fuel are produced from new sources such as fracking, the availability of the proportion of diesel and gasoline fuel is changing. Also, the increase in demand for diesel fuel in the commercial transport sector in the non-OECD countries means there is a shift in gasoline and diesel requirement (Figure 4-1). An increase of gasoline availability compared to diesel means there are avenue in exploring more efficient way to utilise gasoline for automotive purposes and the use of gasoline type fuel in a compression ignition engine is a possibility.

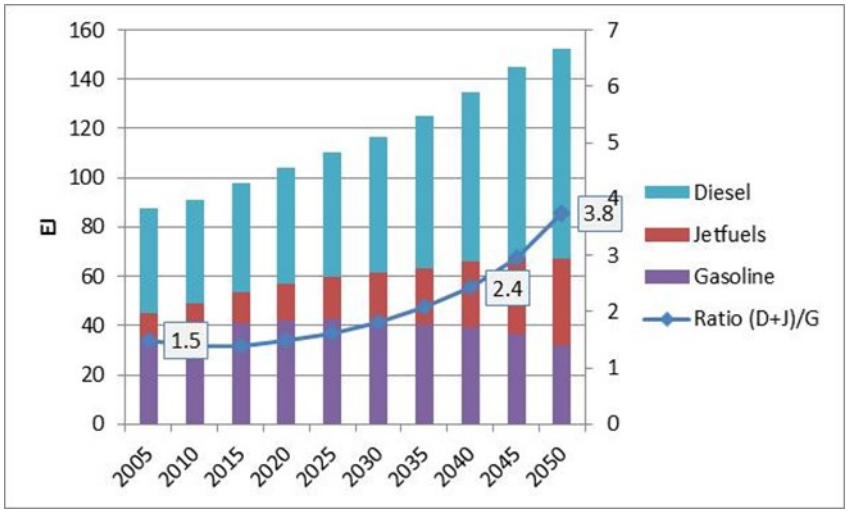

Figure 4-1: Increase of diesel to gasoline ratio prediction until 2050 (World Energy Council, Freeway Scenario)

The use of gasoline type fuel in a compression ignition engine has the benefits of lower emissions but with the high efficiency of a diesel compression ignition engine as described in section 1.3.5. It is possible to test gasoline type fuel in the Hydra diesel engine after careful setting changes and modifications made to the engine. The starting point of this investigation is to look at the makeup and fuel components for gasoline and understand the properties from the perspective of the fuel.

An overview on what basis composition and properties of fuel is determined will be useful here. Composition and properties of fuel are currently determined mainly by:

- availability and economy of production,
- compatibility to fuel transport infrastructure, storage and engine technology
- consideration towards the environment and health in terms of potential accident and emission

The starting point of this investigation starts with a detailed examination of the components, properties and blending techniques for gasoline.

4.2. Types of Hydrocarbons

Before describing the various types of hydrocarbons, it might be useful to explain how carbon and hydrogen atoms are joined together. Carbon atom has four bonds that can be joined with other atoms and hydrogen has one bond. Another useful atom for fuel is the oxygen atom which has two bonds. Using this information, it is possible to combine any combination of hydrogen, carbon and oxygen atom to form molecules.

4.2.1. Alkanes or Paraffins $C_n H_{2n+2}$

Alkanes are open chains of saturated hydrocarbons molecules which are made up of methylene radical, CH_2 and book ended by methyl radical CH_3 (Goodger (1975)). The simplest form of alkanes is methane with one carbon atom and surrounded by four hydrogen atoms. They are stable and unreactive (Goodger (1975)). Table 4-1 shows the list of name for paraffin with different number of carbon atoms. Alkanes that have one hydrogen atom less are radicals and are named with the suffix 'yl' added to the parent alkanes. For example, methane CH_4 will lead to methyl radical CH_3 (Goodger (1975)).

No of carbon atoms	Name	No of carbon atoms	Name
1	methane	6	hexane
2	ethane	7	heptane
3	propane	8	octane
4	butane	9	nonane
5	pentane	10	decane

Table 4-1: List of name for paraffin with different number of carbon atoms

Alkanes can come in the form of a straight chain which is called the normal form and denoted by the prefix n-. Apart from being in a straight chain, alkanes can exist in other forms by replacing one of the side hydrogen atoms with a methyl group. In this case, this carbon atom is now connected to three carbon atoms rather than two that exists in a normal straight chain. This variation is called an isomer of the molecule and is denoted by the prefix iso or i. For example, an iso-octane is a molecule which has 8 carbon atoms and not arranged in a straight chain. A more accurate way to describe a particular isomer is defined by the IUPAC (International Union of Pure and Applied Chemistry). An example of which an iso-octane called 2,2,4-trimethylpentane which is a basic pentane chain with three separate methyl groups attached to the second, second and forth carbon atom along the chain (see Figure 4-2). These isomers have different properties compared to the normal isomers with different boiling points and melting points as straight chains are more stable.

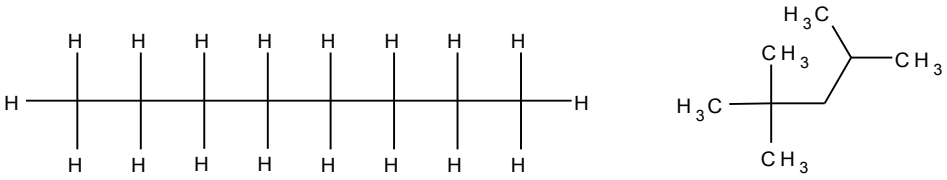

Figure 4-2: The left shows a n-octane C_8H_{18}; the right is the iso-octane (2,2,4 trimethylpentane); the mid-chain carbon atoms left out.

4.2.2. Cycloparaffins or Naphthenes $C_n H_{2n}$

Cycloparaffins are a series of carbon atoms arranged in a ring form starting from the basic C_3H_6. These are saturated hydrocarbons and each of the carbon atoms are connected to two hydrogen atoms. An example of this is the cylcohexane shown in Figure 4-3. The boiling point, freezing point and density of cycloparaffins are slightly

higher than alkanes with the same number of carbon atoms in the molecule. This is because of the higher proportion of carbon atoms over hydrogen atoms which are lighter than carbon atoms.

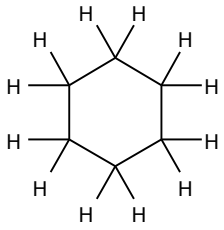

Figure 4-3: Cyclohexane C_6H_{12}

4.2.3. Alkenes (Olefins) $C_n H_{2n}$

Alkenes are open chains structure containing a double bond between the carbon atoms and hence unsaturated. The prefixes in the naming of alkenes follow those of alkanes but with the suffix 'ene' or 'ylene' instead of 'ane'; so alkenes with 2 carbon atoms are called ethylene. The location of the double bonds gives a range of isomers for molecules containing more than 2 cabon atoms. For example, double bond between the first two carbon atoms in a butene chain is called but-1-ene and double bond between the middle two carbon atoms is called butene-2 and is numbered from the end nearer to the double bond. An example of alkenes, 2-methyl-2-butene is shown in Figure 4-4. There are also variations where methyl group branches from the main chain and connected by the double bond.

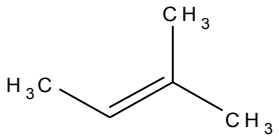

Figure 4-4: 2-methyl-2-butene C_5H_{10}

Alkenes are shown to have a lower boiling point and higher density compared with the corresponding alkanes because of the higher reactivity of the double bond (Goodger (1975)). The double bond will readily unite with a hydrogen atom to form paraffin and sometimes with oxygen atom to form gum (Obert and Jennings (1950)).

In cases where there are more than two double bonds are known as dienes, trienes and so on and collectively known as polyenes.

4.2.4. Alkynes (Acetylenes) $C_n H_{2n-2}$

Alkynes are open chains hydrocarbons containing one triple bond between two carbon atoms. The most basic form of alkynes, acetylene is shown in Figure 4-5. This triple bond is weak and hence alkynes are prone to reactions and has to be stored in acetone solution (Goodger (1975)). Alkynes have a higher boiling point and density compared with alkanes with the same number of carbon atoms.

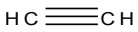

Figure 4-5: Acetylene C_2H_2

4.2.5. Aromatics $C_n H_{2n-6}$

The basic building block for aromatics is a ring of six carbon atoms with alternating double and single bonds between the carbon atoms. The simplest form of an aromatic is C_6H_6 with each carbon atom connecting one carbon atom with a single bond on one side, another carbon atom with a double bond and a hydrogen atom, as shown in Figure 4-6. Multiple of these building blocks can be joined together by sharing 2 common carbon atoms within the ring as shown in Figure 4-7.

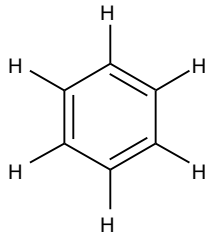

Figure 4-6: Benzene C_6H_6

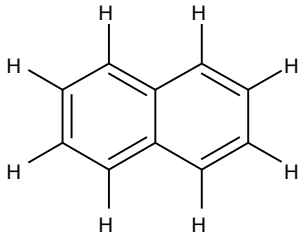

Figure 4-7: Naphthalene $C_{10}H_8$

The boiling point and melting points of aromatics are higher than those of the alkanes and alkenes with the same number of carbon atoms. This is because the ring structure is stable and does not share the characteristics of unsaturated carbon-carbon bond (Goodger (1975)). Additional methyl groups adding to this cyclic structure is added in the side chain rather than breaking up this cyclic structure because of its stability (Goodger (1975)). An example of which is shown in Figure 4-8.

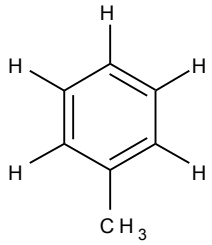

Figure 4-8: Toluene C_7H_8

4.2.6. Monohydric Alcohols Cn H2n+1 OH

This group are alkanes where one of the hydrogen atoms is substituted with an OH group. Alcohols are denoted by substituting the ‘e’ in the name for the alkanes of the corresponding number of carbon with ‘ol’. For example, alcohol with two carbon atoms is called ethanol shown in Figure 4-9. The advantages of alcohols are that it can be produced from abundant and renewable sources such as coal, natural gas or agricultural products. The boiling point of alcohols is higher than the corresponding alkanes.

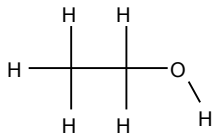

Figure 4-9: Ethanol C_2H_5OH

4.2.7. Bond Energy between Hydrocarbons

As hydrogen, carbon and oxygen atoms bond together, energy is required to break up the bond and once the bond is broken, energy is released from that bonding. Table 4-2 and Table 4-3 show the bond energies found in common hydrocarbon molecules. The exact mechanism of which will not be discussed here but it will be useful to see the different energy required for breaking of the bond and energy released by the breaking of bonds.

Bond	Energy
$\Delta H_a H_2(g)$	435.4
$\Delta H_a O_2(g)$	498.2
$\Delta H_a N_2(g)$	946.2
$\Delta H_a C(gr)$	717.2

Table 4-2: Energy required to break the following bonds (kJ/mol) (Goodger (1975))

From Table 4-2, H_a is the enthalpy of the atomisation of a molecule which is the amount of energy required to break the bonds. From Table 4-3, D(X-Y) and E(X-Y) are the energy to be released from the bond if the bond within the molecule is broken. While balancing reaction equations, these values can be used in conjunction with the number of bonds that are destroyed and formed which will show whether a reaction

consumes or produces energy. This gives an illustration as to the advantages and disadvantages of selecting a particular molecule in terms of the energy produced or consumed when integrating into the gasoline blend.

Bond	Energy
D(H-O)	428.7
E(H-O)	463.1
D(H-OH)	497.5
E(C-H)	414.5
E(C-C)	347.5
E(C=C)	615.5
E(C≡C)	812.2
E(C-O)	351.7

Table 4-3: Energy released from breaking the following bonds (kJ/mol) (Goodger (1975))

4.3. Fuel Properties

It is useful to discuss the different properties of fuel in order to find out what is important for combustion and working properly in the engine. Also, there is a need to understand the importance of each property and how it affects the combustion process and the workings of an engine.

4.3.1. Density

The relative density of liquid fuel is defined as the ratio of weight of a sample of the fuel occupying unit volume at 15°C compared to the weight of water of the same volume. Also, standard density in terms of mass per volume is used. The density of a fuel gives an indication of the type of fuel it is, may it be gasoline, kerosene, diesel, etc. Density also gives an indication of contaminants in a known fuel and it also affects the performance of fuel pumps and injectors (Goodger (1975)). High relative density points to a low spontaneous-ignition temperature and high resistance to knock (Goodger (1975)). Relative density for motor gasoline is between 0.72-0.74 and 0.75-0.85 for kerosene. Density increases as carbon proportion increases, i.e. increasing percentage of double bonds. Typical range of densities of gasoline is shown in Table 4-4.

	Regular unleaded	Premium	Premium plus
Range	725-760	726-762	732-759
Average	735	741	749

Table 4-4: Density of standard commercial German gasoline fuels in kg/m^3 (winter 2003)

4.3.2. Calorific Value

Calorific value is the amount of energy released when burnt measured as heat per unit mass of fuel. This is measured by a calorific bomb where the fuel is burnt inside a container and the temperature rise of the surrounding is measured. This gives the gross calorific value, H_O. However, since this is tested with the condensation of water which does not happen in an engine, a revised lower calorific value, H_U is calculated by subtracting the energy required for condensation of the water vapour (Van Basshuysen and Schäfer (2007)). These values are important since the fuel is the energy carrier and energy contained in a given amount of mass or volume is directly related to fuel economy (Goodger (1975)).

As relative density increases with the rising number of carbon atoms within the hydrocarbon molecule, this decreases the net calorific value. However, volumetric calorific value rises with relative density due to this higher density. This difference will have an implication on storage of fuel especially for aviation purposes where mass is an important factor. Typical calorific value for motor gasoline and kerosene is about 42-44 MJ/kg.

Table 4-5 shows typical ratings for the different types of commercial gasoline. A distinction has to be made here in terms of the gross calorific value and the lower calorific value H_U. Thermal value is the amount of heat generated on its complete combustion. Thermal values of fuel oil have a linear relationship with the API (American Petroleum Institute) gravity, which specifies how heavy or light the hydrocarbons mixture is compared to water, of the products.

Type	Density 15˚C (kg/m3)	Chemical analysis			Calorific value, H_o (MJ/kg)	Calorific value, H_u	
		C (m%)	H (m%)	O (m%)		(MJ/kg)	(MJ/l)
Regular unleaded	735.1	87.47	12.14	0.13	44.17	41.52	30.52
Premium unleaded	751.0	88.40	11.28	0.24	43.44	40.98	30.78
Premium plus	761.0	87.63	10.94	1.33	42.69	40.31	30.67

Table 4-5: Atomic composition and calorific values of different gasoline grades (Van Basshuysen and Schäfer (2007))

4.3.3. Volatility

Volatility can be measured by two properties: distillation and vapour pressure and these two combine to give an overall volatility of the gasoline and kerosene. The volatility of a fuel is important because it affects starting of the engine, amount of deposits, storage stability, etc.

4.3.3.1. Distillation

Given gasoline and kerosene are made up of numerous different hydrocarbons, there is a range of temperature which they evaporate. Distillation gives the fraction of fuel evaporated when heat is applied and the corresponding temperature the fuel is evaporated.

The initial boiling point (i.b.p.) is the initial temperature when the first condensation appears and the final boiling point (f.b.p.) is the maximum temperature reached during the test (Goodger (1975)). It is also shown as a temperature at which 10% (front end volatility), 50% (mid-range volatility) and 90% (back-end volatility) of the corresponding amount of distillate has been distilled. The distillation test gives an indication as to the type of fuel being tested, similar to relative density.

Higher boiling point product has a higher effect on the amount of deposit it generates. Aromatics will have the highest and paraffin the lowest. Deposits cause reduction in gasoline engine cooling and engine volume, hence increase in

compression ratio. This increases the octane requirement which will be discussed in section 4.3.8 Kalghatgi (1990).

The typical range of boiling points for motor gasoline fuel is between 30 and 200˚C and between 150˚C and 300˚C for kerosene. This measure of volatility will determine the fuel system required for metering and appropriate method for storage (Goodger (1975)). Gasoline should contain enough readily volatile constituents with a low boiling point to start quickly in the cold and run efficiently and with low emissions during warm up (Van Basshuysen and Schäfer (2007)). But should not contain too much to prevent excessive evaporation, premature vaporization or vapour lock (Johnson and Auth (1951)). For low mid range volatility, it may cause the engine not to run smoothly, poor warm up, rough acceleration and poor short-trip economy (Lucas (2000)). It should not contain excessive back-end volatility (high back-end components content) preventing it from vaporizing properly and condensing on cylinder wall during cold weather which will be absorbed by the oil and diluting the lubricating oil, increasing wear and exhaust emission (Van Basshuysen and Schäfer (2007)). On the other hand, low high-end hydrocarbon content will lead to loss of fuel economy because of the reduction in high density, high calorific value components in the fuel (Lucas (2000)). Range to be expected is illustrated in Table 4-6.

		Regular	Premium	Premium Plus
Evaporated percentage at 70˚C	Average	37	35	37
	Range	26-46	28-47	24-48
Evaporated percentage at 100˚C	Average	58	55	54
	Range	50-68	48-63	45-61
Evaporated percentage at 150˚C	Average	87	87	87
	Range	81-96	84-95	84-91
Evaporated percentage at 180˚C	Average	93	97	96
	Range	95-99	84-95	95-99

Table 4-6: Distillation values for German gasoline in winter 2003 (percentage by volume) (Van Basshuysen and Schäfer (2007)).

4.3.3.2. Vapour Pressure

Vapour-pressure test indicates the tendency for a substance to vaporize. It increases with temperature and the temperature at which the vapour pressure equals the standard atmosphere, this is the normal boiling point of the liquid (Johnson and Auth (1951)). Vapour pressure also depends on its composition since each component contribute to the vapour pressure in proportion to the mole fraction and to the vapour pressure of the pure component at the temperature of measurement (Johnson and Auth (1951)).

In terms of spark ignition engines which use gasoline, vapour pressure is important for hot/cold start operation as high vapour pressure is required for cold start operation (Van Basshuysen and Schäfer (2007)). Since by vaporization, the composition changes, the vapour pressure of the mixture will vary with the volume of the vapour space (Johnson and Auth (1951)). The vapour pressure of gasoline is around 45-100kPa and lower for kerosene.

4.3.4. Flash Point

Flash point is the temperature of which the fuel must be heated so that the vapour will ignite when an ignition source is applied, i.e. in a spark ignition engine. This is usually not an issue as it is at about -40˚C for gasoline. Kerosene has flash points around ambient temperature. Fire point is the temperature of which the product is heated in order for the inflammable air/fuel mixture to burn continuously. Fire point test is less used as it usually doesn't add anything to the flash point test. Flash point gives an indication for the risk of fire under ambient condition in storage (Goodger (1975)). Gasoline has a flash point below ambient temperature but it is too rich to be ignited unless diluted with air (Goodger (1975)).

4.3.5. Spontaneous Ignition Temperature

The autoignition temperature is the temperature of which a fuel can be autoignited in air without the presence of flame or spark. This is an important property for the prevention of knock in spark ignition engine where ignition is controlled by the spark

plug. The spontaneous ignition temperature decreases with the increase of relative density. The self-ignition temperature of alkanes decreases as the number of carbon increases. Typical spontaneous ignition temperature of gasoline is around 260-280˚C and around 220˚C for kerosene.

4.3.6. Viscosity

Viscosity is the measure of fluid resistance to flow and it is a property related to the pumping and atomisation of fuels. Viscosity can also influence flow through metering orifices but the effect of this is small. Typical viscosity rating for gasoline is 0.5-0.6 centistokes and 3-4 centistokes for kerosene.

4.3.7. Cloud and Pour Point

Cloud point is the haziness that appear in the fuel when wax is formed when solidification point is reached as it is being cooled (Johnson and Auth (1951)). Pour point is the point where oil just barely flows which prescribe the fuel handling quality (Johnson and Auth (1951)). These two properties provide the overall property for the freezing point of the fuel. In gasoline, this value is low compared to normal operating condition and it is in the region of -70˚C and it is about -55˚C for kerosene.

4.3.8. Knock Characteristics and Octane Ratings

Knock characteristic in spark ignition engines is described by the octane number and in general, the higher the octane rating, the more suitable it is as a gasoline fuel. Octane rating describes the resistance to detonation which is called knock. As ignition is controlled by a spark at the appropriate time, autoignition is undesirable. Knocking causes steep pressure rise and higher peak temperature and pressure. This can cause damage to the spark plug, piston, cylinder head gaskets and valves (Van Basshuysen and Schäfer (2007)).

The reference scale for knock in spark ignition engine is formed by the combination of two reference fuels: n-heptane and iso-octane (2,2,4 trimethylpentane). The iso-octane is assigned an ‘octane’ rating of 100 and n-heptane is assigned as 0. The knock intensity of a fuel is tested at given standard conditions and the octane rating

of the tested fuel is compared to the equivalent to that of a mixture of parts of iso-octane (Obert and Jennings (1950)). If a fuel has an octane rating of 75, that will be equivalent to a mixture of 75 parts of iso-octane and 25 parts n-heptane by volume.

There are two octane numbers: motored octane number (MON) and the research octane number (RON). These two values are measured in different conditions with the MON being more severe and that is why RON is usually higher than MON. Typical RON rating for gasoline fuel is between 90 and100. The difference between the two numbers gives the sensitivity of the fuel as the two octane numbers are obtained by different testing condition and shows how the fuel react to these conditions. Typical gasoline has a sensitivity rating of about 10.

Different types of hydrocarbons have different octane ratings. Normal paraffins have the same RON and MON ratings and greatly decreases as the carbon number goes up and only butane is usable in gasoline. Iso-parafins have the same RON and MON ratings and octane ratings increase as branches increase while the number of carbon atom remains the same and sensitivity of them is low. Olefins have medium RON and low MON and decreases as the chain length increases. Because of its low octane rating, it is not used in gasoline. Aromatics have a very high RON and high MON which is why it is usually added to gasoline. A selection of RON and MON values are available in RON, MON and Blending Rating for Various Hydrocarbons (Marshall and Owen (1995).

In relation to octane rating and engine performance, unless the car is equipped with an active knock sensor where the engine will adjust from its knock limited condition, a higher octane rating does not enhance the performance of the car (Lucas (2000)). Since the octane rating is developed with a test engine, the fuel may perform differently in a production engine. Engine testing engineers therefore gives a road octane number which has two numbers, one for accelerating condition and the other for wide open throttle (Lucas (2000)).

For more information on knock and octane number on different types of hydrocarbons, read Lovell (1948).

4.3.9. Acidity

Sulphuric acid from improper refining causes the fuel acidity to rise. This will have an implication on the corrosive property of the fuel on engine components.

4.3.10. Carbon Residue

Some fuels may leave carbonaceous residue which used due to unsuitable refinery methods or contamination which will require controlling (Johnson and Auth (1951)).

4.3.11. Appearance

This is a good indicator of contamination of water, particles or other hydrocarbons and it should appear clear and bright. Particulates block filters and orifices and water can freeze and block lines in sub-zero ambient temperature. Also, oxidation at high temperature may cause gasoline to deteriorate in service and causes change in appearance which is a good indication of inappropriate storage and handling.

4.3.12. Corrosion

Fuel product should be non-corrosive to prevent damage to engine components. As gasoline comes into contact with moisture and oxygen, it can cause corrosion in tank and fuel lines. The corrosiveness of a fuel depends on its water content, oxygenate content (especially alcohols) and sulphur containing compound and any corrosion prevention additive used.

4.3.13. Demulsification

Demulsifying capability of the gasoline is its ability to precipitate water absorbed into the gasoline and is temperature dependent. This ability decreases with the increase of aromatics and even more problematic with increase content of alcohols. Water can be picked up from storage or transportation tanks and form a haze or emulsion. In extreme cases, it might lead to filter blockage.

4.3.14. Gum Content

Gum is formed when gasoline is exposed to oxygen in air that deposits in engine and fuel system. This is undesirable and should be avoided. Pure stable hydrocarbons of

paraffin and naphthene form little gum and reactive hydrocarbons, such as unsaturated hydrocarbons, are prone to oxidation are more liable to form gum.

4.3.15. Electrical Conductivity

The electrical conductivity of gasoline may cause a problem with the risk of static electricity build up while the tank is filled up at a relatively high rate (Lucas (2000)). But this risk is small since the vapour in the storage tank is usually well above the explosive limit. Pure hydrocarbon has a very low conductivity whereas oxygenates and additives may have higher values.

4.3.16. Summary of Properties

Figure 4-10 shows a composite plot of the major properties variation associated with different grades of hydrocarbon ranging from aviation gasoline to diesel. This figure makes the comparison of different properties of the main grades of hydrocarbon fuels easier and shows how the difference properties vary for each grade.

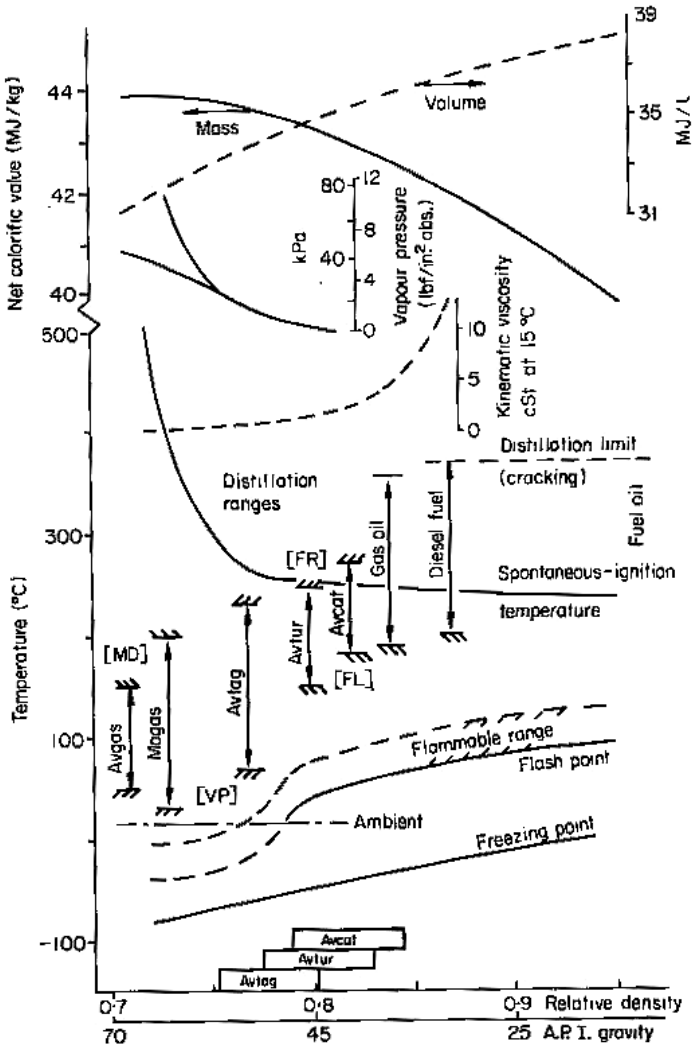

Figure 4-10: Composite plot of properties of different grades of hydrocarbons. Key: Avgas=aviation gasoline; Mogas = motor gas; Avtag = wide-cut gasoline; Avtur = aviation kerosene; Avcat = High-flash kerosene; Limitation to distillation range is as follows: MD = maldistribution; FR = freezing point; VP = vapour pressure; FL = flash point (Goodger (1975))

4.4. Gasoline Properties and Composition

As the properties of fuel in general have been covered, the required gasoline properties and method of control will be discussed. Here is a summary of required properties for gasoline (Lucas (2000)):

1. Burn without knock
2. Be volatile enough to operate in all conditions and not so volatile that will cause a problem for storage
3. Provide good fuel economy and produce low emission

4. Prevent deposits in the fuel system and engine and not hinder the proper functioning of the exhaust system.
5. Capable of being stored and transported safely and adequately from refinery to the moment the fuel is burned.

Gasoline usually has a boiling range of about 30-200C and with a typical relative density of 0.73. The overall quality of gasoline can be considered to be equivalent to that of octane but the range of hydrocarbons contains in gasoline lies between C5 to C12. The net calorific value of gasoline is about 43.9MJ/kg and 31.8MJ/l. The most important quality for gasoline especially in application to spark ignition engine is its anti-knock quality and the closest approximation to this property is the research octane number (RON). This ranges between 95 and 99. The vapour pressure ranges between 45-100kPa and therefore must be stored in vented container to prevent pressure build up. The freezing point of gasoline is about -70C.

Different grades of gasoline have slightly different properties and composition and here is a summary of the key difference between the three main grades that are usually available:

1. Regular gasoline: The regulation set out the octane rating to be no lower than 91 RON and 81 MON. Given its low octane rating, it should only be used in engines with low compression ratio or engines with knock sensors (Van Basshuysen and Schäfer (2007)). Because it has lower density and calorific value, it has a lower thermodynamic efficiency during combustion and hence a higher volumetric fuel consumption of about 5-8% compared with premium gasoline (Van Basshuysen and Schäfer (2007)).

2. Premium gasoline: This is the standard set out by EN228 and the octane number required is min 95 RON and 85 MON. This number is set so that the cost of production of the fuel is kept down, as high octane rating requires higher cost. Fuel economy is increased as higher octane rating also reduces fuel consumption. 95 RON is the optimum between cost of production and fuel economy (Van Basshuysen and Schäfer (2007)).

3. Premium plus: Premium plus has the octane rating of 98 RON and 88 MON. There is usually blended with high octane ether (methyl tertiary butyl ether—MTBE). Premium plus ensures maximum engine efficiency and torque/power (Van Basshuysen and Schäfer (2007)).

Typical premium grade fuel produced by oil companies will claim have some added benefit for using their fuel. Shell V-Power unleaded contains Friction Modification Technology (FMT), enhance octane rating at 99 RON and the ability to remove deposits helping the engine to run smoothly and efficiently. BP claims their BP Ultimate unleaded has a 97 RON rating and a similar engine cleaning, friction reduction property and protection against wear and rust.

As for the legal requirement of the properties of gasoline fuel in the UK, Table 4-7 sets out all the variables that are controlled. Each of these properties and the reason for the requirements are to be discussed here and various additives added to gasoline are also listed and the reasons for their inclusion examined.

Research Octane number (RON)	min 95
Motor Octane number (MON)	min 85
Lead content mg/L	max 5
Density kg/m^3	min 720 max 775
Sulphur content mg/kg	max 50
Existent gum content mg/100ml	max 5
Hydrocarbon type content %(V/V)	
Olefins	max 18
Aromatics	max 35
Benzene content %(V/V)	max 1
Oxygen content %(m/m)	max 2.7
Oxygenates content %(V/V)	
Methanol	max 3.0
Ethanol	max 5.0
Iso-propyl alcohol	max 10.0
Iso-butyl alcohol	max 10.0
Tert-butyl alcohol	max 7.0
Ethers (5 or more C atoms)	max 15.0
Other oxygenates	max 10.0
Vapour pressure	Depending on the class of fuel (for summer or winter application), it ranges between 45min-60max kPa for summer fuel and 70-100kPa for winter fuels.
Volatility	
% (V/V) evaporated at 70˚C	min 20 max 48-50
% (V/V) evaporated at 100˚C	min 46 max 71
% (V/V) evaporated at 150 ˚C	min 75
Final boiling point ˚C	max 210
Distillation residue %(V/V)	Max 2

Table 4-7: Gasoline fuel requirement according to British standard BD EN 228:2004

4.4.1. RON, MON and Antiknock Additives

RON and MON ratings are mainly affected by the composition of hydrocarbon that is blended into the fuel. As different hydrocarbons have different RON and MON ratings, their inclusion into the fuel will affect the overall properties of the fuel. Blending methods and strategies are discussed in Section 4.5.

Additives are also added to increase octane rating of gasoline which is usually around the range of 90-99. Previously, tetraethyl lead and teramethyl lead were

used most widely but because of health and environmental consideration of lead emission, their inclusions in gasoline have been prohibited. Other compounds were used such as iron pentacarbonyl, manganese pentacarbonyl but again their use were limited because of concern on their side effects and toxicity (Van Basshuysen and Schäfer (2007)). Organic compounds such as N-methyl aniline have been tested but there hasn't been an effective anti-knock agent that is soluble in gasoline and free of side effects. The search for the perfect additives in order to increase octane ratings is still on and the maintenance of octane ratings still relies on the composition of hydrocarbons in the fuel.

4.4.2. Lead Content

There has been a gradual reduction of the use of lead as an additive since the 1960s mainly because of its toxicity in exhaust gas. It also increases engine deposits and degradation to the exhaust system. Not all countries have limited the use of lead because it gives valve seat recession protection to older vehicles. Valve seat recession is where the exhaust valve seating is damaged. The limit is 5mg/L but is usually less than this.

4.4.3. Density

The density of gasoline is set to ensure that the fuel contains the correct components for gasoline fuel as density gives an indication on fuel type. Density also ensures that the fuel is free of contamination. Relative density for motor gasoline is between 0.72-0.75.

4.4.4. Sulphur Contents

Sulphur exists as sulphides, thiols and mercaptans (where a sulphur atom is inserted between carbon atom and hydrogen atom). Sulphur forms oxides when combusted and may form sulphuric acid when attached to water at low temperature (Johnson and Auth (1951)). Sulphur is also limited to reduce the emission of sulphur oxides and prevent the forming of hydrogen sulphide during exhaust catalyst warm-up (Lucas (2000)). The sulphur content cannot exceed 50mg/kg. Problem is when

sulphur accumulates in the cylinder once the engine has stopped and leaks into the crankcase. This combines with water, forming sulphuric acid and causes corrosion (Johnson and Auth (1951)). This only applies in winter when engine is cold or poorly ventilated and water is formed in the engine. Sulphur also decreases the efficiency of the catalytic converter which leads to increase of HC, CO and NO_x emissions (Van Basshuysen and Schäfer (2007)).

4.4.5. Gum Content

Gum is formed when gasoline is exposed to oxygen in air that deposits in engine and fuel system. This is tested by evaporating a sample of fuel in a hot stream of air, the residue is called unwashed gum. This unwashed gum is then dissolved in n-heptane and those insoluble left behind in the n-heptane is called existing-gum. The limit on gum is no more than 5mg/100ml. Gum content is related to the type of hydrocarbon used in gasoline.

4.4.6. Hydrocarbon Contents

4.4.6.1. Alkanes

Alkanes are the most abundant hydrocarbon found in crude oil and form the majority of gasoline. The content of alkanes is indirectly managed by other properties such as density, RON and MON ratings. Branched-chain isomers are more suitable for use in gasoline because of their resistance to spontaneous ignition compared with straight chain alkanes.

4.4.6.2. Cycloparaffins

Cycloparaffins are not controlled because they are desirable components of motor gasoline. They have higher energy content per unit volume and higher octane rating compared to straight chain paraffins.

4.4.6.3. Olefins

Olefins content in gasoline generally ranges from 0% to the maximum permissible 18% in volume. It is limited to 18% because they are suspected to be responsible to form ozone. Low boiling point species like 1-hexene C_6H_{12} give

good research octane number (Van Basshuysen and Schäfer (2007)). Because of the olefins' medium RON and limited MON properties, they are more suitable in regular and premium gasoline but less so in premium-plus. Olefins, do not readily react with oxygen, are more desirable for gasoline fuel than straight chain paraffin because of their higher octane ratings partly because of the presence of the double bond (Obert and Jennings (1950)).

Polyenes, i.e. olefins with multiple double bonds are less appropriate for gasoline. This is because they have low stability and leads to colouring of the fuel in storage. It also has the tendency to form gum (Obert and Jennings (1950)). Dienes do have a high reaction rate which may be useful for racing application but they have a low octane rating (Van Basshuysen and Schäfer (2007)).

4.4.6.4. Aromatics

The inclusion of aromatics is the primary way to increase octane rating in gasoline, allowing high compression ratio in engines, lower fuel consumption and enhance the ability to resist auto ignition (Van Basshuysen and Schäfer (2007)). Aromatics also have high gravimetric heat of combustion. Table 4-8 shows the average composition of aromatics in gasoline

The usual content of aromatics is approximately between 31-35% by volume in commercial gasoline and the higher content corresponding to the premium gasoline and lower content tends to be regular gasoline. There are concerns about the emission of benzene due to incomplete combustion of aromatics and there has been increasing pressure to control the use of aromatics because of its link to benzene emission.

Product	Formula	% by volume average	Boiling point/range	Mixed Octane rating	Mixed octane rating MON
Toluene	C7H8	9.3-10.3	110˚C	124	112
Ethyl Benzene	C8H10	9.5-9.8	136˚C	124	107
Xylenes	C8H10		138-144˚C	120-146	103-127
C9 aromatics	C9H11	9.3-11.1	152-176˚C	118-171	105-138
C9+ aromatics (small quantities)	C10H12 C11H13		169-210˚C	114-155	117-144

Table 4-8: Aromatics in gasoline, average in winter 2003 Van Basshuysen and Schäfer (2007)

4.4.6.4.1. Benzene Content

Benzene was often used before it was deemed too toxic to be widely used. Benzene content is limited to less than 1% by volume and its emission comes from unburned benzene in exhaust and evaporated emission and partially combusted aromatics (Lucas (2000)).

4.4.7. Alcohol (and Ether) Content

Alcohol C1-C4 are used in gasoline as they have good octane properties and with their low boiling point, can increase front-end volatility and reduction of CO emission (Lucas (2000)). Also, it produces less hydrocarbon emission and has lower smoke forming properties. However, a maximum is usually imposed on the amount of alcohol allowed in gasoline. This is regulated to prevent undesirable qualities that alcohol brings which includes changes in materials in fuel systems and changing the stoichiometric point of the fuel causing the engine to run lean. Additionally, when alcohol is mixed with gasoline, the alcohol will absorb water from the atmosphere and separate from the gasoline (Obert and Jennings (1950)[)]. Alcohol has much lower energy content compared with gasoline and not volatile enough for easy cold start. The lower energy content can be seen in terms of its calorific value shown in Appendix A. Compared with other hydrocarbons, alcohols have half the calorific value which is significant. This makes alcohol not an ideal component in fuel.

Different types of alcohols are included for different purposes. Methanol is rarely used because it is aggressive towards material in fuel system even though it has a strong effect on water tolerance of the fuel (Lucas (2000)). Also, there is a problem of dissolving methanol in gasoline and usually require a co-solvent such as C4 alcohols (Lucas (2000)).

Ethanol can be included in gasoline fuel of up to 5% by volume but due to high production cost compared to gasoline, it is not usually added unless it is subsidised like in France, Austria and Brazil (Van Basshuysen and Schäfer (2007)). It is not as aggressive on materials as methanol but should still require attention for its inclusion in the blend (Lucas (2000)). Higher alcohols have limited use; e.g. isopropanol is used in a small amount as an anti-icing agent and tertiary butanol is used to co-solve methanol.

MTBE (methyl tert-butyl ether, in Figure 4-11) is often used to the maximum 15% to boost the octane rating for fuel, especially in premium fuel. Since it has a low boiling point at 55C, care has to be taken when blending. Ethers can increase water content and formation of hazes. It also affects cold weather drivability due to the bound oxygen. There is also the problem because of its poor biodegradability and can persist in ground water if spilt (Lucas (2000)).

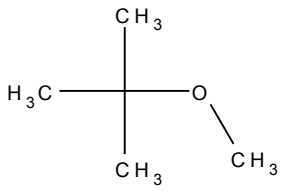

Figure 4-11: Methyl tertiary butyl ether (MTBE) $C_4H_90CH_3$

4.4.8. Vapour Pressure

The lower limit of 45kPa for safe vapour pressure is set for ensuring the vapour in storage tank is kept above the upper explosion point, i.e. over rich (Van Basshuysen and Schäfer (2007)). The upper limit of vapour pressure of about 100kPa is set by the need to prevent evaporation losses and operation when engine is already hot.

4.4.9. Volatility Requirement

There is a balancing required in terms of volatility requirement. Cold starting ability depends on the front-end volatility and generally require E70 (meaning percentage of fuel evaporated at 70˚C) of 20%. A maximum imposed for front-end volatility will help to prevent vapour lock in fuel lines during hot weather condition which can be exacerbated by altitude. Mid-range volatility (E100) partly determines cold weather drivability and that is set at 46% minimum. Carburettor icing also depends on mid-range volatility and suitable additives that will help to prevent it. Back-end volatility (E150) affects exhaust emissions of HC because combustion efficiency depends on heavy hydrocarbons.

4.4.10. Final Boiling Point

The final boiling point of maximum 210˚C is to monitor the overall behaviour of the gasoline and ensuring it does not contain excessive heavy hydrocarbon in gasoline which causes condensation on cylinder wall and leads to emission problems.

4.4.11. Distillation Residue

Controlling distillation residue and limiting it to maximum of 2% in volume is to minimise the amount of residue that can potentially cause harm to components of the engine and affect the efficiency of the functioning of the engine.

4.4.12. Additives

Additives are not expressly controlled but less than 1% is added to the fuel for the following purposes:

4.4.12.1. Exhaust Valve Seat Additives

Protection of exhaust valve seat in old vehicles which was protected by lead content is no longer available. Lead is now replaced by Organic potassium or sodium compound soluble in fuel.

4.4.12.2. Deposits Reducing Additives

Detergents and other additives are used to reduce deposits in injector intake and fuel system. Examples of these additives include poly-isobutene amines, poly-isobutene polyamides and polyether amines. Detergents are also used for controlling the combustion chamber deposit, which happens on the combustion chamber wall and sometimes in the perimeter area of the piston head. Also, additives can also reduce the residues that have already formed.

4.4.12.3. Gum Formation Prevention Additives

Antioxidants are used to prevent the formation of polymer residue (gum) and improve storage stability. Gasoline with olefins and lead are particularly susceptible to oxidation. Active ingredient includes Paraphenylene diamines, sterically impeded aklyphenoles are used.

4.4.12.4. Metal Deactivator Additives

Metal deactivator additives are added to reduce the reactivity of catalyst in the oxidation process like copper ions dissolved in gasoline. Common additives used are N,N' –disalicylidene-,2-propane diamine (Lucas (2000)).

4.4.12.5. Corrosion Protection Additives

Corrosion protection additives are used to protect the fuel distribution link and in the vehicle. It is also particularly useful in new vehicles transported long distances and has long standstill times with an empty tank. These corrosion protection additives will coat the metal surfaces and these additives will be in the form of polar molecule groups (carboxyl, ester or amino acids). Higher level of corrosion protection additives is used in gasoline where alcohols are present.

4.4.12.6. Friction Modifier Additives

Friction modifier reduces the friction between the piston rings/cylinder running surface and aid fuel consumption and requirement for motor oil. The active ingredients for this are carboxyl-, ester-, aminverbindungen.

4.4.12.7. Freezing Point Reducing Additives

Additives reducing the freezing point of the fuel give protection in cold weather. This is to protect the carburettor or the throttle body of the inlet manifold (Lucas (2000)). Cryoscopic additives are used to suppress the freezing point of water and these additives come in the form of light alkyl alcohol and glycols. Another additives used are modern surface effective detergents which form a layer over metal surface and inhibiting the formation of ice.

4.4.12.8. Demulsifier Additives

Demulsifier additives are present to promote the coalescence of water droplet present in gasoline and concentrate them at the interface between water and gasoline phase. This will prevent water haze forming when water is present in gasoline. The additives are usually mixtures of polyoxyalcohols and their derivatives (Lucas (2000)).

4.4.12.9. Anti-static Additives

Anti-static additives are added to prevent the build-up of static electricity which might give rise to the possibility of spark causing ignition. Although the vapour in the storage tank is too rich to ignite, it will still require a small amount of organic material to be added.

4.4.12.10. Drag Reducing Additives

Drag reducing agents are used to increase the flow rate through the pipeline by reducing drag. These are usually high molecular weight polymers that shear readily although there are concerns about engine deposits coming from these additives (Lucas (2000)).

4.4.12.11. Biocide Additives

Biocide additives are added to prohibit the growth of bacteria that exists in the interface between the water and gasoline. Typical additives used are boron compounds, imines, amines and inidazolines (Lucas (2000)).

4.4.12.12. Odorant Additives

Odorant additives are introduced to gasoline to improve the smell especially with the presence of sulphur compounds. However, little success has been achieved with odorant additives (Lucas (2000)).

4.4.12.13. Anti-ORI Additives

Anti-ORI (octane requirement increase) additives are added because the octane rating requirement of an engine increases by 3-5 over the first 10-15000 miles of its life after which it stabilises. Factors affecting this include: lubricant composition, driving pattern, fuel additives and are all caused by engine deposits. Using the following reduces deposits: polyetheramine detergent called techron reduces deposits for several thousand km before re-establishing themselves. A detergent additive called PDP5400 controls intake deposits and reducing ORI.

4.4.13. Manganese

Methylcyclopentadienyl manganese tricarbonyl (MMT) is added as an anti-knock agent and it is seen to be more effective than lead. However, it is used in low concentration because of problems with fuel instability, deposit buildup in engines, lack of response at higher concentration and effect on hydrocarbon emissions from catalyst-controlled car (Owen, Coley et al. (1995)). Even with its favourable octane boosting quality, it is not used widely because of these problems and also its response to highly aromatic gasoline is poor (Owen, Coley et al. (1995)).

4.4.14. Phosphorus and Silicon Content

Phosphorous causes degradation of most exhaust catalyst and therefore controlled by forbidding the addition of any additives containing phosphorous (Lucas (2000)). Silicon is also controlled for similar reason.

4.5. Gasoline Blending Techniques

As gasoline fuel depends on a great number of variables, it is difficult to accommodate all the variables and produces a fuel that is optimised for all variables. Also, it is

important not to be too rigid in the specification of the fuel because the cost of production for such specification will be too high.

Modelling tools are used for blending gasoline and most properties are linear and therefore easy to predict. But some properties, including the important factor of octane rating and vapour pressure, are non-linear and these relationship are usually based on proprietary non-linear models (Lucas (2000)). In practice, fuel is blended generally and making small adjustments by the addition of additives. Blend calculations are done by linear programming produce the desirable results through online analyser measurements.

4.5.1. Octane Blending

A substantial amount of research has been published on the effect of composition of gasoline fuel has on octane rating. Models and empirical equations have been developed to predict octane number and are compared to experimental results.

A simple way to give an idea of how octane rating changes when blended is by blending octane rating. Octane number changes when blended with other compound. This can be seen by the blending octane rating shown in Table 4-9 and an extended version of this table can be found in Appendix A2. Blending octane rating is obtained by combining 20% of the tested material with 80% volume of 60/40 isooctane/n-heptane blend. It can be seen that octane number decreases or increases without any obvious trend and it is a property that has to be taken into account when blending. Generally, olefins have the highest blending values and paraffin has the lowest.

	RON	Blending RON	MON	Blending MON
paraffin				
n-butane	94	113	89.1	114
2,2-Dimethylbutane	91.8	89	93.4	97
Olefins				
1-Butene	97.5	144	79.9	126
4-Methyl-2-pentene	99.3	130	84.3	128
Naphthenes				
Cyclopentane	101	141	84.8	141
Methylcyclopentane	91.3	107	80	99
1,1-Dimethylcyclopentane	92.3	96	89.3	102
Aromatics				
Methylbenzene	120	124	102.5	112
1,3-Dimethylbenzene	118	145	114.5	124
IsoButylbenzene	111	122	98	118

Table 4-9: Blending MON and RON of some hydrocarbons (Marshall and Owen (1995))

Here is a selection of research done in the field of octane number blending and a brief description of the methods applied.

Schoen and Mrstik (1955) predicted the octane rating of a fuel using the octane rating and the olefin contents of the two components being blended. Stewart (1959) extended this to enable prediction for multiple components using olefin content of the components. Auckland and Charnock (1969) used a blending index to obtain the octane number of a mixture linearly but with limited applicability because of its inability to apply generally to all compositions. Healy, Maasen et al. (1959) (ethyl RT-70 method) also proposed similar adaptation of composition properties of fuel sensitivity (RON-MON), olefin and aromatic contents of the components into linear relationship in predicting the octane rating for a blend. Linear blending methods are the simplest to use even though their approximation of a non-linear quality as linear has their limitations.

Myers, Stollsteimer et al. (1975) used linear regression to predict octane number of a gasoline by analysing the content of isoparaffin, aromatics, lead and sulphur. Sarmanaev, Valitov et al. (1980) investigated the octane number with a mixture of paraffinic-hydrocarbons, bezene, toluene, xylene and C9+ aromatics. Zahed, Mullah et al. (1993) used regressional analysis and looking at the content of light and heavy straight run gasoline, reformer gasoline, fluid catalytic cracker gasoline and butane

of the tested gasoline fuel and formed an empirical equation to predict octane rating. It was found that the error for this method to be better than the Stewart method and have a deviational error of 0.54%. Twu and Coon (1996) commented that the Zahed method is only useful for blends within the range of the properties used in the regression model and any blend outside this range is vastly inaccurate.

Rusin, Chung et al. (1981) developed a method which involves transforming the components properties such as RON, MON, contents of olefins, aromatics and paraffins, blending the transformed properties linearly and converting it back to standard values. The errors for this method were found to be approximately four-tenths of an octane number. The transformation method is considered to have the highest accuracy but it requires a large amount of data in order to generate the parameters necessary.

Interaction method proposed by Twu and Coon (1996), Twu and Coon (1997) used the RON, MON, olefin, aromatics and saturates content to predict octane number for the blended gasoline. However, the interaction method (Morris (1975)) involves regression analysis which requires a large amount of data to generate the correlation.

Murty and Rao (2004) presented a way to predict octane number by using an artificial neural network model which was also employed by Pasadakis, Gaganis et al. (2006). This method is based on a higher number of parameters (or weights) which is claimed to improve its robustness over the regression method. Blending model that includes oxygenates as a parameter has been developed by Ghosh, Hickey et al. (2006) and it was based on the analysis of 1471 different gasoline fuels.

There are pros and cons for each of these methods and since these researches involve large tables listing the octane ratings of tested blends or coefficient for blending, it is not produced here. The choice on which will depend on whether the fuel tested has been included as part of that research as not all the research has a full coverage of all the fuels and compositions available. There is not a method that has been proven to be definitive and it is a good illustration as to the difficultly in

predicting the octane rating of a gasoline blend. It is easier to test it experimentally rather than trying to predict the octane rating for a particular blend of gasoline fuel but these researches will give a rough guide to it.

4.5.2. Reid Vapour Pressure Blending

Apart from prediction of octane numbers, prediction for Reid vapour pressure has also been developed using molar proportion, index system, interaction models and blending values are used to predict Reid vapour pressure. This is an alternative for predicting the properties of a gasoline blend to the octane rating. Some relevant references are included here (Stewart (1959), Vazquez-Esparragoza and Bullin (1992)).

4.6. Example of Gasoline Fuel Blends

Using the standard required by regulation and properties desired for internal combustion engines, here are a few examples of the composition of gasoline fuels.

Table 4-10 shows the composition of different types of hydrocarbons found in typical gasoline fuel. Table 4-8 shows the aromatic content of a typical gasoline. Table 4-11 gives you a further break down into different number of carbon atoms in each type of the hydrocarbon present in the fuel. Table 4-12 shows an example devised by Hamilton (1995) which shows the most likely components of gasoline fuel.

These compositions are controlled by the regulation demanding specific range of properties and concentration of different components. This will hopefully be useful when considering the composition of gasoline and as a guideline as to what to include in the fuel.

Component	% vol
Saturates	50-65
Olefins	5-15
Aromatics, total	25-40
Monoaromatics	25-40
Diaromatics	0.5

Table 4-10: Gasoline compositional ranges (Wei (2000))

Number of atoms of carbon	Families of components (% mass)						
	Saturated compounds				Unsaturated compounds		Total
	Linear alkanes	Branched alkanes	Ethers	Cyclic alkanes	Alkenes	Aromatic compounds	
4	5.14	0.30			1.49		6.93
5	1.26	7.84	0.50		10.11	0.50	19.71
6	0.64	6.34	3.00	1.19	5.07	1.23	17.47
7	0.65	3.22		1.05	1.56	8.11	14.59
8	0.48	11.47		0.43	0.34	13.61	26.33
9	0.11	1.12		0.16	0.07	9.49	10.95
10	0.01	0.09		0.09	0.02	2.80	3.01
11		0.10				0.25	0.35
12		0.61					0.61
13		0.01					0.01
Total	8.29	31.10	3.50	2.92	18.66	35.49	99.96

Table 4-11: Composition of a European commercial gasoline (Guibet and Faure-Birchem (1999))

	RON	MON	Boiling Point in ˚C	Density in g/ml @15˚C	Min autoignition temperature in ˚C
15% n-paraffins					
n-butane	113	114	-0.5	gas	370
n-pentane	62	66	35	0.626	260
n-hexane	19	22	69	0.659	225
n-heptane (0:0 by definition)	0	0	98	0.684	225
n-octane	-18	-16	126	0.703	220
30% iso-paraffins					
2-methylpropane	122	120	-12	gas	460
2-methylbutane	100	104	28	0.62	420
2-methylpentane	82	78	62	0.653	306
3-methylpentane	86	80	64	0.664	-
2-methylhexane	40	42	90	0.679	
3-methylhexane	56	57	91	0.687	
2,2-dimethylpentane	89	93	79	0.674	
2,2,3-trimethylbutane	112	112	81	0.69	420
2,2,4-trimethylpentane	100	100	98	0.692	415
12% cycloparaffins					
cyclopentane	141	141	50	0.751	380
methylcyclopentane	107	99	72	0.749	
cyclohexane	110	97	81	0.779	245
methylcyclohexane	104	84	101	0.77	250
35% aromatics					
benzene	98	91	80	0.874	560
toluene	124	112	111	0.867	480
ethyl benzene	124	107	136	0.867	430
meta-xylene	162	124	138	0.868	463
para-xylene	155	126	138	0.866	530
ortho-xylene	126	102	144	0.87	530
3-ethyltoluene	162	138	158	0.865	
1,3,5-trimethylbenzene	170	136	163	0.864	
1,2,4-trimethylbenzene	148	124	168	0.889	
8% olefins					
2-pentene	154	138	37	0.649	
2-methylbutene-2	176	140	36	0.662	
2-methylpentene-2	159	148	67	0.69	
cyclopentene	171	126	44	0.774	

Table 4-12: Composition as envisaged by Hamilton (1995)

4.7. Chapter Conclusion

The different properties of fuel found in gasoline and their importance has been discussed. The requirement of the fuel and the reasons for their control was also shown. This can then be used in considering the application of the gasoline type fuel in a compression ignition engine. For the purpose of this thesis, this was the extent of the

study of gasoline fuel to be used in a compression ignition engine. The next step is to describe diesel fuel properties, composition and blend and its suitability as a compression ignition engine fuel. This can be compared with gasoline with the aim to find a suitable fuel for using gasoline type fuel in a compression ignition engine.

5. HCCI Multi-Zone, Multiple Injection Simulation

5.1. Introduction

To achieve the goal of reducing emission, while respecting limitations on – for example – the rate of pressure rise, in a diesel engine, particularly in PCCI mode, a useful tool to understand how various engine parameters affect the combustion processes in a compression ignition engine is computer simulation. At the level of advanced research, a body of literature exists based on time-dependent (either uRANS or LES), three dimensional simulations which solve the equations of continuity, momentum, energy and species incorporating models of varying complexity to describe diesel atomisation, evaporation and a description of the turbulence, chemical reaction and heat. The effort which is required (e.g. long computational time, the associated cost of running such a simulation and complexity of the required boundary conditions) is not only far beyond the scope of this thesis but also unnecessary if the goal is to provide understanding. An alternative body of research exists which developed largely in the context of HCCI research (Kraft, Maigaard et al. (2000)) based on a more manageable approach in terms of complexity and cost of computational time which provides much insight, albeit with the use of bold assumptions and strong approximations, called by various names including the 'multizone' approach. In the context of HCCI, initial studies by Najt and Foster (1983).

Easley, Agarwal et al. (2001) concluded that the HCCI combustion process is controlled solely by chemical kinetics and, if the charge is truly homogeneous, mixing is insignificant to the combustion process. The onus of calculation is thus placed primarily on providing an adequate description of the autoignition chemistry: this is, in itself, a research area in its own right and results in substantial computational requirement which nevertheless is feasible in the context of the aims of this thesis. Within the HCCI context, there is a variety of calculation methods ranging from consideration of a single homogeneous zone (Fiveland and Assanis (2000), Goldsborough and Van Blarigan (1999)) with heat loss, to that of Kraft, Maigaard et al. (2000) who use a single zone but can nevertheless account for in-cylinder temperature, fuel, and EGR distributions using

probability density functions as well as interaction between a core and the inevitable boundary layer, to the multi-zone model of Aceves, Flowers et al. (2000) which uses a multi-dimensional flow simulation, to calculate the pressure and temperature in the cylinder from intake valve closing to 20 CAD ATDC. The mass in the cylinder is then divided into ten bins (chosen for accuracy and computational time), each of which is designated a specified temperature (hottest in the core to coldest near the walls). As the mixture starts to burn, the computationally intensive multi-dimensional flow simulation is abandoned and the rest of the calculations are carried out using a one dimensional combustion code and a heat transfer correlation. Their computational investigations suggest that, for HCCI conditions, there is no flame propagation and that mixing during combustion does not influence the combustion process. All of these calculations predict cylinder pressure and burn durations well, but not HC and CO emissions.

Easley, Agarwal et al. (2001) developed a more detailed multi-zone model in an effort to explore the effects of temperature stratification, heat loss, and crevice volume on the combustion process and HC, CO, and NOx emissions. They divided the combustion chamber volume into four types of zones: crevice, boundary layer, inner core, and outer core. The inner core zones were considered to be adiabatic and constant mass, while the outer core, boundary layer, and crevice zones were allowed to exchange mass and energy. In this way, they were able to show that, at least in HCCI combustion, CO emissions primarily arise from fuel flowing out of the crevices and boundary layer during expansion and being partially oxidized. The authors note that the calculation is useful for “what- if” studies to investigate the effect of changes in in- cylinder conditions on combustion and emissions. It can highlight the sensitivity of ignition delay, burn duration, and emissions on stratification in mixture composition and temperature. Although it is not intended to be a "predictive" model of HCCI ignition and emissions, the simulation times are relatively short while still providing valuable information about HCCI ignition and combustion processes.

For this purpose, a FORTRAN code simulating HCCI multi-zone engine combustion with EGR previously written has been modified for the purpose of this thesis to include

multiple injections to better simulate diesel engine combustion. The aim is to simulate PCCI diesel type combustion provided that the fuel injection, fuel mechanism and the definition of zones are sufficiently well defined as an initial condition. This provides a useful tool to gain understanding of how the different variables, such as injection timing and various engine conditions, may affect combustion features of immediate practical importance, such as pressure rise rate and ignition timing.

There are certain features which are useful for simulation of combustion in an engine. EGR is a useful and important addition for engine simulation and relatively easy to implement. For HCCI application, even single zone models can form an adequate first approximation for an ideal homogeneous charge. Thus for example, single zone models such as those of Dec (2002) with 857 species and 3606 reactions of the Lawrence Livermore National Laboratory iso-octane capture some of the effects of fuel loading and EGR. Single zone models inevitably have shortcomings and some of these can be mitigated. For example Yasar, Soyhan et al. (2008) applied a double Wiebe function to reduce the fuel burn rate in a single zone model, performing better than a standard Wiebe function model in comparison to experimental data. Bunting, Eaton et al. (2008) used a single zone model to test pure components for surrogate fuel blend, applying a gasoline mechanism containing 1440 species and 6572 reactions.

For a more realistic simulation, a multizone model will more accurately represent the likely inhomogeneity of the fuel distribution and heat transfer. Furthermore a multizone model can be adapted to simulate CI combustion as well. Fiveland and Assanis (2002) included a quasi-dimensional model to model crevice and boundary layer in the simulation. Aceves, Flowers et al. (2005) presented a 40 zones model with 10 temperature zones, each with 4 equivalence ratio zones, determined by a fluid mechanics code. The chemical kinetics model has 179 species and found the result is sensitive to the timing of which the fluid mechanics code switched over to the chemical kinetics code. Bissoli, Cuoci et al. (2013) split the cylinder into 10 zones, CFD and a chemical kinetics mechanism with 430 species and 13500 reactions for n-heptane was used to analyse HCCI combustion.

Comparison of single zone model and multizone model has been reported. In Xu, Liu et al. (2005), the single zone is useful in so far as the rapid parametric study but unable to replicate test results in the case of multizone model.

The ability to include the function of fuel injection will extend the simulation to direct injection engines such as PCCI combustion. Kozarac, Sjeric et al. (2010) implemented a fuel injection feature into the multizone model and also included heat and mass transfer between zones. But for more accurate diesel combustion simulation, a multizone model has been developed for CI engine combustion which includes models for spray, fuel evaporation, entrainment as presented in Poetsch, Ofner et al. (2011). Within the confines of an inhomogeneous multizone representation of PCCI combustion, it is important to represent the autoignition through the choice of an appropriately detailed mechanism of the chemical kinetics. This aspect is thus described next.

5.2. Chemical Kinetics Mechanisms

An important component of the computer program, described below, is its reliance on chemical kinetics calculation so the autoignition of fuel can be accurately modelled under the changing pressure and temperature inside the combustion chamber. Two chemical kinetics mechanisms were used and compared for this investigation: Curran, Gaffuri et al. (1998) provided a detailed mechanism for n-heptane with 550 species and 2450 reactions and Liu (2004) provided a skeletal scheme for n-heptane 44 species. These two were used for this study. Other mechanism such as Ra and Reitz (2008) provided a reduced chemical kinetic mechanism for primary reference fuel n-heptane and iso-octane designed for use in engine combustion simulation. And one of the latest available from the Lawrence Livermore National Laboratory, based on the Mehl, Pitz et al. (2011) mechanism is a detailed n-Heptane mechanism, version 3.1, available on the Lawrence Livermore National Laboratory website. These later mechanisms came after some of this work was done and hence was not incorporated in this work.

The Curran, Gaffuri et al. (1998) mechanism studied n-heptane oxidation through investigating ignition delay and species composition data. The full list of 2450 reactions

is not reproduced here but the main classes of elementary reactions can be summarised as follows:

1. Unimolecular fuel decomposition
2. H-atom abstraction from the fuel
3. Alkyl radical decomposition
4. Alkyl radical + O_2 to produce olefin + $HO^{\cdot}_2$ directly
5. Alkyl radical isomerization
6. Abstraction reactions from olefin by $O^{\cdot}H$, $H^{\cdot}$, $O^{\cdot}$, and $C^{\cdot}H_3$
7. Addition of radical species to olefin
8. Alkenyl radical decomposition
9. Olefin decomposition
10. Addition of alkyl radicals to O_2
11. $R^{\cdot} + R'O^{\cdot}_2 = RO^{\cdot} + R'O^{\cdot}$
12. Alkyl peroxy radical isomerization ($RO^{\cdot}_2 \leftrightarrow Q^{\cdot}OOH$)
13. $RO^{\cdot}_2 + HO^{\cdot}_2 = RO_2H + O_2$
14. $RO^{\cdot}_2 + H_2O_2 = RO_2H + HO^{\cdot}_2$
15. $RO^{\cdot}_2 + CH_3O^{\cdot}_2 = RO^{\cdot} + CH_3O^{\cdot} + O_2$
16. $RO^{\cdot}_2 + R'O^{\cdot}_2 = RO^{\cdot} + R'O^{\cdot} + O_2$
17. $RO_2H = RO^{\cdot} + O^{\cdot}H$
18. $RO^{\cdot}$ decomposition
19. $Q^{\cdot}OOH = QO + O^{\cdot}H$ (cyclic ether formation via cyclization of diradical)
20. $Q^{\cdot}OOH$ = olefin + $HO^{\cdot}_2$ (radical site b to OOH group)
21. $Q^{\cdot}OOH$ = olefin + carbonyl + $O^{\cdot}H$ (radical site g to OOH group)
22. Addition of $Q^{\cdot}OOH$ to O_2
23. Isomerization of $O^{\cdot}_2QOOH$ and formation of ketohydroperoxide and $O^{\cdot}H$
24. Decomposition of ketohydroperoxide to form oxygenated radical species and $O^{\cdot}H$
25. Cyclic ether reactions with $O^{\cdot}H$ and $HO^{\cdot}_2$

The mechanism of Liu (2004) is a much reduced and the 18 steps mechanism is set out in Figure 5-1. This mechanism was developed for investigating the effect of steady strain

on the transient autoignition. The much reduced mechanism is beneficial for developing and testing the functioning of the programme and for comparing engine variables because of its short running time. A typical run may take the shorter mechanism 1 minute whereas it takes the longer mechanism 20 minutes. The shorter mechanism was not applied in previous versions of this program.

No.	Reactions
I	$n\text{-}C_7H_{16} = C_3H_6 + 2C_2H_4 + H_2$
II	$n\text{-}C_7H_{16} + O_2 + OH = RO_2 + H_2O$
III	$RO_2 + O_2 = OR''O_2H + OH$
IV	$OR''O_2H = 2C_2H_4 + CH_2O + CH_3 + CO + OH$
V	$1\text{-}C_6H_{12} + H_2O = C_3H_6 + C_3H_4 + H_2O$
VI	$1\text{-}C_4H_8 + OH = C_2H_4 + CH_3 + CH_2O$
VII	$C_3H_6 + H_2O = C_2H_4 + CH_2O + H_2$
VIII	$C_3H_4 + H_2O = C_2H_4 + CO + H_2$
IX	$C_2H_4 = C_2H_2 + H_2$
X	$C_2H_2 + O_2 = 2CO + H_2$
XI	$CH_4 + H = CH_3 + H_2$
XII	$CH_3 + OH = CH_2O + H_2$
XIII	$CH_2O = CO + H_2$
XIV	$2HO_2 = H_2O_2 + O_2$
XV	$H_2O_2 = 2OH$
XVI	$CO + H_2O = CO_2 + H_2$
XVII	$O_2 + H_2 = 2OH$
XVIII	$2H = H_2$

Figure 5-1: Reduced 18 steps mechanism for n-heptane from Liu (2004)

5.3. Program Description

The FORTRAN computer program calculates the pressure, temperature, species and heat release change in an engine with the included function of heat losses, EGR, multi-zone and multiple injections. First written by Nondas Mastorakos (Mastorakos (2003)), it modelled single zone HCCI engine where fuel was introduced from the start of the cycle combined with calculation of heat loss and homogeneously introduced EGR. This was then further modified by Denis Bosshardt (Bosshardt (2004)) where it was converted into a multizone code but still based on a fuel being introduced homogeneously into the cylinder from the beginning of the cycle. Because both references are not readily available in the open literature, a description of the operation of these codes is reproduced below.

For this thesis, the code was modified again so multiple injections of fuel could be simulated. The code was written so that any amount of fuel can be specified to be introduced into any zone at any CAD. This gives the flexibility to attempt to simulate condition that is closer to PCCI diesel combustion.

5.3.1. Governing Equations

The form of the governing equations is as follows (Mastorakos (2003)), together with an outline of the method of solution.

We assume that during the compression and expansion strokes the mass inside the cylinder does not change. Then, the governing equations for the species mass fractions Yi and the first law of thermodynamics applied to the control volume enclosing the combustion chamber are shown below.

For the species concentration calculation, equation (5-1) gives the change in mass fraction Y_i and ρ is the density in kg/m^3, $\dot{w}_i$ is the chemical production rate and i is the species designation set out in the program.

$$\rho \cdot \frac{dY_i}{dt} = \dot{w}_i \tag{5-1}$$

The change in temperature $\frac{dT}{dt}$ is calculated using equation (5-2) where c_v is the specific heat, h_i is the absolute specific enthalpy of the species i, R is the gas constant, T is the temperature of the whole volume, M_i is the molecular weight, p is the cylinder pressure, A is the area for heat transfer and T_{wall} is the wall temperature of the cylinder.

$$\rho \cdot c_v \cdot \frac{dT}{dt} = -\sum_{i=1}^{N} \left(h_i - \frac{R \cdot T}{M_i} \right) \cdot \dot{w}_i - \frac{p}{V} \cdot \frac{dV}{dt} - h \cdot \frac{A}{V} \cdot (T - T_{wall}) \tag{5-2}$$

The heat release from each zone, calculated using equation (5-3) through CHEMKIN, uses the chemical production rate $\dot{\omega}_i$ in mole/(cm^{3}s), the molecular weight W_i in g/mole and the specific enthalpy h_i in ergs/g of the species i. The heat release from each zone is then added together to find the total heat release from all the zones.

$$\frac{dQ}{dt} = \sum_{i=1}^{i} h_i \dot{\omega}_i W_i \tag{5-3}$$

The heat loss term was taken from Blair (1999). This calculates the surface to volume ratio of the whole cylinder. The heat transfer coefficient h is given by equation (5-4) where λ_{cond} is the conductivity of the mixture, Nu is the Nusselt Number and Re is the Reynolds number given in equation (5-5) where μ is the viscosity of the mixture.

$$\frac{h \cdot B}{\lambda_{cond}} = Nu = 0.49 \cdot \mathrm{Re}^{0.7} \tag{5-4}$$

$$\mathrm{Re} = \frac{2 \cdot \rho \cdot S \cdot B \cdot N}{60 \cdot \mu} \tag{5-5}$$

The volume change, $\frac{dV}{dt}$, is given by equation (5-6) where B is the bore in m, N is engine speed in rpm, S is the stroke in m, θ is the crank angle and l is the conrod length in m.

$$\frac{dV}{dt} = \left(\frac{\pi \cdot B^2}{4} \cdot \frac{2 \cdot \pi \cdot N}{60} \cdot \frac{S}{2} \cdot \sin(\theta) \right) \cdot \left(1 + \frac{\frac{S}{2} \cdot \cos(\theta)}{\sqrt{l^2 - \left(\frac{S}{2}\right)^2 \cdot \sin^2(\theta)}} \right) \tag{5-6}$$

The final differential equation is given in equation (5-7) which assumes constant pressure operation. Bosshardt notes that "...During the calculation, the pressure is assumed to be constant. However, after each step, the ideal gas law is applied to determine the new pressure...". Bosshardt also provide the following flowchart for Mastorakos' single zone calculation procedure show in Figure 5-2.

$$\frac{dp}{dt} = 0 \tag{5-7}$$

“The governing equations are integrated with LSODE (a stiff solver) and the software calls CHEMKIN subroutines, which read the detailed mechanism in an appropriate format: the LSODE and CHEMKIN-II packages are in the public domain.” (Mastorakos (2003)).

“For runs without EGR, the user enters the engine parameters, initial temperature and pressure, and equivalence ratio. The code then gives the time evolution of all species, temperature and pressure as a function of CAD (Crank Angle Degree, taken as −180o at BDC) for one cycle.” (Mastorakos (2003)).

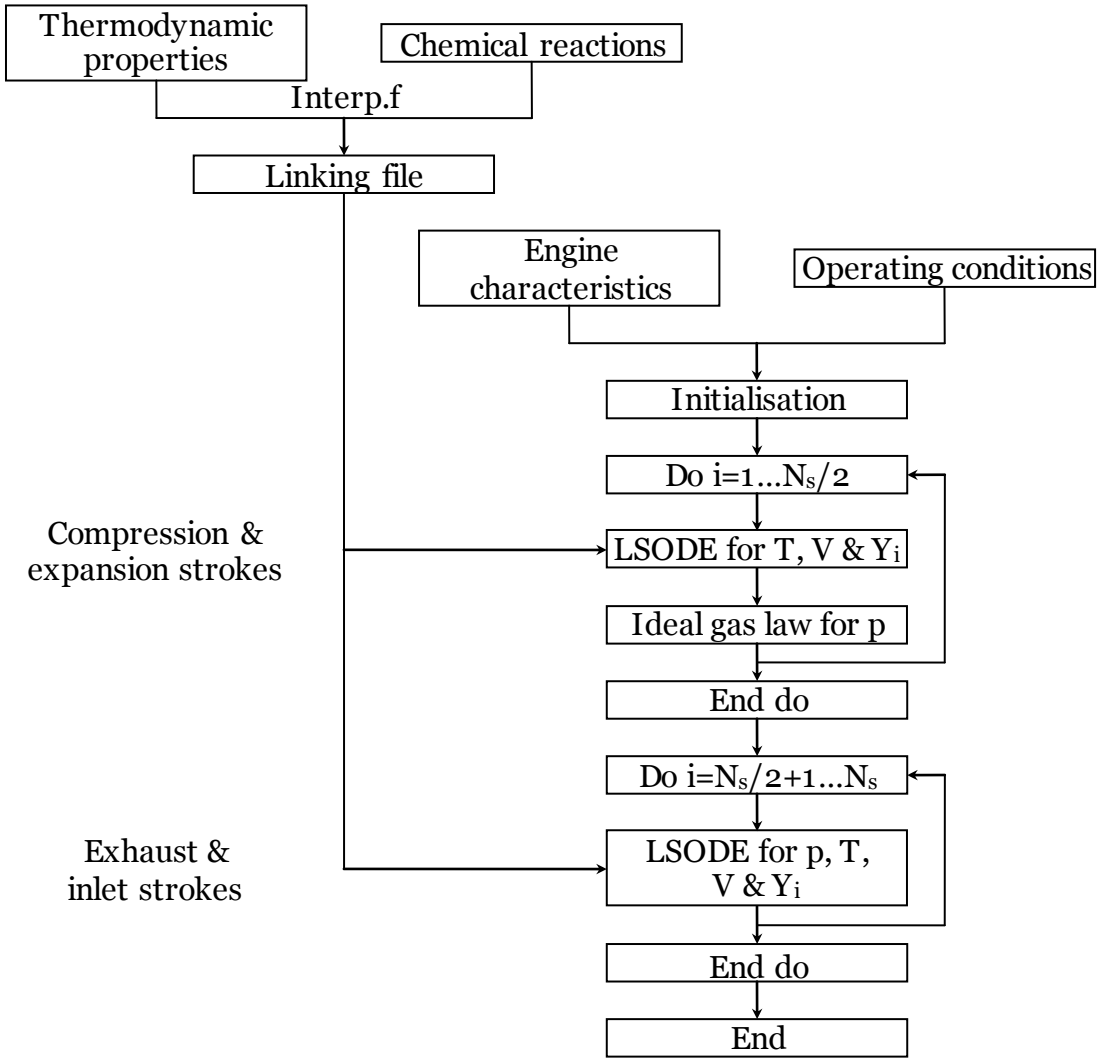

Figure 5-2: Flow diagram of the functioning of the computer program.

“For runs with EGR, the code continues for another cycle, but at constant pressure equal to the ambient. This simulates approximately the evolution of the combustion products assuming that the product gases exposed to the ambient pressure for all the time until the compression stroke begins. In this way, the chemical evolution of the products is taken into account. The resulting gas after this cycle is mixed at a given proportion with the fresh mixture. The temperature of the hot products before

mixing is taken as 900 K, which gives reasonable values of the initial temperature with EGR. Note that this is engine-dependent: in the future, to make accurate runs with EGR, we need to measure this temperature and introduce it to the code such that before the compression stroke, the gases in the cylinder have the correct temperature...." (Mastorakos (2003)).

5.3.2. Input Variables and Initial Subroutine

The main program includes three input variable files. “Detailed.com” contains all the variables declaration and setting out all constants such as gas constant and the number of species for which solution is required. And importantly, it also includes the user input number of zones and injections for the calculation and changes to this will have to be made before the file is compiled. "Species.com" declares all the species within the calculation and assigns the major species such as O_2, CO_2 with their respective species number readable in the program. It also assigns the variable number for temperature, volume and pressure. "Chemkin.com" declares the variables for CHEMKIN for its calculation. The main program contains its own variable declaration.

The first step of the main program is to call the sub routine "Initial" which first calls the three input variable files and the CHEMKIN initialisation subroutine, "Readchk.f", which checks for errors and starts CHEMKIN. The engine and operation variables are read from the file "inparam.dat" which contains the following information:

1. Size of each zone as a volume fraction
2. Initial temperature of the zone in K
3. Heat loss mechanism of the zone (0=no loss, 1=heat loss)
4. Zone in which fuel is injected
5. Fuel injection timing where TDC=0
6. Amount of fuel injected in kg
7. Heat transfer coefficient
8. Mass fraction of EGR in initial mixture
9. Initial press in Pa
10. Final temperature of EGR to be mixed with air in K
11. RPM

12. Bore in m
13. Stroke in m
14. Connecting rod length in m
15. Compression ratio
16. Cylinder wall temperature in K
17. Fuel type (0 for motored, 1 of heptane, 2 for octane)

Inputs 1-3 can be repeated for the desired number of zones and inputs 4-6 can be repeated for the desired number of injections. These are then initialised in the program and calculations such as engine dimension are made here. EGR, if used, is read from “egr.pre” file where species and concentrations are in a file prepared by using the output from the species end products from a previous combustion cycle. The subroutine “initcond” is called which mixes fresh air with EGR species and the respective mass and mean species mass fractions, temperature in cylinder and for each zone is calculated. “initial” then carries on with calculating the fuel mass in the cylinder.

5.3.3. Main Computer Program

Back to the main program, the parameters for the solver LSODE is called, setting out the tolerances for solutions. LSODE is the Livermore Solver for Ordinary Differential Equations (LSODE) provides numerical solution to initial value problem for a system of first-order ordinary differential equations. Then the calculation loop begins for the combustion cycle and calculates for every time step specified, initialising the species mass fraction and rate of heat release. For the start of the compression and expansion strokes, the “fuelinjection” subroutine is called to check whether the time step correspond to a CAD which equals one which has been specified for fuel injection. Then fuel is injected by way of adding injection fuel mass into the specified engine zone and updating the mass fraction of each species with the new added mass of the fuel.

The subroutine “Compressioncal” is then called to perform the main calculation. The calculation for each zone is performed separately and the molecular weight is calculated first. Through another subroutine “derivs” and “LSODE”, density is found

by mass of gas in the zone, the volume and the pressure is found by the bulk gas temperature, density and gas constant. The concentration of each species is found from the mass fraction and each of the kinetic rates and time derivatives are calculated using CHEMKIN by calling the “dot” routine located in “cdot.f” and routines stored in “cklib.f” file.

The differential equations described in the governing equations above are set up with the changes in volume and in species concentration from the kinetic rates from CHEMKIN, and the change in temperature from the calculated heat release, change in volume and heat transfer. With all the differential equations, as shown above, LSODE is then called to solve all the differential equations.

The volume of the cylinder is calculated and the mean species mass fraction is updated. The mean temperature is calculated using the temperature in each zone and the contribution depends on the volume fraction of each zone. The density is calculated from the mass of the gas components and volume and the pressure is calculated as shown in equation (5-8) from the density, gas constant and the mean molecular weight, M_m.

$$p = \frac{\rho \cdot R \cdot T}{M_m} \tag{5-8}$$

For the exhaust and intake stroke, LSODE is once again called from the main program, this time through another subroutine “derivsEGR”. The only difference is that the density is calculated using the quasi constant pressure, temperature, gas constant and mean molecular weight. Otherwise, it is the same as “derivs”.

Finally, the results of species concentration throughout the cycle, the temperature, pressure, volume and heat release are saved to different files. The maximum OH and maximum dT/dt is used as the ignition time and displayed on the command screen.

5.4. Program Validation

The engine conditions have been set out in Table 5-1 which replicate the condition for the Hydra engine at Imperial. In order to verify the basic programming for the newly

modified and added features of the program, a few simple tests were performed to test the program.

Engine stroke	90.55 mm
Engine Bore	93.62 mm
Con rod length	154 mm
Compression ratio	11.5

Table 5-1: Engine dimension used for computer program.

The first test was to check whether the fuel injection occurs as intended and this was checked by looking at the output files of the fuel used which in this case was n-Heptane (C_7H_{16}). The result shows the amount of fuel increases to the desired amount at the correct timing and the program performed as intended.

Next was to verify whether the increase in number of zones changed the result. Tests showed that for the same amount of fuel injected at the same CAD for single zone and multizone (equivalent amount of fuel in all zones) produced the same result. This assured the division into larger number of zones with the same parameters and fuel quantity did not change the way the program performed.

Finally, an even more basic 2 zones test to debug the program was to inject fuel into zone 1 and none in zone 2, then reverse this to inject the same amount of fuel into zone 2 and none in zone 1. This again provided the same result which verifies the program is working properly.

5.5. Chemical Kinetics Mechanisms Comparison

The two chemical kinetics mechanisms by Curran, Gaffuri et al. (1998) (550 species and 2450 reactions) and Liu (2004) (44 species) took vastly different processing time for the same conditions. A typical run time for Liu (2004) was usually 15-30 seconds but the Curran, Gaffuri et al. (1998) processing time can range from 20 minutes to a few hours for one engine cycle. This processing naturally increased if many consecutive cycles were calculated so that EGR can be simulated. There was a clear advantage in using the shorter mechanism in terms of time, especially for programme debugging and parametric studies.

A few tests between the two mechanisms were performed, firstly in stratified HCCI mode where the fuel/air ratio was adjusted to the condition in a total of two zones, as set out in Table 5-2 and the corresponding pressure trace is shown in Figure 5-3. It can be seen the two mechanisms predicted similar trends with Liu's mechanism showing a higher pressure compared to that of Curran, Gaffuri et al. (1998)'s. The ignition timings were, however, almost the same with the differences related to the magnitude of the heat release.

	Size in volume fraction	Phi
Zone 1	0.5	0.1
Zone 2	0.5	0.4

Table 5-2: Condition for mechanism comparison with two zones in HCCI mode with different air/fuel ratio.

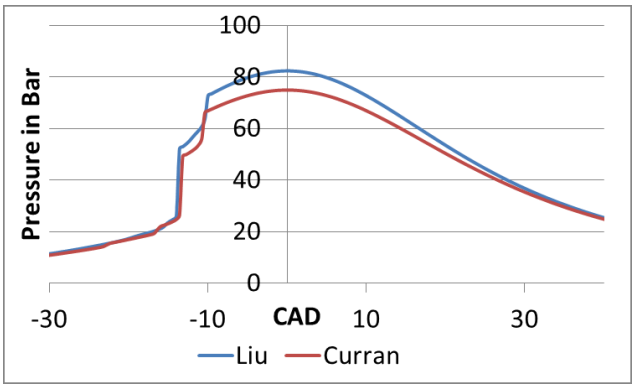

Figure 5-3: Comparison between pressure traces resulting from the use of mechanisms of Curran, Gaffuri et al. (1998) and Liu (2004) using two zones in HCCI mode with different air/fuel ratio.

The second test was closer to a quasi-PCCI condition to consider two injections test, a total of four into two zones, simulating penetrating injection with the condition set out in Table 5-3 and the resulting pressure trace is shown in Figure 5-4. It shows the initial heat release occurred in both mechanisms and with a second heat release for Liu (2004) but not in Curran, Gaffuri et al. (1998). Further investigation showed zone 2 on the Curran, Gaffuri et al. (1998) mechanism failed to ignite and lack the second heat release.

	Zone size as a volume fraction	First injection timing (CAD bTDC)	First injection quantity	Second injection timing (CAD bTDC)	Second injection quantity
Zone 1	0.5	-10	6mg	-5	12mg
Zone 2	0.5	-8	4mg	-3	8mg

Table 5-3: Conditions for the first example of mechanism comparison with two zones in fuel injection mode with double injection.

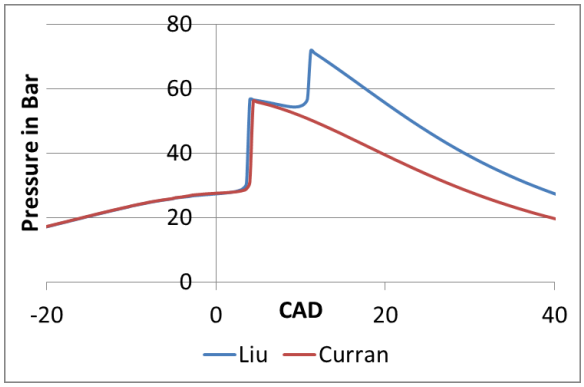

Figure 5-4: Pressure traces for the first example of mechanism comparison using two zones in fuel injection mode with double injection.

Another test is set out in Figure 5-5 corresponding to the conditions set out in Table 5-4 with delayed injection and increase in fuelling compared to the previous case. This time, both mechanisms only had a single heat release with the second zone being presumably either too lean, or the corresponding ignition delay time being too long, to ignite. However, there is a distinct ignition timing difference between the two mechanisms and which of these is the more accurate in predicting combustion would need extensive further investigation and comparison with appropriate experimental data.

	Zone size as a volume fraction	First injection timing (CAD bTDC)	First injection quantity	Second injection timing (CAD bTDC)	Second injection quantity
Zone 1	0.5	-8	8mg	-1	16mg
Zone 2	0.5	-6	2mg	1	4mg

Table 5-4: Conditions for second example of mechanism comparison using two zones in fuel injection mode with double injection

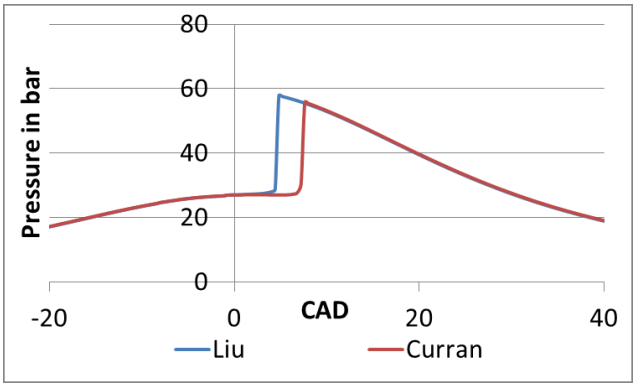

Figure 5-5: Pressure trace for second example of mechanism comparison with two zones in fuel injection mode with double injection.

5.5.1. Sensitivity Test for the Two Chemical Mechanism

This section reports sensitivity tests applied to the two chemical kinetics mechanisms to small changes to the input variables. The range of conditions is shown in Table 5-5 and the resulting pressure histories for both mechanisms are shown in Figure 5-6. Setting condition 1 as the base condition, the fuelling amount was increased in condition 2 for both the first and second injections in both zones 1 and 2 by 1 mg of fuel and the injection timing was advanced by 1 CAD, also for both injection and for both zones for condition 3.

		Zone size as a volume fraction	First injection timing (CAD bTDC)	First injection quantity	Second injection timing (CAD bTDC)	Second injection quantity
Condition 1	Zone 1	0.5	-10	6mg	-5	12mg
	Zone 2	0.5	-8	4mg	-3	8mg
Condition 2	Zone 1	0.5	-10	7mg	-5	13mg
	Zone 2	0.5	-8	5mg	-3	9mg
Condition 3	Zone 1	0.5	-11	6mg	-6	12mg
	Zone 2	0.5	-7	4mg	-4	8mg

Table 5-5: Conditions for sensitivity test for the two reaction mechanisms.

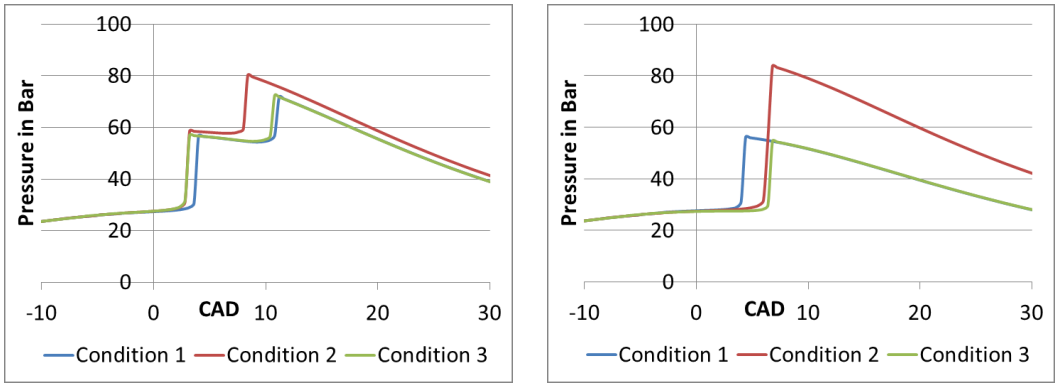

Figure 5-6: Sensitivity testing : pressure for the three conditions of Table 5-5 from Liu (2004) plotted on the left and those from Curran, Gaffuri et al. (1998) on the right.

It can be seen that for the mechanism of Liu (2004), the presence of the two distinct ignition events is present for all three conditions. The increase in fuelling, condition 2, produces a higher peak pressure, as is to be expected, and an earlier second ignition event in zone 2 which is again to be expected due to the higher pressure and temperature reached in the combustion chamber as a whole after the first ignition event. Advancing injection timing, condition 3, shows earlier ignition and pressure rise as expected.

For Curran, Gaffuri et al. (1998), all three conditions result in only a single heat release with condition 2 showing a larger and later pressure rise and heat release compared to condition 1. Further investigation of the heat release showed that for condition 2, zone 2 ignited simultaneously with zone 1 which hence resulted in the larger heat release, whereas zone 2 did not ignite for either condition 1 or 3. For the earlier injection timing case of condition 3, as compared to condition 1, it produces an opposite result from the earlier injection and earlier combustion than in the case of the mechanism of Liu (2004). Quite why this unexpected result comes about is not clear at the time of writing, although some contributory factors may be related to the findings presented in the next section.

5.6. Simulation Results

It is interesting to relate the ignition delay with variables such as the injection timing and intake temperature, compression ratio and air/fuel ratio in HCCI mode. Firstly, the

ignition delay as a function of injection timing can be tested by using the mechanism of Liu (2004) and the engine condition set out in Table 5-6. This test was carried out using the arbitrarily selected common input of an initial intake temperature of the 550K, single zone model, injecting 5mg of fuel at various injection timing without heat transfer and an elevated intake pressure of 2 bar at BDC.

Engine stroke	81.5 mm
Engine Bore	75.0 mm
Con rod length	138 mm
Compression ratio	12
Engine Speed	1500 rpm

Table 5-6: Engine condition for testing ignition delay.

The result of ignition delay as a function of injection timing, ranging from -60CAD to 0CAD is shown in Figure 5-7. The ignition delay here is expressed as an absolute time and it can be related to CAD at 1500rpm by equating 0.018s to 45CAD. It can be seen that ignition delay decrease as the injection timing is retarded which is to be expected as fuel is injected later at a time when cylinder temperature is elevated and hence more suitable for promoting ignition. This further verifies the fuel injection part of the program functions, at least qualitatively, as it should.

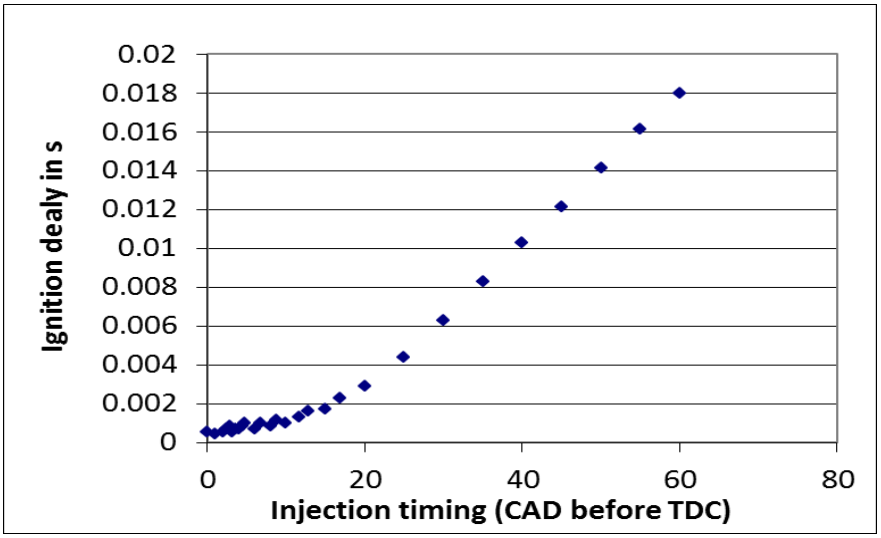

Figure 5-7: Effect of injection timing and ignition delay.

The second simulation, using the mechanism of Liu (2004), investigates the ignition delay which is the time between BDC and ignition and as a function of intake

temperature. Various air fuel ratios ranging from 0.2 to 0.4 and compression ratio ranging from 7 to 15 have been investigated to compare the effects and these are shown in Figure 5-8. The result shows the expected decrease in ignition delay for increased intake temperature, air/fuel ratio and compression ratio. There is also some evidence if not of a negative temperature coefficient, then at least of some reduction in the rate-of-decrease of the ignition time with the 1/T independent variable. This provides some further evidence, if not of correctness of the computer program, then at least that it produces results which are qualitatively as expected with ignition delay times which are broadly as expected (recall that 0.045s correspond to 45 CAD at 1500 rpm).

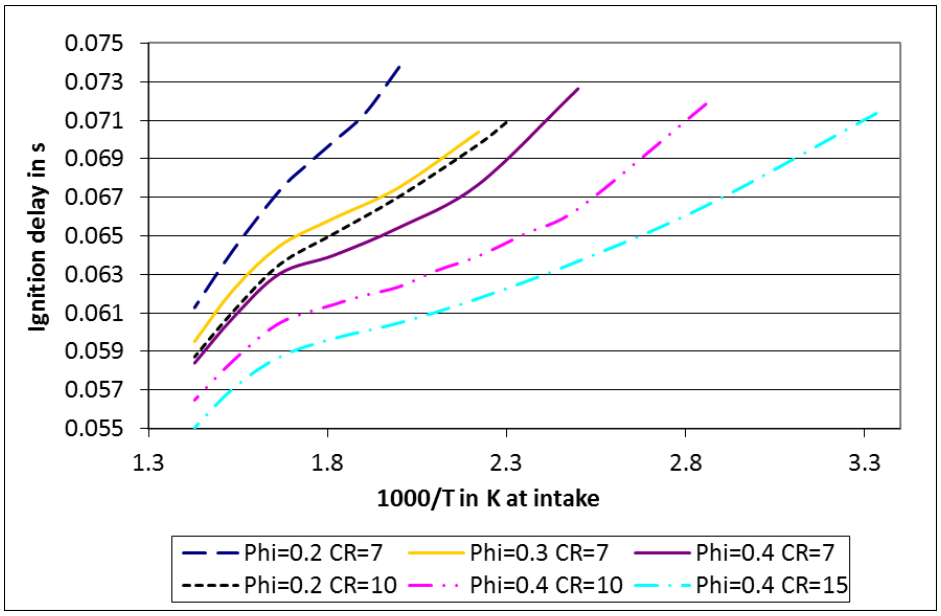

Figure 5-8: Effect of intake temperature variation on ignition delay (time from BDC to ignition) at various air/fuel ratio and compression ratio.

5.7. Engine Condition Simulation

An attempt is presented here to link the prediction of the computer program to some experimental result. A series of numerical experiments were carried out, starting with a three zones representation of the combustion chamber varying the sizes of the zones. The fuel distributions and the injection timings chosen were a simplified attempt to replicate the propagation of the evaporating liquid fuel jet through the combustion

chamber from one zone through to another at a later time. The experimental pressure trace was acquired using the Hydra engine under the conditions set out in Table 5-7.

Variable	Value
Engine Speed	1200 rpm
Intake Air Temperature	70 ˚C
Injection Pressure	30 MPa
Pilot Injection Timing	-10 CAD
Pilot Injection Quantity	5 mg
Main injection Timing	-3.5 CAD
Main Injection Quantity	6 mg

Table 5-7: Experiment condition to be matched for the computer simulation.

The heat release rate, which is calculated as J/m^3s by the program, is plotted here in the graphs to an arbitrary scale (because a large part of the heat release occurs as a quasi-Dirac-delta-like function and it is not possible to show both the computational and the experimental heat release curves to a common scale). After some 20 numerical experiments, it was found that using the condition set out in Table 5-8 produced the closest match, primarily in terms of the timing of the peak of the heat release rate and in the peak pressure rather than in terms of its duration, when using the Liu (2004) mechanism shown in Figure 5-9. The Liu (2004) mechanism was used because of its short processing time and this gave similar results to the experiment for ignition timing and parts of the pressure rise rate. The peak pressure is comparatively well predicted, which provides further confidence that the (despite the strongly impulsive nature of the rate of heat release) energy released by the fuel is, at least qualitatively, correctly calculated. The injection timings between simulation and the experiment could not be made to match and also it was difficult to simulate the effect of multiple injections, present in the experiment. The difficulty in objectively and rationally determining the number of zones and the size of the zones also made setting up the conditions difficult. The difficulty stems not only from the presence of conventional, rather than PCCI, combustion but also from the lack of adequate experimental data about the distribution of fuel vapour.

	Zone size	Fuel injected	Injection timing
zone 1	0.5	6 mg	-15
zone 2	0.25	6 mg	-14
zone 3	0.25	0 mg	-13

Table 5-8: Conditions for three zones simulation of injection progression.

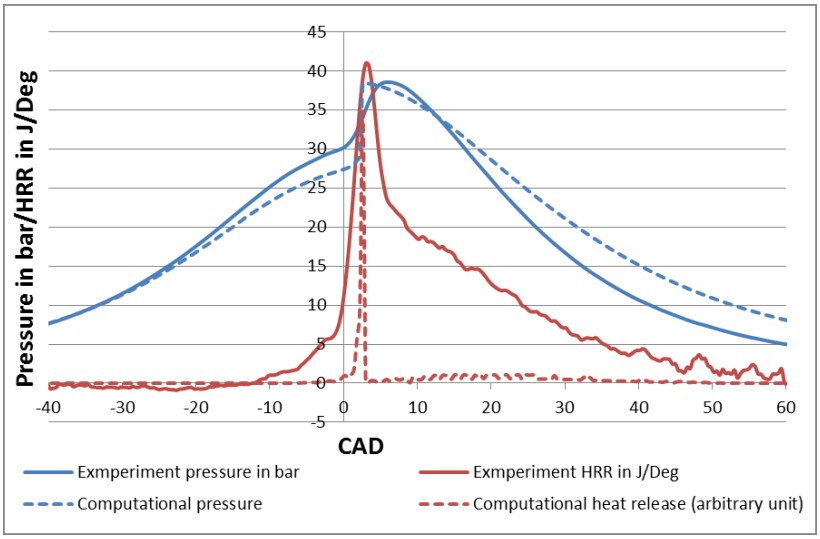

Figure 5-9: Pressure and heat release comparison between the experimental result and an outcome of a three zones combustion simulation using chemical kinetics mechanism from Liu (2004).

The difference is fundamentally due to the computations representing autoignition whereas the combustion in the engine proceeds through a non-premixed flame. This is thus a challenge for the simulation in order to replicate the effect of non-premixed combustion. In reality, the shortcoming is arguably equally that of the current arrangement of the engine, which cannot burn fuel in a PCCI mode, largely because of the inability, as set up in this thesis, to introduce EGR. It is worth recalling that a part, and probably a substantial fraction, of the fuel burns through "… multiple, sequential autoignition with local flames around the autoignition centres. The equivalence ratio is two or lower everywhere combustion takes place to avoid soot formation. This would be the ideal form of combustion and the mixture formation strategy (injector/combustion chamber design, injection pressure and injection strategy, in-cylinder pressure and temperature, flow and fuel volatility...) should aim to achieve this along with the most effective use of the available oxygen..." (Kalghatgi (2015)). It is well known that the rate of pressure rise associated with the autoignition can result in noise which, as the extent

of premixing is increased to further reduce soot emissions, results in unacceptable levels of noise. Being able to assess the rate of pressure rise with the extent, and type, of premixing is one of the objectives of the use of the computer program.

The same condition was used in the Curran, Gaffuri et al. (1998) mechanism, for comparison, and the result can be seen in Figure 5-10. There is a substantial retard, relative to the Liu (2004) mechanism, in the occurrence of the peak rate of heat release for this mechanism although the *shape* of the heat release , at least at the scale necessary for the presentation of both experimental and computational results, but not the pressure trace, is similar to the case in Liu. Somewhat surprisingly, perhaps, the peak pressure is nevertheless once again relatively well predicted (even though its occurrence in time is not). The shape of the heat release profile has detailed differences in the heat release but once again the simulation was unable to replicate the non-premixed flame in the experiment.

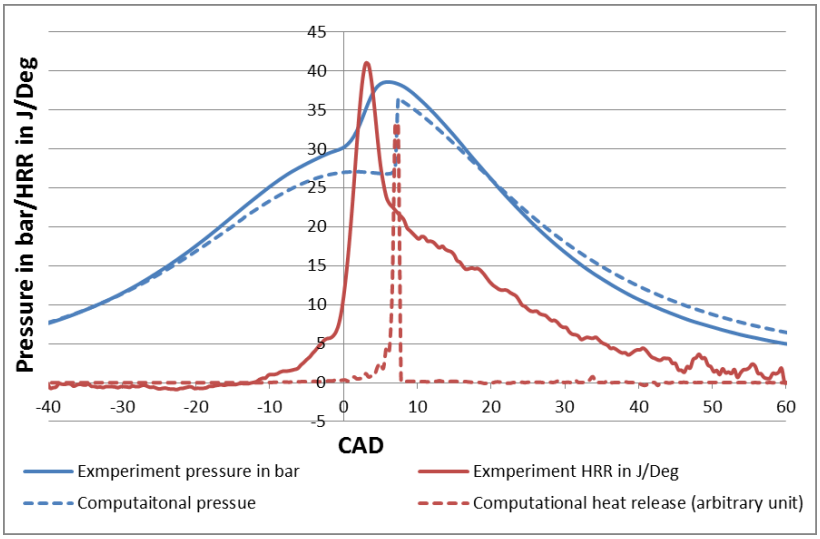

Figure 5-10: Pressure and heat release comparison between the experimental result and an outcome of a three zones combustion simulation using chemical kinetics mechanism from Curran, Gaffuri et al. (1998).

A further test was performed utilising a calculation based on 4 zones with one zone without fuel set out in Table 5-9. The complexity in the specification of the variables in the calculation due to an additional zone increases due to the increase in the number of combinations of permutations in the choice of zone sizes, injected fuel amount and

timing. Again, the Liu (2004) mechanism was used initially and 12 iterations were carried out to produce the pressure and heat release rate shown in Figure 5-11. There are now two separate, identifiable peaks in the heat release rate in this case as two zones ignited at different times, showing that increasing the number of smaller zones can produce multiple ignitions distributed over time and hence, in this sense, better able to replicate the heat release rate corresponding to the non-premixed flame. But it can also be seen that the predicted, the heat releases remain 'impulsive' rates and not continuous as in the case of a non-premixed flame. The peak of pressure is relatively well predicted but the rate of pressure rise is poorly represented. The number of zones and the fuel quantity will be needed to be adjusted and finer tuning is required.

	Zone size	Fuel injected	Injection timing
zone 1	0.4	5 mg	-21
zone 2	0.2	3 mg	-20
zone 3	0.2	2 mg	-19
zone 4	0.2	0	0

Table 5-9: Conditions for a four zones simulation of injection progression.

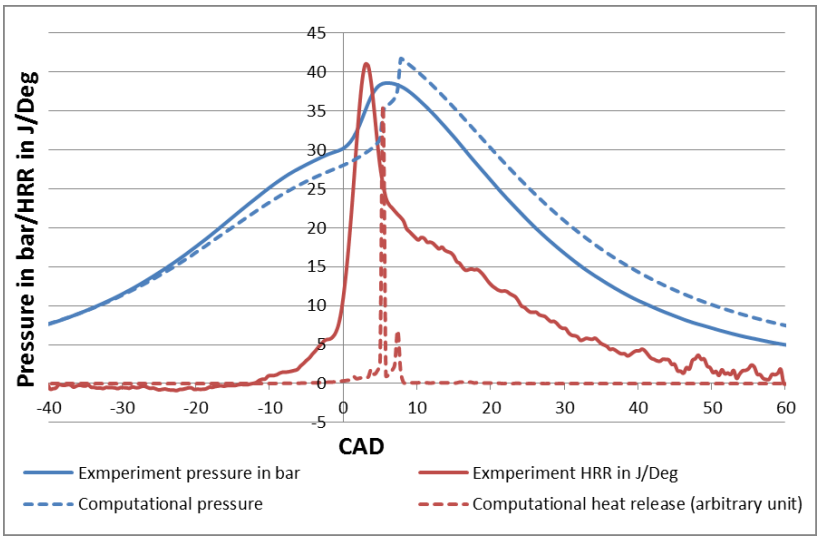

Figure 5-11: Pressure and heat release comparison between the experimental result and an outcome of a four zones combustion simulation using chemical kinetics mechanism from Liu (2004).

The same condition in Table 5-9 was applied using the Curran, Gaffuri et al. (1998) mechanism, shown in Figure 5-12, and although two peaks in the heat release remain,

the timing is far advanced relative to the case predicted using the mechanism of Liu (2004). The temporal development of pressure is very poorly predicted.

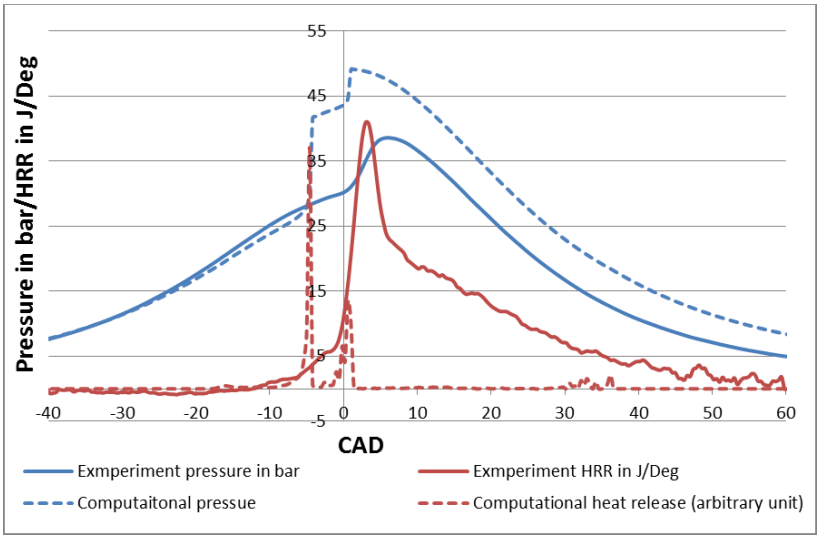

Figure 5-12: Pressure and heat release comparison between the experimental result and an outcome of a four zones combustion simulation using chemical kinetics mechanism from Curran, Gaffuri et al. (1998).

5.8. Increasing the Number of Zones and Injections

In the tests above, the small number of zones and injections show, that even with the same quantity of fuel injected as in the experiment, the entire fuel content in each zone burns more or less impulsively. The calculation is unable to replicate the observed heat release which in fact takes place continuously over a long period of time. This defect can be remedied by increasing both the number of zones and injections used in the computer program. As an example, 30 injections were made into 30 different zones with an interval of 1CAD per injection. The conditions are set out in Table 5-10.

	Zone Volume Fraction	Fuel injected	Injection timing
zone 1	0.043	0.05 mg	-30
zone 2-30	0.033	0.05 mg	At every CAD, ending with 0CAD in Zone 30 (-29CAD in zone 2, -28CAD in zone 3, etc)

Table 5-10: Conditions for a 30 zones with 30 injections simulation.

The results of this test can be seen in Figure 5-13 using the chemical kinetics mechanism from Liu (2004) and Figure 5-14 using the chemical kinetics mechanism from Curran, Gaffuri et al. (1998). The figures show the heat release rate being spread out through time as fuel from different zones undergoes combustion at different time. With further refinement and modelling of the fuel distribution in the zones, a more representative heat release rate can be produced to simulate the real combustion condition.

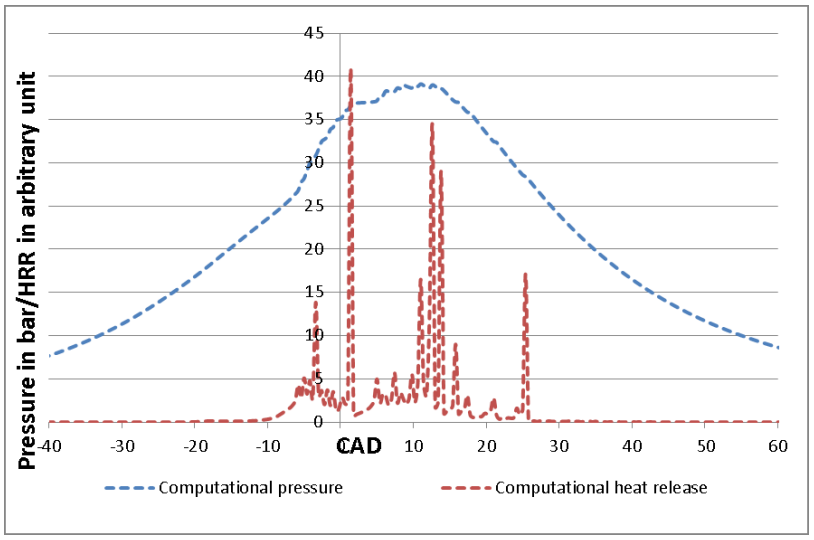

Figure 5-13: 30 zones with 30 injections test using chemical kinetics mechanism from Liu (2004).

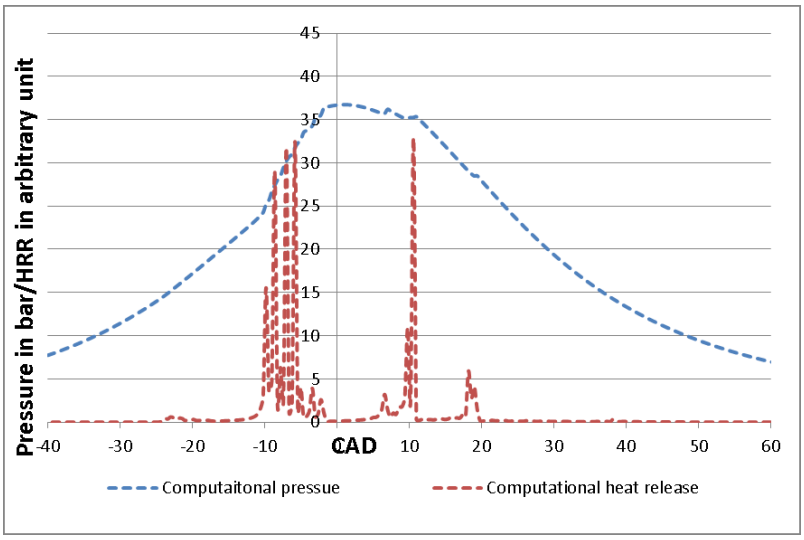

Figure 5-14: 30 zones with 30 injections test using chemical kinetics mechanism from Curran, Gaffuri et al. (1998).

5.9. Chapter Conclusion

This chapter shows the work in modifying a FORTRAN code, written for multizone HCCI simulation using CHEMKIN, to include fuel injection so as to be able to represent the

conditions particularly in PCCI combustion. The fundamental functioning of the program has been demonstrated to remain as it was originally designed and the added feature of the fuel injection shows that it performed as desired. Two chemical kinetics mechanisms were compared. Tests were carried out to look at the effects of injection timing and intake temperature on ignition timing. Nevertheless, attempts were made to replicate the pressure from experimental data and demonstrate the limitations and challenges posed for engine simulation using the computer program. The flexibility of the multizone calculation provides, as intended, the advantage of great flexibility in the volume fraction and fuelling in each zone. The disadvantage is that there is a need for a rational and objective means for assigning the fuelling level to each zone. In principle, such information can be provided by experiment or by a 3D CFD calculation. In the absence of such information, a choice must be made by guesswork. The preliminary results of this chapter suggest that a small number of zones result in inadequate representation of the combustion. A test using a 30 zones model with 30 injections demonstrates that, as might be expected, this larger number of zones with a corresponding distribution of bigger spread of fuel notionally corresponding to an extended duration of injection (as well as to non-premixed combustion) results in a heat release rate which can extend to- albeit through a series of impulses - real heat release rates observed in experiments.

More work is certainly required on the development of the computer program to further verify the functioning of the program and changes should be made to functions such as outputting the heat release rate to J/Deg, instead of the current arbitrary units. It is certainly desirable to compare the results against "true" PCCI experiments. However, there are other concerns of a fundamental nature, beyond the need for a rational method to distribute the fuelling amongst the zones. It is not clear why the chemical kinetics mechanisms should produce such different results relative to each other (let alone against experiment). Other mechanisms can, and should, be employed to compare the performance, both in terms of speed and accuracy. Further investigation is required into the division of zone sizes, fuel distribution for larger number of zones and injections if this is to be used for diesel engine simulation. As it stands, the program forms a good base for the understanding of the analytical description of combustion which is based on

autoignition. The goal is for it to perform parametric studies of engine conditions and injection strategies and used in parallel with the engine testing work.

6. Engine Testing and Combustion Analysis

6.1. Introduction

Chapter 3 described the hardware setup, instrumentation and optical setup of the Hydra optical engine. The hardware was used to perform a series of experiments for basic engine combustion analysis as a capability test for the recently modified engine with newly installed equipment. This also provided useful experience in running the engine. Then a series of engine test points were chosen to investigate their effect on combustion and performance. And using the result of this analysis, the test points for high speed imaging work were selected. The fuel used in this entire investigation was retail diesel fuel.

6.2. Engine Combustion and Analysis Validation

The Hydra engine was required to be tested for basic capability and some elementary tests were carried out to look at the performance of the engine. The first set of tests were done to check the combustion and its analysis using single injection at different injection pressure and fuel injection quantity while varying the start on injection timing. The conditions are summarised in Table 6-1. This was not an exhaustive test but a tool to verify the engine operation and analysis. Note that no skip firing was used in either any of these tests or the subsequent high speed imaging and LII work.

Engine Speed	1200 rpm
Start of Injection (aTDC)	Between -8CAD to 0CAD
For 600 MPa injection pressure	Fuel injected: 8, 10 mg
For 450 MPa injection pressure	Fuel injected: 10mg

Table 6-1: Testing conditions for combustion validation of the Hydra Engine

The combustion analysis carried out by analysing the pressure and heat release traces and the plot for the condition of 8mg of fuel injected at -5 CAD aTDC, with 600bar injection pressure is shown in Figure 6-1 where measurement from a single cycle is on the left and the mean from 50 cycles is on the right. This showed the variability of a

single cycle and the smoothed out values of the mean cycle. The apparent net heat transfer rate, or the term heat release rate, interchangeably used in this thesis and graphs, was calculated using the Woschni heat loss model.

The correct way to find the average heat release rate over a number of cycles is to find each individual heat release rate and then average it, as was practiced here for all calculations. It is important to note that this is different to taking average of pressure first and then calculating the heat release rate from the mean. This is because of the dependence on the fluctuations of instantaneous temperature used in calculating the heat loss and γ is lost if the pressure is first averaged.

Note that there are some fluctuations, or 'noise', associated with the heat release rate (away from the main peak) in the single cycle case as seen in the left figure in Figure 6-1. This issue was noted but the source was only found after the tests in this chapter were carried out. It was found that with the charge amplifier mounted on the frame of the cooling tower, the vibration from the latter caused the fluctuation thorough microphonic effects. This was eventually rectified in results to be presented later in the thesis.

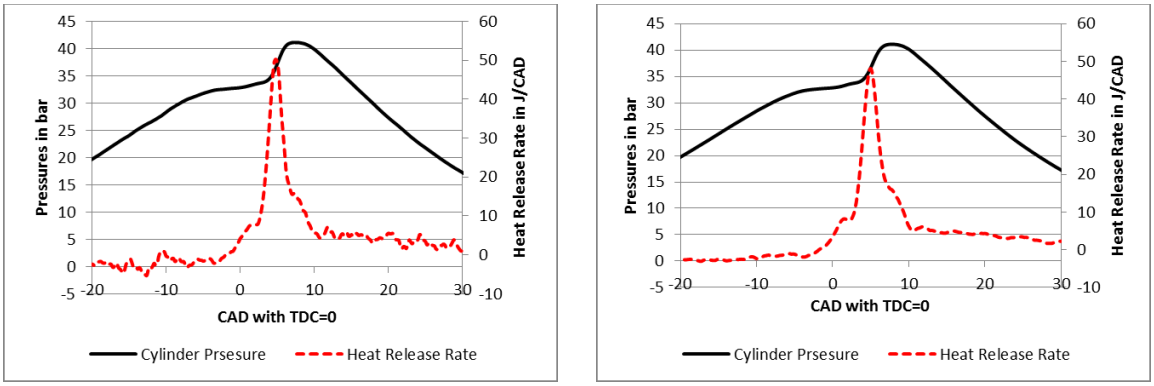

Figure 6-1: Cylinder pressure and heat release rate from a single cycle (left) and the mean of 50 cycles (right) for 8mg of fuel injected at 600bar injection pressure at -5 CAD aTDC

From the heat release calculation and the combustion analysis, some integral results could be calculated. Firstly, the IMEP was calculated from the pressure and change in volume to give the indication of work done by the engine. Figure 6-2 shows the dependence of IMEP on different injection pressures, injection timings and the amount

of fuel injected. The most significant effect was the injected fuel amount with 10mg having a higher IMEP than 8mg. Otherwise, different injection pressures showed little difference with a general trend of a peak IMEP between -4 to 0 CAD aTDC and tailing off for retarded injection.

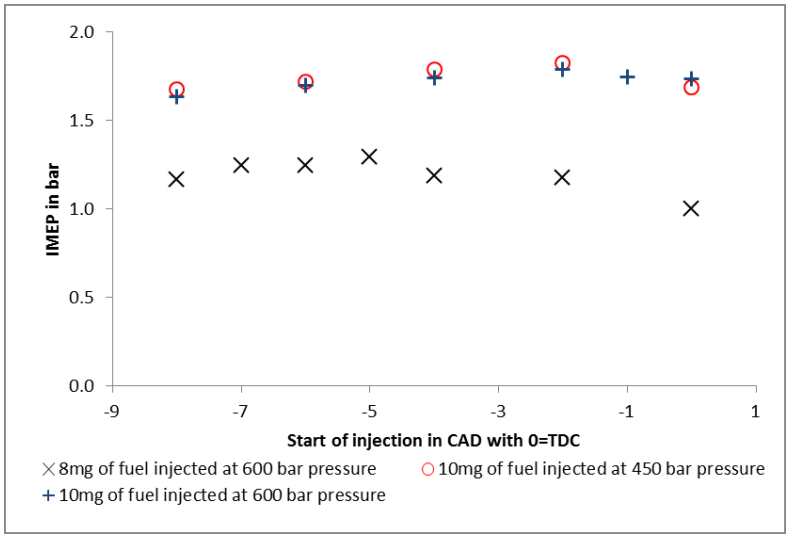

Figure 6-2: IMEP comparison with different injected fuel amount, injection pressure and injection timing.

Maximum pressure rise rate was also investigated against the same set of variables and this is shown in Figure 6-3. The pressure rise rate gives the indication of the combustion noise and the nature of the combustion i.e., high maximum pressure rise rate means more premix combustion and shorter combustion duration. The later the injection resulted in a lower maximum pressure rise rate as the fuel is being ignited during the expansion stroke of the engine cycle. Injection pressure's effect on maximum pressure rise rate is inconclusive. Unsurprisingly, the higher injected fuel amount also produced a higher maximum pressure rise rate.

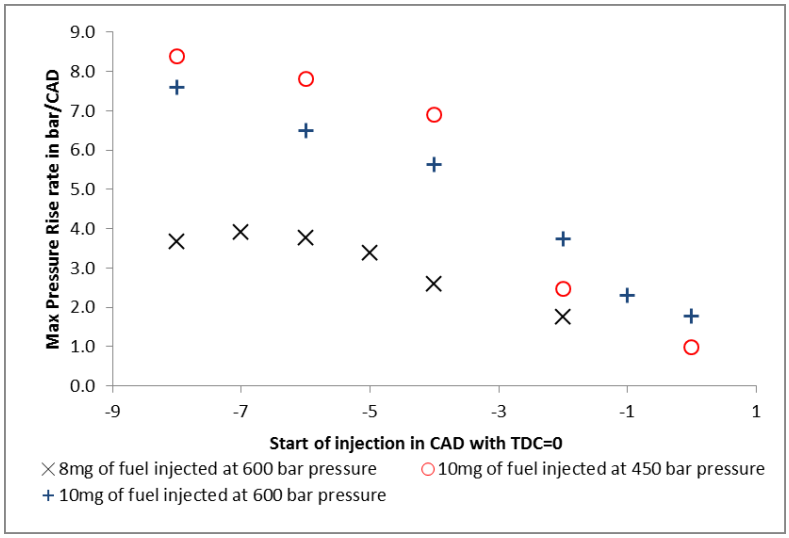

Figure 6-3: Maximum pressure rise rate comparison with different injected fuel amount, injection pressure and injection timing.

Another analysis looked at the CA50 location, the point at which 50% of heat release had taken place. This is shown in Figure 6-4 and it showed that retarded injection resulted, as expected, in a retardation of the CA50 point. The injection pressure and, more surprisingly, amount of fuel injected had little effect on the CA50 position.

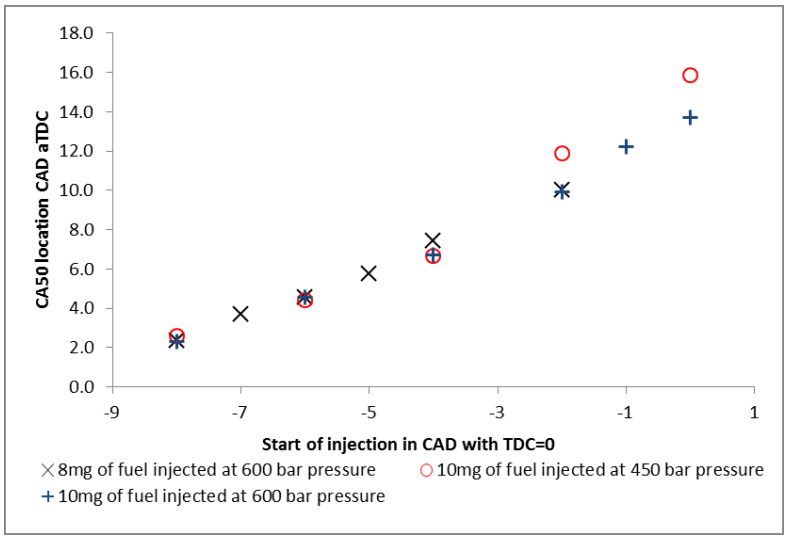

Figure 6-4: CA50 comparison with different injected fuel amount, injection pressure and injection timing.

6.3. Multi Variables Testing

An investigation was carried out to find the set of variables that had the biggest effect on combustion and pressure which could be used for imaging. The variables that could

be changed on the Hydra were the IMEP, CA50, injection pressure, intake temperature, number of injections and, for double injections, the amount of pilot fuel injected and the pilot injection timing. Due to the large number of combinations, the extreme values of these variables were tested against each other and the effects were analysed. Table 6-2 shows the variables and the upper and lower limits that were tested against each other. All tests were run at 1200rpm. These values were chosen as being comfortably within the safe operating range of the engine and posed low risk to damaging the engine.

Variables	Lower limit	Upper limit
IMEP	1 bar	2 bar
CA50	2 CAD	20 CAD
Injection pressure	300 MPa	1100 MPa
Intake temperature	40 ˚C	110 ˚C
Number of injections	1	2
Pilot injection quantity	0.5 mg	5 mg
Pilot injection timing	-20 CAD	-10 CAD

Table 6-2: Variables and the upper and lower limits that were test against each other.

This test yielded 18 test conditions for a single injection as the variation was between IMEP, CA50, injection pressure and intake temperature. For the double injection, with the inclusion of varying pilot injection timing and fuel quantity, the number of tests increased to 64. Note that the injection signal shown in the figures was for timing purposes and its magnitude shown was irrelevant.

6.3.1. Single Injection

For the single injection cases, the effect of injection pressure, intake air temperature, CA50 and IMEP were investigated.

6.3.1.1. Injection Pressure Effect

Injection pressure has an effect on the heat release rate due to the influence on atomisation and evaporation of the fuel, and to the penetration into the combustion chamber and the increased mixing of fuel with air (the higher pressure results in higher mean kinetic energy of the injected fuel and, ultimately, this energy is converted into gaseous turbulence kinetic energy and

hence improved mixing). Two sets of comparisons are shown below with Figure 6-5/ Figure 6-6 and Figure 6-7/Figure 6-8 at the injection pressure of 30MPa and 110MPa, respectively, while sharing the same intake air temperature, IMEP and CA50. The effect of higher injection pressure meant injection timing had to be advanced in order to match the same CA50 timing while the change in injection pressure had little effect on the amount of fuel injected.

At this low load setting, the heat release trace for the lower injection pressure for the early CA50 timing (Figure 6-5) showed a more conventional diesel combustion heat release, despite the positive ignition delay, with a rapid premixed burn phase (the initial peak in heat release) followed by a mixing controlled combustion phase (the plateau region in the heat release after the peak). In contrast, the higher injection pressure (Figure 6-6) showed features of low temperature combustion in the heat release with a two stage ignition phenomena. There was an initial small heat release after a period of ignition delay and this is the first stage Low Temperature Reaction (LTR) phase for both cases with high injection pressure (Figure 6-6 and Figure 6-8). There was then a reduction of this combustion before the main combustion phase.

The difference between the two combustion regimes for the different injection pressure may be explained in two ways: by the different stratification of air/fuel mixture within the combustion chamber between the two injection pressures and the wall/jet interaction creating a different amount of wall wetting and mixture formation.

Figure	Injection Pressure in MPa	Intake air in ˚C	IMEP in bar	Injection Timing	Injected Fuel Quantity in mg	CA50
Figure 6-5	30	110	1	-14 CAD	7	2 CAD
Figure 6-6	110	110	1	-16 CAD	7	2.8CAD
Figure 6-7	30	40	1	-1 CAD	10	20 CAD
Figure 6-8	110	40	1	-1 CAD	10	18 CAD

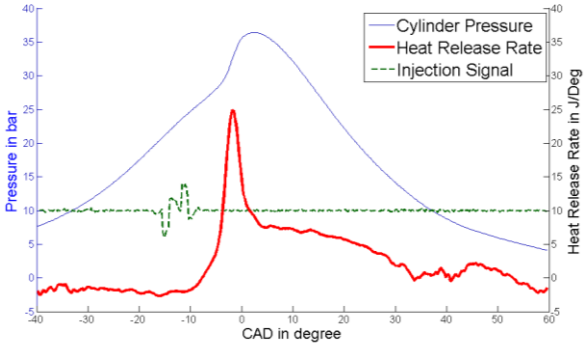

Figure 6-5: 30MPa injection pressure, 110 C intake air temperature with 1 bar IMEP and CA50 at 2CAD.

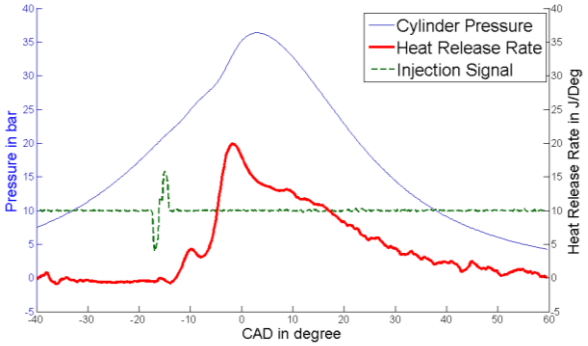

Figure 6-6: 110MPa injection pressure, 110 C intake air temperature with 1 bar IMEP and CA50 at 2.8CAD.

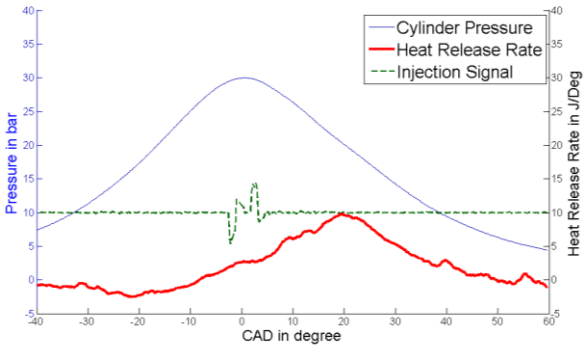

Figure 6-7:30MPa injection pressure, 40 C intake air temperature with 1 bar IMEP and CA50 at 20CAD

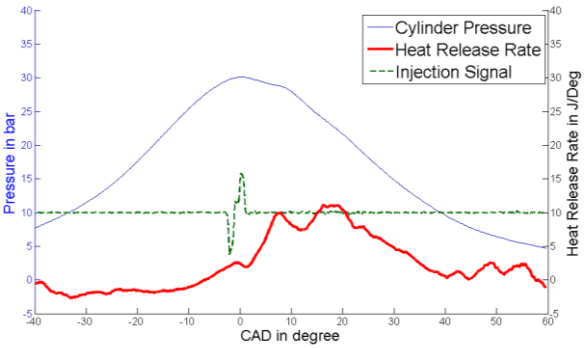

Figure 6-8: 110MPa injection pressure, 40 C intake air temperature with 1 bar IMEP and CA50 at 20CAD.

The distribution of the equivalence ratios within the combustion chamber, due to the higher injection pressure, shorter injection duration and more mixing of fuel and air, is likely to have a better mixed and locally leaner charge. This lean mixture goes through a two stage auto-ignition reaction. The decrease of equivalence ratio, i.e. leaner mixture, increases the amount of the first stage LTR heat release (Splitter, Hanson et al. (2011)). This explains the occurrence of LTR from the higher injection fuel pressure. Conversely, the lower injection pressure results in a locally less well mixed air/fuel charge. This means the locations where

fuel is present is richer and though the first ignition stage is still present, the richer mixture and lower dilution level meant the first ignition stage is merged with the second stage of premixed combustion phase (Musculus, Miles et al. (2013)).

The change of equivalence ratio and its effect on the timing of the two ignitions can be explained by the temperature difference as outlined in Musculus, Miles et al. (2013). A locally richer mixture, and in the case of lower injection pressure, larger droplets, requires more energy to heat the fuel and vaporize it. This means a cooler charge temperature compared to the locally leaner mixture. And this leads to a later first ignition phase which in turn leads to a higher temperature rise and causes the second stage ignition to take place more quickly than in the leaner mixture.

The second possibility is due to the injection jet and wall interaction. For the higher injection pressure, the fuel reaches the piston wall, causing wall wetting and some of that fuel becomes unavailable for immediate combustion. The remaining fuel vapour in the combustion chamber then forms a leaner mixture as compared to the lower injection pressure case which then undergoes LTR before the temperature increases and vaporises the fuel on the wall for combustion during the main combustion event. The may explain the lower peak premixed combustion heat release for the higher injection case as less fuel is available. The wall wetting and vaporising effect can also be affected by the fuel composition and its chemistry as the different constituents of the diesel fuel with different volatility will evaporate at different temperatures and may contribute to two-stage ignition and the long, mixing controlled, combustion period.

There may also be a combination of these two effects which helps to explain the leaner mixture in the combustion chamber for the higher injection case and the presence of LTR. This effect is consistent throughout the tests at other conditions and adheres to the presence of LTR for higher injection pressures. This effect can be investigated through using the imaging technique.

6.3.1.2. Air Intake Temperature Effect

Intake air temperature also had a significant effect on the heat release rate due to its role in the cylinder temperature when the fuel is injected. Two sets of comparison can be seen below in Figure 6-9/Figure 6-10 and Figure 6-11/Figure 6-12 with different intake air temperature. The effect of higher air intake temperature led to less fuel in order to reach the same IMEP and also retarded injection timing to match CA50 timing.

Based on the heat release analysis, the higher intake air temperature (Figure 6-10 and Figure 6-12) gave a sharper and higher heat release rate. Increasing the intake air temperature also reduced the ignition delay. The presence of LTR can also be seen for the higher injection pressure cases (Figure 6-9, Figure 6-10).

Figure	Injection Pressure in MPa	Intake air in ˚C	IMEP in bar	Injection Timing	Injected Fuel Quantity in mg	CA50
Figure 6-9	110	40	2	-0.5 CAD	13	20 CAD
Figure 6-10	110	110	2	4 CAD	11.5	20 CAD
Figure 6-11	30	40	1	-18 CAD	8	6 CAD
Figure 6-12	30	110	1	-14 CAD	7	2 CAD

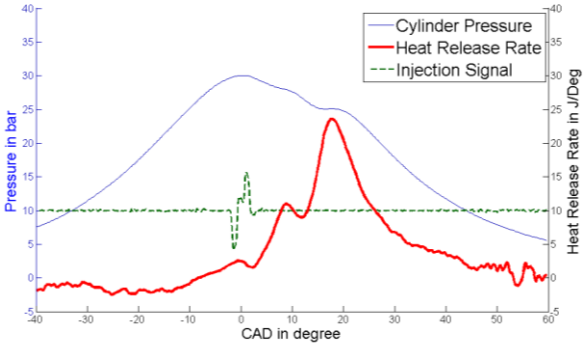

Figure 6-9: 110 MPa injection pressure, 40 C intake air temperature with 2 bar IMEP and CA50 at 20CAD

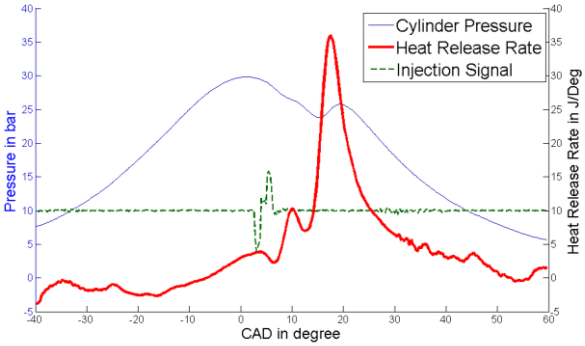

Figure 6-10: 110 MPa injection pressure, 110 C intake air temperature with 2 bar IMEP and CA50 at 20 CAD.

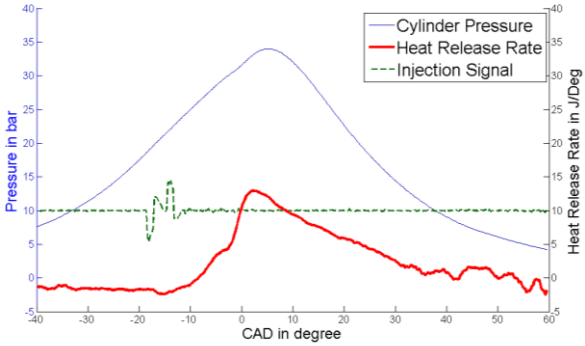

Figure 6-11: 30 MPa injection pressure, 40 C intake air temperature with 1 bar IMEP and CA50 at 6CAD.

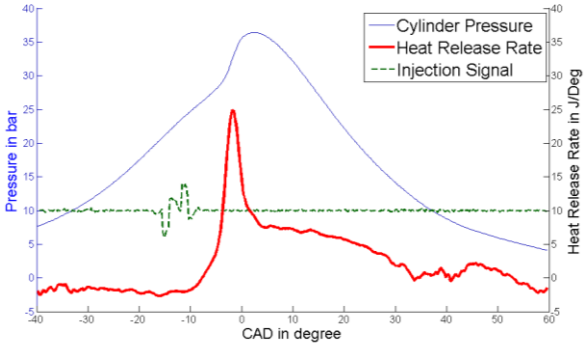

Figure 6-12: 30 MPa injection pressure, 110 C intake air temperature with 1 bar IMEP and CA50 at 2CAD.

6.3.1.3. CA50 Effect

The CA50 timing was changed by injection timing and the extreme values meant that this produced very different heat release characteristics. Two sets of comparison can be seen below in Figure 6-13/Figure 6-14 and Figure 6-15/Figure 6-16 with different CA50 timing. Early CA50 timing required a larger amount of fuel to be injected for the same IMEP.

Figure	Injection Pressure in MPa	Intake air in ˚C	IMEP in bar	Injection Timing	Injected Fuel Quantity in mg	CA50
Figure 6-13	110	110	2	-11 CAD	11	2 CAD
Figure 6-14	110	110	2	4 CAD	11.5	20 CAD
Figure 6-15	30	40	2	-18 CAD	11.5	3.2 CAD
Figure 6-16	30	40	2	-1.5 CAD	12	20 CAD

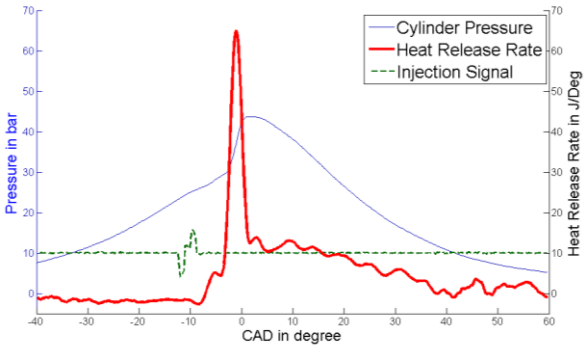

Figure 6-13: 110MPa injection pressure, 110 C intake air temperature with 2 bar IMEP and CA50 at 2CAD

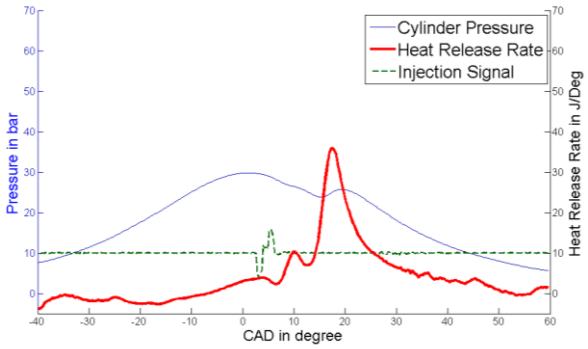

Figure 6-14: 110MPa injection pressure, 110 C intake air temperature with 2 bar IMEP and CA50 at 20CAD.

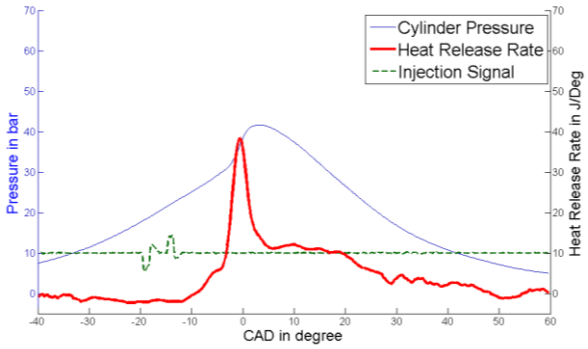

Figure 6-15: 30MPa injection pressure, 40 C intake air temperature with 2 bar IMEP and CA50 at 3.2CAD

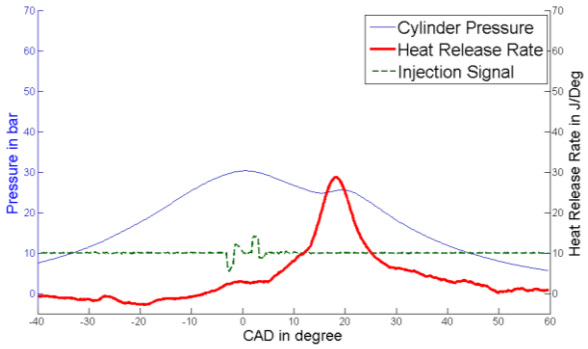

Figure 6-16: 30MPa injection pressure, 40 C intake air temperature with 2 bar IMEP and CA50 at 20CAD

The two values of 2 CAD and 20 CAD chosen for the CA50 timing meant that the combustion took place mostly during the compression stroke for the early CA50 cases (Figure 6-13 and Figure 6-15) and mostly during the expansion stroke for the late CA50 cases (Figure 6-14 and Figure 6-16). The continued compression during combustion contributed to the higher and sharper heat release rate. There was only minimal effect on ignition delay.

6.3.1.4. IMEP effect

The IMEP was altered by injecting a different amount of fuel into the cylinder. It changed the operating point of the engine completely but it is included here for comparison. Two sets of contrasting conditions are shown below in Figure 6-17/Figure 6-18 and Figure 6-19/Figure 6-20. These show that higher IMEP is indeed associated with a larger amount of fuel being injected and later injection timing for higher IMEP with the same CA50 timing.

The heat release traces showed higher IMEP meant higher heat release rate. Other than the magnitude of the heat release rate, the other features of LTR remained. The ignition delay did not appear to change. It is to be noted that the small peak of Heat Release shown around 55CAD in Figure 6-17 was caused by the fluctuation in the pressure reading, caused by the charge amplifier being mounted on the dynamometer frame and not related to a heat release.

Figure	Injection Pressure in MPa	Intake air in ˚C	IMEP in bar	Injection Timing	Injected Fuel Quantity in mg	CA50
Figure 6-17	30	110	1	2.3 CAD	8	20CAD
Figure 6-18	30	110	2	2.4 CAD	11.3	20 CAD
Figure 6-19	110	110	1	3 CAD	9	20 CAD
Figure 6-20	110	110	2	4 CAD	11.5	20 CAD

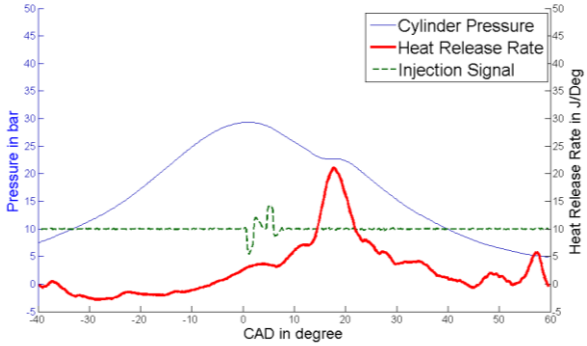

Figure 6-17: 30MPa injection pressure, 110 C intake air temperature with 1 bar IMEP and CA50 at 20CAD.

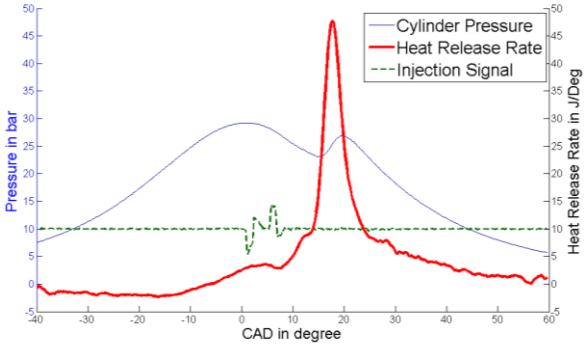

Figure 6-18: 30MPa injection pressure, 110 C intake air temperature with 2 bar IMEP and CA50 at 20CAD.

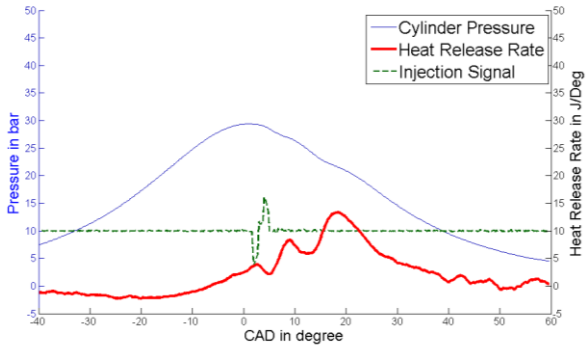

Figure 6-19: 110MPa injection pressure, 110 C intake air temperature with 1 bar IMEP and CA50 at 20CAD.

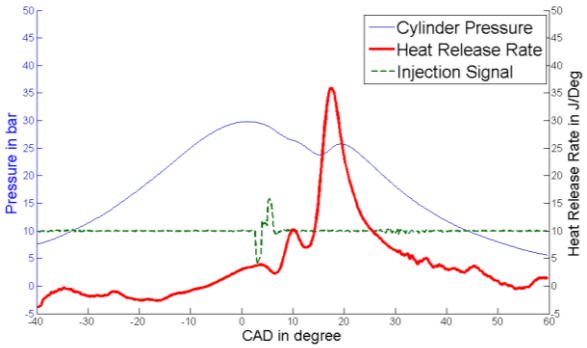

Figure 6-20: 110MPa injection pressure, 110 C intake air temperature with 2 bar IMEP and CA50 at 20CAD.

6.3.2. Double Injection

For the double injection cases, in addition to the variables used for the single injection cases, there were variation of the pilot injection timing and the pilot injection fuel quantity. This resulted in 64 test cases. The effects of the variables altered previously for the single injection also had a similar effect on the double injection so they are omitted and only the more significant results are shown here.

6.3.2.1. Injection Timing of the Pilot Injection

The injection timing of the pilot affects the combustion phasing in the cylinder. Also, the later injection timing of the pilot limited how early the main injection could start. This had an effect on how early CA50 could be achieved. In this example shown here, the IMEP was 1 bar and fuel was injected at 110MPa injection pressure and 110C Intake temperature. The pilot injection fuel quantity was fixed at 5mg and the variable was the pilot injection timing of -10 and -20 CAD along with the early and late CA50 to supplement the comparison, shown in Figure 6-21/Figure 6-22 for early CA50 and Figure 6-23/Figure 6-24 for late CA50. The fuel required for the second injection was higher for the same IMEP and a later CA50, due to the cooling of the combustion chamber for the later injection. Also, early pilot injection required more fuel for the same IMEP compared to late pilot injection.

From the combustion analysis, the effect of pilot injection timing was found to be small for the early CA50 timing case (Figure 6-21 and Figure 6-22) and they both showed a similar heat release profile although the early pilot injection (Figure 6-21) showed a more sustained heat release compared to the late pilot injection case. The late CA50 timing, i.e. late main injection (Figure 6-23 and Figure 6-24), showed a negative ignition delay meaning the fuel from the pilot injection was already combusting before the start of the main injection. This is the effect of this high pilot fuel injection amount and this effect was found to a lesser extent in the lower pilot fuel injection amount. This is not shown here.

Figure	IMEP in bar	Injection Pressure in MPa	Intake air Temp in ˚C	Pilot injection timing in CAD	Pilot injection Fuel quantity in mg	Main injection timing in CAD	Main injection fuel quantity in mg	CA50
Figure 6-21	1	110	110	-20	5	-13	1	6.8
Figure 6-22	1	110	110	-10	5	-3.5	1	8.8
Figure 6-23	1	110	110	-20	5	4	3	10.8
Figure 6-24	1	110	110	-10	5	6	1.5	10.8

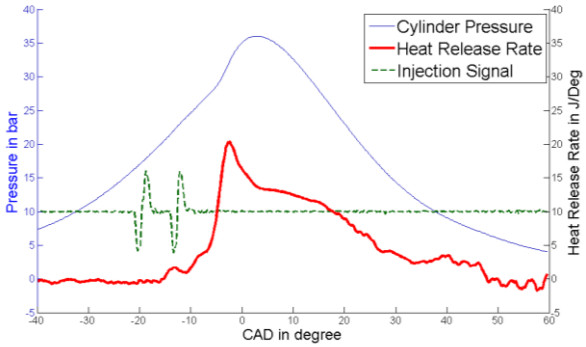

Figure 6-21: Early pilot injection and early CA50 timing.

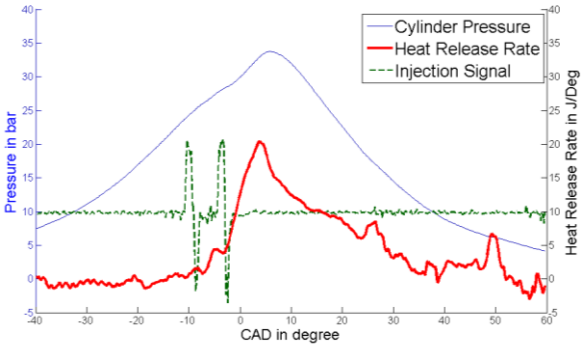

Figure 6-22: Late pilot injection and early CA50 timing.

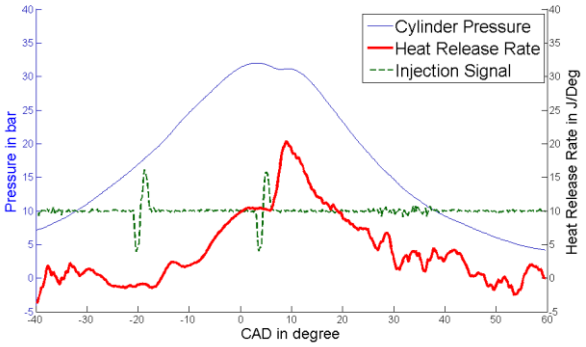

Figure 6-23: Early pilot injection and late CA50 timing.

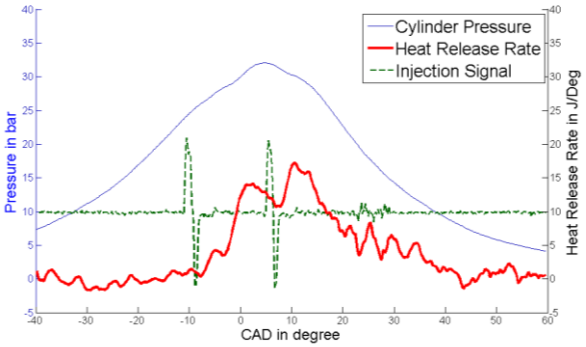

Figure 6-24: Late pilot injection and late CA50 timing.

6.3.2.2. Injection Fuel Quantity of the Pilot Injection

The other variable to alter was the pilot injection fuel quantity and fixing other variables. This example compares the lower fuel injection amount of 0.5mg with a higher injection amount of 5mg, along with an early and late CA50 timing. This is shown in Figure 6-25/Figure 6-26 for early CA50 timing and Figure 6-27/Figure 6-28 for late CA50 timing. There did not appear to be a significant difference in fuel consumption for different fuel amounts in the pilot injection. But the main injection timing had to be significantly compensated for the different pilot

injected fuel amount to match the CA50. This was expected due to the early combustion of the larger amount of fuel in the pilot.

Figure	IMEP in bar	Injection Pressure in MPa	Intake air Temp in ˚C	Pilot injection timing in CAD	Pilot injection Fuel quantity in mg	Main injection timing in CAD	Main injection fuel quantity in mg	CA50
Figure 6-25	2	30	110	-10	0.5	-6	10.5	9.1
Figure 6-26	2	30	110	-10	5	-3.5	4.7	10.1
Figure 6-27	2	30	110	-10	0.5	4	10.5	18.8
Figure 6-28	2	30	110	-10	5	12.5	6.5	18.1

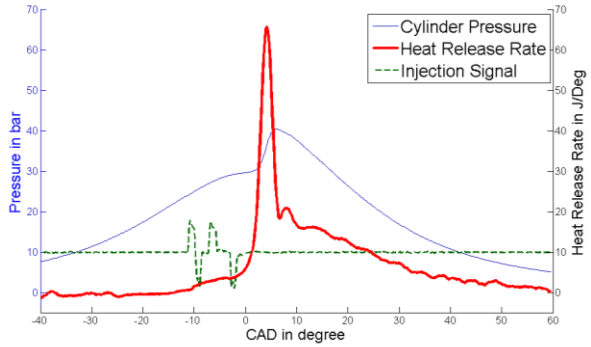

Figure 6-25: Pilot injection of 0.5mg and early CA50 timing.

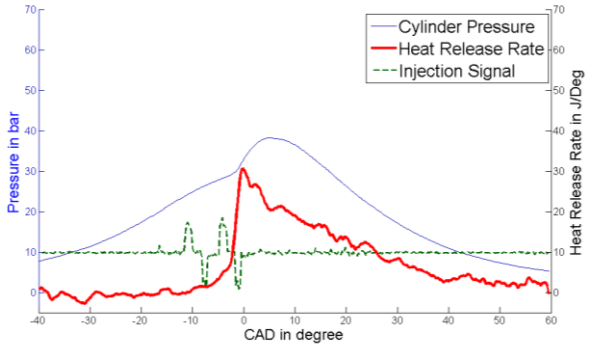

Figure 6-26: Pilot injection of 5mg and early CA50 timing.

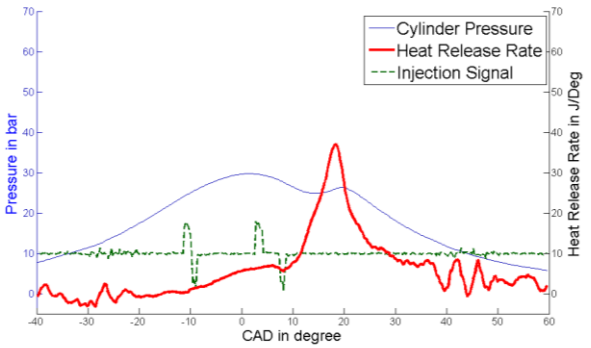

Figure 6-27: Pilot injection of 0.5mg and late CA50 timing.

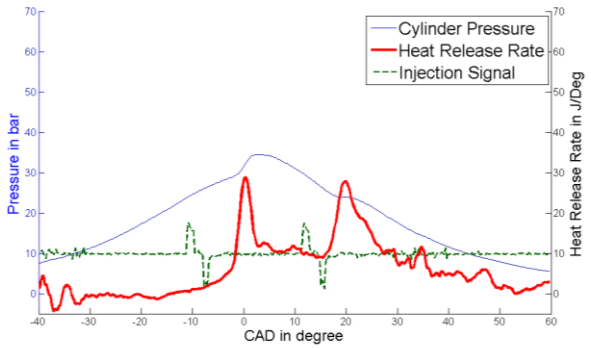

Figure 6-28: Pilot injection of 5mg and late CA50 timing.

From the analysis of the heat release rate, it appeared that the larger pilot injection (Figure 6-26 and Figure 6-28) produced a lower peak heat release rate. This was because the amount of fuel was split between the injections with less fuel combusting at a given time. The increase in the amount of fuel during pilot injection reduced the ignition delay. For the larger pilot fuel injection and late CA50 timing case (Figure 6-28), there were two separate peaks of heat release.

This was due to the extremely late injection of the main injection in order to match the CA50. It is not a realistic operating point but is included to illustrate the effect of these variables.

6.3.2.3. Fuel Injection Pressure

Returning to the variable of fuel injection pressure and its effects on the double injection case, below are comparisons between two cases of different injection pressure, again comparing early and late CA50 timing. Figure 6-29/Figure 6-30 and Figure 6-31/Figure 6-32 compare injection pressures of 30MPa and 110MPa with a high intake temperature, late pilot injection and a high pilot injected fuel amount. The total injected fuel amount and the difference in timing between the two injection pressures is small.

Figure	IMEP in bar	Injection Pressure in MPa	Intake air Temp in ˚C	Pilot injection timing in CAD	Pilot injection Fuel quantity in mg	Main injection timing in CAD	Main injection fuel quantity in mg	CA50
Figure 6-29	2	30	110	-10	5	-3.5	4.7	10.1
Figure 6-30	2	110	110	-10	5	-3.5	5	8.7
Figure 6-31	2	30	110	-10	5	12.5	6.5	18.1
Figure 6-32	2	110	110	-10	5	13.5	5.5	18.1

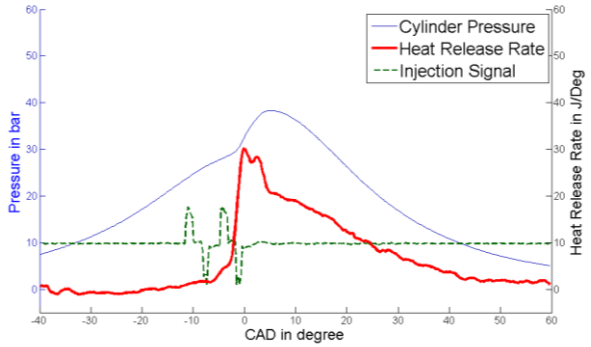

Figure 6-29: Injection pressure of 30Mpa and early CA50 timing.

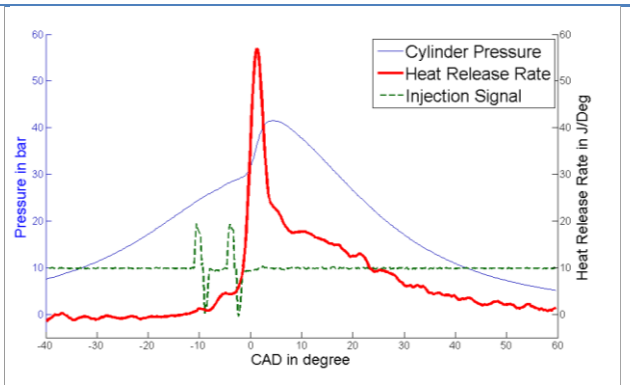

Figure 6-30: Injection pressure of 110Mpa and early CA50 timing.

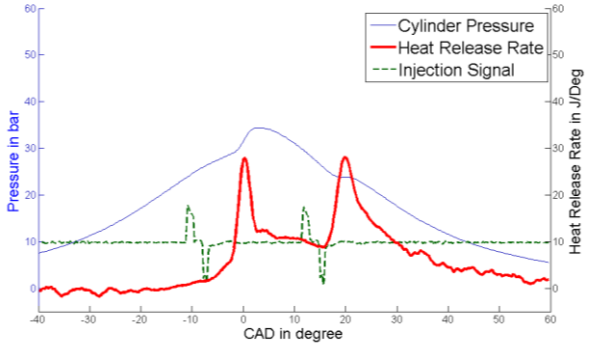

Figure 6-31: Injection pressure of 30Mpa and late CA50 timing.

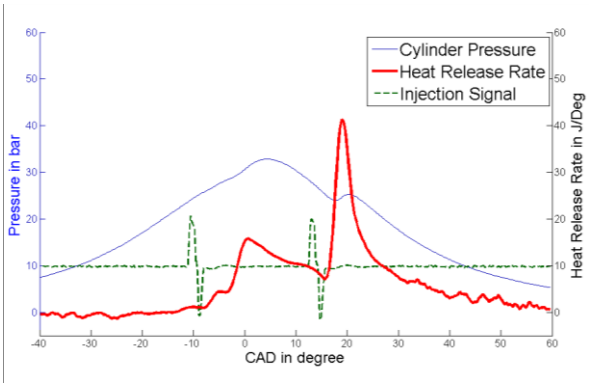

Figure 6-32: Injection pressure of 110Mpa and late CA50 timing.

The heat release rate showed quite different combustion between the two injection pressures. The higher injection pressure (Figure 6-30 and Figure 6-32) showed a sharper rise in heat release rate after the main injection which could be explained by the more homogeneous charge of fuel and air and a more premixed combustion. The lower injection pressure presumably had a more stratified charge and a more progressive mixing controlled combustion diffusional flame. For the late CA50 cases (Figure 6-31 and Figure

6-32), there was enough time separation for the pilot injection to ignite and combust before the main injection took place.

This is not the same as the single injection case where the heat release rate rises more rapidly at low than at high injection pressure. This can be explained by the different combustion regime these are operated under. With a double injection, the negative ignition delay means it is conventional diesel combustion. For the single injection case, the larger ignition delay meant it is in the region of a Premixed Charged Compression Ignition. For conventional diesel combustion with double injection, the fuel injected during the main injection is entering an already combusting gaseous environment which is a different condition than for a single injection. Although it can still be seen in Figure 6-32 that the LTR took place after the pilot injection at around -8CAD.

6.4. Chapter Conclusion

This chapter shows work on investigating the combustion modes through pressure analysis and heat release rate and the functioning of the engine and its instrumentation. An extensive series of engine variables were tested. The fuel amount injected naturally affected the IMEP, changed the magnitude of the heat release rate and also gave more prominent features to the heat release characteristics. Increase in injection pressure produced higher mixing rate for fuel and air and, for the single injection case, produced a leaner mixture which it underwent a two-stage auto-ignition process and resulted in a lower peak heat release rate. Increase in air intake temperature reduced the ignition delay and increased the magnitude of the heat release rate. The range of CA50 timing chosen meant that early CA50 timing led to ignition and combustion during the compression stroke and later CA50 timing led to ignition and combustion during the expansion stroke. This had a significant effect to the magnitude of the heat release rate with a higher rate of heat release for the early CA50 case.

For the double injection cases, the heat release rate did not show much difference between injecting the pilot injection at -20CAD and -10CAD. Increasing the amount of fuel injected at pilot resulted in the peak rate of heat release being lower as the combustion was spread out through time. There was negative ignition delay for cases with a large time separation between pilot and main for the higher pilot injected fuel amount because the pilot had enough fuel injected to be a standalone combustion event. Higher injection pressure meant a higher peak heat release rate in the double injection case as the fuel was injected into an already combustion environment and the better mixed charge with better atomisation meant a stronger premixed burn.

Based on the investigation described in this chapter, the most interesting variable in terms of mixing and physical processes in combustion was the injection pressure. The greatest potential for visualisation was injection pressure.

7. High Speed Imaging in Hydra Engine

Utilising the optical capability of the Hydra, high speed imaging work involved measuring injection penetration, combustion luminosity, CH Cheminluminescence, and the measurement of engine swirl. The variables investigated were injection timing and injection pressure. There was a process of establishing the operating procedure for the engine and the best practice for setting up the lighting, imaging and cleaning. Also the balance between maximising the data acquired between engine optical components cleaning and the usable amount of data in the form of high speed images had to be determined. Although the engine is capable of skip-firing, all tests were conducted with continuous firing.

7.1. Combustion Luminosity

The imaging of combustion luminosity was chosen partly because it was not hindered by the lack of accessibility from the side window and measurements could be taken over full range of crank angle. Some tests using both single and double injections were carried out while varying injection pressure and injection timing in order to gain experience in the operation. Combustion luminosity gives information on combustion and soot formation processes, and comparative information on signal intensities and locations. The combustion luminosity consists of soot incandescence and chemiluminescence and these signals are dependent upon species temperature, optical properties and imaging equipment.

7.1.1. Experimental Condition and Optical Setup

A typical operating condition of modern diesel engines consists of a pilot injection followed by a main injection. A condition tested, similar to that found in the corresponding I4 metal engine's calibrated ECU value (Soulopoulos (2014)), was a double injection with an early pilot injection and the condition is shown in Table 7-1. This gave an IMEP of 2.2 bar. The images were captured through the glass piston crown and using the 45 degree mirror. The visible combustion luminosity was recorded by a Photron Ultima APX-RS high speed camera which could record at

10,000fps (1 frame every 0.72CAD) at a resolution of 512x512. A diagram of the optical setup is shown in Figure 7-1. The mirror used was Edmunds Optics enhanced aluminium, 4-6λ wave mirror that had a reflective wavelength range between 450-650nm.

The camera viewing direction was at right angle towards the 45 degree mirror. The correct aperture (f stop) was chosen so that the camera's sensor did not get over exposed and focused at the imaging plane with the piston at the appropriate CAD of interest to minimise the effect of any optical distortion that the incorrect distance between the glass piston and the imaging plane may cause. The scale in the imaging plane was established as part of the calibration process and images shown below have a scale with the origin being the axis of the bore where the injector was also located.

Variable	Value
Engine Speed	1200 rpm
Intake Air Temperature	25 ˚C
Injection Pressure	40 MPa
Pilot Injection Timing	-15 CAD aTDC
Pilot Injection Quantity (Duration)	2 mg (0.26ms/1.9CAD)
Main Injection Timing	-2 CAD
Main Injection Quantity (Duration)	10 mg (0.52ms/3.7CAD)
IMEP	2.2 bar

Table 7-1: Testing condition of combustion luminosity imaging test.

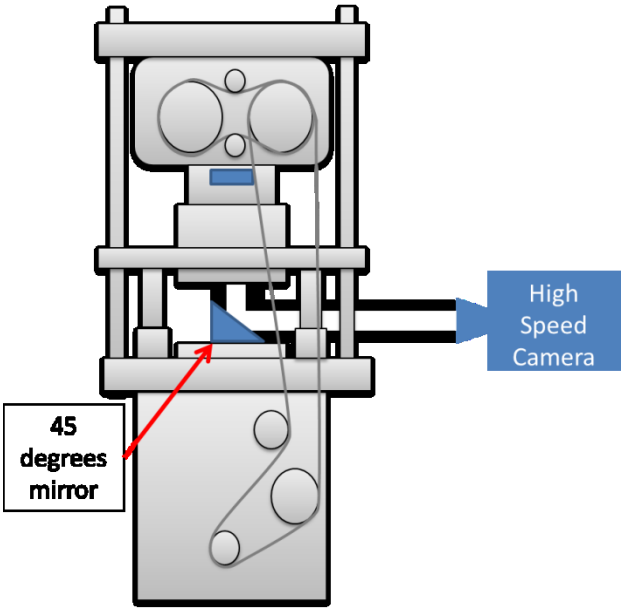

Figure 7-1: Optical setup for high speed imaging of combustion luminosity.

7.1.2. High Speed Images and Combustion Analysis

The average of 100 cylinder pressures and heat release rate of this double injection test case is shown in Figure 7-2. The high speed images for this condition are shown in Figure 7-3 and show a series of images throughout the engine cycle starting from 1.6 CAD, when combustion luminosity starts to be visible, to 24.6 CAD. It can be seen that the main (liquid) injection is visible for the first image as the combustion luminosity also faintly illuminated the sprays; here the combustion has started during the main injection event. The combustion luminosity naturally followed the trend of the apparent net heat transfer rate shown in Figure 7-2 and Figure 7-3.

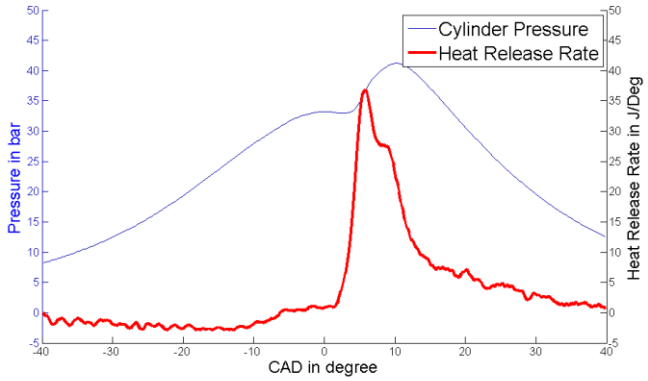

Figure 7-2: Cylinder pressure and heat release rate of double injection, 2.2 bar IMEP for combustion luminosity test case. Averaged formed over 100 cycles.

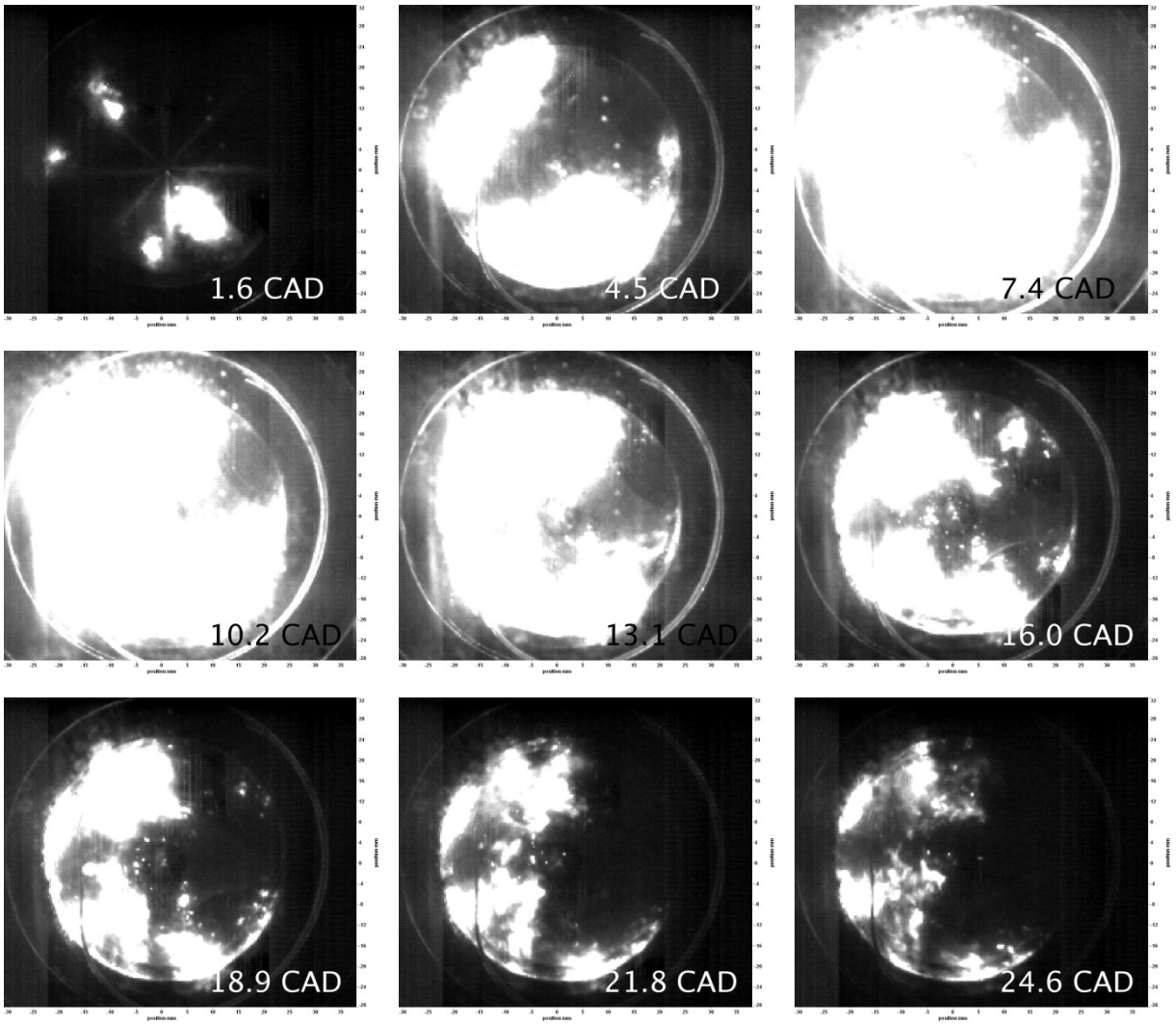

Figure 7-3: High speed images of combustion luminosity of a double injection, 2.2 bar IMEP test case from a single cycle. The outer right ring visible is the edge of the underside of the piston and the inner ring is the wall of the piston bowl. Other features are marks on the optics and 0CAD is TDC.

The figure shows that ignition took place at several sites, ranging from more or less the exit of the injector to the edge of the combustion bowl. Referring to the heat release rate, as the temperature increased, more fuel underwent premixed combustion all over the combustion chamber and then progressed to non-premixed combustion after 13CAD with the reduction of the apparent net heat transfer rate. The combustion process can then be identified from the images. The burn phase was concentrated towards the wall of the piston bowl, with brighter spots at the tip of the spray.

A few observations can be made from these images. First, the signal was saturated as the combination of the camera shutter speed (limited to the separation between frame rates at 10,000fps) and the camera lens aperture setting meant too much light fell onto the detector. This would have to be adjusted so the full range of luminosity could be recorded. To find the correct f stop is a process of trial and error as the appropriate value could be found only when the engine was in operation and the images being recorded. Secondly, the combustion luminosity lay towards the left side of the combustion chamber and the combustion luminosity becomes more uniform as the combustion stability improves with increased number of combustion cycles. Combustion stability was dependent on the engine reaching a thermal equilibrium and this took approximately more than 30 seconds of continuous firing. This in turn resulted in increasingly fouled optical windows and viewing mirror so there was a balance to be struck between maximising the number of imaging cycles and the need to establish combustion stability. The focusing also had to be improved to increase the sharpness of the images.

7.2. CH Chemiluminescence

Using the same operating point as the combustion luminosity images above, another imaging technique applied was chemiluminescence and the species investigated was CH chemiluminescence. CH chemiluminescence generally identifies the location of combustion where there are rich mixtures. OH and C_2 chemiluminescence can also be

imaged by applying different filters but due to the availability of filters and time, CH chemiluminescence measurement was conducted.

For CH chemiluminescence, the Ealing 35-3318 CH filter at 430nm centre wavelength, 10nm Full width half maximum with a transmissivity around 45% was used. The pressure trace and apparent net heat transfer were the same as for Figure 7-2 and with the same optical arrangement but with the filter attached to the high speed camera. The images were taken at 10,000fps. The corresponding CH chemiluminescence images at the same crank angle as the combustion luminosity images are shown in Figure 7-4

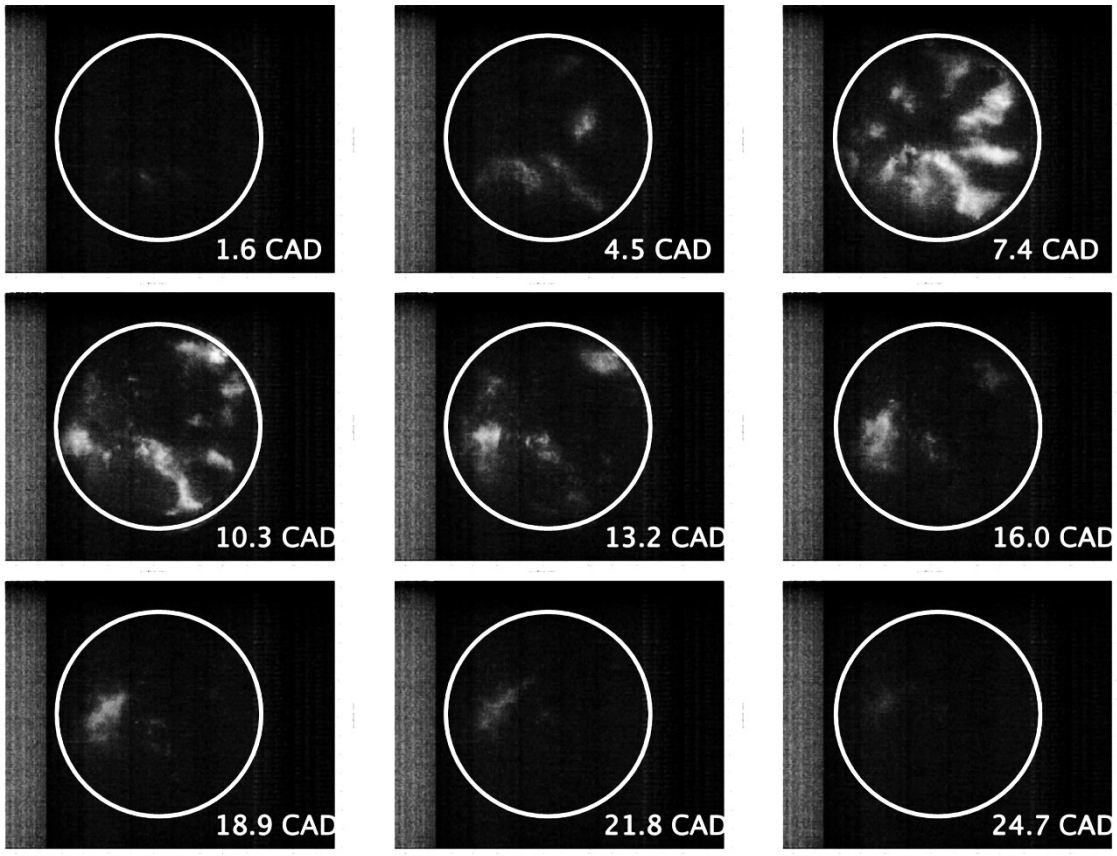

Figure 7-4: CH chemiluminescence high speed images of a double injection, 2.2 bar IMEP test case for a single cycle with the white circle marking the piston bowl wall.

The signal had low intensity and the main structure can be seen at 7.4CAD where it coincided more or less with the fuel injection jet paths which were aligned with the eight nozzles of the injector. Because these are images taken from different cycles, care is required in directly comparing the combustion luminosity locations with the CH

chemiluminescence images. This could be remedied by taking the chemiluminescence image and the combustion luminosity image simultaneously to analyse single cycle variation. Additionally, multiple sets of images and taking an average of the signals can be taken and compared. The signal intensity could also be improved by using a filter with a higher transmissivity than the filter with 45%, which was used here because it was available.

7.3. Fuel Injection Spray Imaging: Illumination through the Cylinder Liner Windows

Other than combustion luminosity and chemiluminescence, the fuel spray could also be investigated by looking at its penetration length, the spray angle and lift off length. The requirement for such measurements was a light source to illuminate the fuel as it was injected into the combustion chamber and for this purpose the spray was, for preliminary measurements, illuminated from a cylinder liner window, as shown in Figure 7-5. The light source chosen was a household 20W LED and with the high speed camera acquiring the image through the piston crown.

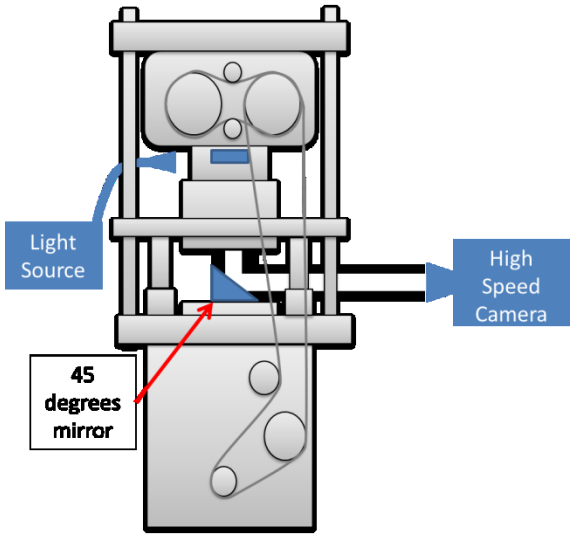

Figure 7-5: Optical arrangement for illumination of fuel injection through the cylinder liner.

The condition for this injection imaging is shown in Table 7-2. Because the metal piston bowl blocked optical access through the liner between -30 CAD to 30 CAD, an injection timing of 35 CAD was chosen. The high speed camera was operated at

20,000fps (0.36 CAD per frame). It should be emphasized that injection at 35 CAD aTDC is not a realistic injection timing as the in- cylinder condition is very different to what is normally used in conventional diesel combustion. This was a mean to explore the imaging technique where, if it is proved to be interesting, the optical setup of the engine can be changed to allow for optical access near TDC.

Variable	Value
Engine Speed	1200 rpm
Intake Air Temperature	25˚ C
Injection Pressure	40 MPa
Injection Timing	35 CAD aTDC
Injection Quantity	10 mg

Table 7-2: Testing condition for the fuel injection spray imaging using a light source through the cylinder liner.

The images resulting from the use of a light source through the side windows are shown in Figure 7-6. This verifies that the injection equipment produces a symmetrical injection and that the injection equipment was working correctly after the issues encountered with it. The injection timing was correct and all eight sprays were present.

It can be seen that the sprays near the top of the images tended to be brighter than those near the bottom of the image. This is because light was scattered and/or absorbed as it entered from the sprays at the top of image through the window, causing the jet towards top left and top right to be the brightest. The same can be said with the tip of the top spray which was brighter than the rest of the spray because light was blocked by the tip. This illumination direction was effective in leaving out the valves and cylinder head in the background and effective in visualising two out of eight sprays. While this illumination method had its uses, the unrealistic injection timing at which this had to take place was an unacceptable limitation. Although much less convenient, the next step was to position a light source such that the illumination was along the axis of the cylinder which thereby eliminated the issues of light absorption and “black out” around combustion TDC.

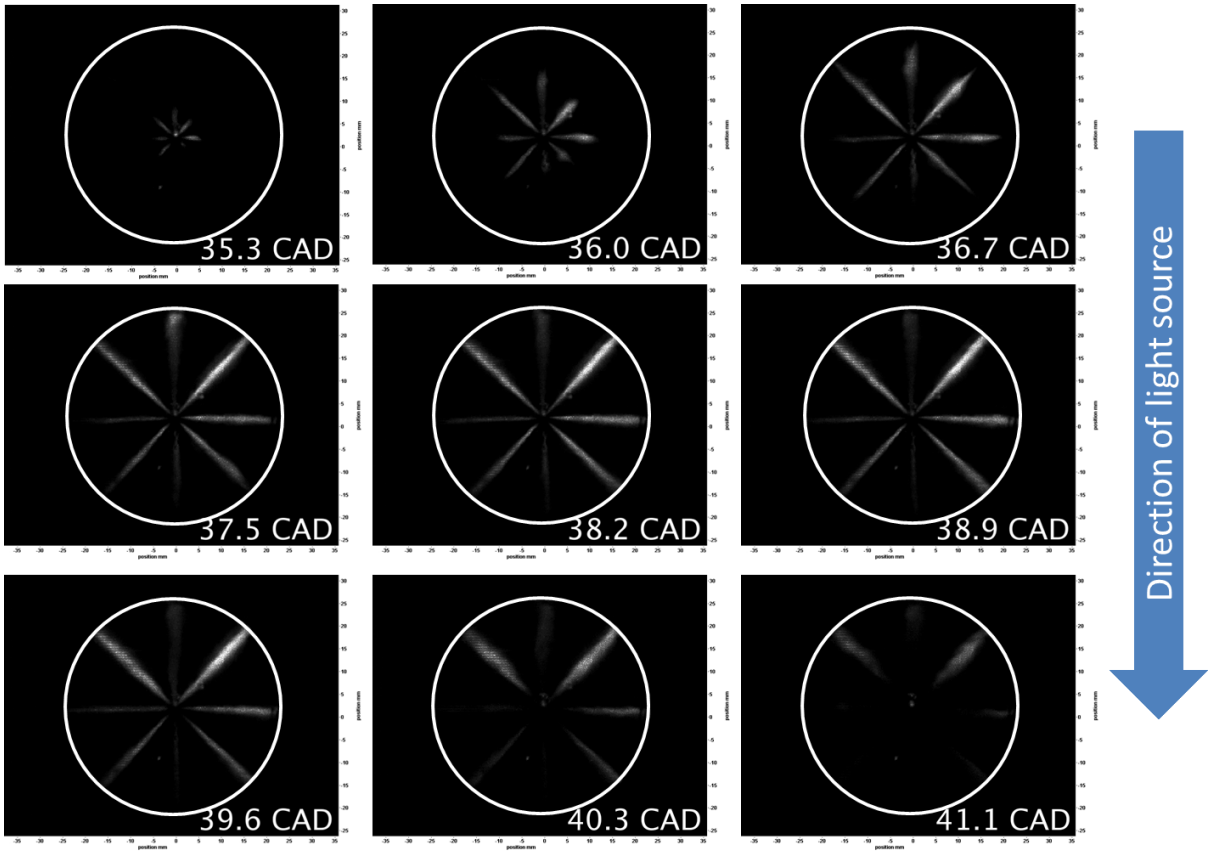

Figure 7-6: Fuel injection spray high speed images using a light source through cylinder lining, with the light source coming from the top of the image.

7.4. Fuel Injection Spray Imaging: Light source through Piston

The fuel injection spray imaging was improved by using a 150W, fibre optic dual gooseneck microscope illuminator which was aligned to illuminate the spray through the piston crown. The optical setup is shown in Figure 7-7. The challenge was the reflection from metal of the hydraulic platform, cylinder head and piston crown glass that saturated the camera and limited the ability to image the fuel injection spray itself. The condition used for this figure is set out in Table 7-3. The high speed images were taken at 20,000fps.

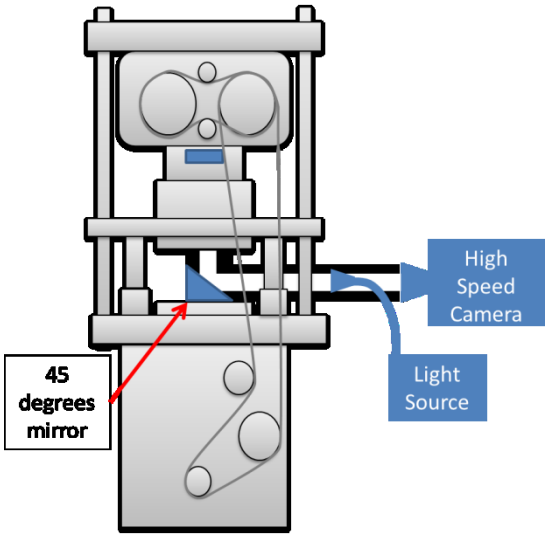

Figure 7-7: Optical setup for fuel injection spray imaging with a light source through the piston.

Variable	Value
Engine Speed	1200 rpm
Intake Air Temperature	25 ˚C
Injection Pressure	40 MPa
Pilot Injection Timing	-15 CAD
Pilot Injection Quantity	5 mg
Main Injection Timing	-2 CAD
Main Injection Quantity	10 mg

Table 7-3: Testing condition for fuel injection spray imaging with light source through the piston.

The initial resulting images of the two injections can be seen in Figure 7-8. This shows the fuel spray but there were, nevertheless, a few undesirable aspects with this setup as can be seen from these images. There was bright reflection from the bottom of the metal piston (marked with circle 1) and also a bright reflective spot on the engine head itself (marked with circle 2) which diminished the clarity of the image. Also, the images were obscured by the collection oil deposits on both the mirror and crankshaft facing side of the piston window after less than 1 minute of running. The level of these extraneous sources of interference in the images meant that various algorithms for background subtractions and averaging did not improve the clarity of the images.

A solution based on better alignment through trial and improvement of the light source to avoid these bright reflective spots on the image was required. Also, the source of the copious contamination of the windows and mirrors had to be identified and removed. The source was eventually identified as being a leak from the crankcase and the solution was a new design of crank case piston sealing as described in Section 3.3.

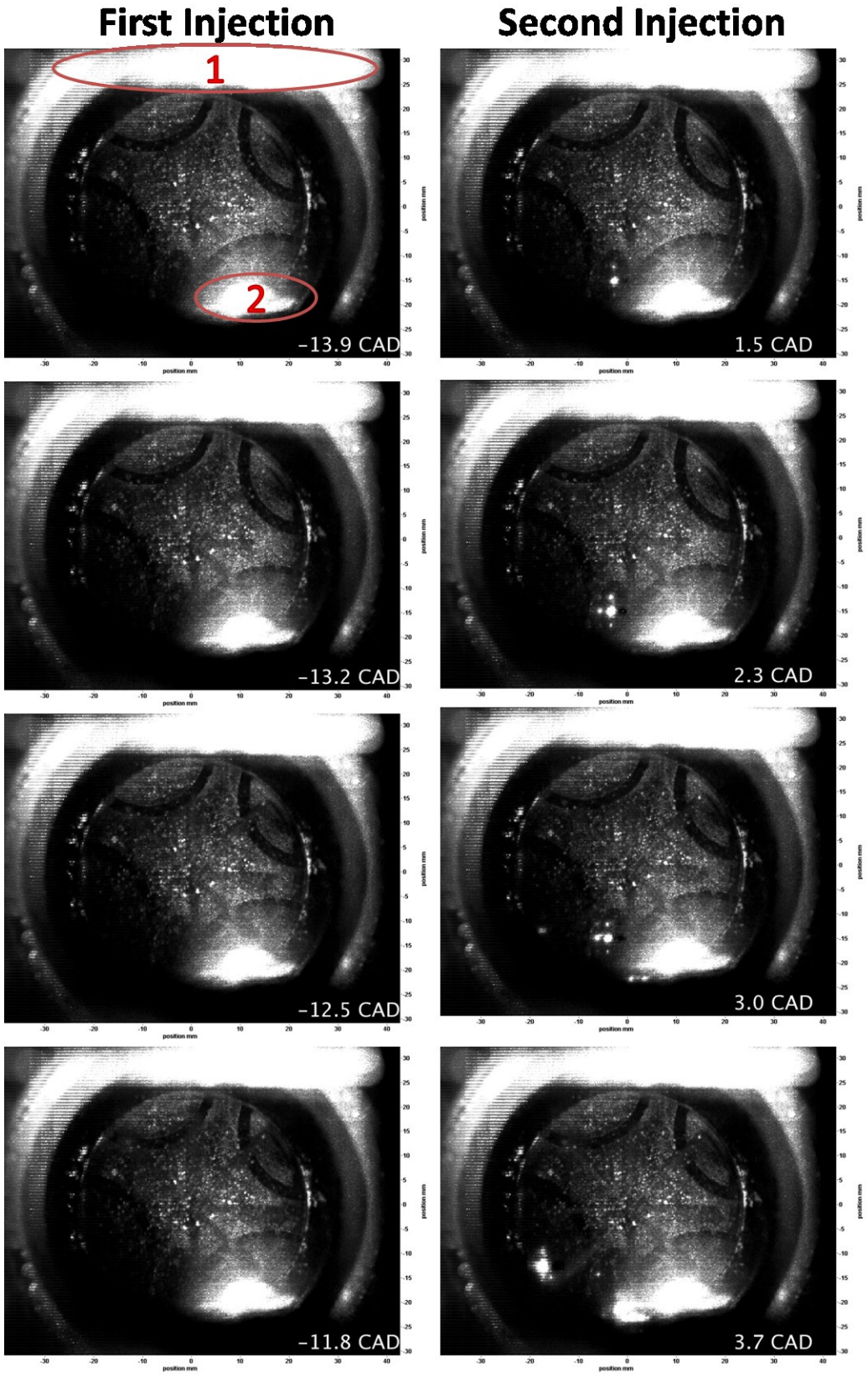

Figure 7-8: Images of injections using light through the piston.

7.5. In-Bowl Swirl Measurement

Based on the analysis of the high speed images taken from the Hydra, an estimate of the swirl velocity could be measured. Swirl is important to the mixing of air and fuel as it provides the additional convection to transport the fuel vapour away from the dense liquid core of the spray and directly into the surrounding air. This was measured by tracking the movement of the visible flame front from the images and measuring the distance travelled in a given time, taking multiple readings and averaging the readings. The swirl number or swirl ratio is give in equation (7-1) where R_s is the swirl ratio, ω_s is the swirl angular velocity of the solid body of gas which has the same angular momentum as the actual velocity (Lumley (1999)), in rad/s and N is the engine speed in rps. The result of the calculation is shown in Table 7-4. An accurate measurement of swirl can be done by measuring the angular momentum which is dependent upon the density of the combusting charge but this is not possible through this imaging technique. At least it can be assumed that the average density of the charge before and after combustion is the same. This result based on tracking the visible flame front which may change not only due to the swirl motion, but also depended on the increase or decrease of combustion and affected the result.

$$R_s = \frac{\omega_s}{2\pi N} \tag{7-1}$$

Variable	Value
Average tangential velocity	10.0 m/s
Radius of combustion Bowl	0.023m
Angular velocity	430 rad/s
Swirl rotational speed	4130rpm
Engine speed	1200rpm
Swirl number	3.44

Table 7-4: In-bowl swirl ratio measurement and calculation

7.6. Imaging Based on Conditions Using Production Engine Calibration

Conditions from the corresponding production Ford Puma four-stroke, 2.2L, Euro V diesel test engine at Imperial could be used, in principle, as test cases. The current lack of EGR and boost and different bowl geometry in the Hydra meant that it was not a completely representative test but the fuel injection equipment was the same as the production engine Soulopoulos (2014). Four operating conditions were acquired from the production engine map and these are shown in Table 7-5. Out of these conditions, it was decided to focus on the second test point (highlighted) because it had a low enough BMEP to prevent damage to the Hydra engine, but nevertheless high enough fueling to be visualised and to have strong combustion luminosity for imaging.

Engine Speed [RPM]	BMEP [bar]	Torque [Nm]	Injection pressure [MPa]	Pilot injection timing [CAD]	Pilot Injection fuel quantity [mg/stk]	Main injection timing [CAD]	Main injection fuel quantity [mg/stk]
1200	1.04	18.2	22.8	-8.6	1.54	-3.6	4.34
1200	1.99	34.8	25.0	-10.6	1.68	-5.6	6.59
1200	4.01	70.2	36.1	-7.5	1.98	-0.3	12.86
1200	5.99	104.8	47.5	-8.6	1.98	2.6	19.39
1200	7.99	139.8	62.8	-13.2	1.74	1.5	26.10

Table 7-5: Testing conditions from production engine at Imperial Soulopoulos (2014).

The imaging arrangement for this experiment provided the light source through the piston crown and took high speed images through the same path. The engine had been modified since the previous spray fuel injection spray imaging and now had much reduced oil deposits on mirror and piston window. Also the imaging technique had been improved to provide better focus, improved lighting direction and with improved clarity in the images.

7.6.1. Combustion Stability

The engine intake temperature was set at 60C. The averaged in-cylinder pressure and heat release of a combustion cycle can be seen in Figure 7-9. A series of 23 continuously fired cycles were analysed which was approximately the number of cycles for imaging before the cleaning procedure was required. Through the engine pressure traces and apparent net heat transfer analysis, it was found that the first 5 sets did not reach combustion stability and were therefore discarded. The next 18 recorded cycles were relatively stable and, along with the images, were used for the analysis. The fluctuation of the heat release rate after 30CAD arose once again from the microphonic effect caused by the vibration of the charge amplifier mounted on the frame of the dynamometer. This problem was identified and remedied by removing it from the frame.

The mean of the pressure from the 18 cycles and the standard deviation variation is shown in Figure 7-10. It shows the maximum pressure with a mean of 40.1bar ±1 and a mean peak pressure location of 7.1CAD ±1 CAD and quantifies the combustion stability after the initial starting up period.

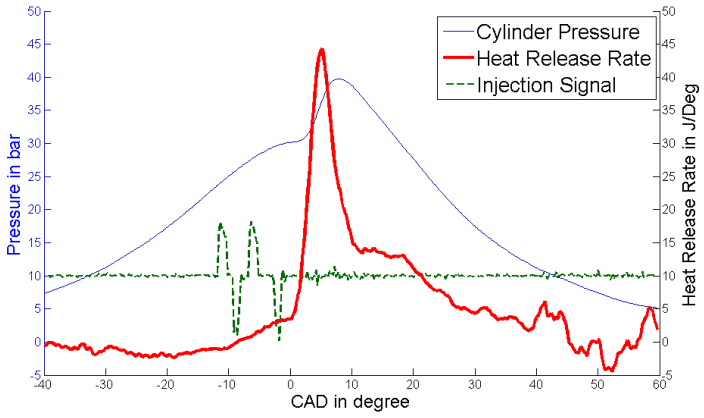

Figure 7-9: Pressure trace and heat release rate for an injection schedule in the Hydra engine taken from the comparable production 4-cylinder engine. The injection signal shows the start of injection after the initial rise in signal and the needle closes as the signal revert. The injection duration is the flat period between the two opposing signals.

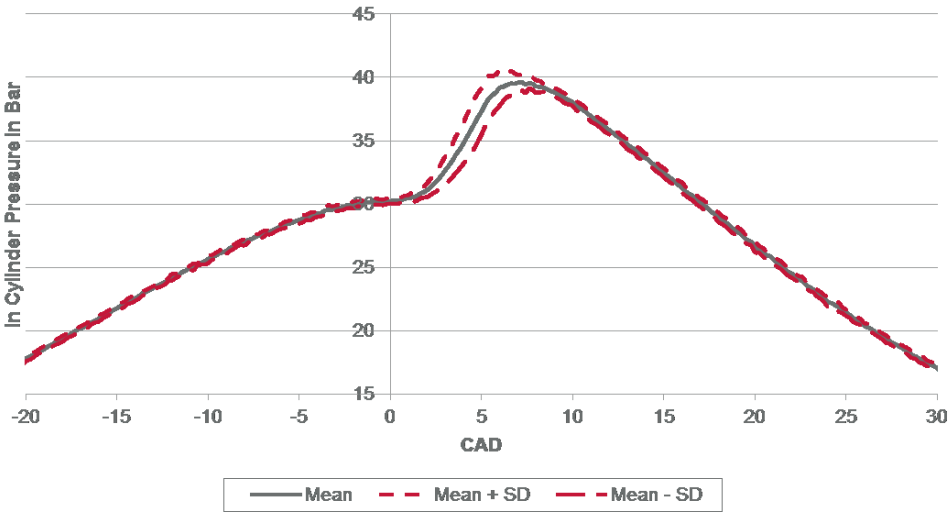

Figure 7-10: Mean cylinder pressure and its lower and upper standard deviation.

7.6.2. High Speed Images of Fuel Injection Spray and Combustion Luminosity

The injection images and combustion images were from a single cycle. These had, however, to be recorded separately as the camera setting for each was different due to the amount of light scattered by the spray, externally illuminated as described before, compared to the "self-illuminated" condition for the combustion luminosity images. This is shown in Figure 7-11. The pilot and main fuel injection events can be seen and the evaporation (and implied mixing) of the pilot injection can be seen at -5.8 CAD. The combustion luminosity from a single cycle is unstructured and it is difficult to find any pattern. It may be useful in the future to process the images further, such as taking an average and to try to find a pattern.

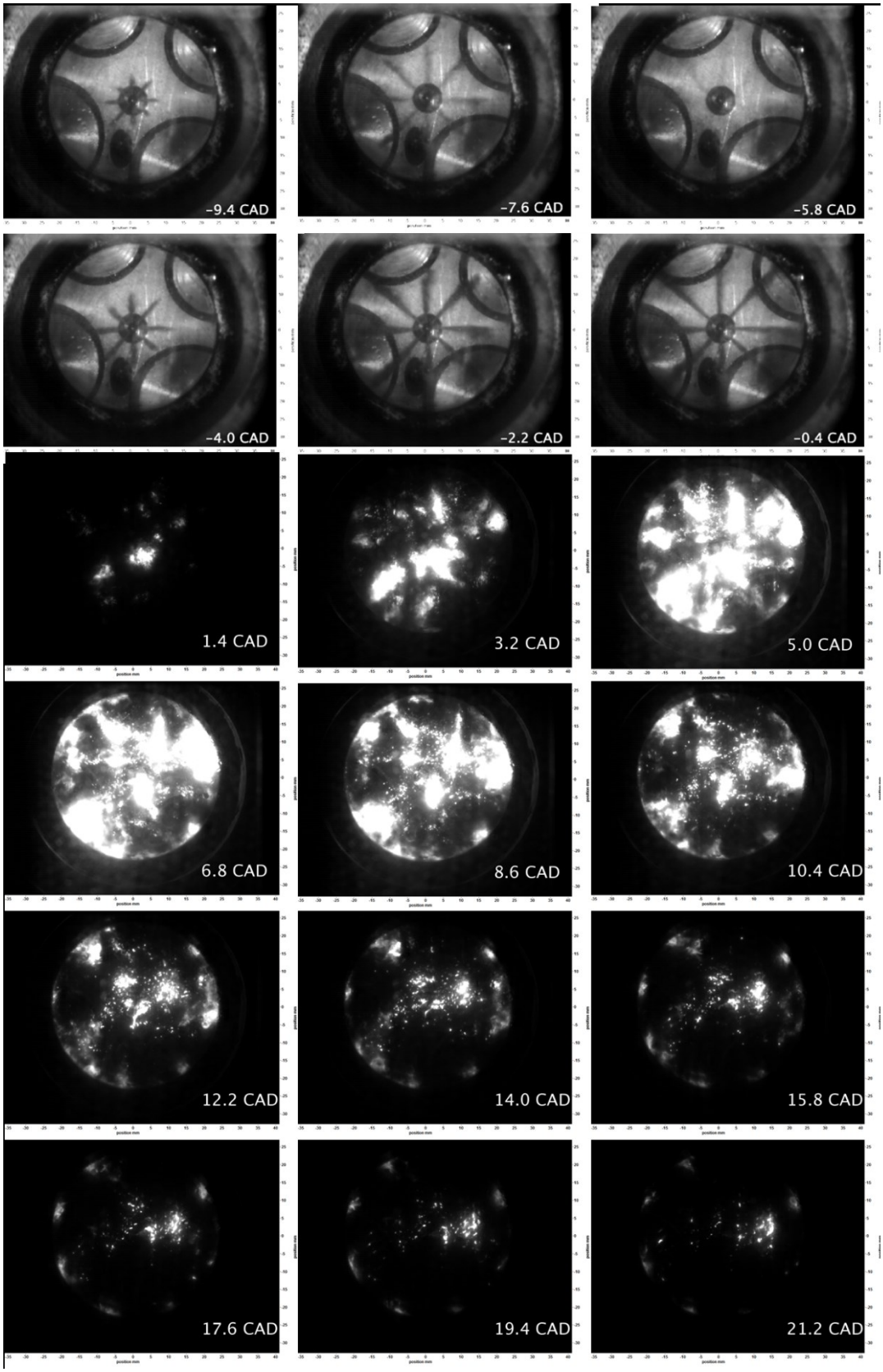

Figure 7-11: Injection and combustion luminosity images from two different single cycles for a condition taken from the production I4 engine at Imperial College. 0 CAD is TDC.

The combustion images were then averaged from 18 consecutive cycles. These images are shown in Figure 7-12. More structures can be seen from the averaged combustion luminosity. It can be seen that the combustion was concentrated along the path of the 8 sprays coming from the injector, slightly modified by the swirling motion of the cylinder. As the luminosity peaked around 5-6.8 CAD, the combustion luminosity began to appear towards the edge of the combustion bowl in the area within the vortex generated between adjacent spray tips created by bowl wall impingement. Then the mixing control burn phase can be reasonably assumed to occur between 12.2 CAD and 21.2 CAD. This set of images can be used as a base case against which others conditions can be assessed as other variables are altered.

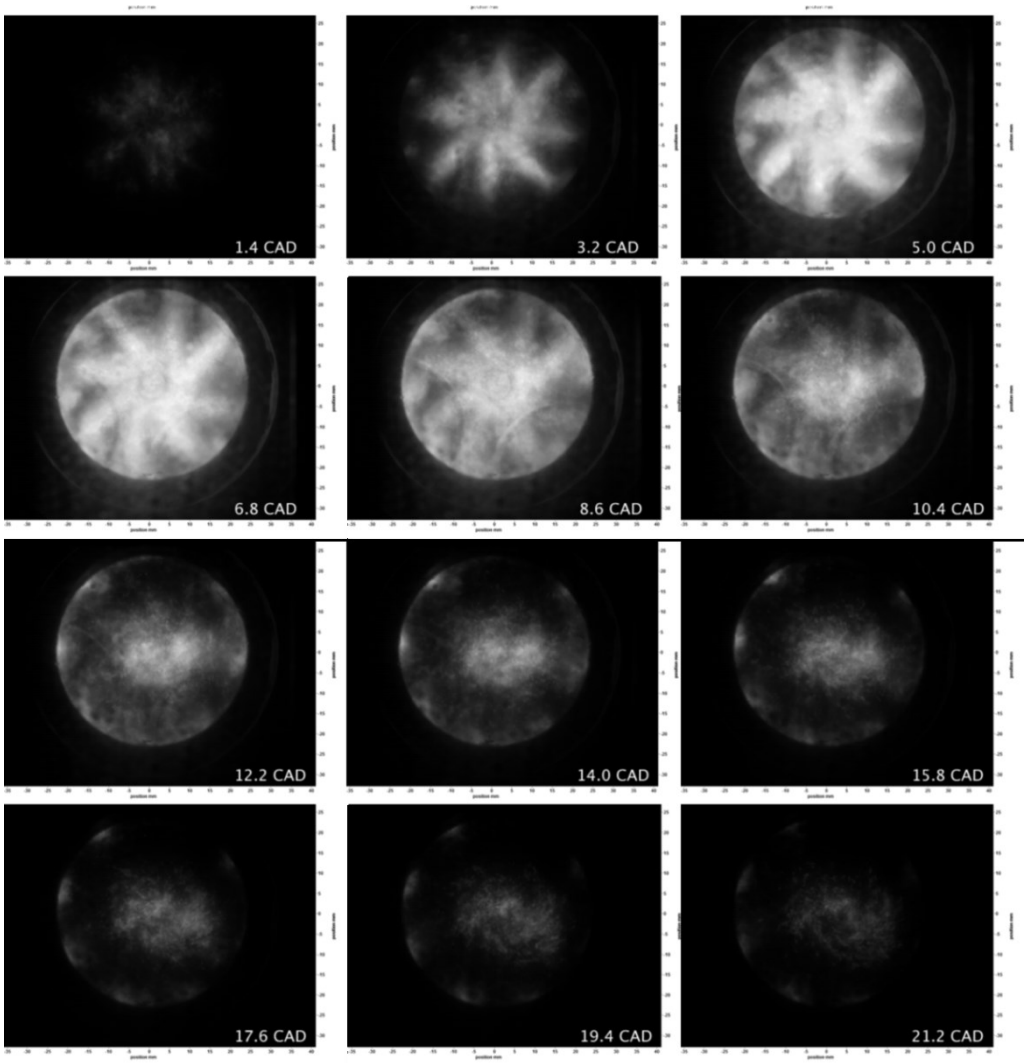

Figure 7-12: Combustion luminosity images averaged over 18 consecutive cycles for a condition taken from the production I4 engine at Imperial College.

7.7. Injection Spray Penetration at Difference Injection Pressure and Timing

Injection penetration is a function of injection duration and injection pressure. There is a balance to be struck between the increase in mixing and improvement in atomisation which accompanies higher injection pressure and excessive fuel penetration that causes wall wetting and hence higher unburnt hydrocarbon emission. This balance is further influenced by varying the injection duration which can be controlled (as outlined in section 1.3.3.1) by the splitting of the fuel into a number of separate, discrete injections. This can reduces wall wetting at high injection pressure while maintaining the amount of fuel injected to maintain the engine load.

With the improved imaging of fuel injection sprays described above, the effect of injection pressure and injection timing on injection penetration was evaluated. The effect of the first pilot injection on a second main injection was also studied.

7.7.1. Testing Condition and Setup

The conditions tested ranged from injection pressures of between 30MPa and 110MPa and injection timings fixed at -10 CAD and 0 CAD respectively. These injection pressures and timings are typical of conventional modern diesel operating condition. The engine speed was kept at 1200rpm, to prevent breakage, given that the inertial stresses vary as the square of the engine speed, with the intake temperature at 70˚C. A series of single injections were recorded at each condition and, since there were 8 holes for each injection, 8 sprays were studied per run. High speed images were taken to find penetration length and the effect of different injection pressure and injection timing. The variables and testing conditions are set out in Table 7-6. The images were taken using illumination through the piston bowl with the high speed camera recording through the same path at 20,000 fps. A total of 5 sets of high speed images were recorded for each condition.

Injection pressure in MPa	Injection timing	Fuel Injected in mg
30	-10 CAD	10
70	-10 CAD	10
110	-10 CAD	10
30	0 CAD	10
70	0 CAD	10
110	0 CAD	10

Table 7-6: Testing conditions for fuel injection penetration study with variation of injection pressure and timing. This condition equates to approximately 1.5 bar IMEP.

7.7.2. Image Processing

Using MATLAB, the fuel injection spray images were adjusted for contrast and processed by subtracting a similarly contrast-adjusted background image, the image immediately before the start of injection. After the subtraction, the intensity of each image that did not reach a certain user-set threshold were discarded and the image was turned into a binary image that showed only the fuel injection spray. As an example of the raw and processed images for the condition of 30MPa injection at -10 CAD see Figure 7-12.

The processed images were then passed through another MATLAB code that measured the penetration length. This was based on the extracting each individual jet from the 8 sprays from the injector and measuring the location of the tip of the spray. The result of the computer programme was checked with a set of data measured by hand and this result is plotted in Figure 7-13. This comparison comprised of 215 samples collected by the two methods and they showed good correlation, with an R^2 value of 0.99 for the fitted trend line. Given the time consuming process of manual measurement, the computer programme was an appropriate tool for measuring the tip penetration length.

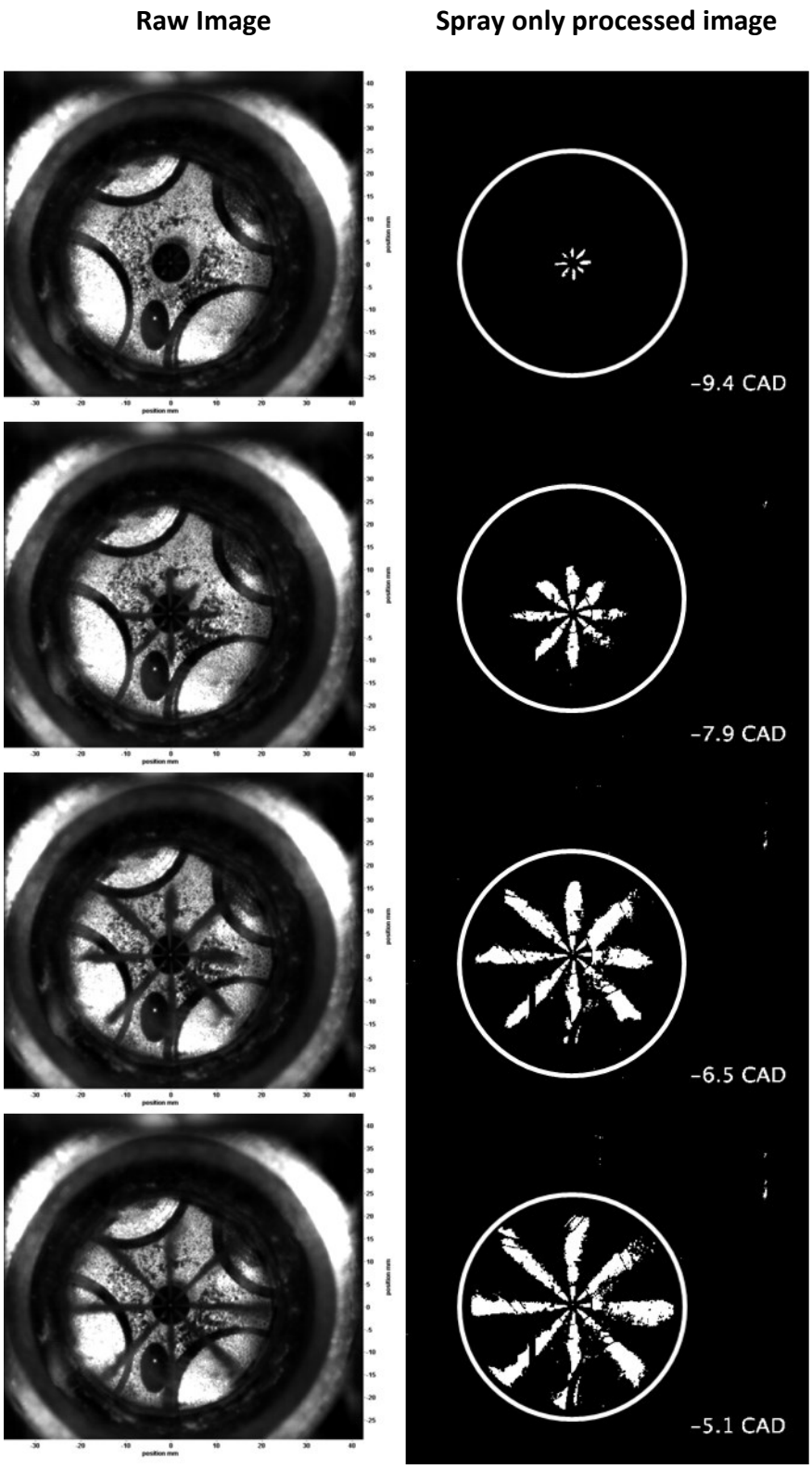

Figure 7-13: Example of the raw fuel injection spray image at 30MPa injection pressure injected at -10 CAD and a processed image with only the fuel spray extracted.

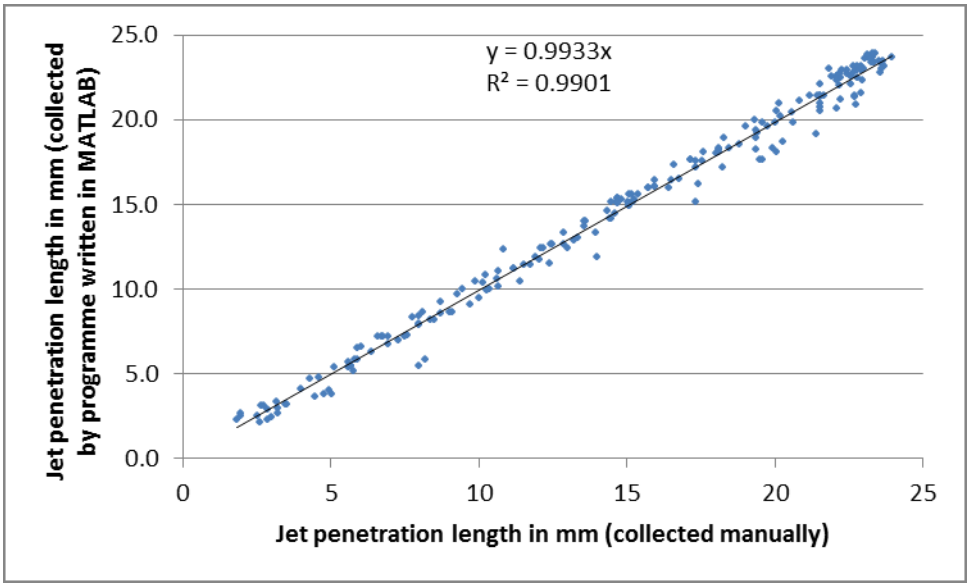

Figure 7-14: Correlation between the computer programme acquired tip penetration length compared to the manually collected values.

There was some optical 'flare' from the engine head features such as the valve which caused difficulty in the measurement of fuel injection spray penetration length. The injector itself created a difference in background colour which needed adjustments: the circular valves and glow plug that can be seen were significantly darker and obscured the measurement of some of the spray, especially the spray jet pointing downwards. These limitations would have to be taken into account when the results were being analysed.

7.7.3. Results of Tip Penetration Length as a Function of Injection Pressure and Timing

7.7.3.

The speed of tip penetration at different injection pressures and at different injection timings can be seen in Table 7-7 which was calculated by averaging 40

7.7.3.

sprays' penetration length over the injection duration until the spray reached the side wall of the combustion bowl. The processed images of the fuel injection sprays at different injection pressures injected at -10 CAD and the cylinder pressure and heat release rate are shown in Figure 7-15. The images for injection at 0 CAD are very much similar and only the statistical data is presented here. The first, expected, observation was that the tip penetration speed increased for increasing injection

pressure. From the heat release rates, it can be seen that the first stage ignition was present for the two higher injection pressure cases. The penetration lengths as a function of CAD after the start of injection are shown on Figure 7-15 where the error bars represents the standard deviation of the measured sample. The error of the measured spray tip penetration based on standard deviation is around ±1.4mm throughout the measurement range. This error arises mainly from the spray to spray variations of the injections.

Injection Pressure	-10 CAD	0 CAD
30 MPa	42 m/s	44 m/s
70 MPa	73 m/s	68 m/s
110 MPa	94 m/s	88 m/s

Table 7-7 Spray time-of-flight based velocity with different injection pressures at different injection timings

The results show injection at -10 CAD has marginally faster penetration speed for both 70 MPa and 110 MPa injection pressure, presumably because of lower cylinder pressure and gas density that the sprays were injected into compared to 0CAD. The cylinder pressure at -10 CAD was 24.3 bar and at 0 CAD, it was 28.5 bar. Other factors such as pressure waves in the injection line and the stability of injection could also have had an effect on the result. Finally, the differences in the spray velocities at the two injection timings were within the error margin from the dataset.

The results can be further investigated by acquiring more samples in order to further improve their accuracy. However, there were inherent variations, as shown by the variation in the standard deviation of the dataset, between injections or even across the 8 different holes. Also, there is an uncertainty in the timing of the imaging camera through triggering which requires further investigation. This can potentially add an uncertainty of ±0.18 CAD to the start of injection timing which is half the time step between images. Although the triggering equipment and timing is set constant for all measurements, the delay through the acquisition system has not been verified. This may have an effect on the determination of the start of injection with the images. From these results, the next step was to compare the measured tip

penetration values with various spray penetration models available. Also, the first stage ignition heat release observed here was investigated.

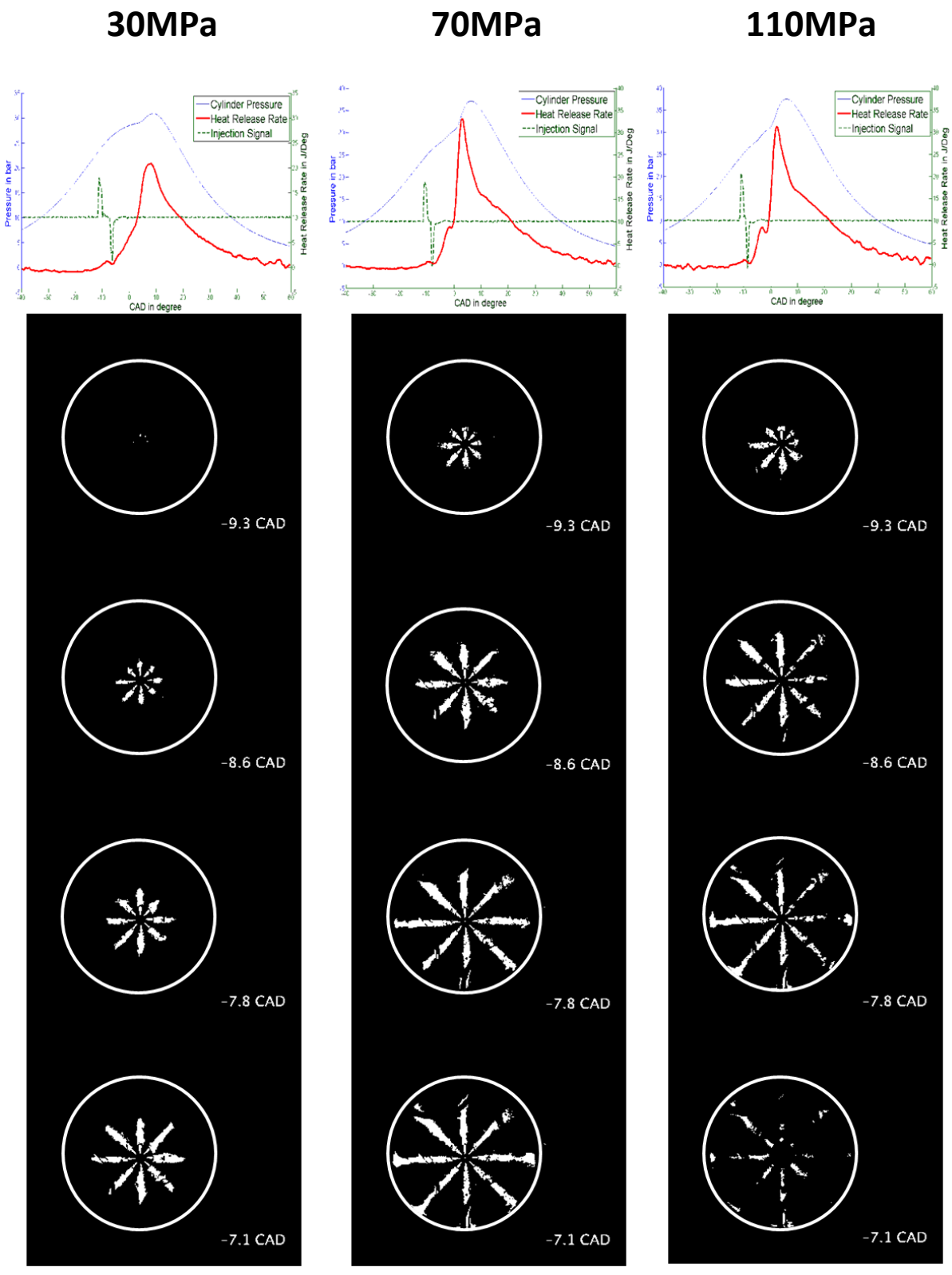

Figure 7-15: Processed fuel injection spray images at different injection pressures at -10CAD and the corresponding cylinder pressure trace and heat release rate.

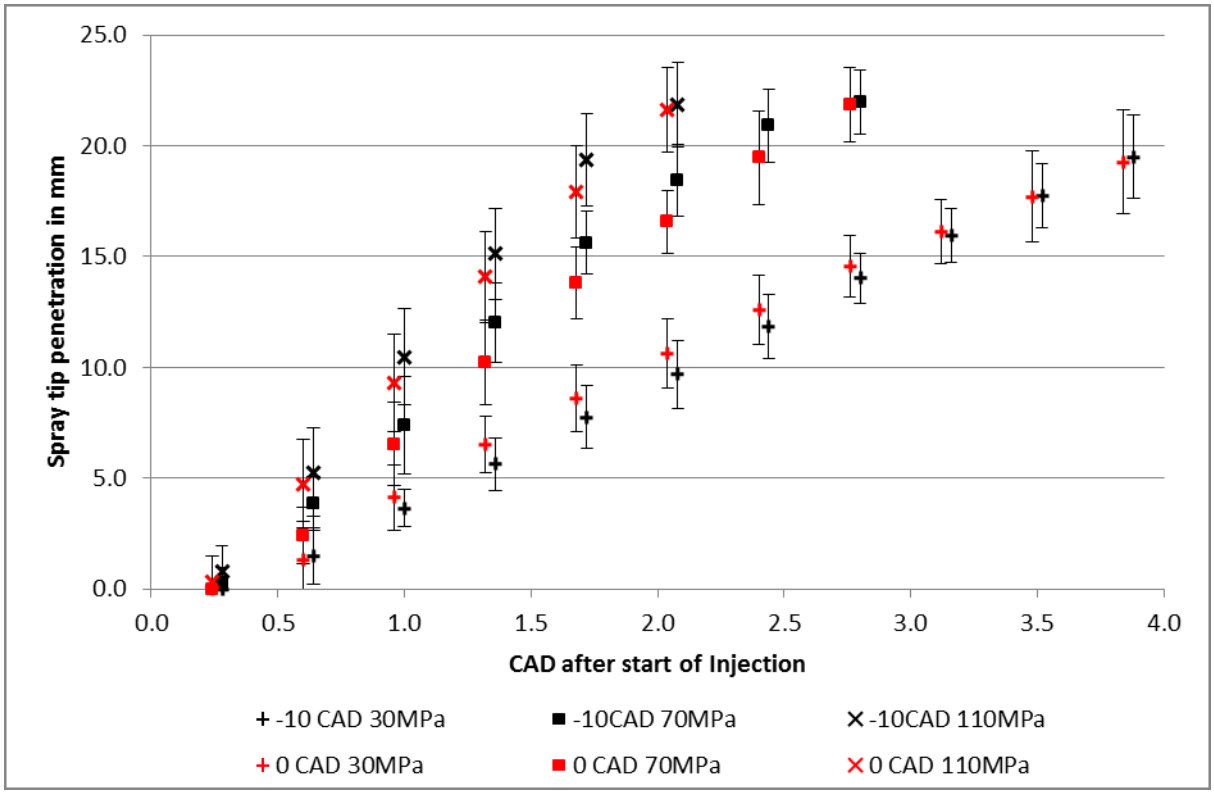

Figure 7-16: Tip penetration length with different injection pressure and at two injection timings as a variable. The "error bars" are the standard deviation of the dataset.

An estimation of the kinetic energy induced into the mixture in the combustion chamber by the injection of fuel can be made by equating the mean kinetic energy from the fuel injection and the increase in the kinetic energy of the gas in the cylinder, ignoring the turbulence kinetic energy of the gas flowing through the valve, any other sources of production and ignoring dissipation.. This can be found using equation (7-2) where the left hand side is the fuel injection mean kinetic energy and the right hand side is the increase in the gas phase turbulent energy in the cylinder. In this equation, m_f is the mass of fuel injected, V_{fuel} is the velocity at which the fuel is injected in m/s, ρ_m is the density of the fuel and air mixture in the cylinder in kg/m^3, u is the turbulent velocity in m/s and V_d is the cylinder displacement in m^3. This can be rearranged to form equation (7-3) to find the turbulent velocity.

$$\frac{m_f V_{fuel}^2}{2} = \rho_m \frac{u^2}{2} V_d \qquad (7\text{-}2)$$

$$u^2 = \frac{m_f V_{fuel}^2}{\rho_m \, {}^{V_d}/_2} \tag{7-3}$$

This can be compared to the turbulent fluctuating velocity due to the piston motion, u in m/s, and without swirl, given in equation (7-4) (Heywood (1988)). The piston speed, $\bar{V}_P$ in m/s can be found using equation (7-5) where N is engine speed in rps and S is the engine stroke in m. The values used for the engine variable used in the equations are shown in Table 7-8. The turbulent fluctuating velocity due to the piston motion was 1.8m/s.

$$u \approx 0.5 \, \bar{V}_P \tag{7-4}$$

$$\bar{V}_P = 2NS \tag{7-5}$$

Variable	Value
Fuel density	830 kg/m^3
Mass of fuel injected	5x10^{-6} kg
Cylinder density of fuel and air	11.2 kg/m^3 for TDC
Engine Displacement	6.23x10^{-4} m^3
Engine Speed	20 rps
Stroke	9.06x10^{-2} m
Turbulent fluctuating velocity due to piston motion	1.8 m/s

Table 7-8: Engine variable for calculating the kinetic energy induced by fuel injection in the cylinder

The calculated results for the cylinder turbulent velocity due to fuel injection are shown in Table 7-9. The cylinder turbulent velocity due to the fuel injection, as a percentage of the turbulent velocity due to piston motion is significant. At high injection pressure of 110MPa, the fuel injection adds 180% turbulent velocity and this significant increase has a large influence on the mixing of the fuel and air. This will have an important impact on the air/fuel ratio given the increase of energy for mixing.

	30MPa	70MPa	110MPa
Velocity of fuel injected in m/s (Measured above)	44	68	88
Fuel injection induced turbulent velocity in m/s	1.7	2.6	3.3
Fuel injection induced turbulent velocity as a percentage of turbulent velocity due to piston motion	92%	140%	180%

Table 7-9: Calculated cylinder turbulent velocity and fuel induced kinetic energy at different injection pressure injected at TDC.

7.8. Comparison of Injection Penetration with Calculated Values from Literature

The fuel injection spray penetration measurements are here compared to various spray penetration correlations in the literature for free spray: widely cited correlations of injection spray penetration are those of Yule and Filipovic (1992) and Hiroyasu and Arai (1990). Hiroyasu and Arai (1990) proposed the penetration length for two different periods to be determined differently. For the period before the breakup length, equation (7-6) describes the penetration length S in m, while equation (7-7) provides the penetration length after the break up length has been reached. C_2 and C_3 are fitted constants, ΔP is the pressure difference between injection pressure and ambient pressure in Pa, ρ_g is the ambient density in kg/m^3, D_N is the nozzle diameter in m, t is the time after start of injection in seconds and t_B is the breakup length of the spray given in equation (7-8) where C_4 is also a constant. The suggested constants from the paper are 0.39 for C_2, 2.95 for C_3 and 28.65 for C_4 though these may have to be adjusted to suit individual cases.

For $0 < t < t_b$:

$$S = C_2 \left(\frac{2\Delta P}{\rho_g}\right)^{0.5} t \qquad (7\text{-}6)$$

For $t > t_b$:

$$S = C_3 \left(\frac{\Delta P}{\rho_g}\right)^{0.25} D_N^{0.5} t^{0.5} \qquad (7\text{-}7)$$

$$t_b = C_4 \frac{\rho_l D_N}{\left(\rho_g \Delta P\right)^{0.5}} \quad (7\text{-}8)$$

Yule and Filipovic (1992) proposed the correlation for the penetration length S (in m) given in (7-9), where C_1 was given as 3.8 and t_B is the breakup length of the spray given in equation (7-10).

$$S = C_1 \left(\frac{\Delta P}{\rho_g}\right)^{0.25} D_N^{0.5} t^{0.5} tanh\left[\left(\frac{t}{t_B}\right)^{0.6}\right] \quad (7\text{-}9)$$

$$t_g = 3.75 \times 10^5 D_N^{-0.28} \rho_g^{-0.05} \Delta P^{-1.37} \quad (7\text{-}10)$$

For the calculations of the conditions pertaining to the injection pressure variation, the values used for the variables are shown in Table 7-10. The adjusted constants for the Hiroyasu calculation were 0.53 for C_2 and 3.8 for C_3. As the injector had a cone angle of 140˚ and the above high speed imaging only accounts for the horizontal component of the spray a trigonometric correction has been applied to the correlation. An illustration of this is shown in Figure 7-16. The results of the calculation are shown in Figure 7-18 for the case of injection at -10 CAD and in Figure 7-19 for the case of injection at 0 CAD.

Variable	Value
Fuel density	830 kg/m^3
Cylinder pressure	28 bar for 0 CAD 24.3 bar for -10 CAD
Cylinder density	11.1 kg/m^3 for 0 CAD 9.92 kg/m^3 for -10 CAD
Nozzle diameter	1.20E-04 m
Intake temperature	343 K

Table 7-10: Values used for various variables for calculating the injection penetration length.

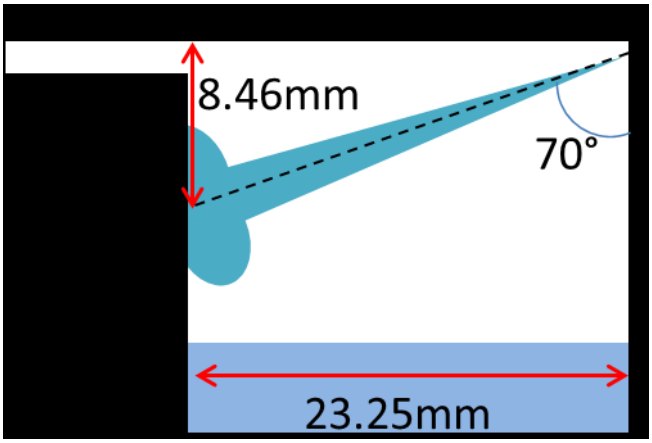

Figure 7-17: Diagram showing a cross section of the combustion bowl with a spray towards the side of the piston with the associated spray angle.

The relationship shows reasonable agreement at the two higher injection pressures but both correlations overestimate for injection at 30MPa. The Yule/Filipovic correlation results in a reduced rate of penetration after an initial period of higher penetration rate that takes into account the different behaviour of the near nozzle and the downstream zones. The correlation underestimates the tip penetration for higher injection pressure while overestimating for the lower injection pressure. The Hiroyasu correlation fits better with the measured data though it still diverges as times goes on, underestimating for higher injection pressure and overestimating for lower pressure. The pattern and accuracy are similar for both injection timings.

There are many potential reasons for these differences: high variability between sprays, accuracy of spray penetration measurement and the uncertainty to the exact start time of the camera timing with the maximum error of 0.36CAD which is the time step between each image is taken. More importantly, the use of common rail injection equipment and higher injection pressure in this case (injection pressures of only up to 15MPa was evaluated in Hiroyasu correlation) compared to the correlations will have an impact. Also, the correlation given is for free jet and the expected strong flow within the bowl in this experiment can be reasonably be expected to reduce the penetration distances for the given values of the variables in Table 7-10. This might explain the improved agreement between correlations and measurements at the higher pressures. Given these many sources, one could comment that the agreement is remarkably good.

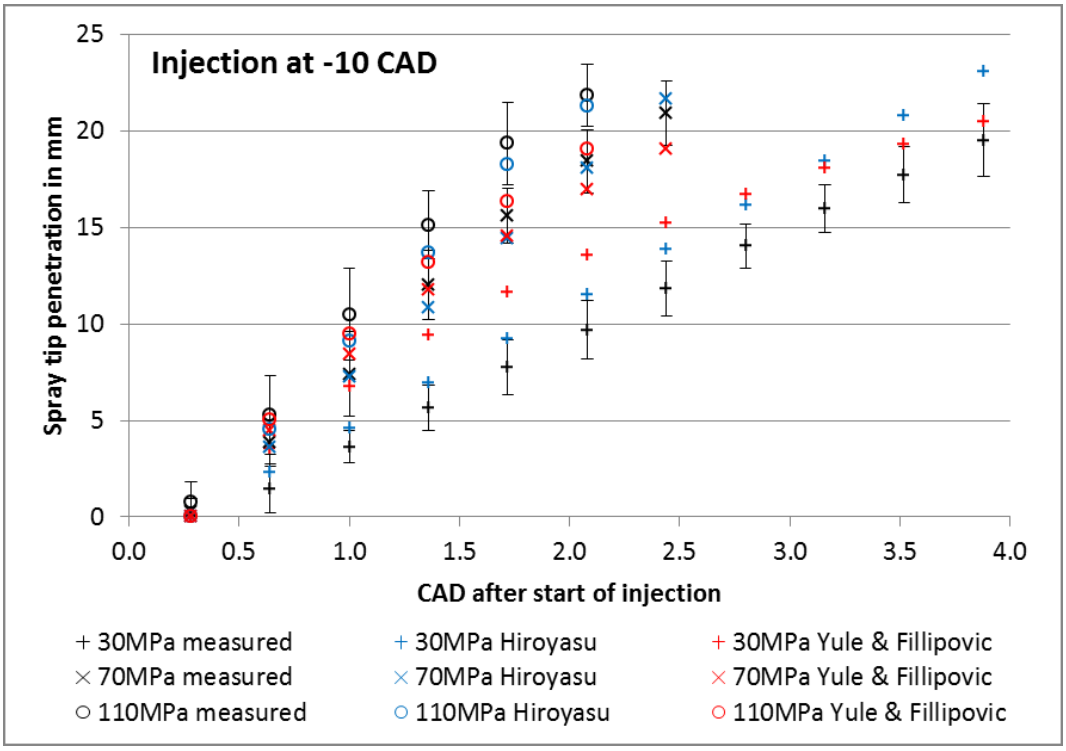

Figure 7-18: Comparison of the measured tip penetration length injected at -10CAD with the values from the correlations of Yule/Filipovic and Hiroyasu.

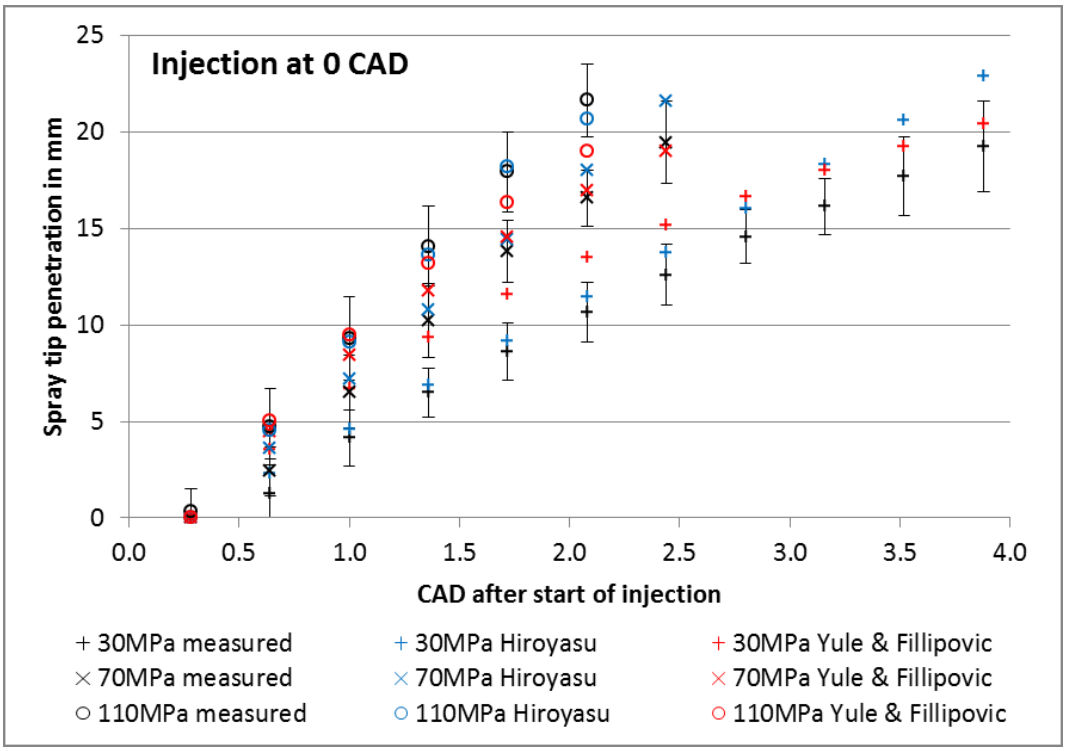

Figure 7-19: Comparison of the measured tip penetration length injected at 0CAD with the values from the correlations of Yule/Filipovic and Hiroyasu.

7.9. Observation on LTR/First Peak of the Apparent Net Heat Transfer Rate

There is, at least for the two higher injection pressures, a small local maximum before combustion TDC in the apparent net heat transfer rate (ANHTR) before the peak in the peak ANHTR, as discussed in 6.3.1.1. This may be a sign of the low temperature reaction. The two peaks are also of comparable magnitude, although the relative magnitude of the two peaks depends strongly on the details of operation. It is therefore interesting to use the pressure traces obtained in the Chapter 6 to examine images from the first maximum of the ANHTR. This low temperature reaction (LTR) is generally not easily visible as it features a blue flame.

Figure 7-20 to Figure 7-22 show that the magnitude of the first peak of ANHTR increases as the injection pressure increases and in fact the first peak. This was not present in the 30MPa case. The images up to TDC were analysed using the background subtraction technique that was similarly used for the fuel injection spray penetration measurement in section 7.2.2. The imaging stopped at TDC because the images were collected for tip penetration measurements and the combustion luminosity produced soon after TDC would have saturated the camera. The result of this can be seen in Figure 7-23 where the raw images for one instance for injection pressure of 110MPa is shown and the processed images for two instances are shown on the right showing the locations for the ANHTR peak.

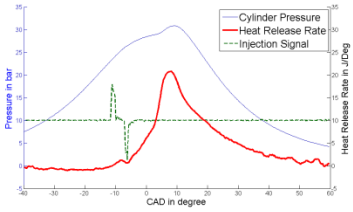

Figure 7-20: No First peak ANHTR for 30MPa injection pressure.

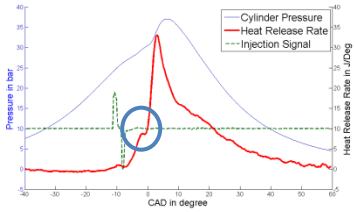

Figure 7-21: First peak ANHTR circled for 70MPa injection pressure

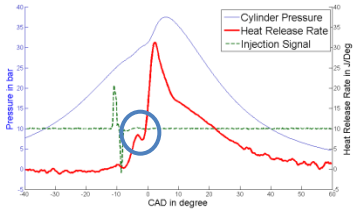

Figure 7-22: First peak ANHTR circled for 110MPa injection pressure

The ignition was barely visible in the raw images and although the first peak ANHTR takes place between -5 CAD and 0 CAD, detectable traces was only available near TDC.

The processed images show faint and sporadic chemiluminescence that grows, concentrated mainly towards the side of the combustion bowl. The ignition sites also followed the trajectories of the fuel jets. As with combustion images, there is cycle to cycle variation and since there were only 5 examples taken, showing the individual instances is arguably more appropriate than the mean of 5 cycles. The low number of cycles was because these were taken for the fuel tip penetration measurements and each containing 8 jets.

The background to the occurrence of this first peak of ANHTR can be related to the low temperature reaction described in section 1.3.1 and 6.3.1.1. For higher injection pressure, the injection duration is shorter and results in more mixing of fuel and air, creating better mixed and locally leaner charge. The turbulent energy contribution to the cylinder motion in terms of velocity at high injection pressure, shown in Table 7-9, demonstrates the significant contribution to turbulent motion inside the cylinder. This increase in mixing produces leaner charge.

Further work can be done with more high speed images of these first stage ignition locations where mean locations of these ignitions sites can be found. Further measurements, such as detection of formaldehyde chemiluminescence which characterises the first stage auto ignition can be performed. Investigations into the relationship between air/fuel ratio and low temperature reactions, as investigated in Hartmann, Lucka et al. (2003) can help to verify the link between the two. This relationship can also be further investigated by visualisation through shadowgraph, Mie scattering and LIF can also be done similar to the work done in Pickett, Kook et al. (2009).

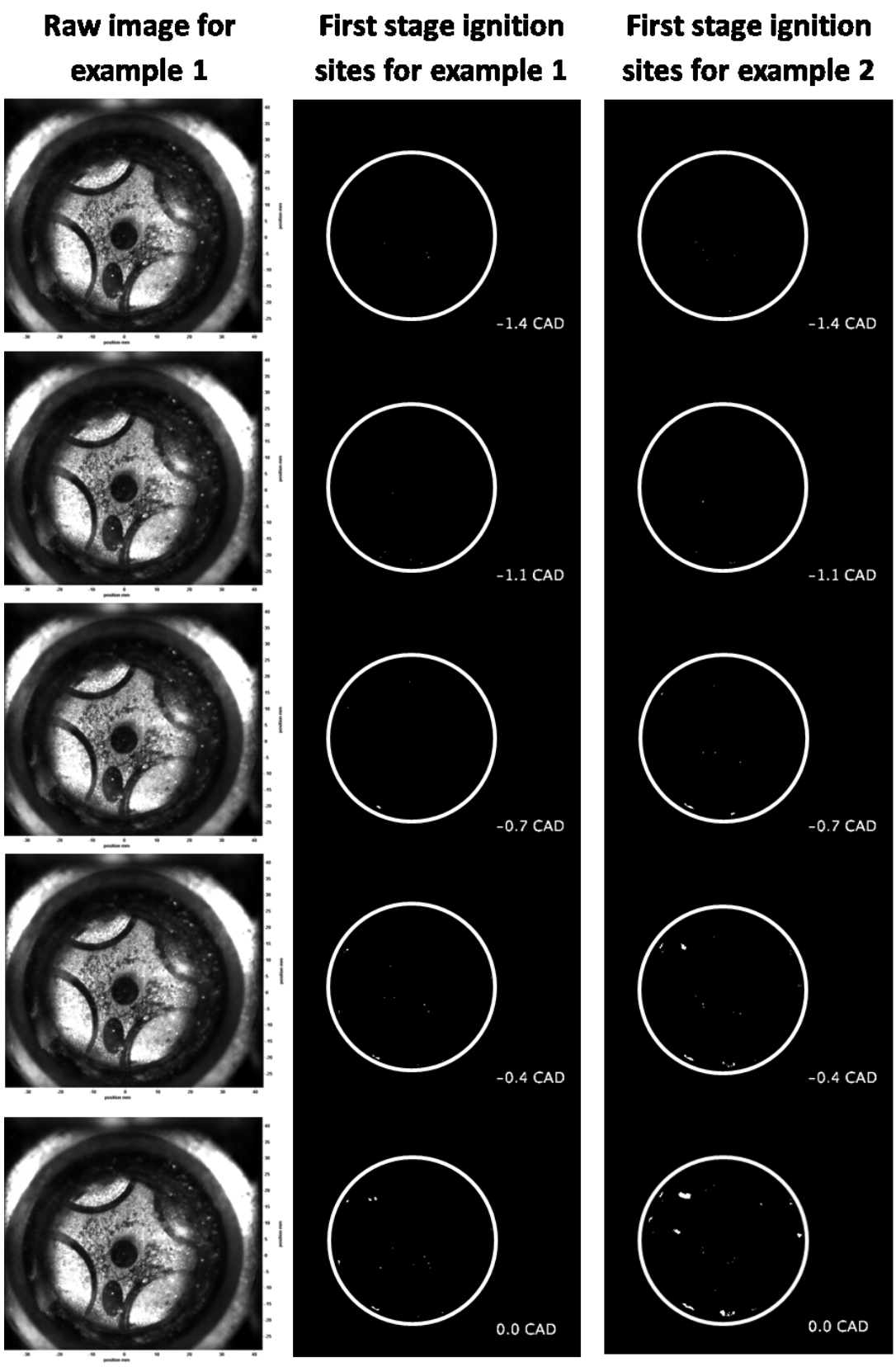

Figure 7-23: Raw image of the first stage ignition for injection pressure of 110MPa and the processed images without background showing the locations of the first stage ignition from 2 examples.

7.10. Effect of Time Delay between the First and Second Injection

The effect of the separation in time between the first and second injection, if any, provides information on the behaviour of consecutive injections for multiple-injection. The main variable affecting the spray dynamics is presumably the separation in time between two consecutive injections and this would affect the environment into which the second injection is injected.

The conditions for this test were an engine speed of 1200rpm, as used in other tests, with intake air temperature of 70˚C along with double injections and a set injection pressure of 70 MPa, the midpoint of the testing range investigated. The fuel injection quantities were fixed at 5mg for both injections, as a low enough value to keep engine load low to protect the engine but high enough so visualisation can be performed and with the same fuel quantity for both injections so the two can be compared. The second injection timing was also fixed so only the first injection timing was varied to test for the effect. The testing conditions are set out in Table 7-11. The optical setup was the same as for the preceding investigation of the penetration length with both the light source and high speed camera optical access through the piston crown at 20,000fps. High speed images were taken to find the penetration lengths as a function of time, from which the velocity of each spray can be derived and thus also the effect of varying the timing of the first injection.

Injection pressure in MPa	First injection timing	Amount of fuel for first injection in mg	Second injection timing	Amount of fuel for second injection in mg
70	-10 CAD	5	-5 CAD	5
70	-15 CAD	5	-5 CAD	5
70	-20 CAD	5	-5 CAD	5

Table 7-11: Conditions for testing the effect of the time delay between first and second injection.

The average velocity profile for each condition at different time interval is shown in Figure 7-24. This was calculated from 5 samples of 8 sprays, giving 40 individual sprays.

The general observation was, as expected, that the velocity of the first injection increased as the injection timing advanced, presumably because of the lower gas pressure and density in the combustion chamber. The second injections, all at -5 CAD, showed a different velocity profile and velocity with the one where first injection took place at -20CAD having the lowest average velocity. The other two injections with first injection at -15 CAD and -10 CAD had similar velocity. The second injection where the first injection took place at -10 CAD show quite a low injection velocity in the first two data points. This may be due to the pressure wave effect in the injector fuel line as the first injection had only finished and this affected the beginning of the second injection. But, by the third data point, the velocity has recovered to as high a value as the other two injection scenarios.

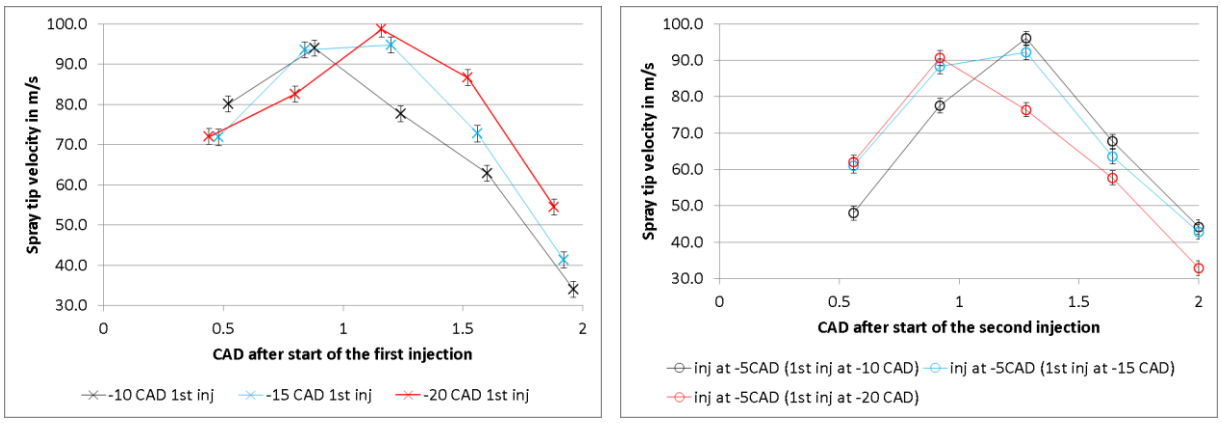

Figure 7-24: The velocity of the spray tip of (a) the first injection on the left and of (b) the second injection (fixed at -5CAD) on the right as a function of CAD after the start of respective injection with the injection timing of the first injection as a variable. The measurement error of 2m/s which is represented in the error bars.

There are some errors associated with the fuel tip penetration measurement method. Each pixel on the images represents 0.1mm and the spray extraction image processing will generate the error of ±0.05mm. This translates to a measurement error of 2m/s which is represented in the form of error bars shown in the figures. There is also the spray to spray variation that leads to the variability of the graph. Then the question is how well the image processing extracts the spray and that is difficult to quantify. But by applying the same image processing process to all the images, the spray length is consistent relative to each other so one can be confident that the result is comparable among the spray at least.

The interaction between multiple injections on diesel combustion is well known and, in particular, the importance of the dwell angle between consecutive injections on this interaction is also well known. One hypothesis for the source of the interaction between injections is that due to the 'slipstream' generated by the first pulse which might affect - and probably augments - both the penetration rate and also the tip velocity of the second jet. In this experiment, Figure 7-24(b) shows that there is not, in fact, a significant effect on the tip velocity of the second injection by the first. The reason for this is presumably that the slipstream effect is maintained for a matter of only a few CAD. Thus the hypothesis is incorrect over dwell angles - as used here - of the order of 5°CAD. This is not to say that alternative hypotheses do not exist. One, for example, is that the kinetic energy of an injection has to be dissipated into turbulent kinetic energy (as calculated above and shown in Table 7-9) and this increased turbulence augments mixing (and chemical reaction) in the combustion chamber, thereby generating an interaction with the following injection.

Figure 7-25 shows the processed images of the second injection as a function of the time of the first injection. The one observation that can be made is that the image at -2.3CAD, for first injection timing at -20CAD (bottom right image), has there are a lot more pockets of fuel compared to the case when the first injection was at -10CAD (bottom left image). This may be related to the dispersion of fuel from the first injection in the cylinder and its interaction with the second. This interaction is not obvious through these images but more work should be done to investigate the effect of shorter dwell timing between the first injection and the second injection.

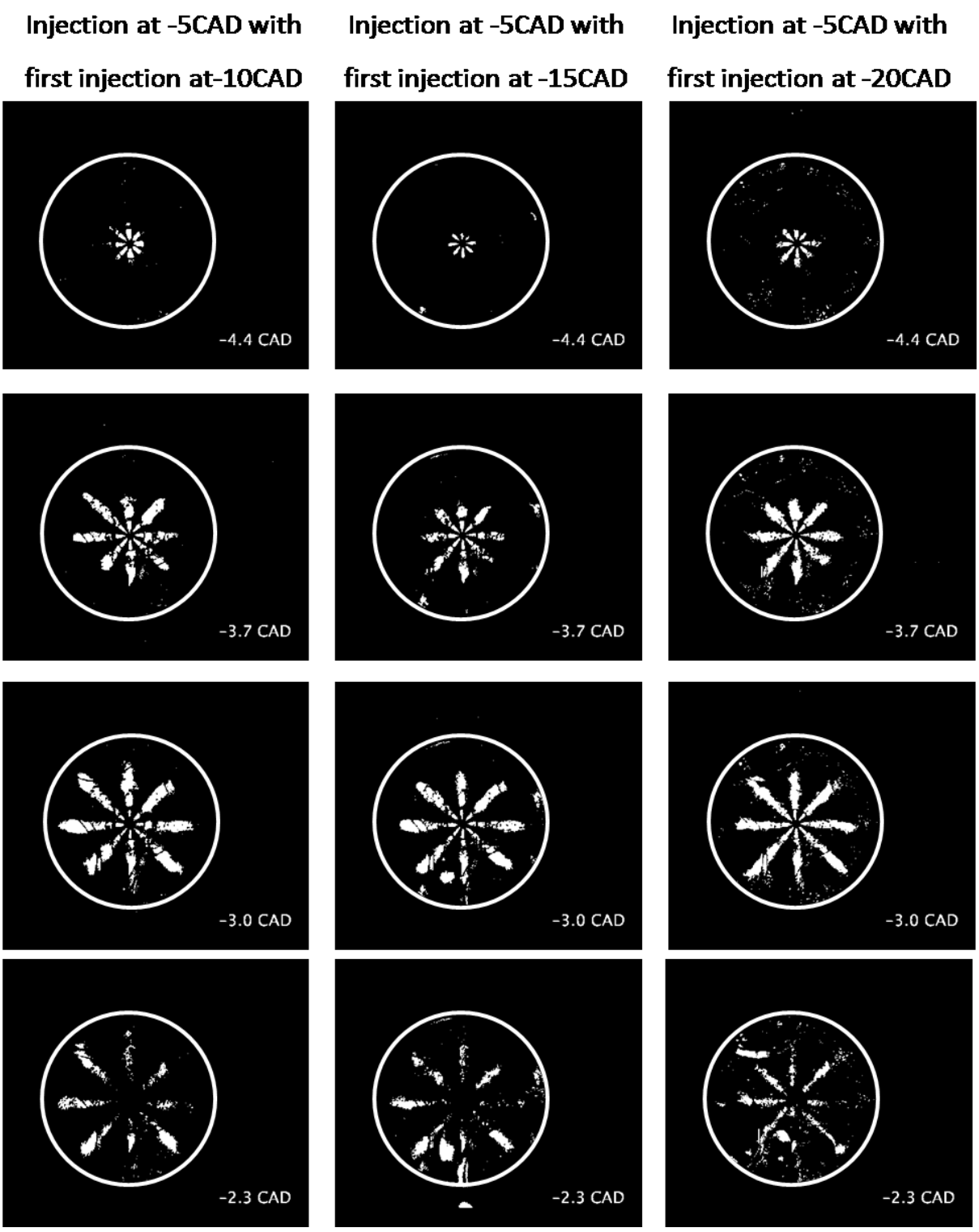

Figure 7-25: Visualisation of diesel spray injected at -5CAD after the first injection at -10CAD, -15 CAD and -20CAD.

7.11. Injection Pressure Effect on Combustion Luminescence

The combustion luminosity derives from the addition of chemiluminescence and soot (thermal) emissivity which is recorded as an image of the aggregate line of sight luminosity over the whole volume of the combustion chamber. Note that the signal received is dependent on the optical density of the whole line of sight and it may well be that the density is such that some of the emission are re-absorbed by the optical medium (primarily the soot). The optical density is the aggregate of all the signals through the depth of the piston bowl.

Some of the conditions for this investigation, set out in Table 7-12, are continuing the investigation of injection pressure variations but using double injection instead of a single injection. The pilot injection quantity used was higher than would be usual in a production engine but this condition provided the more interesting combustion characteristics in terms of heat release rate found during the engine testing phase. The main injection timing was varied so the CA50 was matched at 8CAD between the three injection pressures. But in reality, the injection timing of the three injection pressures for the same CA50 were all at the same time at -3.5CAD. The high speed camera viewed the combustion chamber through the piston crown and there was no need for a lighting source as the combustion luminosity itself was to be recorded. 25 sets of images were taken with the camera triggering at -3CAD and recorded for 120 images at 20,000fps.

Variable	Value
Engine Speed	1200 rpm
Intake Air Temperature	70 ˚C
Injection Pressure	30, 70 and 110 MPa
Pilot Injection Timing	-10 CAD
Pilot Injection Quantity	5 mg
CA50 (main injection timing adjusted accordingly)	8 CAD (main injection at -3.5 CAD)
IMEP	1.7 bar (main injection quantity of 6mg)

Table 7-12: Testing condition for fuel injection spray imaging with light source through the piston.

7.11.1. Combustion analysis

The cylinder pressure and heat release rate is shown in Figure 7-26 for 30MPa injection pressure, Figure 7-27 for 70MPa injection pressure and Figure 7-28 for the 110MPa injection pressure. The LTR/cool flame phase was less prominent for the 30MPa case but similar between 70MPa and 110MPa cases. There was ignition before the start of the main injection for the 70MPa and 110MPa cases, presumably due to the better atomised spray at the higher injection pressure and more intense mixing creating a mixture that could be ignited earlier than when using the 30MPa injection pressure. The dip in heat release after the initial heat release was probably also affected by the evaporative cooling effect of the second injection, but it is also caused by the presence of the first ignition phase cool flame as discussed previously. From the heat release rate, it could be expected that the combustion luminosity will have a similar pattern for the 70MPa and 110MPa cases.

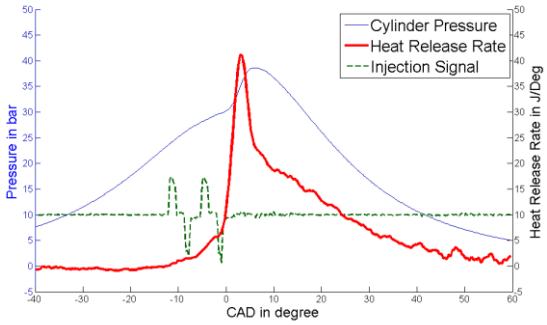

Figure 7-26: Cylinder pressure and heat release rate for 30MPa injection pressure.

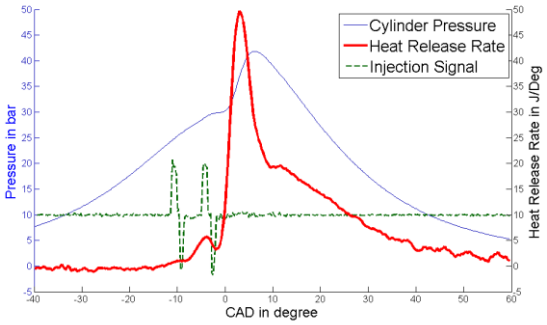

Figure 7-27: Cylinder pressure and heat release rate for 70MPa injection pressure.

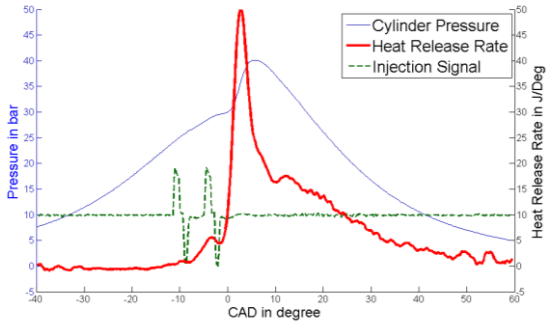

Figure 7-28: Cylinder pressure and heat release rate for 110MPa injection pressure.

7.11.2. Image processing

Different methods in processing the recorded natural luminosity images were explored. The first was to calculate the average of the signal at each frame of the set of high speed images across the set of data. The second was based on the spatial locations of the signal and the probability of the occurrence at the locations over the dataset and a probability function map of the locations was produced. These methods are described in further detail below.

7.11.2.1. Method 1: Simple Averaging

The first method was to average the 25 sets of images at each frame (every 0.36 CAD) of the set of high speed images which produced a phase-averaged luminosity signal and location. The result was a set of greyscale images. To enhance the legibility of the resulting figure, a false colormap was applied to the intensity scale which is normalised against the highest signal level to 1. For the purposes of comparison, these two representations are shown in Figure 7-29 for the case of the 30MPa injection pressure. The colormap images have better contrast and detail and are more useful for visualising the results. Note the images have a ring of signal outside the piston bowl wall and that is a reflection of the luminosity signal on the base of the metal piston below the glass piston.

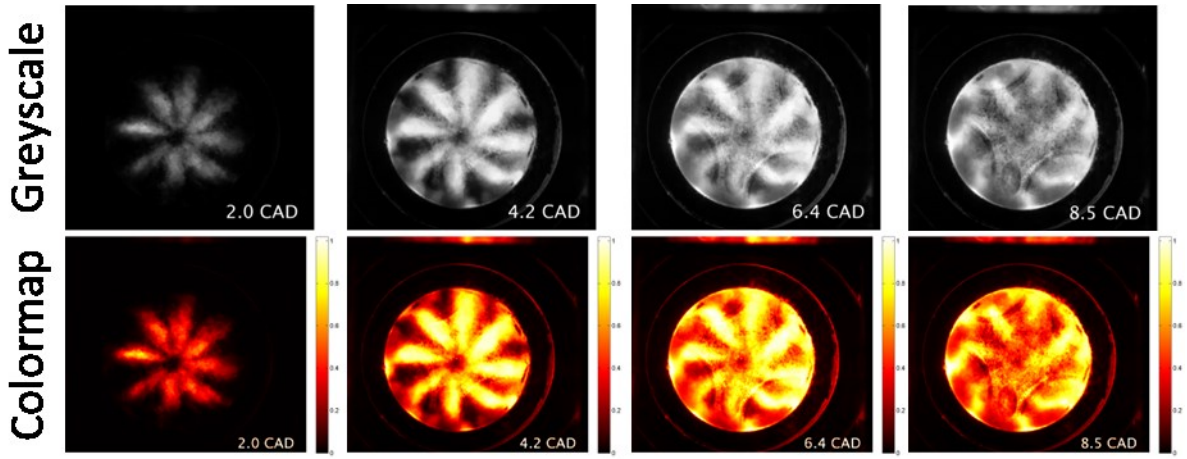

Figure 7-29: Comparing greyscale and colormap images from ensemble average combustion luminosity at 30MPa injection pressure. The colormap scales is normalised to the highest value of each image and set to 1.

7.11.2.2. Method 2: Probability Function of Luminosity Locations

The second image processing method was to map the locations of the signal and plot these as a probability function map for each step as explained here. Each frame from each set was set a threshold and the locations of the signals were turned into a binary image. The threshold was chosen so the resulting binary images represented the locations of the combustion luminosity and without noise such as the reflection shown in the averaging image above. The binary images derived from the population of 25 for each time step were then added to form a frequency distribution of luminosity location. The maximum possible frequency at each pixel was therefore equal the number of sets recorded, which was 25 in this case. The aggregate image of luminosity frequency was normalised to provide an image of the spatial distribution of probability of a detection of a luminosity signal and rendered as a false colour map.

The data set and the comparison between the two is shown in Figure 7-30. It can be seen that the probability of detection of a luminosity signal eliminates the reflective outer ring better than the simple phase-averaging method. It also shows better defined combustion luminosity structures and more focused view of the combustion. This was therefore the method chosen for the data acquired.

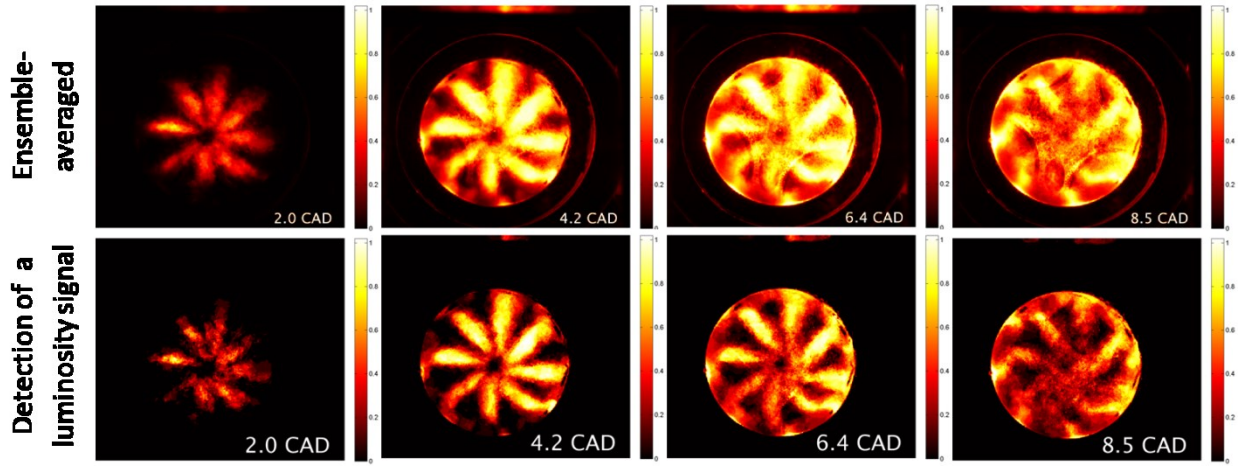

Figure 7-30: Comparison between colormap images of normalised averaged values and probability of detection of a luminosity signal at 30MPa injection pressure.

7.11.3. Comparing the Effect of Injection Pressure on the Probability of Detection of a Luminosity Signal

The first comparison shown is the normalised, ensemble averaged luminosity for each condition as a function of crank angle. This was calculated by the summation of absolute signal level from each pixel from all the images of the whole data set from every crank angle and then finding the ensemble average at each pixel at each time interval. This value was then normalised for all three injection pressure conditions by the maximum value from all three injection pressures and the result is shown in Figure 7-31.

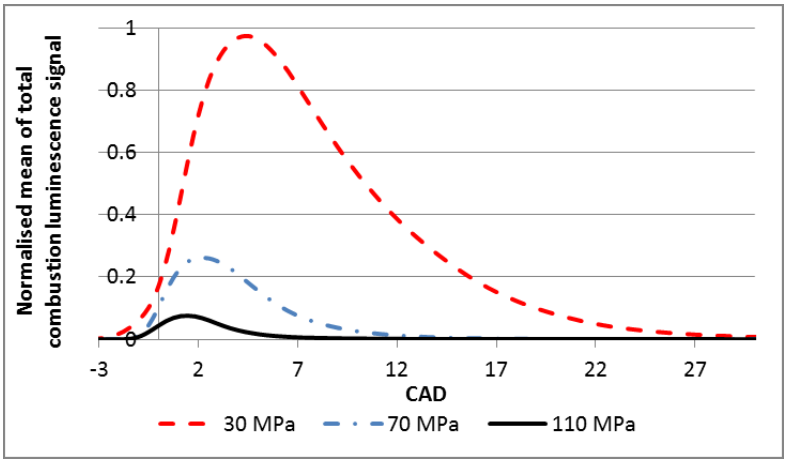

Figure 7-31: Normalised ensemble averaged luminosity signal as a function of CAD with injection pressure as a variable.

The figure shows that luminosity starts at more or less the same CAD that the luminosity and the CAD at which maximum luminosity arises both decreases as the injection pressure increases. Also, the duration of luminosity decreases with injection pressure increase, an observations which might not be foreseen from the ANRHT in Figure 7-26 to Figure 7-28 above. This can be further illustrated by the probability of detection of a luminosity signal at various CAD for the three injection pressure of 30MPa, 70MPa and 110MPa, shown in Figure 7-32. Note that the contour levels in each image was normalised against the maximum value at each CAD, so these are not comparable to each other in terms of absolute value.

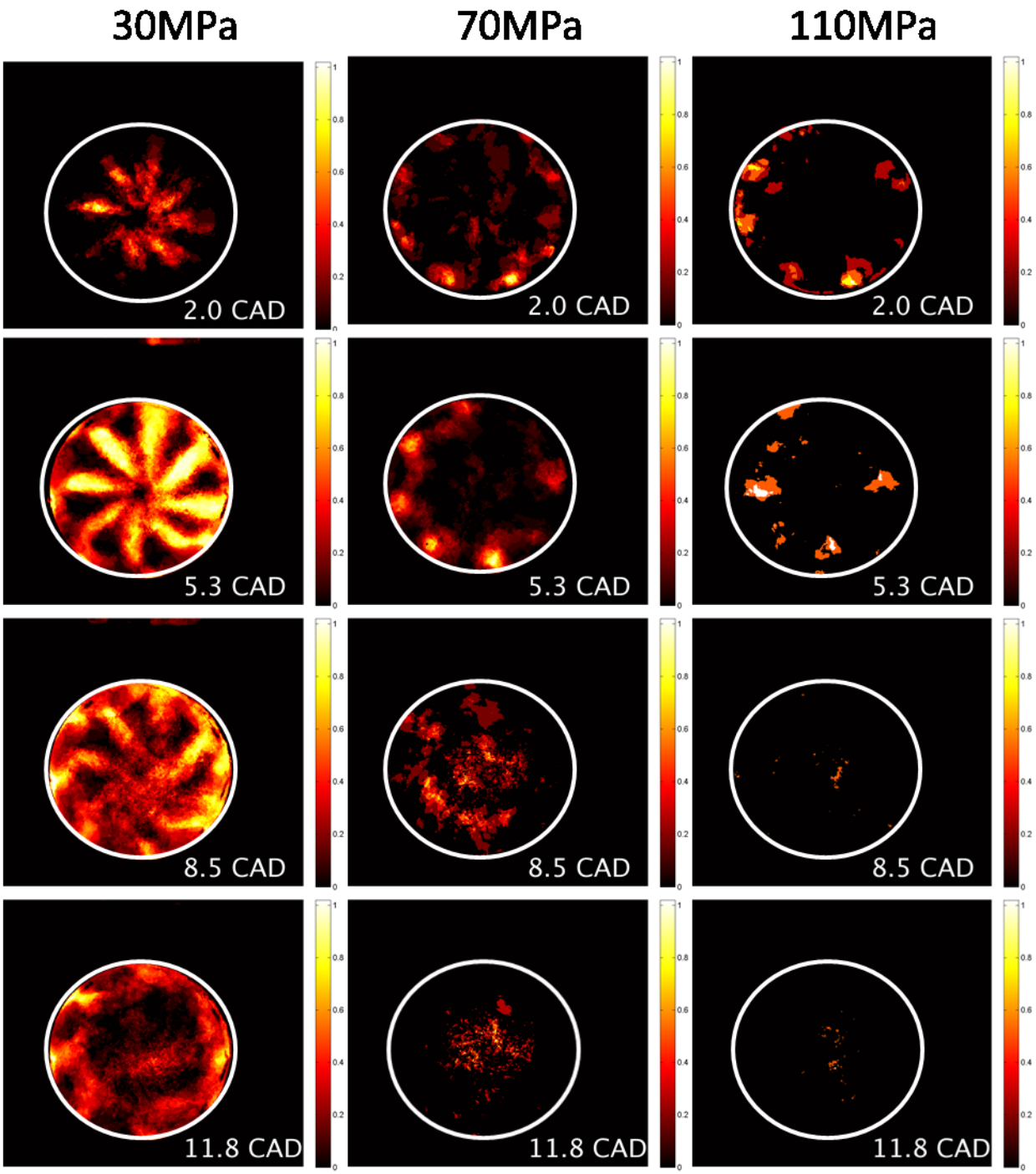

Figure 7-32: Comparison of normalised probability of detection of a luminosity signal at different injection pressure. Note that the contour levels in each image was normalised against the maximum value at each CAD, so these are not comparable to each other in terms of absolute value.

For the 30MPa injection pressure case, the combustion luminosity lay both on the spray trajectory as well as around the wall of the combustion bowl where the spray

is known to have impinged. Note that the effect of the swirl is visible on both the part of the luminescence around the spray trajectory as well as on the bowl's wall. This is emphasized by the image shown in Figure 7-33 with the spray jet path overlaid onto the combustion luminosity at 5.3CAD and further illustrated by a drawing highlighting the sooting areas. The swirl structure of the flow is clearly visible. Note that the exhaust valves lie towards the top of the image which may have an influence on the relative temperature distribution in the combustion chamber. As the combustion progressed, the luminosity was increasingly concentrated towards the wall of the combustion bowl.

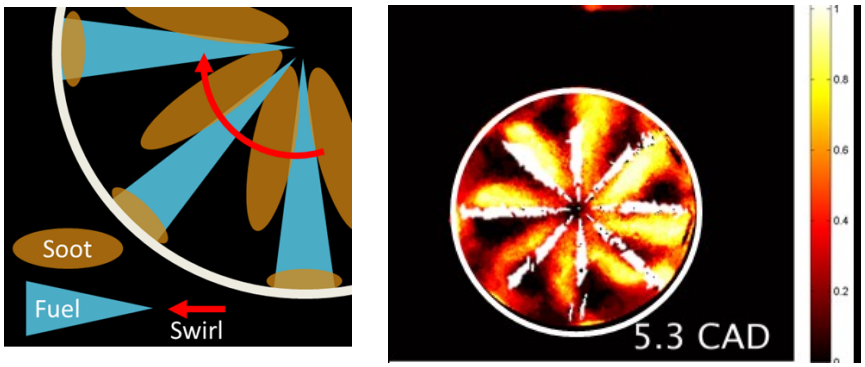

Figure 7-33: Illustration of soot location and a superposition of the injection spray locations over the probability of detection of a luminosity signal image for 30MPa case at 5.3CAD.

In contrast, for the 70MPa injection pressure case, the combustion luminosity for the premixed combustion phase was not detected about the spray trajectory but rather first appeared, and was concentrated, towards the wall of the combustion bowl. The luminosity locations were between the tips of the injections spray which coincides with the vortex structure after the spray wall interaction of the sprays, as described in section 1.3.6.5.

These luminosity locations are illustrated in Figure 7-34 showing the fuel jet spray path overlaid onto the combustion luminosity image and highlighting the sooting areas. Due to the mixing and interaction between two adjacent sprays, this sooting vortex region highlighted was presumably relatively richer than other locations, producing higher combustion luminosity. The relative reduction of combustion luminosity compared to the 30MPa case, in Figure 7-31, was caused by a

combination of improved atomisation of fuel and improved mixing with air, the consequent leaner charge then producing lower combustion luminosity. As the combustion progressed (after 8.5CAD in Figure 7-32), the luminosity concentrated towards the centre of the combustion chamber during the premixed combustion phase as it progressed from the outer edge to the middle.

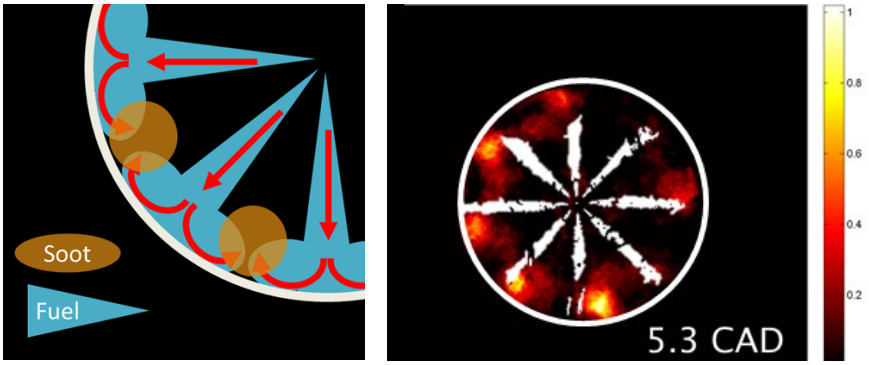

Figure 7-34: Illustration of soot location and a superposition of the injection spray locations over the probability of detection of a luminosity signal image for 70MPa case at 5.3CAD.

For the 110MPa injection pressure case, the combustion luminosity was again towards the wall of the combustion bowl. Similarly to 70MPa case, the locations of combustion luminosity concentrated in the area between the spray tips, where the adjacent spray jets mixed together after the wall impingement. The images show a continuation of the trend apparent in the 70Ma injection images, although the luminosity was weaker compared to the other two injection pressures.

Comparing with the combustion luminosity recorded for the conditions using production engine calibration shown in Figure 7-12, the 30MPa injection images were the most similar. This is to be expected given that the injection pressure for the production engine calibration was 25MPa. The high level of combustion luminosity concentrated towards the centre of the combustion bowl in both the 25MPa and 30MPa cases. Further work can be done to analyse the emission from the different conditions and apply different injection pressures tested here to the metal engine to relate to the soot emission.

7.12. Initial Combustion Luminosity

This sub-section identifies the locations where the combustion luminosity first appeared and compares these between the three injection pressures. The images shown occur at different CAD because they have different first occurrence of combustion luminosity. But the difference was only small, with the start of second injection at -5CAD for the 30MPa case, -4.6CAD for the 70MPa case and -4.8CAD for the 110MPa case. It is to be noted that the beginning of visible combustion luminosity does not necessarily mean the start of ignition. This is because the combustion luminosity from processes such as the first stage ignition cool flame phase was not easily visible, especially with the dynamic range of the sensitivity of the camera set up to avoid saturation at the highest luminosity.

Figure 7-35 shows the first probability of detection of a luminosity image where there were a reasonable number of ignition sites so the locations can be representative of the condition. As might be expected from previous combustion luminosity images, namely Figure 7-32, for the 30MPa injection pressure the first visible combustion luminosity towards the centre of the combustion bowl and, as the injection pressure increased, these locations moved towards the wall of the piston bowl.

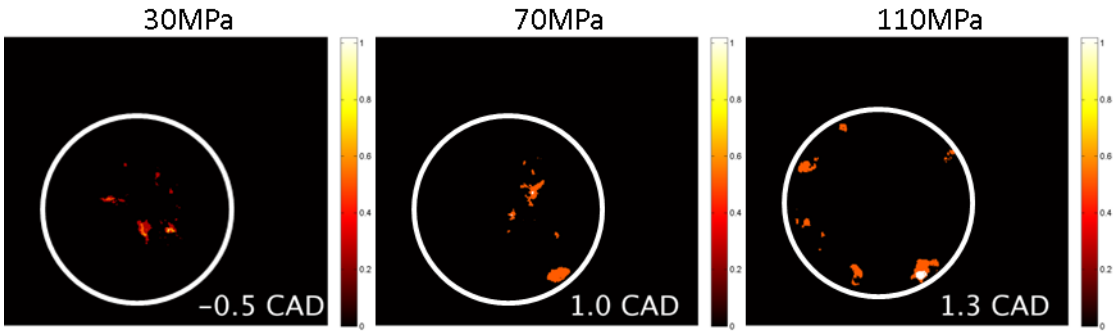

Figure 7-35: initial ignition sites at different injection pressures.

Further analysis was carried out by looking at the subsequent visible combustion luminosity and its development. This is shown in Figure 7-36. The first few frames showed little activity for the lower injection pressure cases while the 110MPa had more luminosity locations appearing simultaneously soon after first detection of combustion

luminosity. This maybe a sign of a more uniform distribution of the fuel and air mixture producing conditions favourable for ignition at more isolated locations than at lower injection pressures. As with the previous observations, the locations are towards, or at, the wall of the bowl for higher injection pressure cases due to the ignitable fuel air mixture forming near the combustion bowl wall at higher injection pressure.

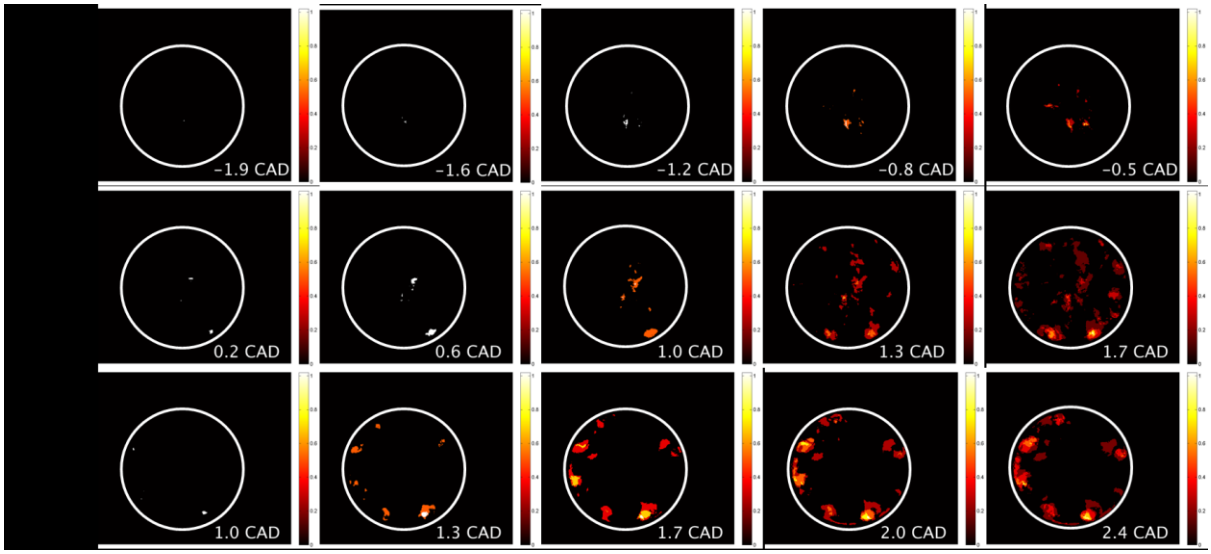

Figure 7-36: Probability of detection of a luminosity signal location images after the start of combustion luminosity detection for the 3 different injection pressures.

Finally, Figure 7-36 shows the superposition of the probability of detection of a luminosity signal onto an instantaneous image. This shows one instance of the variations between different injections. An example of this is shown in Figure 7-36 for the case of 30MPa at -0.5CAD. The benefit of this image is that the instantaneous image also shows the fuel injection and it can be seen that the combustion luminosity came from between the sprays instead of along the spray trajectory. This analysis can be applied to all images but is a time consuming task if every instantaneous image were to be analysed individually. This is example nevertheless shows the possibilities of this analysis.

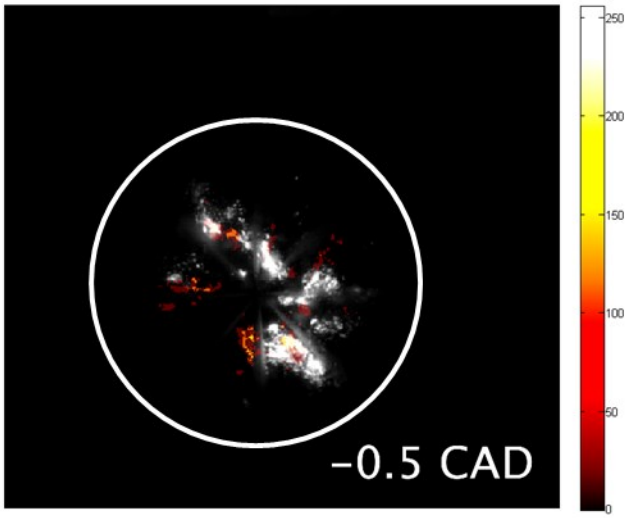

Figure 7-37: Probability of detection of a luminosity signal location images (coloured) superimposed on an instantaneous luminosity image (greyscale) at 30MPa injection pressure at -0.5CAD.

7.13. Proper Orthogonal Decomposition (POD) Analysis of Combustion Luminosity

A further analysis on the combustion luminosity images was carried out to find whether there were any underlying structures, in the context of the method of Proper Orthogonal Decomposition (POD) was used, in the temporal development of the combustion luminosity at a given injection pressure and whether there were common features amongst the injection pressures. The steps, taken from Petrou and Petrou (2010), can be summarised as follow: (a) any image can be represented as a vector with length equal to the number of pixels in the image; (b) that (a) implies a hyperspace in which each image is represented as a single POINT; (c) that a set of images is a cluster of points in this hyperspace; (d) that there exists a new, "natural" coordinate system which is aligned with axes of symmetry (in the least mean square sense) of this cluster; (e) the autocorrelation matrix of the cluster in the new coordinate system is 'diagonal'; (f) the tricky step is the following: an axis of symmetry necessarily implies a direction in which the variance of the cloud is 'large' and that is what a 'feature' is.

7.13.1. Mathematical Background

The analysis has been set out in Holmes, Lumley et al. (1996). The ensemble scalar field **U** consists of the dataset, in this case k samples of combustion luminosity intensities. Each image was transformed into a one dimensional array and collated into a single matrix as shown in equation (7-11).

$$\boldsymbol{U} = [\boldsymbol{u}^1\ \boldsymbol{u}^2\ \ldots\ \boldsymbol{u}^k] \tag{7-11}$$

Then find the autocorrelation function **R**:

$$\boldsymbol{R} = \boldsymbol{U}^T\ \boldsymbol{U} \tag{7-12}$$

And solve the eigenvalue problem to find λ:

$$\boldsymbol{R}\ \boldsymbol{\varphi} = \boldsymbol{\lambda}\boldsymbol{\varphi} \tag{7-13}$$

The set of eigenvalues can then be arranged in ascending order $\lambda_j \geq \lambda_{j+1}$ and order the same with the corresponding φ. The POD modes n can then be found and a snapshot $\tilde{u}$ for each mode can be reconstructed:

$$\widetilde{\boldsymbol{u_n}} = \boldsymbol{\varphi_n U} \tag{7-14}$$

The number of modes corresponds to the number of sets of data. The quotient $\frac{\lambda_j}{\sum_{i=1}^{k}\lambda_i}$ is the proportion of the variance that each eigenvector represents.

7.13.2. POD Analysis Results

The POD analysis was carried out on the combustion luminosity images for the three injection pressures and 25 modes were created for each time interval for each injection pressure across the set. An example of the result is shown at 4.6CAD in Figure 7-38 showing the first 5 modes of from the POD analysis for the three injection pressures along with, in the left most column, the corresponding images from the phase-averaged probability density of combustion luminosity sites. The absolute values and the colour of each mode is not important but locations of the maximum signal (red shades) are.

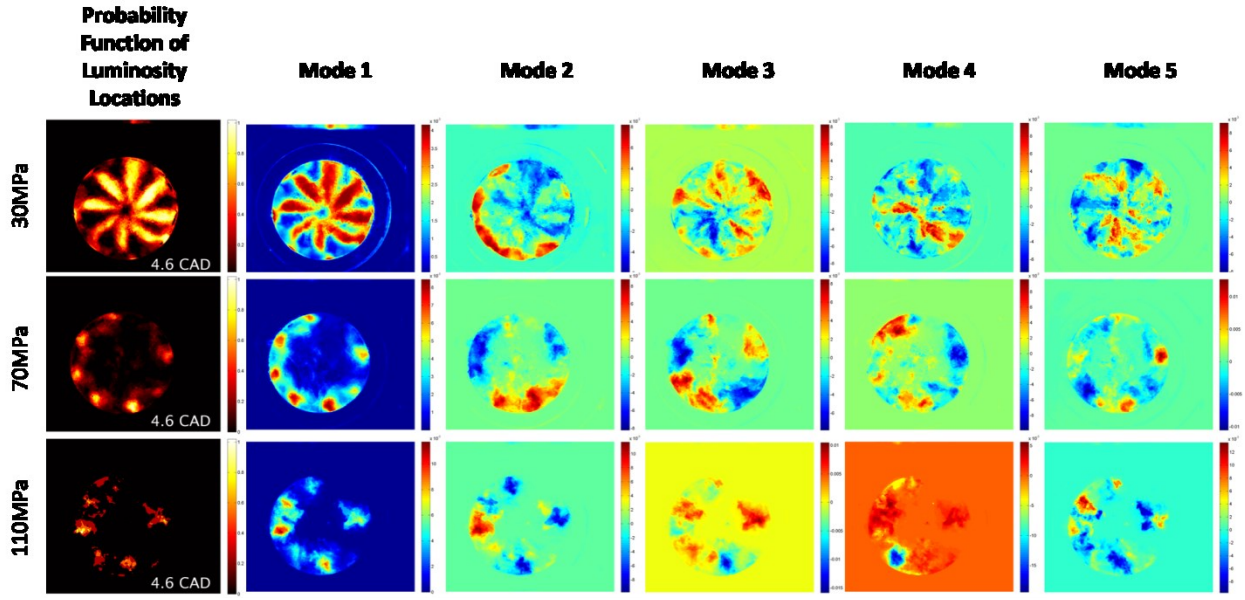

Figure 7-38: First 5 modes for the three injection pressures at 4.6CAD along with, on the left most column, the images from the phase-averaged probability density of combustion luminosity sites.

Unsurprisingly, mode 1 was similar to the averaged image, showing the most frequently appearing features for all three injection pressures. Mode 2 shows that there is large variability, i.e. 'structure', associated with the combustion adjacent to the wall of the bowl for all three injection pressures. (In addition, for the 30 MPa injection pressure, there is some weak structure along the trajectories of sprays at 10, 1 and 4 o'clock). For the 30 MPa case, the strength of mode 2 between 5 and 10 o'clock might not be surprising given its coincidence with the clearly 'weaker' luminosity associated with the asymmetry present in the mean image on the far left of the row. In contrast, for the two higher injection pressures, the weak luminosity - and hence asymmetry - in the mean images lies between 12 and 4 and 6 o'clock: that is to say at the opposite side for that of the low injection pressure, which is surprising. Even more surprising is that the structure in mode 2 is associated with the sprays with strong luminosity, which is also the opposite of the result for the results for the 30 MPa. Thus the distinct structures for the 30MPa case have some similarity with the averaged image for the 70MPa, showing the combustion "structures" to be near the combustion bowl wall. This is highlighted in Figure 7-39. This is an interesting result showing 30MPa consisted of both its own combustion

characteristics of strong combustion luminosity towards the centre and also the feature of the 70MPa/110MPa cases where the combustion luminosity concentrated towards the bowl wall, in the vortex area in between sprays created by wall impingement.

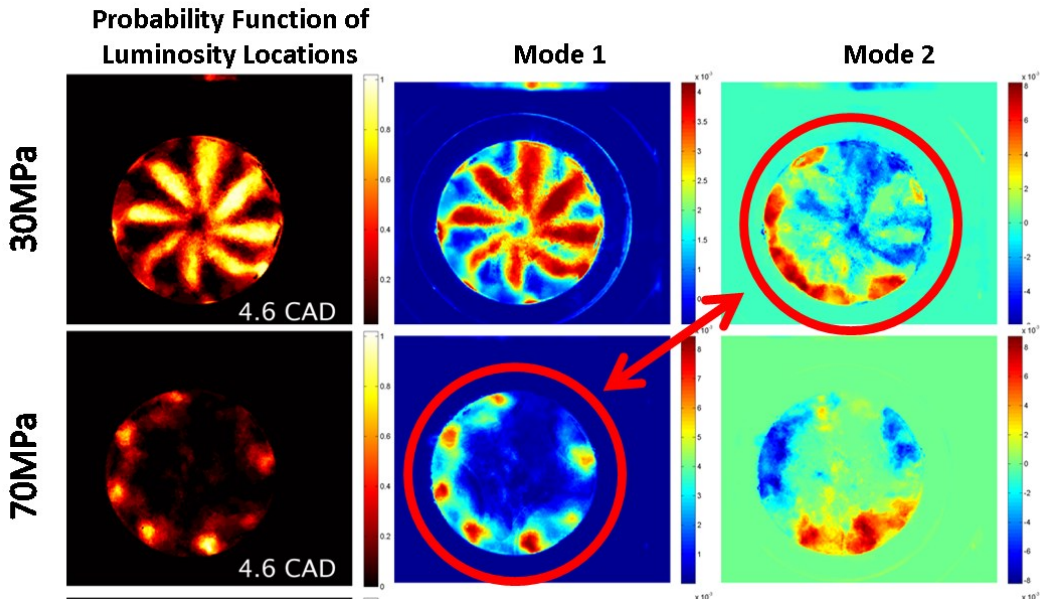

Figure 7-39: Enlarged comparison showing the similarities between mode 2 of the 30 MPa injection pressure case and mode 1 of the 70 MPa case.

The significance of the structures revealed by the POD analysis are to show that the mean spray pattern of an injector hides as much as it reveals, given that the generation of pollutants can be expected to be radically different between the 'free trajectory' across the bowl and the combustion adjacent to the wall. Some of this structure would have been revealed by images of the rms fluctuation about the mean intensity : what could not have been revealed by an rms plot is the 'coherence' in the rms structure and that coherence can also be expected to modify the amount and pattern of pollutant generated adjacent to the wall of the bowl.

A study was carried out to find whether there is a combustion phasing and ignition timing variation and its effect on the subsequent POD analysis. The CA10 values from the pressure trace of each set of images were analysed and it was found that the standard deviation of the CA10 points for the set of images at each injection

pressure was found to be 0.2CAD, 0.1CAD and 0.1CAD for 30MPa, 70MPa and 110MPa injection pressure respectively. Given that the high speed images were taken at an interval of 0.36CAD, the difference is not large enough to be isolated by shifting the reference point of the POD analysis. In terms of the heat release rate, the standard deviation of the cumulative heat release rate at -0.4CAD for the three cases, which was the mean CAD for CA10, was only 1.1% among the data set. This means the change in the combustion phasing/ignition timing is too small to alter the result of the POD analysis.

Before the presentation of the higher modes, it is important to examine the relative energies associated with each mode and the different injection pressures. The relative energies of the first 20 modes of the different injection pressures are shown In Figure 7-40, which shows that both the 30MPa and the 110MPa cases have relatively strong first 3 modes whereas the 70MPa case dropped rapidly after the first mode. As the mode number increases, fewer coherent structures could be identified, with only the 30MPa injection pressure case showing a pattern of stronger signal in the areas between injection sprays in mode 3. This is the power of POD which has the ability to isolate different structures that are not immediate obvious in a set of fluctuating and turbulent processes.

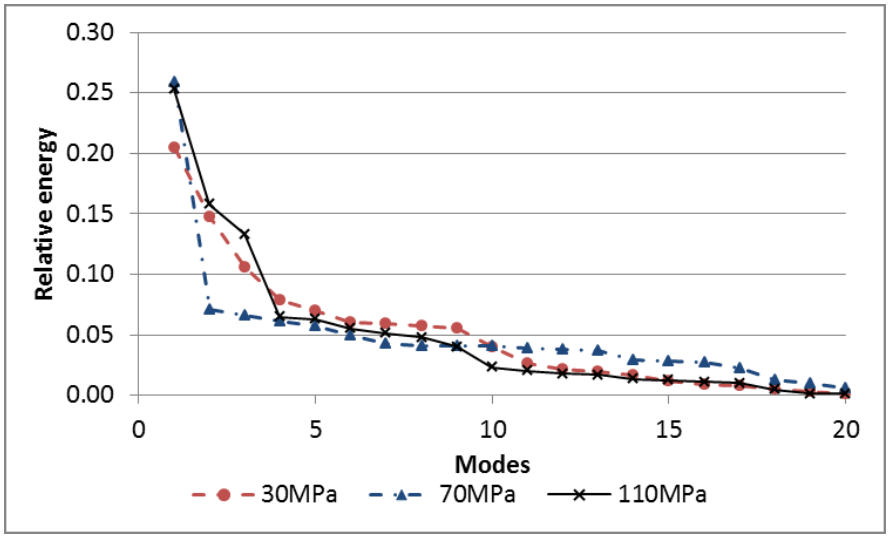

Figure 7-40: Relative energy of the first 20 modes for the three injection pressures.

Figure 7-41 shows the first three modes for the three injection pressures with 'snapshot' shown at seven crank angles. These can be compared with the probability function of luminosity locations images shown on the top row. This figure thus gives an overview of the development of the three modes as a function of crank angle. Similar analysis to the one made earlier on the 30MPa injection pressure can be made regarding the different combustion features throughout the first three modes. This applies to a certain extent for the 70MPa at 1.7CAD where mode 2 and 3 shows some evidence of activities along injection spray path. In some respect, mode 1 of the 30MPa case corresponded to mode 2/3 of the 70MPa case and mode 2 of the 30MPa case corresponded to mode 1 of the 70MPa case.

This can be seen as a description of the combustion modes that take place with the two injection pressures. While the 30MPa case is dominated by combustion luminosity along the injection spray itself, there is also a secondary component of combustion in the vortex mixing area in between the spray tips created by wall impingement. Whereas in contrast, this latter is the dominant feature for the 70MPa case while the combustion luminosity along the injection spray itself is a minor feature. This complexity was not present in the 110MPa case and only a small amount of luminosity from the vortex mixing area between the spray tips was visible and POD analysis failed to provide more information due to the low level of signal.

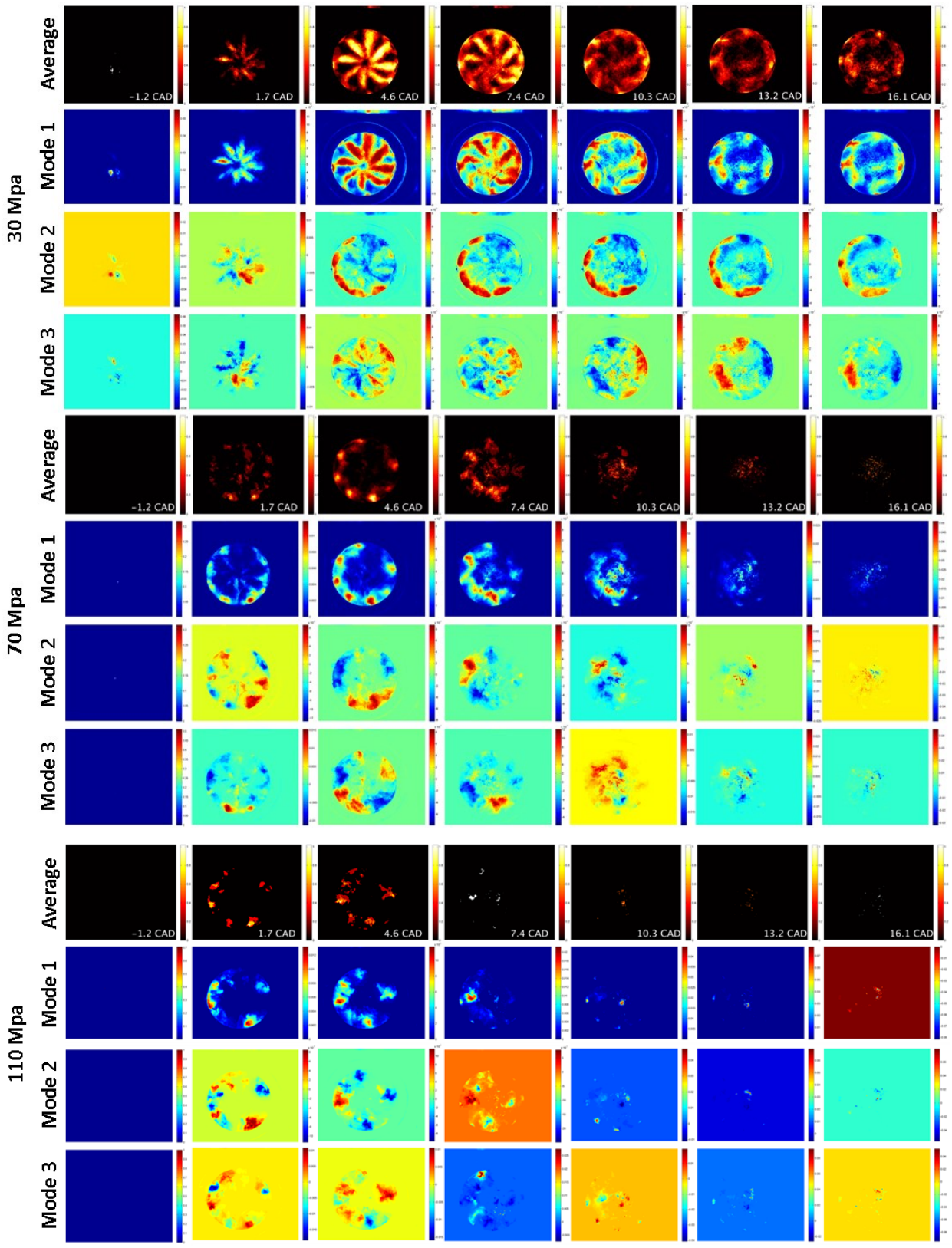

Figure 7-41: Comparison of different injection pressure and the first 3 modes through different CAD.

7.14. Chapter Conclusion

High speed imaging work was carried out and described in this chapter. The setup and imaging capability were tested and different lighting options were explored and found the best route was to illuminate through the piston crown. Imaging filters such as CH chemiluminescence was used and proved to be an useful tool for further investigation.

Swirl measurements were taken and found the swirl to be 3.44. Then high speed images of a condition from a "set point" in the calibration of the production engine were taken as a reference for other testing condition. Different injection pressures and timings were tested to find the injection penetration lengths and mixing processes. An image processing code was developed for finding the injection spray penetration length. The injection spray penetration length results from the experiment were compared with two spray length penetration models and reasonable agreement was shown. Observations on first stage ignition/LTR from the previous chapter were further investigated using high speed images showing some evidence of its presence and confirmed the difficulty in visualising it.

The effect that the first injection has on the second injection was also investigated and effects of the dwell time between the two injections have on injection velocity. The combustion luminosity and its variation with injection pressure was analysed and methods of presenting the results were explored. The relationship between the increase in injection pressure and the reduction of combustion luminosity was clear. The locations of the start of combustion luminosity were examined and POD analysis on the combustion luminosity images was performed. This analysis identified combustion features along injection jet paths, between the jet paths and the vortex zones between spray jet tips created by wall impingement.

Further work can be carried out on using different filters to look at chemiluminescence such as OH, C_2 and CH to further provide information on variables such as injection pressure and timings. The CH chemiluminescence work can be extended by making a more statistically reliable averaged to be compared with the combustion luminosity

images. More work can be done on the injection penetration tests with a higher number of samples to provide greater statistical confidence in the findings. The spray angle can be found from the injection images with further image processing development.

Further work can be done to analyse the emission from the production engine, applying the conditions and injection pressures used in for the high speed imaging work on the Hydra. Also, the first stage ignition/cool flame can be investigated by measuring formaldehyde chemiluminescence and LIF. Other engine variables such as intake temperature, injection timing and injected fuel quantity can be investigated for combustion luminosity analysis and other optical diagnostic techniques.

The engine should be modified to include synthetic EGR through the introduction of CO_2 and perhaps simulate the effect of boost by scaling the injection pressure and inlet temperature.

8. Initial Results from Laser Induced Incandescence in Hydra Engine

8.1. Introduction

The result from the high speed imaging work with variation of injection pressure can be extended further and the laser diagnostic linked to combustion luminosity on soot distribution is Laser Induced Incandescence (LII). This can be used to visualise the soot particles within the combustion chamber at different injection pressures and in particular at CAD after natural luminescence is detectable which, to a crude approximation, is also the point at which soot oxidation ceases. Thus, such images show, broadly speaking, the soot which will become the "engine out" emission.

Two forms of LII were attempted here but the result of only one is presented due to equipment and timing constraint. The result for the planar LII technique, as reviewed in chapter 1, to visualise the distribution of soot particles in the combustion chamber is presented for various injection pressures. The other technique is the two color time resolved LII for individual soot particle temperature evolution, as described in Chapter 2, and this gives the size of soot particles. The calibration of the equipment is described here and the experiment can be performed when the equipment eventually becomes available. The combination of the two techniques will give an overview of the soot characteristics and distribution at different injection pressures.

8.2. LII Equipment and Experimental Setup

The Hydra engine was setup with incorporation of two diametrically opposed side windows in the cylinder liner and gave access of the laser sheet to the combustion chamber across the top of the piston for intervals before -30 CAD and after 30 CAD. The image of soot incandescence was taken through the glass piston crown using the 45 degree mirror for both the planar LII and two color LII. The laser used for energising the soot particles was a Quanta-Ray Pro 270-10Hz laser operating at 532nm wavelength with 900mJ per pulse. The laser pulse had a width of 1-2ns. A focused laser sheet was formed using a series of cylindrical lens from Thorlab the focal lengths of -50mm,

150mm and 1000mm and the sheet had a width of 25mm. The associated optical arrangement is shown in Figure 8-1.

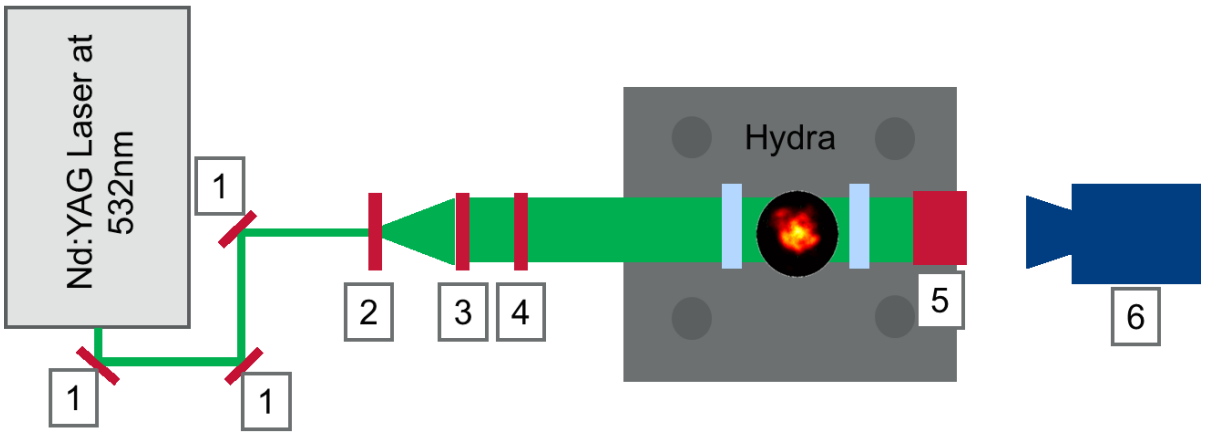

Figure 8-1: Optical setup for the laser sheet forming through the Hydra for LII. Key: 1.Mirrors, 2. F=-50mm cylindrical lens to expand the laser beam, 3. F=150mm cylindrical lens to collimate the expanded laser beam to 2.5cm, 4. F=1000mm cylindrical lens to focus the laser beam into a thin sheet, 5. Beam dump, 6. CCD Camera with intensifier

For planar LII, the CCD camera used was a LaVision FlowMaster 3S with an intensifier together with a Shamrock FF01-405/10-25 filter that had a centred wavelength of 406nm with guaranteed minimum bandwidth of 10 nm and a full width half maximum (FWHM) of 14.1nm to acquire 2D images of the LII signal. The bandwidth filtered most of the chemiluminescence and other "non-black body" incandescence so the resulting signal should be from the LII only.

For time resolved two colour LII, the light collecting optics was a Cassegrain CS600 with a 600mm working distance consisting of a primary 150mm focal length mirror and a secondary 56mm mirror separated by a distance of 245mm between them. This gave a probe volume of 200µm in diameter and 1.8mm in length. The light collected was passed through an Edmund Optics UV/VIS patchcord 1000 micron fibre with 0.22 numerical aperture which had FC Connectors on both ends. This was connected to a Thorlab F280FC-A collimator, with peak transmission wavelength at 543 nm, a 18.07 mm focal length and a numerical aperture of 0.15. The advantage of the Cassegrain optics compared to a lens system is that it prevents chromatic aberrations for different wavelengths as it consists only of reflective elements instead of refractive elements.

Also, in order to perform simultaneous 2D and time resolved LII, the outer surface of the circular back facing front mirror enabled a 45 degree mirror to be mounted so the planar LII image could be taken.

From the collimator, two photomultiplier tubes (PMT) from Hamamatsu were used to detect the two colour signal through a dichroic mirror and a set of filters. The layout is shown in Figure 8-2. For the PMT detecting in the infrared region (red PMT), the detection was through a Samrock FF605 - Di02 dichroic, which transmitted light above 605nm, and a Samrock FF01-643/20-25 filter onto the Hamamatsu H10721-20. This filter had a centred detection wavelength of 643 with a FWHM of 25nm. For the PMT detecting in the ultraviolet range (blue PMT), the incoming light was reflected between 350 – 596 nm from the Samrock FF605 - Di02 dichroic and through a Samrock FF01-395/11-25 filter and onto the Hamamatsu H10721-210 PMT. This had a centred detection wavelength of 395 with a FWHM of 20nm. The oscilloscope used in for acquiring the signal was the Tektronix DPO 4054 with bandwidth of 500Mhz and sampling rates of up to 2.5GS/s. The PMTs were connected to a power source which supplied the operating voltage of 5V and a gain power supply which could be varied between 0-5V for adjusting the gain.

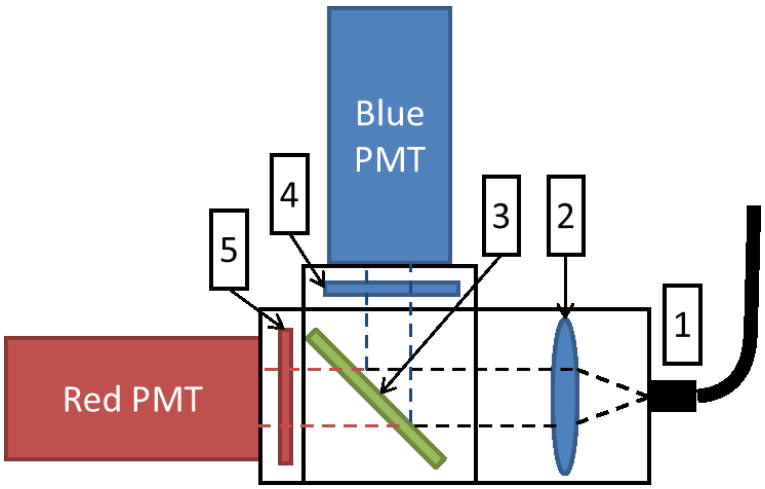

Figure 8-2: Layout of the two color LII system. Note 1. Edmund Optics UV/VIS patchcord 1000 micron fibre, 2. collimator from Thorlab F280FC-A, 3. Samrock FF605 - Di02 dichroic, 4. Samrock FF01-395/11-25 filter and 5. a Samrock FF01-643/20-25 filter.

8.3. Two Color LII Calibration

This thesis will only cover the calibration part of two color LII as the equipment had to be returned for repairs and was not returned in time before the thesis was competed. The calibration process for the two color LII was similar to that described in Chapter 2. It involved performing the red/blue ratio calibration, gain calibration which then enabled the temperature to be calculated from the signal ratio between the two PMTs.

8.3.1. Red/Blue Ratio Calibration

The red/blue ratio calibration process used a reference, calibrated light source to find the transmission of filter, dichroic and Cassegrain optics. The reference light source used was a Hamamatsu Xenon Lamp Calibrated Light Source L7810 with a known spectral radiance across the wavelengths. This was measured by a set of collimating lens, connected through an optical fibre into a Thorlabs CCS100 spectrometer. Using the same collimating lens, fibre and spectrometer, the spectrum of the light was measured after it has passed through the filter and dichroic for both red and blue dichroic/filter. The ratio between the reference spectrum and spectrum after the dichroic/filter was the transmissivity of the filter and dichroic. The result of the measurement, in Figure 8-3, shows the transmissivity of the red and blue set of dichroic and filters. The total transmissivity of the whole system (including light collecting optics) can also be found by including the light collecting optics of the Cassegrain, optical fibre and collimator.

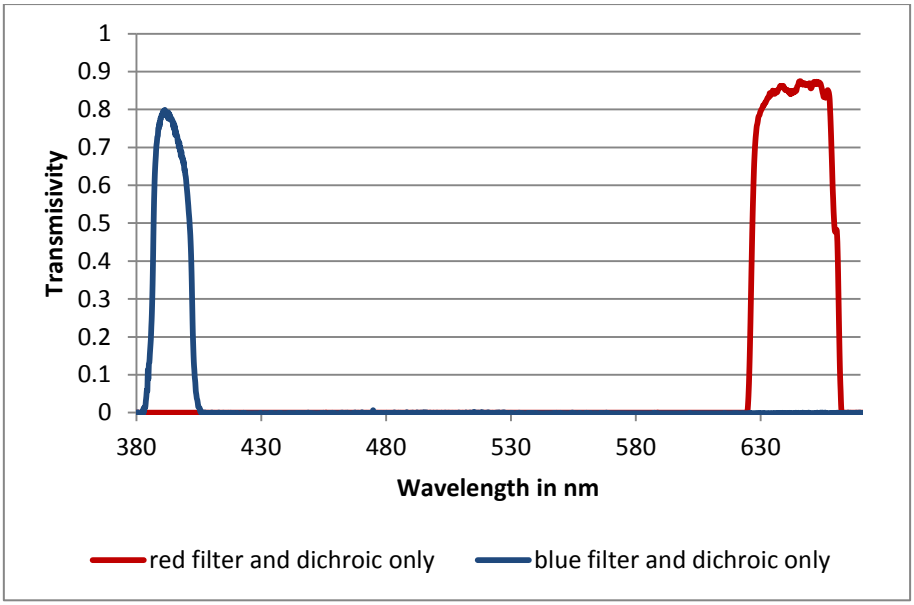

Figure 8-3: The transmissivity of the blue and red filter and dichroic

The transmissivity of the red and blue filters was then used for the temperature and signal ratio calibration using the LII signal (equations 2.22) in Chapter 2. The result of the calculation using the transmissivity found above is shown in Figure 8-4. This gives the relationship for the temperature at a given signal ratio at two wavelengths for this experiment. This can be used for finding the temperature of the measured soot particle in the LII experiment while the signal duration provides information on the size.

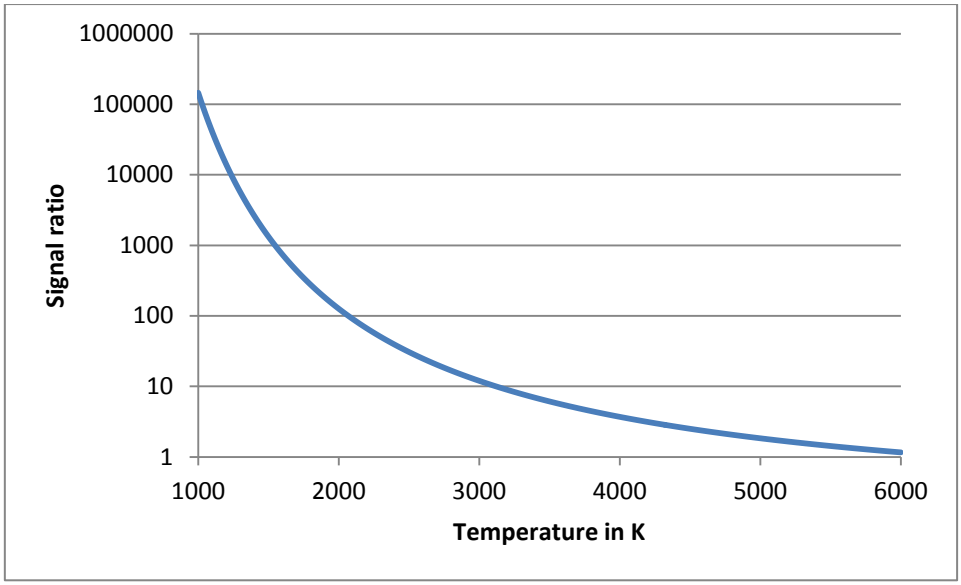

Figure 8-4: Signal ratio of the two color LII system and the corresponding temperature in Kelvin

8.3.2. PMT Gain Calibration

The gain of the PMTs between a range of 0-10 (corresponding to 0-5V) was calibrated so the difference in the gains between the two PMT could be adjusted for the signal ratio calculation. This was done using the calibrated light source, together with a Labsphere integrating sphere and measuring the signal through a light chopper. A spectrometer was used to measure the light in the integrating sphere so the intensities could be compared. Figure 8-5 shows the layout and setup of the gain calibration.

The intensity of the calibrated light source was adjusted by putting neutral density filters between the light source and the integrating sphere. The spectrum was measured and the background was deducted. This spectrum measurement was integrated and normalised against the value at 6V. The amplitude of the PMT signal (produced by the light chopper) was measured using an oscilloscope at different voltage settings and the gain was calculated by dividing this amplitude by the normalised spectrum measurement. Multiple measurements of these were made with both red and blue PMT and at different gain voltage settings and the mean values were found. The relative gain could then be plotted against the voltage setting and the relationship between them could be found.

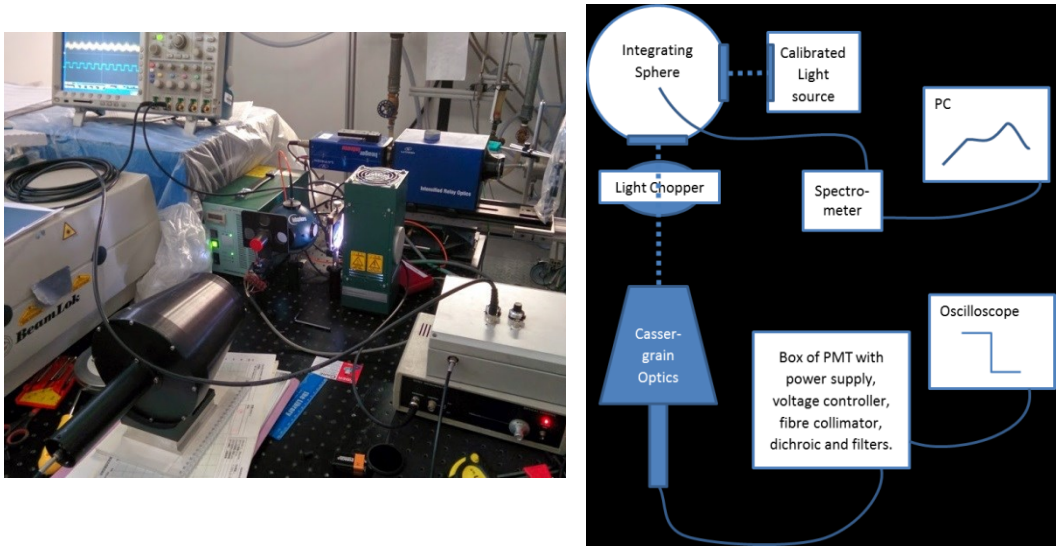

Figure 8-5: Gain calibration setup and layout.

The power received by the red and blue PMTs can be found by multiplying the known spectral radiance of the calibrated light source and the transmissivity of the light transmission optics and filter. This gave a value in micro Watt per cm^2 which can then be converted to µWatt by multiplying by the cross section area of the light collection optics which was $0.00126cm^2$. A calibration factor for each PMT could be found by dividing the power (in µW) into each PMT by its output signal (in V) at its corresponding gain setting.

The final calibration factor at each gain setting could be calculated by dividing the calibration factor from above by the relative gain at that voltage found earlier. This can be done for all the voltage setting for both PMTs.

A few attempts were made to perform this calibration but it was found in the process of this that the PMTs were faulty and had to be returned to the manufacturer for checks. This was the extent of the two color LII work on the Hydra engine. The experiment and the data analysis would have been similar to that shown in Chapter 2.

8.4. Planar LII Testing on a Candle Flame

For the planar LII, and in order to ensure the system was functioning, tests of the system were performed by the taking LII measurements of a candle flame where soot is present and oxidised within the flame.

Three images from planar LII of the candle flame are shown in Figure 8-6, showing different shapes of the candle as it flickered. The high laser irradiance meant the soot particles were sublimated and there was no obvious evidence of laser signal attenuation across the flame. The images were not corrected for the Gaussian laser profile. A bright horizontal streak which is noticeable towards the middle of the images was present which could be related to laser profile. (Note that the images have been cropped and adjusted so they fill the centre of the frame. This means that the images are not 'registered' in the vertical direction and this accounts for the different across these images.) Given that these images were presented only when the laser sheet was present, this implies that the signal was the product of laser excitation and not, for example, from natural soot incandescence.

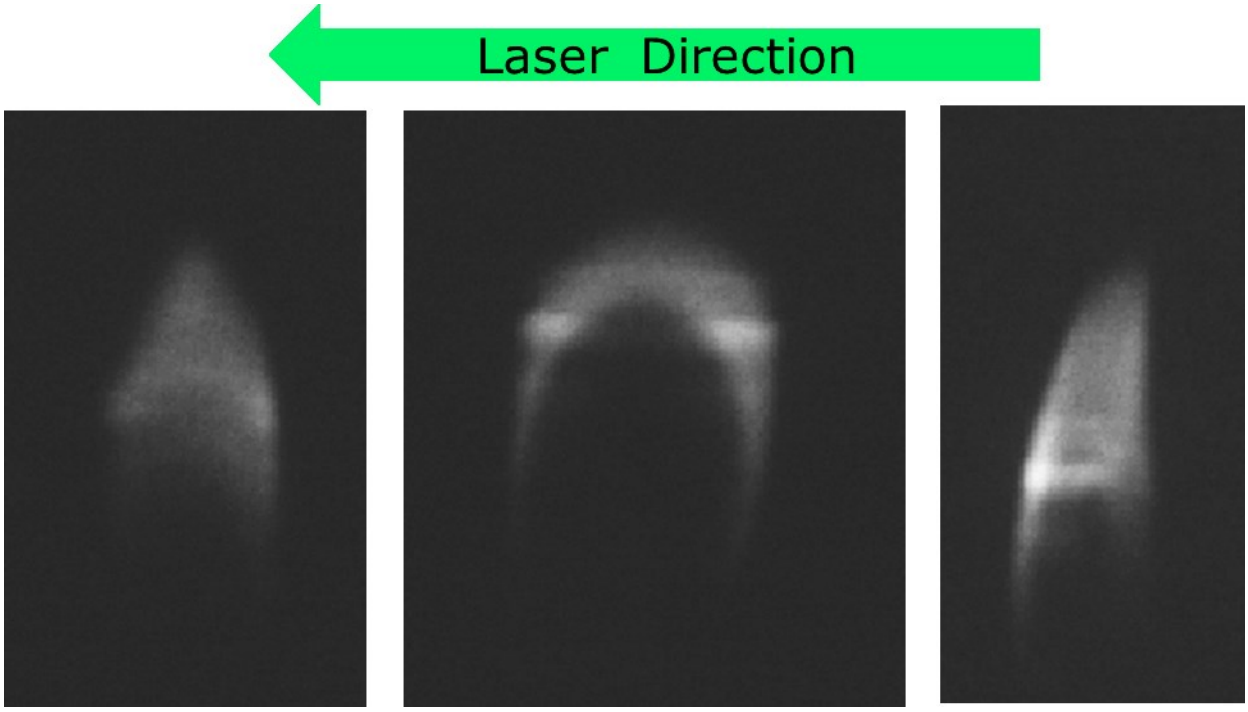

Figure 8-6: Three instantaneous examples of LII imaging of a candle flame.

8.5. Planar LII in Hydra Engine

The application of planar LII in the Hydra engine was set up as described above. The aim of this part of the work was to give further information on the soot distribution relatively late in the soot oxidation process and provide a comparative quantification for the three injection pressures studied in Chapter 7 by using planar LII.

8.5.1. Laser Synchronisation

The main challenge for the LII measurement in the Hydra engine was the synchronisation of the laser with the engine. This was mainly done by using a TTL pulse sent at a set CAD from the LabVIEW controller software, with the aid of the shaft encoder, and this triggered the laser and acquisition equipment. The timing of the TTL pulse had to be advanced so as to take into account the delays involved in the chain of processes between laser and camera as described below. These delays were found through visualising the signals using an oscilloscope.

For the laser control, the trigger from LabVIEW was connected to the timing card of the DaVis controlling computer which controled the image acquisition and laser. The trigger, through the timing card, in turn controlled the flash lamp and the Q-Switch of the laser, using the option of “External cyclic trigger” as the trigger source in the DaVis software. Given the engine was running at 1200rpm, this meant the engine cycle ran at 10Hz, the same as the optimum laser repetition rate. For the image acquisition, the output of the laser QSwitch signal was used to trigger the intensifier of the camera. The camera was triggered by the TTL pulse from LabVIEW with a delay to coincide with the Qswitch output of the laser. The camera exposure was set at 50 µs with an offset of 27 µs and the intensifier delay and gate were both 10000ns.

8.5.2. LII Images with Varying Injection Pressure

The engine condition used for this LII investigation was the same as those performed for the high speed images and this is set out in Table 8-1. The imaging CAD was set at 33 CAD (recall that the metal piston blocked the laser path through the quartz side

windows on the cylinder liner between -30 CAD and 30 CAD). An illustration of the laser sheet across the combustion chamber at 33 CAD aTDC is shown in Figure 8-7.

Variables	Value
Engine Speed	1200 rpm
Intake Air Temperature	70 C
Injection Pressure	30, 70 and 110 MPa
Pilot Injection Timing	-10 CAD
Pilot Injection Quantity	5 mg
Main injection adjusted so CA50 matched	8 CAD
IMEP	1.7 bar

Table 8-1: Testing condition for injection pressure variation for LII

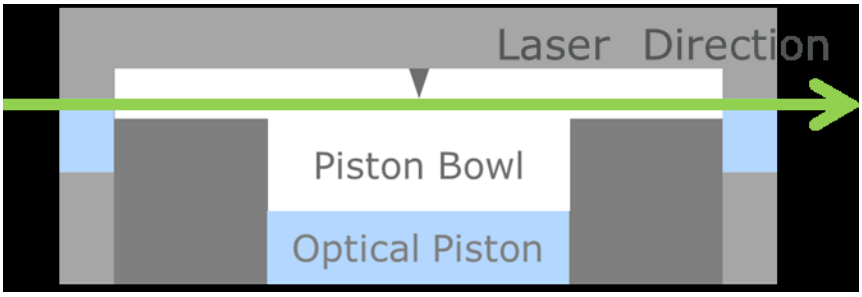

Figure 8-7: Diagram illustrating the laser path through the combustion chamber, through the two windows of the cylinder liner. The LII signal was viewed through the optical piston crown.

For the experiment, 400 images were acquired for each condition and the images were processed by applying a threshold for a minimum signal level for each image, then the complete set of images were averaged. The signal was normalised against the maximum signal for each injection pressure and a colormap was applied. The processed images are shown in Figure 8-8. The laser direction was from the top of the image towards the bottom.

The images show the relative location and intensity of the LII signal and soot location. There was a higher soot count and intensity from lower injection pressure case compared to higher injection pressure case, similar to the result from the high speed images recorded at much earlier values of CAD. It is emphasized that at 33 CAD aTDC the natural soot incandescence at this relatively late CAD is undetectable, largely because both soot oxidation has ceased (it stops at about 1300K) and the

non-black body radiation at the surrounding gas temperature is weak. This is illustrated in Figure 8-9 showing at 30 CAD, there was no detectable combustion luminosity from the high speed images. Thus LII is essentially visualizing the soot which will ultimately form the 'engine out' emission. The LII signals for all cases were concentrated towards the centre of the bore (note that the illumination plane is outside the piston bowl), presumably at the imaging plane as the in-cylinder air movement convected the soot towards the centre. This is more obvious for the 30MPa case with a larger concentration of soot. So the relative amount of soot gives an indication as to the soot emission at different injection pressures.

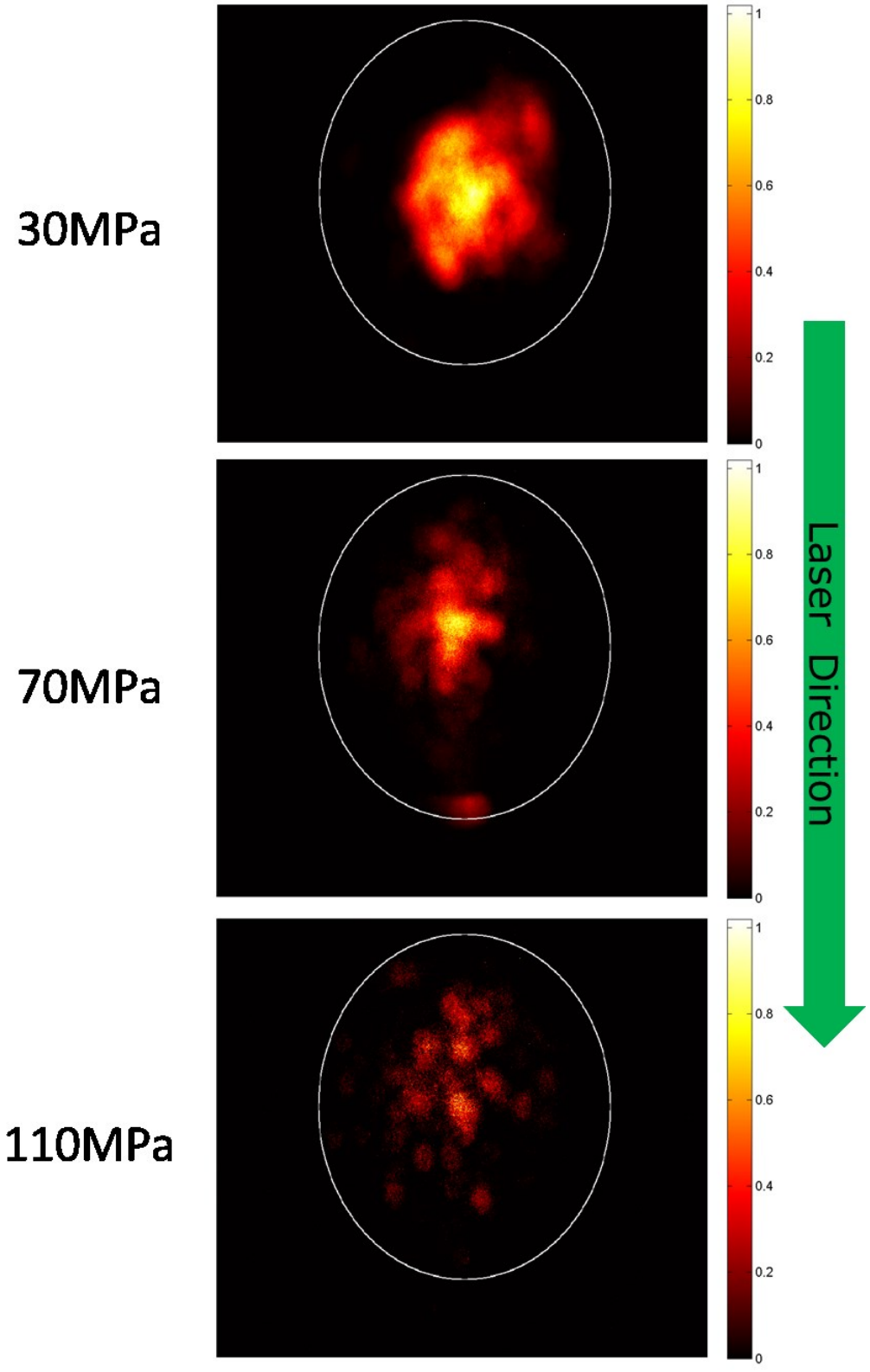

Figure 8-8: Processed LII image of soot distribution at different injection pressure. Each image was normalised to the maximum of each image and the white circle outlines the piston bowl.

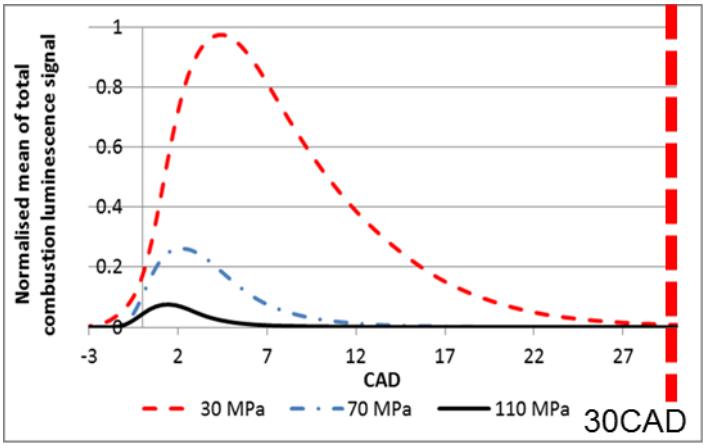

Figure 8-9: Combustion luminosity variation for different injection pressures and the location which the LII images were taken, i.e. after 30 CAD.

It has to be noted that the Gaussian laser profile was not corrected for. This can be corrected by finding the laser profile using a laser profile camera as described in Chapter 2 or alternatively the procedure described in the Appendix B. Once found, the Gaussian profile can be normalised and divided across the image which will correct for the image.

Laser attenuation may have occurred as the laser sheet traversed across the combustion chamber, being absorbed by soot particles (and perhaps, by some gaseous species). But because of the high power setting of the laser, any reduction of the laser irradiance will only have a small effect on the LII signal, as discussed in Aronsson, Sjöholm et al. (2010) and in section 1.5.6 of this thesis. Another consideration was signal attenuation which might arise because of the presence of soot or other particles in the line of sight between the camera and laser sheet where the LII signal originated. An assumption can be made that this reduction of LII signal is uniform throughout the entire measurement set and at each of the condition. So a comparison between results remains valid.

Further analysis of the LII signal count was performed to compare the different injection pressures. The total LII signal counts from every image at different injection pressures were averaged and normalised against the value at 30MPa and the results are shown in Figure 8-10. This demonstrates the change in signal level between the

lower injection pressure of 30MPa and the higher injection pressures of 70MPa and 110MPa. The signal is some measure of the amount of soot at each injection pressure.

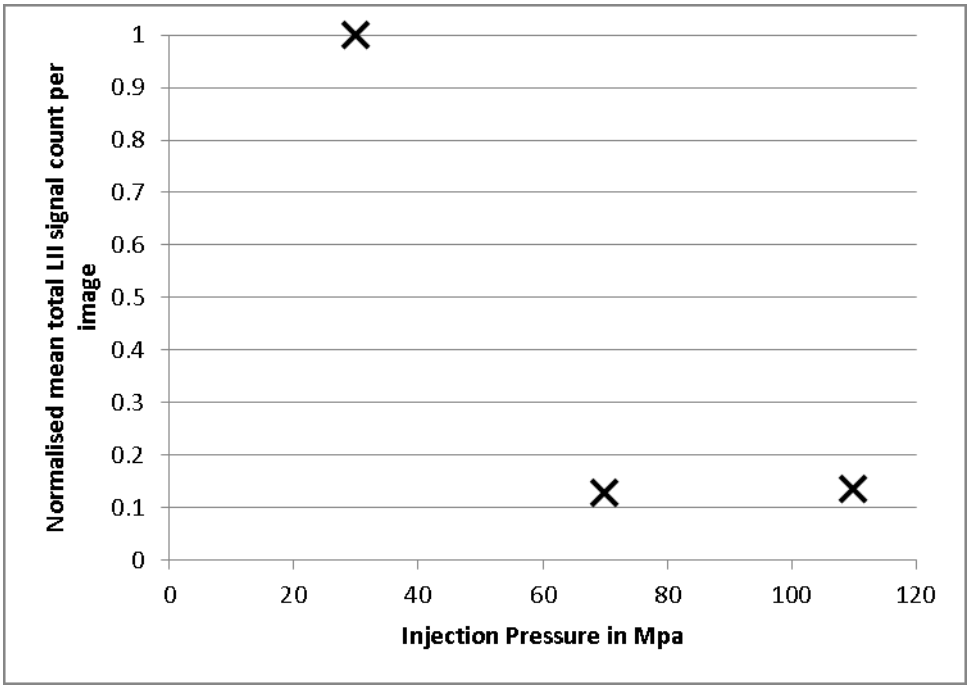

Figure 8-10: Normalised mean total LII signal count per image for different injection pressure.

There is an uncertainty to the reading taken at 70MPa due to the order of which the signal was acquired. One set of the 30MPa and one set of 110MPa was acquired immediately after the cleaning of windows and mirror. This meant the 70MPa images were always taken after a period of running the engine. This is an undesirable order in which to take the images and illustrates the need for better of design of the experimental method, lacking here due to time constraint. This prolonged running meant the signal may be affected by the fouling of the window and mirror with soot and oil which can be significant even over a short period of time. Further work must be done to investigate the effect of the order in which the images are taken and to take a set of images at 70MPa injection pressure immediately after windows and mirror cleaning.

Another analysis was done to find the average LII signal per pixel which may give some information as to the size of the soot particle. As each pixel covered

approximately 0.01mm^2, it was possible that the LII signal falling onto the camera pixel could came from isolated soot particle. The magnitude of this signal can provide information about the size of the soot particles. It is of course possible that the signal came from multiple soot particles but this analysis could be used as a guide.

The LII signals from each pixel of the whole set of images for each injection pressure were averaged and normalised against the signal at 30MPa and the result is shown in Figure 8-11. The error bars show the standard deviation from the data set and this variation is seen to be quite large. The trend shows decreasing LII signal as injection pressure was increased which could indicate a reduction of soot particle size and/or reduction of number of particles within the imaging pixel. This is an estimation based on the data acquired, taking into account of the meaning of the signal and the error involved.

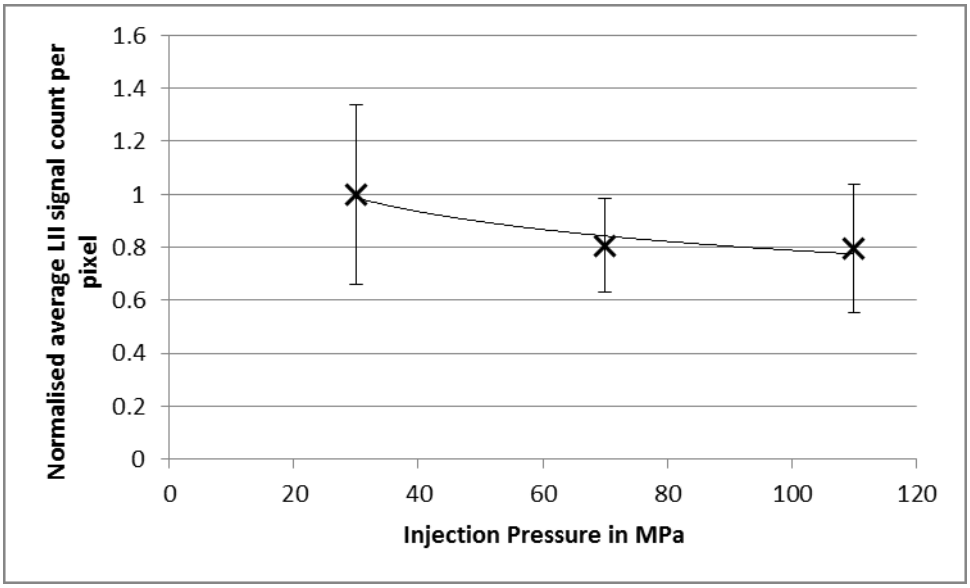

Figure 8-11: Normalised average LII signal count per pixel for different injection pressure, with error bars showing the standard deviation from each data set.

8.6. Chapter Conclusion

This chapter describes the calibration for two color LII which would have provided information for temperature evolution and particle size on soot within the combustion

chamber for different injection pressures. Due to equipment unavailability and timing constraint, it was not possible to carry out this part of the investigation. Further work can be carried out to perform these measurements to see if there is any correlation between injection pressure and soot particle size.

Investigations of planar LII at the different injection pressures, taken at 33 CAD, were carried out and the mean locations of the LII signal were shown. The normalised magnitude of these signals was also compared which it showed a decrease in the amount of soot as injection pressure increased. Further work can be done in the processing of the images to correct for laser profile, signal and laser attenuation. It will be useful to look at the effect of laser irradiance and the relative strength of the LII signal and avoid sublimating the soot particles with lower laser irradiance. More samples should be taken to investigate the extent of window fouling effects on 70MPa case.

9 Conclusion and Further Work

This thesis has covered diverse aspects of diesel engine combustion both experimentally and computationally. In terms of the latter, a new configuration of a "Hydra" optically accessed single cylinder engine has been designed, based on a modern Ford Euro V Puma cylinder head and valve train, and commissioned in the laboratory together with fully variable injection timing. The engine has been used for high speed imaging of combustion luminosity and laser induced incandescence (LII), accompanied by heat release analysis for a range of injection schedules. In readiness for extension of research into gasoline compression ignition, the thesis includes an extensive description of gasoline properties. Computationally, and in view of the promising nature of 'premixed enough' compression ignition engines in terms of reducing the emissions of particulates, a FORTRAN program in the multi-zone formalism has been de-bugged, extended and exercised in a preliminary way.

For the “LII in vacuum” work, carried out at Herriot-Watt University under the supervision of Professor Douglas Greenhalgh, the process of modelling and calibration was described. The heat loss mechanism was modelled using various particle sizes, pressure and laser fluence level. Time resolved, two color LII and ELS signals were collect at 10^{-3} mbar for agglomerates at various laser irradiances, ranging from 5% (20W) to 30% (120W). Soot samples were collected for TEM analysis and results showed the morphology, size distribution and number of primary particles present in the aggregates. Data were collated giving maximum temperature, agglomerates sizes and velocity. A comparison of the experiment result with the model has been carried out which illustrated the potential for improving the model used to explain LII heat loss mechanism.

For the LII in vacuum work, it was found that:

- Compared to the TEM analysis, the particle size found using LII were larger than those found on the TEM samples. This may have been because the signal to noise level was low in the absence of the use of the PMT cooling system.

- The unwelcome effect of optical “tweezing” was found to exist because of the high beam waist gradient in focusing when using a continuous wave laser causing particles to be trapped inside the beam and hence affecting the result. This was confirmed by iCCD images of the measurement volume.
- This increased the residence time in laser and also affected the velocity measurement caused by particles collision and deflecting the intended particle trajectory.
- Micro-explosions of soot particle through ionisation by laser were found and the mechanism of its operation discussed.

The setup of the Hydra optical diesel engine at Imperial College London has been described along with the installed instrumentation, data acquisition and control. Details of the injection equipment and the LabVIEW acquisition programme are recorded. Modifications to the engine components throughout the period of the work, such as belt drive, piston rings and hydraulic platform have been recorded for future reference. The start-up procedure and engine window cleaning process is also set out for the benefit of users in future.

The components, properties and blending of gasoline fuel and their importance have been described. The requirement of the fuel and the reasons for their control was also shown. This is the starting point in investigating the application of the gasoline type fuel in a compression ignition engine.

The work in modifying a FORTRAN code written for multizone HCCI simulation using CHEMKIN to include fuel injection function was described. The fundamental logic of the original single-zone program has been demonstrated to remain valid in the context of a multi-zone application - in particular the work transfer between individual zones of burnt gases (i.e. products) as these are compressed by the subsequent combustion of reactants in other zones and the added feature of the fuel injection performs as desired. Two chemical kinetics mechanisms were compared. Tests were carried out to look at the effects of injection timing and intake temperature on ignition timing. Attempts were made to replicate the pressure and heat release rate from experimental data and

demonstrate the limitations and challenges posed for engine simulation using the computer program.

Work on validating the combustion analysis and the functioning of the engine and its instrumentation was carried out. A series of variables were investigated and it was found that:

- Increase in injection pressure produced higher mixing rate for fuel and air and for the single injection case, resulting in the formation of leaner mixtures which generally underwent a two-stage auto-ignition process with a lower peak value of the rate of heat release rate.
- An increase in air intake temperature reduced the ignition delay and increased the magnitude of the heat release rate.
- The range of CA50 timing chosen meant that early CA50 timing led to ignition and combustion during the compression stroke and later CA50 timing led to ignition and combustion during the expansion stroke. This had a significant effect to the magnitude of the heat release rate with a higher rate of heat release for the early CA50 case.

For the double injection cases, it was found that:

- The heat release rate was not strongly dependent on the timing of the pilot injection between -20CAD and -10CAD compression TDC.
- For larger amount of fuel injected at pilot, the peak rate of heat release was lower because the combustion was spread out through time. There was negative ignition delay for cases with a large time separation between the pilot and main as the fuel amount injected for the pilot was increased because the pilot was large enough to be a “standalone injection” in a cycle.
- Higher injection pressure meant a higher peak heat release rate in the double injection case as the fuel was injected into an already combusting environment and the better mixed charge with better atomisation meant a stronger premixed burn.

The process of the high speed imaging work was carried out and described. The setup and imaging capability were tested and different lighting options were explored. It was found that the best route for illumination was through the piston crown. Different imaging filters such as CH chemiluminescence were used and should prove to be a useful tool for further investigation in future work. High speed images of a ECU set point from the Ford production engine, also at Imperial, were taken as a reference for other testing condition. An image processing code was developed for finding the injection spray penetration length. The injection pressures and timings were varied to find the injection penetration lengths and mixing processes. The effect that the first injection has on the second injection was also investigated, as were the effects of the dwell time between the two injections have on injection velocity. The combustion luminosity as a proxy for soot concentration, and its variation with injection pressure was analysed and methods of presenting the results were explored. It was found that:

- The swirl number of the flow in the combustion bowl was estimated to be 3.44.
- Spray penetration length was compared with two calculated values of spray length penetration from literature and reasonable agreement was found, despite the radically different fuel injection equipment involved.
- Observations on first stage ignition/cool flame were further investigated using high speed images showing some evidence of its presence while also confirming the difficulty in visualising it.
- The relationship between the increase in injection pressure and the reduction of combustion luminosity was established.
- The locations of the start of combustion luminosity were examined and POD analysis on the combustion luminosity images was performed where "modes", or eigenimages, along injection jet paths, between the jet paths and the vortex zones between spray jet tips created by wall impingement were identified.

The equipment calibration for two color LII at Imperial which would have provided information for temperature evolution and particle size on soot within the combustion chamber for different injection pressures was described. Due to equipment availability

and timing constraint, it was not possible to carry out this part of the investigation Investigations of planar LII at the different injection pressures, taken at 33 CAD, were carried out and the mean locations of the LII signal were shown. The normalised magnitude of the LII signals was compared and it was found that:

- The decrease in the amount of soot as injection pressure increased; in line with the finding from the high speed imagining work.
- A trend of decreasing LII signal per pixel which may imply a decrease in soot particle size as injection pressure increases.

9.1 Further Work

Further work can be carried out for the LII in vacuum part:

- Changing the laser to a high duty cycle, semi-CW regime, in order that the particles are not trapped inside the beam will improve the experiment. This should eliminate the problems mentioned in the thesis with iCCD camera, LII signal and ELS signal. However, a method will have to be found for synchronising the soot particle with the laser.
- Cooling the PMTs to lower the baseline noise in order to detect smaller particles.
- Testing different types of soot may be a productive avenue to explore, so different soot morphology can be assessed for its effect on the experiment and result. This can be done with an inverted burner where the soot is quenched and more closely modelled combustion soot rather than those found in the experiment described in the thesis.
- Performing experiments to see the effect of pressure, as shown in the modelling, to isolate the effect on the overall heat loss mechanism such as sublimation, conduction and radiation.
- Investigating the ionisation of soot particles in a laser field.

For the setup of the Hydra engine optical diesel engine, improvements can be made by:

- Using a more realistic combustion bowl design to closer replicate a production engine.
- Adding exhaust gas recirculation (perhaps in simulation from, either using a burner or reduced oxygen content by a controlled gas supply from gas bottles).
- Extending the experiments to combustion regimes which were explicitly avoided in this thesis, either for fear of breaking the engine or due to lack of time or equipment availability. These regimes would include higher engine speeds (which will change the turbulence levels in the bowl), higher values of IMEP (which will change the amount of bowl-wall impingement, which will also be dependent on injection schedule as a further variable in this context) which may, ultimately, necessitate either the significant strengthening of the Bowditch piston or its complete removal; the investigation of low temperature combustion consequent on the use of large amounts of EGR, as well as the extensive use of simultaneous PLIF (OH as well as fuel tracer), LII and chemiluminescence to identify combustion regimes.
- Improving optical access through the piston crown as the current piston as it did not allow optical access from bore around TDC. An improvement can be made by machining an indent into the piston and inserting windows into the slot. More extensive, but more expensive and potentially more fragile, designs exist in the literature.
- Considering the option of a fully optical piston to improve optical access into the top land above the bowl.
- The entire metal window carrier in the bore of the engine could be replaced by a full optical annulus for complete, all round optical access to the combustion chamber, and in particular to the top land above the piston crown, further enhancing the optical access.

For the use of gasoline in compression ignition engines, further work should be carried out on diesel fuel properties, composition and blend and compared with suitably lowered octane number gasoline, with the aim to find a suitable gasoline like fuel.

The computer programme can be further tested and improved by:

- Using the recent advances in the description of chemical kinetics for diesel fuels.
- Better specification of the "initial conditions" for the multizone model of the zones, with help of either prediction from a CFD code or experiment.
- Performing a parametric study of engine conditions and injection strategies in parallel with the engine testing work.

For the high speed imaging work on Hydra, further work can be carried out on:

- Using different filters to look at chemiluminescence such as OH, C2 and CH to further provide information on the effect of variables such as injection pressure and timings.
- Extending the CH chemiluminescence by measuring more cycles to be compared with the combustion luminosity images.
- The injection penetration tests with a higher number of samples to provide better statistical basis for the findings.
- Extending the investigation of the effect of variation of injection pressure on combustion luminosity by changing the pilot injection quantity from 5mg to a more conventional injection quantity of 1.5/2mg and compare the results at different injection pressures.
- Finding the diesel fuel spray angle from the injection images with further image processing development.
- Measuring the emission from the various conditions and use different injection pressures more closely allied to the Ford production engine at Imperial.
- Use formaldehyde chemiluminescence and LIF to investigate the first stage ignition/cool flame.
- Other engine variables such as intake temperature, injection timing and injected fuel quantity can be investigated for combustion luminosity analysis and other optical diagnostic techniques.

- The engine can be modified to include EGR through the introduction of CO_2 and simulate the effect of boost by scaling the injection pressure and inlet temperature.

For the LII in Hydra work, further work can be carried out on:

- Performing two color time resolved LII measurements to find soot particle sizes and to find correlation, if any, between injection pressure and soot particle size.
- Improving the processing of the images by correcting for laser profile, signal and laser attenuation.
- Finding the effect of laser irradiance and the relative strength of the LII signal and avoid sublimating the soot particles with lower laser irradiance.
- Acquiring more samples to investigate the window fouling effect on 70MPa case.
- Testing more engine variables to find the soot distribution and particle sizes.
- Performing LII at other CAD with modified and improved optical access.
- Investigate the effect of EGR on soot concentration, distribution and particle sizes.

References

Abdelghaffar, W. A., K. Karimi, et al. (2007). Fuel Spray Penetration in High Pressure Diesel Engines, SAE International.

Aceves, S. M., D. L. Flowers, et al. (2005). Analysis of Premixed Charge Compression Ignition Combustion With a Sequential Fluid Mechanics-Multizone Chemical Kinetics Model, SAE International.

Aceves, S. M., D. L. Flowers, et al. (2004). "Spatial Analysis of Emissions Sources for HCCI Combustion at Low Loads Using a Multi-Zone Model." SAE 2004-01-1910: 147-158.

Aceves, S. M., D. L. Flowers, et al. (2002). "Piston-Liner Crevice Geometry Effect on HCCI Combustion by Multi-Zone Analysis." SAE 2002-01-2869.

Aceves, S. M., D. L. Flowers, et al. (2000). "A Multi-Zone Model for Prediction of HCCI Combustion and Emissions." Sae Transactions **109**(3): 431-441.

Akagawa, H., T. Miyamoto, et al. (1999). "Approaches to Solve Problems of the Premixed Lean Diesel Combustion." Sae Transactions **108**(3): 120-132.

Akihama, K., Y. Takatori, et al. (2001). "Mechanism of the Smokeless Rich Diesel Combustion by Reducing Temperature." Sae Transactions **110**(3): 648-662.

Andersson, Ö. and P. C. Miles (2014). Diesel and Diesel LTC Combustion. Encyclopedia of Automotive Engineering, John Wiley & Sons, Ltd.

Andrae, J., D. Johansson, et al. (2005). "Co-oxidation in the auto-ignition of primary reference fuels and n-heptane/toluene blends." Combustion and Flame **140**(4): 267-286.

Andrae, J. C., P. Bjornbom, et al. (2007). "Autoignition of toluene reference fuels at high pressures modeled with detailed chemical kinetics." Combustion and Flame **149**(1-2): 2-24.

Andrae, J. C., T. Brinck, et al. (2008). "HCCI experiments with toluene reference fuels modeled by a semidetailed chemical kinetic model." Combustion and Flame **155**(4): 696-712.

Appel, J., B. Jungfleisch, et al. (1996). "Assessment of soot volume fractions from laser-induced incancescence by comparison with extinction measurements in laminar, premixed, flat flames." Symposium (International) on Combustion **26**(2): 2387-2395.

Aronsson, U., C. Chartier, et al. (2009). "Analysis of the Correlation Between Engine-Out Particulates and Local Φ in the Lift-Off Region of a Heavy Duty Diesel Engine Using Raman Spectroscopy." SAE Int. J. Fuels Lubr. **2**(1): 645-660.

Aronsson, U., J. Sjöholm, et al. (2010). "Analysis of EGR Effects on the Soot Distribution in a Heavy Duty Diesel Engine using Time-Resolved Laser Induced Incandescence." SAE **2010-01-2104**.

Ashkin, A., J. M. Dziedzic, et al. (1986). "Observation of a single-beam gradient force optical trap for dielectric particles." Opt. Lett. **11**(5): 288-290.

Atzler, F., A. Weigand, et al. (2007). Emissions Reduction Potential of High EGR Rates in D.I. Diesel Engines. International conference on engines for automobile; ICE 2007, Naples, Italy, Society of Automotive Engineers.

Auckland, M. and D. Charnock (1969). "The development of linear blending indices for petroleum properties." J of the Inst. of Petroleum **55**(545): 322-329.

Axelsson, B., R. Collin, et al. (2000). "Laser-Induced Incandescence for Soot Particle Size Measurements in Premixed Flat Flames." Appl. Opt. **39**(21): 3683-3690.

Axelsson, B., R. Collin, et al. (2001). "Laser-induced incandescence for soot particle size and volume fraction measurements using on-line extinction calibration." Applied Physics B: Lasers and Optics **72**(3): 367-372.

Badami, M., P. Nuccio, et al. (1999). "Influence of Injection Pressure on the Performance of a DI Diesel Engine with a Common Rail Fuel Injection System." SAE Paper 1999-01-0193 **108**(3): 195-205.

Baert, R., D. Beckman, et al. (1996). "New Egr Technology Retains Hd Diesel Economy With 21st Century Emissions." SAE **960848**.

Bakenhus, M. and R. D. Reitz (1999). "Two-Color Combustion Visualization of Single and Split Injections in a Single-Cylinder, Heavy-Duty D.I. Diesel Engine Using an Endoscope-Based Imaging System." Sae Transactions **108**(3): 1567-1584.

Balthasar, M., F. Mauss, et al. (2002). "A computational study of the thermal ionization of soot particles and its effect on their growth in laminar premixed flames." Combustion and flame **129**(1–2): 204-216.

Benedict, L. X., N. G. Chopra, et al. (1998). "Microscopic determination of the interlayer binding energy in graphite." Chemical Physics Letters **286**(5–6): 490-496.

Bengtsson, P. E. and M. Aldén (1995). "Soot-visualization strategies using laser techniques." Applied Physics B: Lasers and Optics **60**(1): 51-59.

Beyer, V. (2006). A study of laser-induced incandescence under high vacuum conditions. Cranfield, Cranfield University.

Beyer, V., D. Greenhalgh, et al. (2014). Ionisation of soot aggregates and primary particles in a laser field. 10th International Conference Series on Laser-Light and Interactions with Particles 2014 (LIP2014) Marseille.

Beyer, V. and D. A. Greenhalgh (2006). "Laser induced incandescence under high vacuum conditions." Applied Physics B Lasers and Optics **83**(3): 455-467.

Bissoli, M., A. Cuoci, et al. (2013). "Detailed Kinetic Analysis of HCCI Combustion Using a New Multi-Zone Model and CFD Simulations." SAE Int. J. Engines **6**(3): 1594-1609.

Bizon, K., G. Continillo, et al. (2009). "POD-based analysis of cycle-to-cycle variations in an optically accessible diesel engine." Proceedings of the Combustion Institute **32**(2): 2809-2816.

Bizon, K., G. Continillo, et al. (2010). "POD-based analysis of combustion images in optically accessible engines." Combustion and flame **157**(4): 632-640.

Bladh, H. and P. E. Bengtsson (2004). "Characteristics of laser-induced incandescence from soot in studies of a time-dependent heat- and mass-transfer model." Applied Physics B: Lasers and Optics **78**(2): 241-248.

Bladh, H., J. Johnsson, et al. (2007). "On the dependence of the laser-induced incandescence (LII) signal on soot volume fraction for variations in particle size." Applied Physics B **90**(1): 109-125.

Bladh, H., J. Johnsson, et al. (2008). "On the dependence of the laser-induced incandescence (LII) signal on soot volume fraction for variations in particle size." Applied Physics B: Lasers and Optics **90**(1): 109-125.

Blair, G. P. (1999). Design and Simulation of Four-stroke Engines, Society of Automotive Engineers.

Bobba, M., M. Musculus, et al. (2010). "Effect of Post Injections on In-Cylinder and Exhaust Soot for Low-Temperature Combustion in a Heavy-Duty Diesel Engine." SAE Int. J. Engines **3**(1): 496-516.

Bockhorn, H. (1994). Soot formation in combustion : mechanisms and models. Berlin, Springer.

Bockhorn, H., H. Geitlinger, et al. (2002). "Progress in characterization of soot formation by optical methodsPresented at the Bunsen Discussion on Formation and Degradation of Hydrocarbons in High-Temperature Reactions, Bad Herrenalb, Germany, 7–11 October, 2001." Physical Chemistry Chemical Physics **4**(15): 3780-3793.

Boiarciuc, A. (2006). "Soot volume fractions and primary particle size estimate by means of the simultaneous two-color-time-resolved and 2D laser-induced incandescence." Applied physics. B, Lasers and optics **83**(3): 413-421.

Boiarciuc, A., F. Foucher, et al. (2007). "Estimate Measurement of Soot Diameter and Volume Fraction inside the Bowl of a Direct-Injection-Compression-Ignition Engine: Effect of the Exhaust Gas Recirculation." Combustion Science and Technology **179**(8): 1631-1648.

Bond, T. C. (2011). "`Bounding the Role of Black Carbon in the Climate System'-A Summary Assessment." Em: 11-12.

Borgqvist, P., P. Tunestal, et al. (2012). Gasoline Partially Premixed Combustion in a Light Duty Engine at Low Load and Idle Operating Conditions, SAE International.

Bosshardt, D. (2004). Parameters Affecting The Variability of Heat Release in Autoignition Engines **A thesis submitted in partial fulfilment of the requirements for the Master of Science Degree of the University of London and the Diploma of Membership of Imperial College**

Bougie, B., L. C. Ganippa, et al. (2006). "On particulate characterization in a heavy-duty diesel engine by time-resolved laser-induced incandescence." Applied Physics B: Lasers and Optics **83**(3): 477-485.

Bougie, B., L. C. Ganippa, et al. (2007). "Soot particulate size characterization in a heavy-duty diesel engine for different engine loads by laser-induced incandescence." Proceedings- Combustion Institute **31**(1): 685-691.

Bruneaux, G. (2001). "Liquid and Vapor Spray Structure in High Pressure Common Rail Diesel Injection." Atomization and Sprays **11**(5): 533-556.

Bruneaux, G. (2001). A Study of Soot Cloud Structure in High Pressure Single Hole Common-Rail Diesel Injection Using Multi-Layered Laser-Induced Incandescence.

Bruneaux, G. (2005). "Mixing Process in High Pressure Diesel Jets by Normalized Laser-Induced Exciplex Fluorescence-Part II: Wall Impinging Versus Free Jet." SAE 2005-01-2097.

Bruneaux, G. (2008). Study of the Effect of Wall Guiding on Direct Diesel Injection by Optical Diagnostics. COMODIA. Sapporo, Japan. **MD3-1**.

Bruneaux, G., M. Causse, et al. (2011). "Air Entrainment in Diesel-Like Gas Jet by Simultaneous Flow Velocity and Fuel Concentration Measurements, Comparison of Free and Wall Impinging Jet Configurations." SAE Int. J. Engines **5**(2): 76-93.

Bruneaux, G. and D. Maligne (2009). "Study of the Mixing and Combustion Processes of Consecutive Short Double Diesel Injections." SAE 2009-01-1352: 169-188.

Bruneaux, V., D. Verhoeven, et al. (1999). "High-Pressure Diesel Spray and Combustion Visualization in a Transparent Model Diesel Engine." Sae Transactions **108**(4): 2122-2136.

Bryce, D. J., N. Ladommatos, et al. (2000). "Quantitative Investigation of Soot Distribution by Laser-Induced Incandescence." Appl. Opt. **39**(27): 5012-5022.

Bunting, B. G., S. Eaton, et al. (2008). A Comparison of HCCI Ignition Characteristics of Gasoline Fuels Using a Single-Zone Kinetic Model with a Five Component Surrogate Fuel, SAE International.

Campbell, J. W., A. D. Gosman, et al. (2008). "Analysis of Premix Flame and Lift-Off in Diesel Spray Combustion using Multi-Dimensional CFD." Sae Sp **2008-01-0968**: 249-268.

Castleman, A. W. and R. G. Keesee (1988). "Gas-Phase Clusters: Spanning the States of Matter." Science **241**(4861): 36-42.

Cenker, E., G. Bruneaux, et al. (2013). "Study of Soot Formation and Oxidation in the Engine Combustion Network (ECN), Spray A: Effects of Ambient Temperature and Oxygen Concentration." SAE Int. J. Engines **6**(1): 352-365.

Chartier, C., O. Andersson, et al. (2011). "Effects of Post-Injection Strategies on Near-Injector Over-Lean Mixtures and Unburned Hydrocarbon Emission in a Heavy-Duty Optical Diesel Engine." SAE Int. J. Engines **4**(1): 1978-1992.

Chartier, C., U. Aronsson, et al. (2009). "Analysis of Smokeless Spray Combustion in a Heavy-Duty Diesel Engine by Combined Simultaneous Optical Diagnostics." SAE 2009-01-1353.

Chartier, C., J. Sjoholm, et al. (2012). "Air-Entrainment in Wall-Jets Using SLIPI in a Heavy-Duty Diesel Engine." SAE Int. J. Engines **5**(4): 1684-1692.

Chen, H., D. L. Reuss, et al. (2013). "A practical guide for using proper orthogonal decomposition in engine research." International Journal of Engine Research **14**(4): 307-319.

Choi, D., P. C. Miles, et al. (2005). "A Parametric Study of Low-Temperature, Late-Injection Combustion in a HSDI Diesel Engine." JSME International Journal Series B Fluids and Thermal Engineering **48**(4): 656-664.

Collin, R., J. Nygren, et al. (2004). "The Effect of Fuel Volatility on HCCI Using Simultaneous Formaldehyde and OH PLIF." SAE 2004-01-2948 **113**(4): 1800-1808.

Crua, C., D. A. Kennaird, et al. (2003). "Laser-induced incandescence study of diesel soot formation in a rapid compression machine at elevated pressures." Combustion and Flame **135**(4): 475-488.

Crua, C., T. Shoba, et al. (2010). High-Speed Microscopic Imaging of the Initial Stage of Diesel Spray Formation and Primary Breakup, SAE International.

Curran, H. J., P. Gaffuri, et al. (1998). "A Comprehensive Modeling Study of n-Heptane Oxidation." Combustion and Flame **114**(1–2): 149-177.

de Ojeda, W., P. Zoldak, et al. (2008). Development of a Fuel Injection Strategy for Diesel LTC. SAE 2008-01-0057, Detroit, MI, Warrendale.

Dec, J. E. (1997). "A Conceptual Model of DI Diesel Combustion Based on Laser-Sheet Imaging." Sae Transactions **106**(3): 1319-1348.

Dec, J. E. (2002). A Computational Study of the Effects of Low Fuel Loading and EGR on Heat Release Rates and Combustion Limits in HCCI Engines, SAE International.

Dec, J. E., M. L. Davisson, et al. (2008). "Detailed HCCI Exhaust Speciation and the Sources of Hydrocarbon and Oxygenated Hydrocarbon Emissions." SAE 2008-01-0053.

Dec, J. E. and C. Espey (1992). "Soot and fuel distributions in a DI diesel engine via 2-D imaging." Sae Transactions **922307**.

Dec, J. E. and W. Hwang (2009). "Characterizing the Development of Thermal Stratification in an HCCI Engine Using Planar-Imaging Thermometry." SAE 2009-01-0650.

Dec, J. E. and M. Sjoberg (2004). "Isolating the Effects of Fuel Chemistry on Combustion Phasing in an HCCI Engine and the Potential of Fuel Stratification for Ignition Control." Sae Sp: 43-62.

Dec, J. E., A. O. Zur Loye, et al. (1992). "Soot Distribution in a DI Diesel Engine Using 2-D Laser-Induced Incandescence Imaging." Sae Transactions **920115**(3): 277.

Desantes, J. M., R. Payri, et al. (2006). "Development and validation of a theoretical model for diesel spray penetration." Fuel **85**(7–8): 910-917.

Dibble, R. W. and R. E. Hollenbach (1981). "Laser rayleigh thermometry in turbulent flames." Symposium (International) on Combustion **18**(1): 1489-1499.

Dodge, L. G., S. Simescu, et al. (2002). "Effect of Small Holes and High Injection Pressures on Diesel Engine Combustion." SAE 2002-01-0494.

Dreier, T., B. Bougie, et al. (2006). "Modeling of time-resolved laser-induced incandescence transients for particle sizing in high-pressure spray combustion environments: a comparative study." Applied Physics B: Lasers and Optics **83**(3): 403-411.

Duffy, K. P., S. Faulkner, et al. (2004). LATEST DEVELOPMENTS IN HEAVY DUTY DIESEL HCCI, Editions TECHNIP.

Easley, W. L., A. Agarwal, et al. (2001). "Modeling of HCCI Combustion and Emissions Using Detailed Chemistry." Sae Transactions **110**(3): 1045-1061.

Eastwood, P. (2008). Particulate emissions from motor vehicles. Hoboken, N.J., Wiley ; Chichester : John Wiley [distributor].

Eckbreth, A. C. (1977). "Effects of laser-modulated particulate incandescence on Raman scattering diagnostics." Journal of Applied Physics **48**(11): 4473-4479.

Ekoto, I., W. Colban, et al. (2008). Distribution of Unburned Hydrocarbons for Low Temperature Light-Duty Diesel Combustion. COMODIA 2008. Saporo, Japan, Japan Society of Mechanical Engineers.

Espey, C., J. E. Dec, et al. (1994). Quantitative 2-D Fuel Vapor Concentration Imaging in a Firing D.I. Diesel Engine Using Planar Laser-Induced Rayleigh Scattering. International congress, Detroit; MI, SAE International.

Espey, C., J. E. Dec, et al. (1997). "Planar Laser Rayleigh Scattering for Quantitative Vapor-Fuel Imaging in a Diesel Jet." Combustion and Flame **109**(1/2): 65-86.

Fang, T., R. E. Coverdill, et al. (2009). "Air-fuel mixing and combustion in a small-bore direct injection optically accessible diesel engine using a retarded single injection strategy." Fuel **88**(11): 2074-2082.

Fang, T., C.-F. Lee, et al. (2010). Effects of Injection Pressure on Low-sooting Combustion in an Optical HSDI Diesel Engine Using a Narrow Angle Injector, SAE International.

Fielding, J., J. H. Frank, et al. (2002). "Polarized/Depolarized Rayleigh Scattering for Determining Fuel Concentrations in Flames." Proceedings- Combustion Institute **29**(2): 2703-2710.

Fikri, M., J. Herzler, et al. (2008). "Autoignition of gasoline surrogates mixtures at intermediate temperatures and high pressures." Combustion and flame **152**(1-2): 276-281.

Fiveland, S. B. and D. N. Assanis (2000). "A Four-Stroke Homogeneous Charge Compression Ignition Engine Simulation for Combustion and Performance Studies." Sae Transactions **109**(3): 452-468.

Fiveland, S. B. and D. N. Assanis (2002). Development and Validation of a Quasi-Dimensional Model for HCCI Engine Performance and Emissions Studies Under Turbocharged Conditions, SAE International.

Flynn, P. F., R. P. Durrett, et al. (1999). "Diesel Combustion: An Integrated View Combining Laser Diagnostics, Chemical Kinetics, and Empirical Validation." Sae Transactions **108**(3): 587-600.

Fontanesi, S., A. D'Adamo, et al. (2013). Assessment of the Potential of Proper Orthogonal Decomposition for the Analysis of Combustion CCV and Knock Tendency in a High Performance Engine, SAE International.

Gardiner, W. C., Y. Hidaka, et al. (1981). "Refractivity of combustion gases." Combustion and Flame **40**: 213-219.

Geitlinger, H., T. Streibel, et al. (1998). "Two-dimensional imaging of soot volume fractions, particle number densities, and particle radii in laminar and turbulent diffusion flames." Symposium (International) on Combustion **27**(1): 1613-1621.

Genzale, C. L., L. M. Pickett, et al. (2010). "2010-01-0610 Liquid Penetration of Diesel and Biodiesel Sprays at Late-Cycle Post-Injection Conditions." Sae Sp: 93-110.

Genzale, C. L., R. D. Reitz, et al. (2008). "Effects of Piston Bowl Geometry on Mixture Development and Late-Injection Low-Temperature Combustion in a Heavy-Duty Diesel Engine." Sae Sp **2008-01-1330**: 245-270.

Ghosh, P., K. J. Hickey, et al. (2006). "Development of a Detailed Gasoline Composition-Based Octane Model." Industrial and Engineering Chemistry Research **45**: 337-345.

Goldsborough, S. S. and P. Van Blarigan (1999). A Numerical Study of a Free Piston IC Engine Operating on Homogeneous Charge Compression Ignition Combustion, SAE International.

Goodger, E. M. (1975). Hydrocarbon fuels : production, properties, and performance of liquids and gases. London, Macmillan.

Greenhalgh, D. (2014). A new look at why soot particles explode when heated in LII systems. IEA TL Meeting, Stavanger

Guibet, J.-C. and E. Faure-Birchem (1999). Fuels and engines : technology, energy, environment. Paris, Éditions Technip.

Hamilton, B. (1995). "FAQ: Automotive Gasoline." from http://blizzard.rwic.und.edu/~nordlie/cars/gasoline.html.

Harada, A., N. Shimazaki, et al. (1998). The Effects of Mixture Formation on Premixed Lean Diesel Combustion. In-cylinder diesel particulate and NOx control, Detroit; MI, Sea.

Hartmann, L., K. Lucka, et al. (2003). "Mixture preparation by cool flames for diesel-reforming technologies." Journal of Power Sources **118**(1–2): 286-297.

Hasegawa, R. and H. Yanagihara (2003). "HCCI Combustion in DI Diesel Engine." SAE 2003-01-0745 **112**(3): 1070-1077.

He, X., R. P. Durrett, et al. (2008). "Late Intake Valve Closing as an Emissions Control Strategy at Tier 2 Bin 5 Engine-Out NOx Level." SAE 2008-01-0637 1-18.

Healy, W., C. Maasen, et al. (1959). "A new approach to blending octanes." 24th Meeting of the American Petroleum Institute's Division of Refining, New York: 39.

Herold, R. E., J. M. Krasselt, et al. (2009). "Investigations into the Effects of Thermal and Compositional Stratification on HCCI Combustion - Part II: Optical Engine Results." SAE 2009-01-1106

Hessel, R. P., D. E. Foster, et al. (2008). "Modeling Iso-octane HCCI Using CFD with Multi-Zone Detailed Chemistry; Comparison to Detailed Speciation Data Over a Range of Lean Equivalence Ratios." SAE 2008-01-0047

Heywood, J. B. (1988). Internal combustion engine fundamentals. New York, McGraw-Hill.

Higgins, B., D. Siebers, et al. (1998). "Effects of an ignition-enhancing, diesel-fuel additive on diesel-spray evaporation, mixing, ignition, and combustion." Symposium (International) on Combustion **27**(2): 1873-1880.

Hildingsson, L., G. Kalghatgi, et al. (2009). Fuel Octane Effects in the Partially Premixed Combustion Regime in Compression Ignition Engines, SAE International.

Hiroyasu, H. and M. Arai (1990). Structures of Fuel Sprays in Diesel Engines, SAE International.

Hofeldt, D. L. (1993). "Real-Time Soot Concentration Measurement Technique for Engine Exhaust Streams." Sae Transactions **102**(4): 45.

Hofmann, M., W. G. Bessler, et al. (2003). "Laser-Induced Incandescence for Soot Diagnostics at High Pressures." Appl. Opt. **42**(12): 2052-2062.

Holmes, P., J. L. Lumley, et al. (1996). Turbulence, coherent structures, dynamical systems, and symmetry. Cambridge ; New York, Cambridge University Press.

Horibe, N., H. Tanaka, et al. (2011). Selection of Injection Parameters for Various Engine Speeds in PCCI-Based Diesel Combustion with Multiple Injection, SAE International.

Hountalas, D. T., D. A. Kouremenos, et al. (2003). "2003-01-0340 Effect of Injection Pressure on the Performance and Exhaust Emissions of a Heavy Duty DI Diesel Engine." Sae Sp: 45-56.

Huestis, E., P. A. Erickson, et al. (2007). In-Cylinder and Exhaust Soot in Low-Temperature Combustion Using a Wide-Range of EGR in a Heavy-Duty Diesel Engine. Powertrain & fluid systems, Rosemont, IL, Society of Automotive Engineers.

Hultqvist, A., M. Christensen, et al. (1999). "A Study of the Homogeneous Charge Compression Ignition Combustion Process by Chemiluminescence Imaging." Sae Transactions **108**(3): 2114-2127.

Hwang, W., J. Dec, et al. (2008). "Spectroscopic and chemical-kinetic analysis of the phases of HCCI autoignition and combustion for single- and two-stage ignition fuels." Combustion and flame **154**(3): 387-409.

Idicheria, C. A. and L. M. Pickett (2005). "Soot Formation in Diesel Combustion Under High-EGR Conditions." SAE 2005-01-3834 **114**(4): 1559-1574.

Idicheria, C. A. and L. M. Pickett (2007). "Effect of EGR on diesel premixed-burn equivalence ratio." Proceedings- Combustion Institute **31**(2): 2931-2938.

Idicheria, C. A. and L. M. Pickett (2007). "Formaldehyde Visualization Near Lift-Off Location in a Diesel Jet." SAE 2006-01-3434

Idicheria, C. A. and L. M. Pickett (2007). Quantitative Mixing Measurements in a Vaporizing Diesel Spray by Rayleigh Imaging. Society of Automotive Engineers, Detroit, MI, Society of Automotive Engineers.

Idicheria, C. A. and L. M. Pickett (2011). "Ignition, soot formation, and end-of-combustion transients in diesel combustion under high-EGR conditions." International Journal of Engine Research **12**(4): 376-392.

Ikeda, Y., M. Kaneko, et al. (2001). Local A/F Measurement by Chemiluminescence OH*, CH* and C2* in SI Engine, SAE International.

Inagaki, K., S. Miura, et al. (1998). Quantitative Soot Concentration Measurement with the Correction of Attenuated Signal Intensity Using Laser-Induced Incandescence. The Fourth International Symposium COMODIA 98.

Inagaki, K., S. Takasu, et al. (1999). "In-Cylinder Quantitative Soot Concentration Measurement by Laser-Induced Incandescence." SAE 1999-01-0508.

Ishibashi, Y. and H. Morikawa (2007). "An Experimental Approach to the Controlled Auto-Ignition." Sae Sp **2007-01-0173**: 1-8.

Ishibashi, Y. and H. Morikawa (2008). "A macroscopic Understanding of the Controlled Auto-Ignition for Vehicle Engines." Sae Sp: 1-10.

Iwabuchi, Y., K. Kawai, et al. (1999). "Trial of New Concept Diesel Combustion System-Premixed Compression-Ignition Combustion." Sae Transactions **108**(3): 142-151.

Jacobs, T. J. and D. N. Assanis (2007). "The attainment of premixed compression ignition low-temperature combustion in a compression ignition direct injection engine." Proceedings-Combustion Institute **31**(2): 2913-2920.

Jacobs, T. J., S. V. Bohac, et al. (2005). "2005-01-0166 Lean and Rich Premixed Compression Ignition Combustion in a Light-Duty Diesel Engine." Sae Transactions **114**(3): 382-393.

Jaroń-Becker, A., A. Becker, et al. (2004). "Ionization of N 2, O 2, and linear carbon clusters in a strong laser pulse." Physical Review A **69**(2): 023410.

Joachain, C. J., N. J. Kylstra, and R. M. Potvliege. (2011). Atoms in Intense Laser Fields, Cambridge University Press.

Johansson, J., J. Fedor, et al. (2012). "Anisotropic hot electron emission from fullerenes." The Journal of Chemical Physics **136**(16): 164301.

Johnson, A. J. and G. H. Auth (1951). Fuels and combustion handbook. New York,, McGraw-Hill.

Juneja, H., Y. Ra, et al. (2004). "Optimization of Injection Rate Shape Using Active Control of Fuel Injection." SAE 2004-01-0530 193-210.

Kalghatgi, G. (2015). A. Taylor.

Kalghatgi, G., L. Hildingsson, et al. (2009). Low NOx and Low Smoke Operation of a Diesel Engine Using Gasoline-Like Fuels. Preceedings of the ASME Internal Combustion Engine Division 2009 Spring Technical Conference. Milwaukee, Wisconsin.

Kalghatgi, G., P. Risberg, et al. (2003). A Method of Defining Ignition Quality of Fuels in HCCI Engines. Premixed charge CI engines, Yokohama, Japan, SAE 2003-01-1816

Kalghatgi, G., P. Risberg, et al. (2007). "Advantages of Fuels with High Resistance to Autoignition in Late-Injection, Low-Temperature, Compression Ignition Combustion." SAE 2006-01-3385 **115**(4): 623-634.

Kalghatgi, G. T. (1990). Deposits in gasoline engines, United States, Warrendale, PA (United States) ;Society of Automotive Engineers.

Kalghatgi, G. T. and R. A. Head (2004). "The Available and Required Autoignition Quality of Gasoline - Like Fuels in HCCI Engines at High Temperatures." SAE 2004-01-1969 221-236.

Kalghatgi, G. T., P. Risberg, et al. (2006). Advantages of Fuels with High Resistance to Auto-ignition in Late-injection, Low-temperature, Compression Ignition Combustion, SAE International.

Kalghatgi, G. T., P. Risberg, et al. (2007). Partially Pre-Mixed Auto-Ignition of Gasoline to Attain Low Smoke and Low NOx at High Load in a Compression Ignition Engine and Comparison with a Diesel Fuel, SAE International.

Kalghatgi, G. T., P. Risberg, et al. (2007). Partially Pre-Mixed Auto-Ignition of Gasoline to Attain Low Smoke and Low NOx at High Load in a Compression Ignition Engine and Comparison with a Diesel Fuel. Society of Automotive Engineers; Fuels & emissions conference, Cape Town, South Africa, Society of Automotive Engineers.

Kamimoto, T. and M. H. Bae (1988). High combustion temperature for the reduction of particulate in diesel engines, United States, Society of Automotive Engineers,Warrendale, PA.

Karra, P. and S. C. Kong (2008). "Diesel Emission Characteristics Using High Injection Pressure with Converging Nozzles in a Medium-Duty Engine." SAE 2008-01-1085: 95-110.

Kashdan, J. T., N. Docquier, et al. (2004). "Mixture Preparation and Combustion Via LIEF and LIF of Combustion Radicals in a Direct-Injection, HCCI Diesel Engine." SAE 2004-01-2945

Kashdan, J. T., S. Mendez, et al. (2007). "On the Origin of Unburned Hydrocarbon Emissions in a Wall-Guided, Low NOx Diesel Combustion System." SAE **2007-01-1836**.

Kashdan, J. T. and J. Papagni (2005). "LIF Imaging of Auto-ignition and Combustion in a Direct Injection Diesel-fuelled HCCI Engine." SAE **2005-01-3739**.

Kastner, O., F. Atzler, et al. (2006). Multiple Injection Strategies and Their Effect on Pollutant Emission in Passenger Car Diesel Engines. Conference on Thermo- and Fluid Dynamic Processes in Diesel Engines. THIESEL, Valencia.

Kastner, O., F. Atzler, et al. (2008). Evaluation of Injection Strategies for Passenger Car Diesel Engines to Meet Euro 6 Legislation Limits. Thiesel 2008: Thermo-and fluid dynamic processes in Diesel Engines. Universidad Polit´ecnica de Valencia, Valencia, Spain.

Kennaird, D. A., C. Crua, et al. (2002). In-Cylinder Penetration and Break-Up of Diesel Sprays Using a Common-Rail Injection System, SAE International.

Kim, D., I. Ekoto, et al. (2008). In-cylinder CO and UHC Imaging in a Light-Duty Diesel Engine during PPCI Low-Temperature Combustion. 2008 SAE International powertrains fuels and lubricants congress, Shanghai, China, Society of Automotive Engineers.

Kimura, S. (2002). "An experimental analysis of low-temperature and premixed combustion for simultaneous reduction of NO_x and particulate emissions in direct injection diesel engines." International Journal of Engine Research **3**(4): 249-259.

Kimura, S., O. Aoki, et al. (2001). "Ultra-Clean Combustion Technology Combining a Low-Temperature and Premixed Combustion Concept for Meeting Future Emission Standards." Sae Transactions **110**(4): 239-246.

Kimura, S., O. Aoki, et al. (1999). "New Combustion Concept for Ultra-Clean and High-Efficiency Small DI Diesel Engines." Sae Transactions **108**(3): 2128-2137.

Knafl, A., T. Jacobs, et al. (2006). The Load Limits of Low Temperature Premixed Compression Ignition Diesel Combustion. The 2nd International Symposium on "Clean and High-Efficiency Combustion in Engines", Tianjin, China.

Koci, C. P., Y. Ra, et al. (2009). "2009-01-0925 Multiple-Event Fuel Injection Investigations in a Highly-Dilute Diesel Low Temperature Combustion Regime." Sae Sp: 353-374.

Kock, B. F. (2005). "Comparison of LII and TEM sizing during synthesis of iron particle chains." Proceedings of the Combustion Institute **30**(1): 1689.

Kock, B. F., T. Eckhardt, et al. (2002). "In-cylinder sizing of diesel particles by time-resolved laser-induced incandescence (TR-LII)." Proceedings of the Combustion Institute **29**(2): 2775-2782.

Kock, B. F., B. Tribalet, et al. (2006). "Two-color time-resolved LII applied to soot particle sizing in the cylinder of a Diesel engine." Combustion and Flame **147**(1-2): 79-92.

Kohse-Hoinghaus, K. and J. B. Jeffries (2002). Applied combustion diagnostics. New York ; London, Taylor & Francis.

Kokjohn, S., R. D. Reitz, et al. (2012). "Investigation of Fuel Reactivity Stratification for Controlling PCI Heat-Release Rates Using High-Speed Chemiluminescence Imaging and Fuel Tracer Fluorescence." SAE Int. J. Engines **5**(2): 248-269.

Kolodziej, C. P., S. Ciatti, et al. (2014). Extension of the Lower Load Limit of Gasoline Compression Ignition with 87 AKI Gasoline by Injection Timing and Pressure, SAE International.

Komninos, N. P., D. T. Hountalas, et al. (2007). "A parametric investigation of hydrogen hcci combustion using a multi-zone model approach." Energy Conversion and Management **48**(11): 2934-2941.

Kondo, K., T. Aizawa, et al. (2013). Uncertainty in Sampling and TEM Analysis of Soot Particles in Diesel Spray Flame, SAE International.

Kook, S., C. Bae, et al. (2005). "The Influence of Charge Dilution and Injection Timing on Low-Temperature Diesel Combustion and Emissions." SAE 2005-01-3837 **114**(4): 1575-1595.

Kook, S. and L. M. Pickett (2012). "Soot Volume Fraction and Morphology of Conventional, Fischer-Tropsch, Coal-Derived, and Surrogate Fuel at Diesel Conditions." SAE Int. J. Fuels Lubr. **5**(2): 647-664.

Kook, S., L. M. Pickett, et al. (2009). "Influence of Diesel Injection Parameters on End-of-Injection Liquid Length Recession." SAE 2009-01-1356

Kook, S., L. M. Pickett, et al. (2008). Liquid-Phase Diesel Spray Penetration during End-of-Injection Transient. COMODIA. Sapporo, Japan. **MD3-1**.

Koylu, U. and G. Faeth (1996). "Spectral extinction coefficients of soot aggregates from turbulent diffusion flames." Transactions of the ASME-C-Journal of Heat Transfer **118**(2): 415-421.

Köylü, Ü. Ö. (1997). "Quantitative analysis of in situ optical diagnostics for inferring particle/aggregate parameters in flames: Implications for soot surface growth and total emissivity." Combustion and flame **109**(3): 488-500.

Kozarac, D., M. Sjeric, et al. (2010). Introducing Initial Conditions with Non-uniform Mixtures and Fuel Injection into the Multi Zone HCCI Simulation Model, SAE International.

Kraft, M., P. Maigaard, et al. (2000). "Investigation of Combustion Emissions in a Homogeneous Charge Compression Injection Engine: Measurements and a New Computational Model." Proceedings- Combustion Institute **28**(1): 1195-1202.

Kuboyama, T., Y. Moriyoshi, et al. (2009). "An Experimental Study of a Gasoline HCCI Engine Using the Blow-Down Super Charge System." SAE 2009-01-0496 195-204.

Lachaux, T. and M. P. Musculus (2007). "In-cylinder unburned hydrocarbon visualization during low-temperature compression-ignition engine combustion using formaldehyde PLIF." Proceedings-Combustion Institute **31**(2): 2921-2929.

Laguitton, O., C. Crua, et al. (2007). "The effect of compression ratio on exhaust emissions from a PCCI diesel engine." Energy Conversion and Management **48**(11): 2918-2924.

Lechner, G. A., T. J. Jacobs, et al. (2005). "2005-01-0167 Evaluation of a Narrow Spray Cone Angle, Advanced Injection Timing Strategy to Achieve Partially Premixed Compression Ignition Combustion in a Diesel Engine." Sae Transactions **114**(3): 394-404.

Lee, T. and R. D. Reitz (2003). "The Effect of Intake Boost Pressure on MK (Modulated Kinetics) Combustion." JSME International Journal Series B Fluids and Thermal Engineering **46**(3): 451-459.

Lehre, T., B. Jungfleisch, et al. (2003). "Size Distributions of Nanoscaled Particles and Gas Temperatures from Time-Resolved Laser-Induced-Incandescence Measurements." Appl. Opt. **42**(12): 2021-2030.

Leider, H. R., O. H. Krikorian, et al. (1973). "Thermodynamic properties of carbon up to the critical point." Carbon **11**(5): 555-563.

Lequien, G., E. Berrocal, et al. (2013). Effect of Jet-Jet Interactions on the Liquid Fuel Penetration in an Optical Heavy-Duty DI Diesel Engine, SAE International.

Liu, F., K. J. Daun, et al. (2006). "Some theoretical considerations in modeling laser-induced incandescence at low-pressures." Applied Physics B **87**(1): 179-191.

Liu, F., G. J. Smallwood, et al. (2005). "Effects of primary particle diameter and aggregate size distribution on the temperature of soot particles heated by pulsed lasers." Journal of Quantitative Spectroscopy and Radiative Transfer **93**(1-3): 301-312.

Liu, K. and D. C. Haworth (2011). Development and Assessment of POD for Analysis of Turbulent Flow in Piston Engines, SAE International.

Liu, S. (2004). "Effects of strain rate on high-pressure nonpremixed n-heptane autoignition in counterflow." Combustion and flame **137**(3): 320-339.

Lovell, W. G. (1948). "Knocking Characteristics of Hydrocarbons." Industrial & engineering chemistry **40**(12): 2388.

Lucas, A. G. (2000). Modern petroleum technology. Vol.2, Downstream. Chichester, Wiley.

Lumley, J. L. (1999). Engines : an introduction. Cambridge, UK ; New York, Cambridge University Press.

Manente, V., B. Johansson, et al. (2009). Effects of Different Type of Gasoline Fuels on Heavy Duty Partially Premixed Combustion, SAE International.

Manente, V., P. Tunestal, et al. (2007). "A Study of Glow Plug Ignition Engine by Chemiluminescence Images." SAE **2007-01-1884**.

Manin, J., S. Skeen, et al. (2014). "Effects of Oxygenated Fuels on Combustion and Soot Formation/Oxidation Processes." SAE Int. J. Fuels Lubr. **7**(3).

Manzello, Samuel L., Eui J. Lee, et al. (2005). "Use of laser-induced ionization to detect soot inception in premixed flames." Applied Optics **44**(24): 5105-5111.

Marshall, E. L. and K. Owen (1995). Motor gasoline. Cambridge, Royal Society of Chemistry.

Martin, G. C., C. J. Mueller, et al. (2008). "Early Direct-Injection, Low-Temperature Combustion of Diesel Fuel in an Optical Engine Utilizing a 15-Hole, Dual-Row, Narrow-Included-Angle Nozzle." SAE Int. J. Engines **1**(1): 1057-1082.

Mastorakos, E. (2003). Control in Inhomogeneous Charged Compression Ignition Engines: Task 1. Numerical Study of HCCI Combustion. First, Second, Third and fourth Progress Reports to Honda R & D Co., Ltd, Japan

Mehl, M., W. J. Pitz, et al. (2011). "Kinetic modeling of gasoline surrogate components and mixtures under engine conditions." Proceedings- Combustion Institute **33, Numb 1**: 193-200.

Melton, L. A. (1984). "Soot diagnostics based on laser heating." Applied Optics **23**(13): 2201.

Menkiel, B., A. Donkerbroek, et al. (2012). "Measurement of in-cylinder soot particles and their distribution in an optical HSDI diesel engine using time resolved laser induced incandescence (TR-LII)." Combustion and flame **159**(9): 2985-2998.

Menkiel, B. a. and L. Ganippa (2012). Investigation of soot processes in an optical diesel engine, Brunel University.

Meyer, T. R., S. Roy, et al. (2005). "Simultaneous planar laser-induced incandescence, OH planar laser-induced fluorescence, and droplet Mie scattering in swirl-stabilized spray flames." Appl. Opt. **44**(3): 445-454.

Michelsen, H. A. (2003). "Understanding and predicting the temporal response of laser-induced incandescence from carbonaceous particles." The Journal of Chemical Physics **118**(15): 7012-7045.

Michelsen, H. A., F. Liu, et al. (2007). "Modeling laser-induced incandescence of soot: a summary and comparison of LII models." Applied Physics B **87**(3): 503-521.

Miles, P. C. (2000). The Influence of Swirl on HSDI Diesel Combustion at Moderate Speed and Load. Combustion in diesel and SI engines, Paris, Sae.

Miles, P. C., D. Choi, et al. (2004). "Rate-limiting processes in late-injection, low-temperature diesel combustion regimes." Proc. Conf. Thermo Fluid Proc. Diesel Eng. — Thiesel.

Miles, P. C., R. Collin, et al. (2007). "Combined measurements of flow structure, partially oxidized fuel, and soot in a high-speed, direct-injection diesel engine." Proceedings of the Combustion Institute **31**(2): 2963-2970.

Mollenhauer, K. P. D. I. and H. Tschoeke (2010). Handbook of diesel engines. Heidelberg, Springer.

Morgan, N., A. Smallbone, et al. (2010). "Mapping surrogate gasoline compositions into RON/MON space." Combustion and Flame **157**(6): 1122-1131.

Morgan, R. E., M. R. Gold, et al. (2003). Characterisation of the Soot Formation Processes in a High Pressure Combusting Diesel Fuel Spray, SAE International.

Morris, W. (1975). "The interaction approach to gasoline blending." NPTA 73rd Annual General Meeting, Paper number AM-75-30.

Mueller, C. J. and G. C. Martin (2002). "Effects of Oxygenated Compounds on Combustion and Soot Evolution in a DI Diesel Engine: Broadband Natural Luminosity Imaging." SAE 2002-01-1631 **111**(4): 518-537.

Mueller, C. J., G. C. Martin, et al. (2004). "An Experimental Investigation of In-Cylinder Processes under Dual-Injection Conditions in a DI Diesel Engine." SAE 2004-01-1843: 53-72.

Mueller, C. J., W. J. Pitz, et al. (2003). "Effects of Oxygenates on Soot Processes in DI Diesel Engines: Experiments and Numerical Simulations." SAE 2003-01-1791 **112**(4): 964-982.

Munch, K. (1992). Investigation of Spray Penetration and Fuel Distribution Inside the Piston Bowl of a 1. 9 L Di Diesel Engine Using Two-Dimensional Mie Scattering, Society of Automotive Engineers, 400 Commonwealth Dr, Warrendale, PA, 15096, USA.

Murata, Y., J. Kusaka, et al. (2008). "Miller-PCCI Combustion in an HSDI Diesel Engine with VVT." SAE 2008-01-0644 103-116.

Murty, B. S. N. and R. N. Rao (2004). "Global optimization for prediction of blend composition of gasolines of desired octane number and properties." Fuel Processing Technology **85**(14): 1595-1602.

Musculus, M. P. and L. M. Pickett (2005). "Diagnostic considerations for optical laser-extinction measurements of soot in high-pressure transient combustion environments." Combustion and Flame **141**(4): 371-391.

Musculus, M. P. B. (2004). "On the Correlation Between NO~x Emissions and the Diesel Premixed Burn." SAE 2004-01-1401 **113**(4): 631-651.

Musculus, M. P. B. (2007). "Multiple Simultaneous Optical Diagnostic Imaging of Early-Injection, Low-Temperature Combustion in a Heavy-Duty Diesel Engine." SAE 2006-01-0079 **115**(3): 83-110.

Musculus, M. P. B. and K. Kattke (2009). "Entrainment Waves in Diesel Jets." SAE 2009-01-1355

Musculus, M. P. B., T. Lachaux, et al. (2007). "End-of-Injection Over-Mixing and Unburned Hydrocarbon Emissions in Low-Temperature-Combustion Diesel Engines." SAE 2007-01-0907: 49-76.

Musculus, M. P. B., P. C. Miles, et al. (2013). "Conceptual models for partially premixed low-temperature diesel combustion." Progress in Energy and Combustion Science **39**(2–3): 246-283.

Myers, M. E., J. Stollsteimer, et al. (1975). "Determination of Gasoline Octane Numbers from Chemical Composition." Analytical Chemistry **47**(13): 2301-2304.

Naber, J. D. and D. L. Siebers (1996). "Effects of Gas Density and Vaporization on Penetration and Dispersion of Diesel Sprays." Sae Transactions **105**(3): 82-111.

Naik, C. V., W. J. Pitz, et al. (2005). "Detailed Chemical Kinetic Modelling of Surrogate Fuels for Gasoline and Application to an HCCI Engine." SAE 2005-01-3741 **114**(4): 1381-1387.

Najt, P. M. and D. E. Foster (1983). Compression-Ignited Homogeneous Charge Combustion, SAE International.

Namer, I. and R. W. Schefer (1985). "Error estimates for Rayleigh scattering density and temperature measurements in premixed flames." Experiments in Fluids **3**(1): 1.

Ni, T., J. A. Pinson, et al. (1995). "Two-dimensional imaging of soot volume fraction by the use of laser-induced incandescence." Appl. Opt. **34**(30): 7083-7091.

Noehre, C., M. Andersson, et al. (2006). "Characterization of Partially Premixed Combustion." SAE **2006-01-3412**.

O'Connor, J. and M. Musculus (2013). "Post Injections for Soot Reduction in Diesel Engines: A Review of Current Understanding." SAE Int. J. Engines **6**(1): 400-421.

O'Connor, J. and M. Musculus (2014). "In-Cylinder Mechanisms of Soot Reduction by Close-Coupled Post-Injections as Revealed by Imaging of Soot Luminosity and Planar Laser-Induced Soot Incandescence in a Heavy-Duty Diesel Engine." SAE Int. J. Engines **7**(2): 673-693.

Obert, E. F. and B. H. Jennings (1950). Internal combustion engines, analysis and practice. Scranton,, International Textbook Co.

Okude, K., K. Mori, et al. (2004). "2004-01-1907 Premixed Compression Ignition (PCI) Combustion for Simultaneous Reduction of NOx and Soot in Diesel Engine." Sae Transactions **113**(4): 1002-1013.

Owen, K., T. Coley, et al. (1995). Automotive fuels reference book. Warrendale, Pa., Society of Automotive Engineers.

Park, S. W. and C. S. Lee (2004). "Macroscopic and microscopic characteristics of a fuel spray impinged on the wall." Experiments in Fluids **37**(5): 745-762.

Parrish, S. E., G. Zhang, et al. (2012). "Liquid and Vapor Envelopes of Sprays from a Multi-Hole Fuel Injector Operating under Closely-Spaced Double-Injection Conditions." SAE Int. J. Engines **5**(2): 400-414.

Pasadakis, N., V. Gaganis, et al. (2006). "Octane number prediction for gasoline blends." Fuel Processing Technology **87**(6): 505-509.

Per Risberg , Gautan Kalghagi and Hans-Erik Angstorm (2004). "The influence of EGR on Auto-ignition quality of gasoline-like fuels in HCCI engines." SAE **2004-01-2952**.

Per Risberg , Gautan Kalghagi and Hans-Erik Angstorm (2005). "Auto-ignition quality of Diesel-like fuels in HCCI Engines." SAE **2005-01-2127**.

Petersen, B., P. C. Miles, et al. (2012). "Equivalence Ratio Distributions in a Light-Duty Diesel Engine Operating under Partially Premixed Conditions." SAE Int. J. Engines **5**(2): 526-537.

Petrou, M. and C. Petrou (2010). Image Processing: The Fundamentals, John Wiley & Sons.

Pickett, L. M. (2005). "Low flame temperature limits for mixing-controlled Diesel combustion." Proceedings of the Combustion Institute **30**(2): 2727-2735.

Pickett, L. M., J. A. Caton, et al. (2006). "Evaluation of the equivalence ratio-temperature region of diesel soot precursor formation using a two-stage Lagrangian model." International Journal of Engine Research **7**: 349-370.

Pickett, L. M. and L. Hoogterp (2008). "Fundamental Spray and Combustion Measurements of JP-8 at Diesel Conditions." Sae Sp: 135-146.

Pickett, L. M., S. Kook, et al. (2009). "Transient Liquid Penetration of Early-Injection Diesel Sprays." SAE 2009-01-0839

Pickett, L. M., S. Kook, et al. (2009). "Visualization of Diesel Spray Penetration, Cool-Flame, Ignition, High-Temperature Combustion, and Soot Formation Using High-Speed Imaging." SAE 2009-01-0658

Pickett, L. M., S. Kook, et al. (2009). "Visualization of Diesel Spray Penetration, Cool-Flame, Ignition, High-Temperature Combustion, and Soot Formation Using High-Speed Imaging." SAE Int. J. Engines **2**(1): 439-459.

Pickett, L. M., J. Manin, et al. (2011). "Relationship Between Diesel Fuel Spray Vapor Penetration/Dispersion and Local Fuel Mixture Fraction." SAE Int. J. Engines **4**(1): 764-799.

Pickett, L. M., J. Manin, et al. (2013). Transient Rate of Injection Effects on Spray Development, SAE International.

Pickett, L. M., D. L. Siebers, et al. (2005). "2005-01-3843 Relationship Between Ignition Processes and the Lift-Off Length of Diesel Fuel Jets." Sae Transactions **114**(3): 1714-1731.

Pickett, L. M., D. L. Siebers, et al. (2005). Relationship Between Ignition Processes and the Lift-Off Length of Diesel Fuel Jets, SAE International.

Poetsch, C., H. Ofner, et al. (2011). Assessment of a Multi Zone Combustion Model for Analysis and Prediction of CI Engine Combustion and Emissions, SAE International.

Polonowski, C. J., C. J. Mueller, et al. (2011). "An Experimental Investigation of Low-Soot and Soot-Free Combustion Strategies in a Heavy-Duty, Single-Cylinder, Direct-Injection, Optical Diesel Engine." JSAE **20119091**.

Quay, B., T. W. Lee, et al. (1994). "Spatially resolved measurements of soot volume fraction using laser-induced incandescence." Combustion and flame **97**(3-4): 384-392.

Ra, Y. and R. D. Reitz (2008). "A reduced chemical kinetic model for IC engine combustion simulations with primary reference fuels." Combustion and Flame **155**(4): 713-738.

Rusin, M. H., H. S. Chung, et al. (1981). "A Transformation Method for Calculating the Research and Motor Octane Numbers of Gasoline Blends." Industrial & Engineering Chemistry Fundamentals **20**(3): 195-204.

Rusly, A., M. K. Le, et al. (2013). "Effect of Injection Pressure on Transient Behaviour of Wall-Interacting Jet Flame Base in an Automotive-Size Diesel Engine." SAE Int. J. Fuels Lubr. **6**(3): 615-626.

Sarmanaev, R. S., R. B. Valitov, et al. (1980). "Influence of Gasoline Hydrocarbon Composition on Octane Number." Chemistry and Technology of Fuels and Oils **16**(11-1): 773-776.

Schoemaecker Moreau, C., E. Therssen, et al. (2004). "Two-color laser-induced incandescence and cavity ring-down spectroscopy for sensitive and quantitative imaging of soot and PAHs in flames." Applied Physics B: Lasers and Optics **78**(3-4): 485-492.

Schoen, W. and A. Mrstik (1955). "Calculating gasoline blend octane ratings." Industrial & engineering chemistry **47**(9): 1740-1742.

Schraml, S., S. Will, et al. (2000). "Performance Characteristics of TIRE-LII Soot Diagnostics in Exhaust Gases of Diesel Engines." Sae Sp(1552): 67-74.

Schulz, C., J. Gronki, et al. (2004). "2004-01-1917 Multi-Species, Laser-Based Imaging Measurements in a Diesel Spray." Sae Transactions **113**(4): 1032-1042.

Schulz, C., B. F. Kock, et al. (2006). "Laser-induced incandescence: recent trends and current questions." Applied Physics B-Lasers and Optics **83**(3): 333-354.

Schulz, C., V. Sick, et al. (1996). "Quantitative 2D single-shot imaging of no concentrations and temperatures in a transparent SI engine." Symposium (International) on Combustion **26**(2): 2597-2604.

Seinfeld, J. H. and S. N. Pandis (2006). Atmospheric chemistry and physics : from air pollution to climate change. Hoboken, N.J., Wiley.

Sellnau, M., J. Sinnamon, et al. (2011). "Gasoline Direct Injection Compression Ignition (GDCI) - Diesel-like Efficiency with Low CO2 Emissions." SAE Int. J. Engines **4**(1): 2010-2022.

Shaddix, C. R. and K. C. Smyth (1996). "Laser-induced incandescence measurements of soot production in steady and flickering methane, propane, and ethylene diffusion flames." Combustion and Flame **107**(4): 418-452.

Sheinson, R. S. and F. W. Williams (1975). "Cool flames. Use of the term in combustion chemistry and analytical chemistry." Analytical Chemistry **47**(7): 1197-1198.

Siebers, D. and B. Higgins (2001). Flame Lift-Off on Direct-Injection Diesel Sprays Under Quiescent Conditions, SAE International.

Siebers, D., B. Higgins, et al. (2002). "Flame Lift-Off on Direct-Injection Diesel Fuel Jets: Oxygen Concentration Effects." Sae Transactions **111**(3): 1490-1509.

Siebers, D. L. (1985). "Ignition Delay Characteristics of Alternative Diesel Fuels: Implications on Cetane Number." SAE **852102**.

Siebers, D. L. (1998). "Liquid-Phase Fuel Penetration in Diesel Sprays." Sae Transactions **107**(3): 1205-1227.

Silke, E. J., W. J. Pitz, et al. (2008). "Understanding the Chemical Effects of Increased Boost Pressure under HCCI Conditions." SAE 2008-01-0019

Singh, S., R. Reitz, et al. (2007). "Simultaneous Optical Diagnostic Imaging of Low-Temperature, Double-Injection Combustion in a Heavy-Duty Di Diesel Engine." Combustion Science and Technology **179**(11): 2381-2414.

Sjoberg, M. and J. E. Dec (2006). "Smoothing HCCI Heat-Release Rates Using Partial Fuel Stratification with Two-Stage Ignition Fuels." SAE 2006-01-0629

Sjoberg, M. and J. E. Dec (2008). "Influence of Fuel Autoignition Reactivity on the High-Load Limits of HCCI Engines." SAE 2008-01-0054 377-396.

Sjoberg, M. and J. E. Dec (2009). "Influence of EGR Quality and Unmixedness on the High-Load Limits of HCCI Engines." SAE 2009-01-0666

Sjöberg, M. and J. E. Dec (2007). "Comparing late-cycle autoignition stability for single- and two-stage ignition fuels in HCCI engines." Proceedings of the Combustion Institute **31**(2): 2895-2902.

Sjoberg, M., J. E. Dec, et al. (2005). "Potential of Thermal Stratification and Combustion Retard for Reducing Pressure-Rise Rates in HCCI Engines, Based on Multi-Zone Modelling and Experiments." SAE 2005-01-0113.

Sjoberg, M., J. E. Dec, et al. (2007). Thermodynamic and Chemical Effects of EGR and Its Constituents on HCCI Autoignition. SAE 2007-01-0207 Detroit MI, Warrendale.

Sjöholm, J., R. Wellander, et al. (2011). "Challenges for In-Cylinder High-Speed Two-Dimensional Laser-Induced Incandescence Measurements of Soot." SAE Int. J. Engines **4**(1): 1607-1622.

Smallbone, A. J., N. Morgan, et al. (2010). "Simulating Combustion of Practical Fuels and Blends for Modern Engine Applications Using Detailed Chemical Kinetics." SAE 2010-01-0572 281-294.

Smyth, K. C. and W. Gary Mallard (1981). "Laser-Induced Ionization and Mobility Measurements of Very Small Particles in Premixed Flames at the Sooting Limit." Combustion Science and Technology **26**(1-2): 35-41.

Smyth, K. C. and C. R. Shaddix (1996). "The Elusive History of m = 1.57 - 0.56i for the Refractive Index of Soot." Combustion and Flame **107**(3): 314-320.

Snelling, D. R., F. Liu, et al. (2000). Evaluation of the nanoscale heat and mass transfer model of LII: preduction of the excitation intensity, Pittsburgh, PA, USA, American Society of Mechanical Engineers (ASME).

Snelling, D. R., F. Liu, et al. (2004). "Determination of the soot absorption function and thermal accommodation coefficient using low-fluence LII in a laminar coflow ethylene diffusion flame." Combustion and flame **136**(1-2): 180-190.

Snelling, D. R., G. J. Smallwood, et al. (2000). "2000-01-1994 In-Situ Real-Time Characterization of Particulate Emissions from a Diesel Engine Exhaust by Laser-Induced Incandescence." Sae Transactions **109**(4): 1914-1925.

Sorensen, C. M. (2001). "Light scattering by fractal aggregates: a review." Aerosol science and technology **35**(2): 648.

Soulopoulos, N. (2014).

Splitter, D., R. Hanson, et al. (2011). Reactivity Controlled Compression Ignition (RCCI) Heavy-Duty Engine Operation at Mid-and High-Loads with Conventional and Alternative Fuels, SAE International.

Stewart, W. (1959). "Predict octanes for gasoline blends." Petroleum Refiner **38**: 135-139.

Stewart, W. (1959). "Predict RVP of blends accurately." Petroleum Refiner **38**: 231-234.

Sun, Y. and R. D. Reitz (2008). "Adaptive Injection Strategies (AIS) for Ultra-Low Emissions Diesel Engines." SAE 2008-01-0058: 407-422.

Sutton, J. A. and J. F. Driscoll (2004). "Rayleigh scattering cross sections of combustion species at 266, 355, and 532 nm for thermometry applications." Optics Letters **29**(22): 2620-2622.

Swaminathan, N. and K. N. C. Bray (2011). Turbulent premixed flames. Cambridge, Cambridge University Press.

Talley, D. G., V. G. McDonell, et al. (2001). Optical patternation method. US.

Tanabe, K., S. Kohketsu, et al. (2005). "Effect of Fuel Injection Rate Control on Reduction of Emissions and Fuel Consumption in a Heavy Duty Dl Diesel Engine." SAE 2005-01-0907: 1-12.

Tropea, C., A. Yarin, et al. (2007). Combustion Diagnostics. Springer Handbook of Experimental Fluid Mechanics, Springer Berlin Heidelberg**:** 1241-1315.

Tufail, K. (2015).

Twu, C. H. and J. E. Coon (1996). "Predict octane numbers using a generalized interaction method." Hydrocarbon Processing **75**(2): 51-58.

Twu, C. H. and J. E. Coon (1997). "Estimate octane numbers using an enhanced method." Hydrocarbon Processing **76**(3): 65-68.

Van Basshuysen, R. and F. Schäfer (2007). Modern engine technology : from A to Z. Warrendale, PA, SAE International.

Vander Wal, R. L. (1994). "Laser-induced incandescence: Development and characterization towards a measurement of soot-volume fraction." Applied physics. B, Lasers and optics **59**(4): 445-452.

Vander Wal, R. L. (1996). "Laser-induced incandescence: detection issues." Appl. Opt. **35**(33): 6548-6559.

Vander Wal, R. L. (2005). Soot Nanostructure: Definition, Quantification and Implications, SAE International.

Vander Wal, R. L., T. M. Ticich, et al. (1999). "Can soot primary particle size be determined using laser-induced incandescence?" Combustion and flame **116**(1-2): 291-296.

Vazquez-Esparragoza, J. and J. Bullin (1992). "How to estimate Rvp of blends." Hydrocarbon Processing ; Vol/Issue: 71:8: Pages: 135-138.

Veazey, W., C. R. Company, et al. (1964). Handbook of chemistry and physics, Chemical Rubber Pub. Co.

Viollet, Y., J. Chang, et al. (2014). "Compression Ratio and Derived Cetane Number Effects on Gasoline Compression Ignition Engine Running with Naphtha Fuels." SAE Int. J. Fuels Lubr. **7**(2): 412-426.

Viskup, R., T. Stanger, et al. (2013). Development of In-Situ, Full Stream, Laser Induced Incandescence Technique for Measurement of Transient Soot Emissions, SAE International.

Vogel, A. (1946). "Physical properties and chemical constitution Part XI aliphatic hydrocarbons." Journal of the Chemical Society: 133.

Vogel, S., C. Hasse, et al. (2005). "Numerical simulation and laser-based imaging of mixture formation, ignition, and soot formation in a diesel spray." Proceedings of the Combustion Institute **30**(2): 2029-2036.

Vogel, T., S. Riess, et al. (2013). Soot Formation of Different Diesel-Fuels Investigated by Chemical Luminescence and Laser Induced Incandescence, SAE International.

Wagner, H. G. (1981). "Soot formation, an overview." Particulate Carbon, Formation During Combustion: 1–29.

Walter, B. and B. Gatellier (2002). "Development of the High-Power NADITM Concept Using Dual-Mode Diesel Combustion to Achieve Zero NOx and Particulate Emissions." SAE Transactions 2002-01-1744 **111**(4): 779-787.

Wang, T. C., J. S. Han, et al. (1999). "Direct Visualization of High Pressure Diesel Spray and Engine Combustion." SAE 1999-01-3496.

Weall, A. and N. Collings (2009). Gasoline Fuelled Partially Premixed Compression Ignition in a Light Duty Multi Cylinder Engine: A Study of Low Load and Low Speed Operation, SAE International.

Weeks, R. W. and W. W. Duley (1974). "Aerosol-particle sizes from light emission during excitation by TEA CO[sub 2] laser pulses." Journal of Applied Physics **45**(10): 4661-4662.

Wei, D. p. (2000). "Study on the Lubricity of Gasoline Fuels II. The Chemical Composition of Gasoline Fuels." Acta Petrolei Sinica Petroleum Processing Section **16**(3): 38-47.

Weigand, A., F. Atzler, et al. (2008). Combustion Strategies for EU6 and Beyond in Small D.I. Diesel Engines. Emission Control Conference,. Dresden.

Will, S., S. Schraml, et al. (1998). "Performance Characteristics of Soot Primary Particle Size Measurements by Time-Resolved Laser-Induced Incandescence." Appl. Opt. **37**(24): 5647-5658.

Will, S., S. Schraml, et al. (1996). "Comprehensive two-dimensional soot diagnostics based on laser-induced incandescence (LII)." Symposium (International) on Combustion **26**(2): 2277-2284.

Williams, M. M. R. and S. K. Loyalka (1991). Aerosol science : theory and practice : with special applications to the nuclear industry. Oxford ; New York, Pergamon Press.

Witze, P. O., S. Hochgreb, et al. (2001). "Time-Resolved Laser-Induced Incandescence and Laser Elastic-Scattering Measurements in a Propane Diffusion Flame." Appl. Opt. **40**(15): 2443-2452.

Woiki, D., A. Giesen, et al. (2000). "Time-resolved laser-induced incandescence for soot particle sizing during acetylene pyrolysis behind shock waves." Proceedings of the Combustion Institute **28**(2): 2531-2537.

Won, H. W., N. Peters, et al. (2013). Partially Premixed Combustion of Gasoline Type Fuels Using Larger Size Nozzle and Higher Compression Ratio in a Diesel Engine, SAE International.

Xu, H., M. Liu, et al. (2005). Modelling of HCCI Engines: Comparison of Single-zone, Multi-zone and Test Data, SAE International.

Yanagihara, H. (2001). Ignition Timing Control at Toyota "UNIBUS" Combustion System. A new generation of engine combustion processes for the future?, Rueil-Malmaison, France, Technip.

Yasar, H., H. S. Soyhan, et al. (2008). "Double-Wiebe function: An approach for single-zone HCCI engine modeling." Applied Thermal Engineering **28**(11–12): 1284-1290.

Yokota, H., Y. Kudo, et al. (1997). "A New Concept for Low Emission Diesel Combustion." Sae Transactions **106**(3): 1479-1490.

Yule, A. J. and I. Filipovic (1992). "On the break-up times and lengths of diesel sprays." International Journal of Heat and Fluid Flow **13**(2): 197-206.

Zahed, A. H., S. A. Mullah, et al. (1993). "Predict Octane Number for Gasoline Blends." Hydrocarbon Processing **72**(5): 85-87.

Zhang, X., K. Smith, et al. (2004). "Numerical Characterization of Particle Beam Collimation: Part II Integrated Aerodynamic-Lens-Nozzle System." Aerosol science and technology **38**(6): 619-638.

Zhang, X., K. A. Smith, et al. (2002). "A Numerical Characterization of Particle Beam Collimation by an Aerodynamic Lens-Nozzle System: Part I. An Individual Lens or Nozzle." Aerosol Science and Technology **36**(5): 617-631.

Zhao, F. Q. and H. Hiroyasu (1993). "The applications of laser Rayleigh scattering to combustion diagnostics." Progress in Energy and Combustion Science **19**(6): 447.

Zhao, H. (2010). Advanced direct injection combustion engine technologies and development. Boca Raton, CRC Press ; Oxford : Woodhead Pub.

Zhao, H. and N. Ladommatos (1998). "Optical diagnostics for in-cylinder mixture formation measurements in IC engines." Progress in Energy and Combustion Science **24**(4): 297-336.

Appendix A Hydrocarbon Properties

A.1 Properties of Various Hydrocarbons (Goodger (1975))

C_xH_y	Name	Relative density(20/4˚C)	b.p. (˚C)	f.p.(˚C)	Comb $-\Delta H^{\circ}_r$ (MJ/kg)*	$(F/A)_s$
Alkanes						
CH4	methane	0.415(-162)	-161.5	-184	55.54	0.0582
C2H6	ethane	0.561(-100)	-88.3	-172	51.4	0.0623
C3H8	propane	0.585(-44)	-44.5	-190	50.38	0.064
C4H10	butane	0.6(0)	0.6	-135	49.56	0.0649
C5H12	pentane	0.626	36.2	-131.5	48.68	0.0654
C6H14	hexane	0.66	69	-94.3	48.35	0.0658
C7H16	heptane	0.684	98.4	-90	48.11	0.0661
C8H18	octane	0.707	124.6	-56.5	47.93	0.0663
C9H20	nonane	0.718	150.6	-51	47.79	0.0664
isomers						
C7H16	2,2,3-trimethyl-butane (triptane)	0.69	81	-26		0.0661
C8H18	2,2,4-trimethyl-pentane	0.691	99.5	-108	47.84	0.0663
n-olefins						
C2H4	ethylene (ethene)		-103.8	-169.4	50.33	0.0678
C3H6	propylene (propene)	0.610(-47)	-47	-185.2	48.95	0.0678
C4H8	butylene (but-1-ene)	0.668	-2		48.49	0.0678
C5H10	α-amylene (pent-1-ene)	0.641	34	-139	47.81	0.0678
C6H12	1-hexylene (hex-1-ene)	0.673			47.61	0.0678
C7H14	1-heptylene (hept-1-ene)	0.697			47.47	0.0678
C8H16	1-octylene (oct-1-ene)	0.716	99		47.43	0.0678
isomers						
C4H8	isobutene (2-methylprop-1-ene)		-6.5	-147		0.0678
C7H14	2,3,3-trimethyl-but-1-ene	0.705	79	-112		0.0678

*This is equivalent to the gross calorific value.

C_xH_y	Name	Relative density(20/4˚C)	b.p. (˚C)	f.p.(˚C)	Comb -ΔH°_r (MJ/kg)*	$(F/A)_s$
Acetylenes						
C2H2	acetylene (ethyne)	0.621(-82)	-83.8	-81.5	49.95	0.0755
C3H4	propyne	0.679(-27)	-27.5	-104.7	48.4	0.0726
Naphthenes						
C3H6	cyclopropane	0.72(-79)	-34.4	-126.6		0.0678
C4H8	cyclobutane	0.703	13	-50		0.0678
C5H10	cyclopentane	0.751	49.5	-93	46.96	0.0678
C6H12	cyclohexane	0.778	81	6.5	46.61	0.0678
C7H14	cycloheptane	0.811				0.0678
Isomer						
C6H12	Methylcyclo-pentane	0.794	72			0.0678
Aromatics						
C6H6	benzene	0.878	80	5.5	41.86	0.0755
C7H8	toluene	0.866	110.5	-95	42.47	0.0743
C8H10	ortho-zylene	0.879	144	-27.1		
isomers						
C8H10	ehtylbenzene	0.868	136.5	-95	43.03	0.0733
C9H12	isopropylbenzene	0.863	153	-97		0.0726
n-Aliphatic monohydric alcohols						
CH3OH	methyl alcohol (methanol)	0.793	65	-97	22.69	0.1549
C2H5OH	ethyl alcohol (ethanol)	0.789	78.5	-116	29.69	0.1114
C3H7OH	propyl alcohol (propan-1-ol)	0.804	97.5	-127	33.65	0.0969
isomer						
C3H7OH	isopropanol (propan-2-ol,sec-propyl alcohol)	0.786	82.5	-88		0.0969

A.2 RON, MON and Blending Rating for Various Hydrocarbons (Marshall and Owen (1995))

	RON	Blending RON	MON	Blending MON
paraffin				
n-butane	94	113	89.1	114
isobutane	101.5	122	97.6	120
2-Methylbutane	92.3	100	90.3	104
2,2-Dimethylbutane	91.8	89	93.4	97
2,3-Dimethylbutane	103	96	94.3	106
2,2-Dimethylpentane	92.8	89	95.6	93
2,3-Dimethylpentane	91.1	88	88.5	90
2,2,3-Trimethylbutane	111.5	112	101	112
2,2,4-Trimethylpentane	100	100	100	100
Olefins				
1-Butene	97.5	144	79.9	126
1-Pentene	90.9	118	77.1	109
2-Methyl-1-butene	102	146	81.9	132
2-Methyl-1-pentene	94.2		81.5	
2-Methyl-2-pentene	97.8	159	83	148
4-Methyl-2-pentene	99.3	130	84.3	128
2-Methyl-1-hexene	90.7	118	78.8	108
2-Mwthyl-2-hexene	90.4	129	79.5	118
2,3-Dimethyl-1-pentene	99.3	130	84.2	121
2,3-Dimethyl-1-hexene	96.3	118	83.6	109
Diisobutylene (DIB)	105	168	88.6	150
Naphthenes				
Methylcyclopropane	102	NA	81.2	NA
Cyclopentane	101	141	84.8	141
Methylcyclopentane	91.3	107	80	99
1,1-Dimethylcyclopentane	92.3	96	89.3	102
1,1,2-Trimethylcyclohexane	95.7	NA	87.7	NA
Aromatics				
Methylbenzene	120	124	102.5	112
Ethylbenzene	108	124	97.9	107
1,3-Dimethylbenzene	118	145	114.5	124
1,4-Dimenthylbenzene	117	146	108	126
n-Propylbenzene	110.5	127	98.7	129
Isopropylbenzene	112.5	132	99.3	124
n-Butylbenzene	103.5	114	93.6	116
IsoButylbenzene	111	122	98	118

Appendix B Rayleigh Temperature Measurement of McKenna Burner

B.1 Introduction

This part of work was done for gaining experience in laser diagnostic technique regarding alignment, experimental technique and data processing procedure. The technique used was Rayleigh temperature measurement of a McKenna burner at different air/fuel ratio. The theory was described in section 1.4.10.

B.2 Experiment Setup

The laser used was a Continuum Surelite SLIII-10 at 532nm with a beam diameter of 9.5mm and the imaging equipment used was an Andor Dh534-18F-03 CCD camera. This was connected to the triggering box which simultaneously controlled the firing of the laser and the camera gating and triggering. The laser beam was focused in one direction to form a laser sheet.

The burner used was a McKenna burner which produced a uniform premixed flame across the circular surface of the burner. This gave a uniform distribution of species and temperature across the surface of the burner which was useful for understand the operation of Rayleigh scattering temperature measurement. The fuel used was methane mixed with air for combustion. A ring of nitrogen flowed around the flame to contain the flame and to prevent fluctuations caused by the surrounding atmosphere. The burner was cooled by a flow of water.

For the experiment, nitrogen was used to calibrate the Rayleigh signal and used to flow through the burner instead of methane and air. Ideally, calibration should be done with a gas with similar Rayleigh cross section as the medium measured as the difference will cause error which can be significant. The chemical composition during combustion will also affect the Rayleigh cross section. More details of errors encountered can be found in Dibble and Hollenbach (1981) and Namer and Schefer (1985). But this can be minimised by applying a Rayleigh cross section factor as described by Equation (1.5).

Three air/fuel ratios were used for this experiment and nitrogen was used to look at ambient non-combusting flow. The three air/fuel ratios are 1.05, 1.31 and 0.84. 300 images were taken for each condition, along with 50 nitrogen only and background images.

B.3 Image Processing

A background image provides the pattern noise of the CCD array. This was subtracted by every image taken to minimise the effect of this noise and this will be the first step of the image processing. The nitrogen image was used for finding the laser intensity profile as this laser had a Gaussian profile. This profile was normalised, as shown in Figure B-1 and every image was divided by this profile.

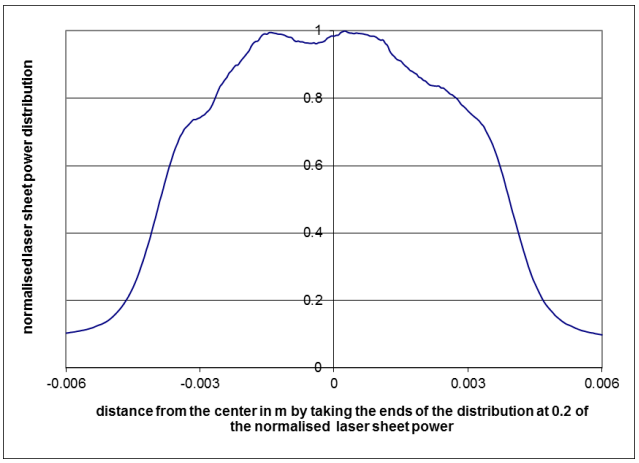

Figure B-1: Normalised laser profile for Rayleigh temperature measurement

For the 300 images from each of the setting, each was subtracted by the background image and correct for the laser sheet profile. The mean and the standard deviation were found. The same was also done with the nitrogen image and the mean of for these nitrogen images was used to calibrate for the temperature as it represented the Rayleigh signal at 293K.

On the nitrogen image, there are a few spots with high count probably because of Mie scattering by dust particles and has to be filtered as it will interfere with the overall average of the nitrogen signal. This was done by a median filter with an array of [3x3] as spatial information was not as important and only the overall signal was required. Then

a mean was obtained from the rest of the elements which gave a count representing the Rayleigh signal at 20˚C for nitrogen.

B.4 Result and Analysis

Once the mean count was acquired for the nitrogen at 20˚C and the three equivalence ratio settings, the temperature and count can be related by using Equation (1.5). The nitrogen image was used as the reference for this equation. The Rayleigh cross section for nitrogen is well documented and the Rayleigh cross section for the difference equivalence ratio can be found by estimating the products of combustion at the given equivalence ratio (Heywood (1988)). By multiplying the mole fraction of each of these products of combustion with their respective Rayleigh cross section, the total Rayleigh cross section can be found for each of the equivalence ratio. Table B-1 shows the various air and fuel flow rate and their respective equivalence ratio and Rayleigh cross section ratio to nitrogen. The uncertainties of these three air/fuel ratios were calculated and it was found the air/fuel ratios have the following uncertainties: 1.05±0.14, 1.31±0.08 and 0.84±0.09.

Air flow rate in l/min ± 1	20	25	20
Methane flow rate in l/min ± 0.25	2	2	2.5
λ	1.05±0.14	1.31±0.17	0.84±0.09
Rayleigh cross section ratio between combustion products and nitrogen	0.90±0.01	0.91±0.01	0.88±0.01

Table B-1: Various flow rates of air and fuel and their respective equivalence ratio and Rayleigh cross section ratio to nitrogen

Using this information with the Rayleigh cross section, the temperature can be calculated and Table B2-2 shows the calculated results from the measure Rayleigh signal. It can be seen that the highest temperature was the value closest to stoichiometry which was expected. There was the possibility of heat loss as the image area was above the flame itself and the issue of signal attenuation by the flame. This result can be verified by directly measuring the temperature within the image area with a thermal couple.

λ	1.05	1.31	0.84	Nitrogen
Rayleigh signal count	290	320	296	1365
Standard deviation for signal count	29.8	25.9	25.5	127
Temperature in K	1250	1110	1190	293

Table B-2: Different equivalence ratio and their corresponding calculated temperature

Looking at the variation of signal count for the three different equivalence ration, the probability density function can be plotted to look at the spread of the measurement. This is shown in Figure B-2. This shows there is a small variation of signal count and a shape that was expected.

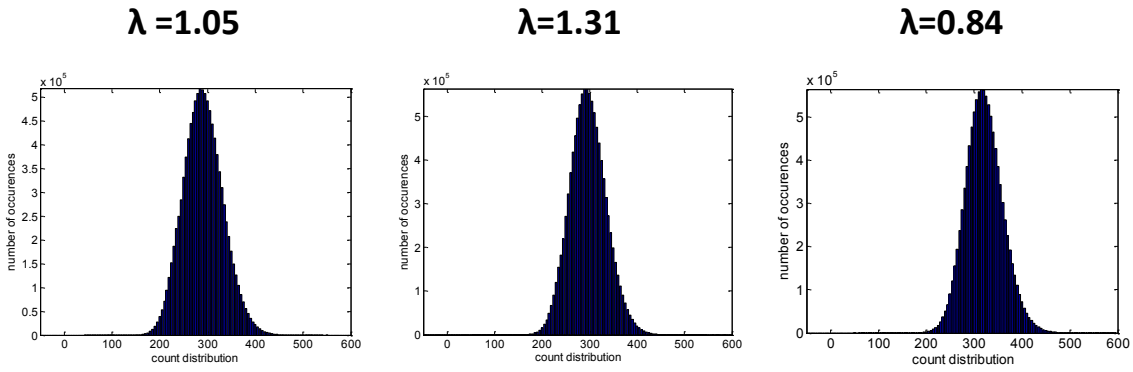

Figure B-2: PDF of signal count at different equivalence ratio

Figure B-3 shows the mean temperature distribution and the respective standard deviation for the three equivalence ratio and the nitrogen image. For the λ=1.05 image, there are two bands of higher values across the image and it can be explained by the variation of laser intensity due to normalised light intensity not being uniform (Espey, Dec et al. (1997)). There are also spots of high temperature as a result of low count values which was caused by the pixels with such low values suggesting a feature inherent within the instrument which could be investigated further.

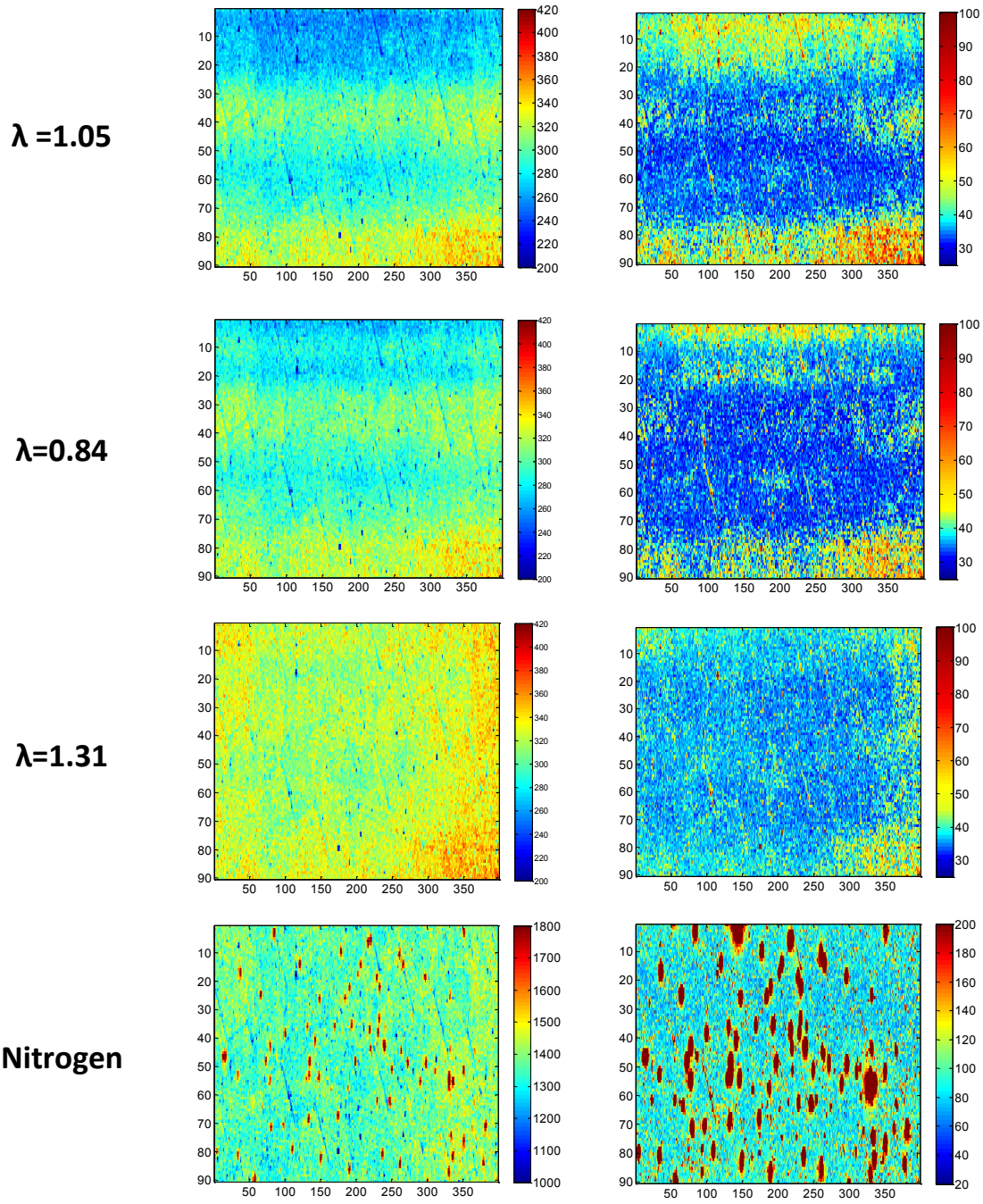

Figure B-3: Mean images (left) and standard deviation images (right) at three equivalence ration and nitrogen image.

Looking at the count variation at a cross-section at a point on the x-axis, the count variation can be seen and the variation of count can be assessed whether it is image specific or equipment specific. Figure B-4 show the signal variation across the image at two different locations. This illustrated there were a general pattern of variation that was specific to all the images which is most likely to be related to the laser profile, camera sensitivity or even the burner itself.

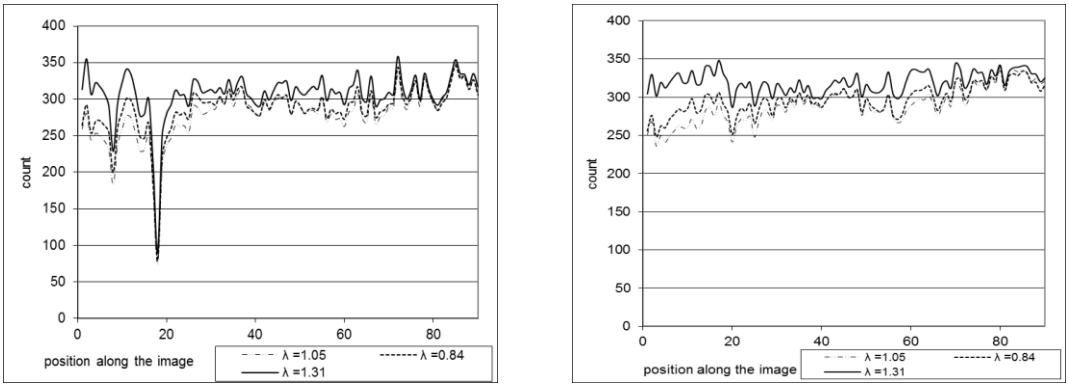

Figure B-4: Count variation at pixel axis x=115 (left) and x=270 (right) from the processed images

Finally, the normalised image of temperature distribution of the three equivalence ratio are shown here in Figure B-5, giving a varying distribution of signal for the three equivalence ratios. The band feature exists and the λ=1.31 case is more uniform because of lower temperature and higher signal count, hence less obvious variation.

λ =1.05 **λ=1.31** **λ=0.84**

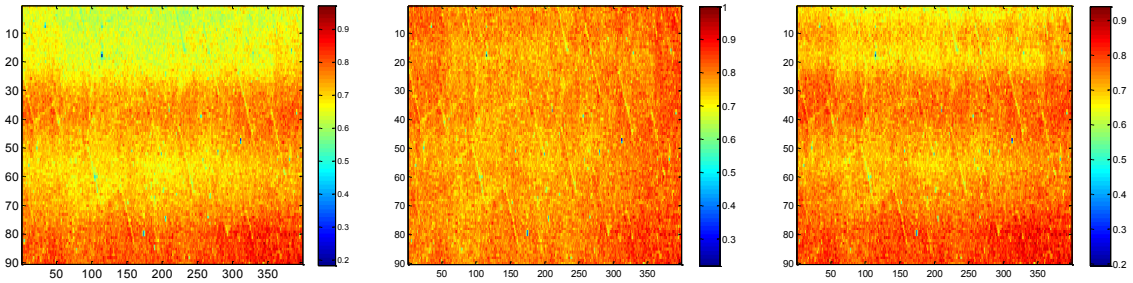

Figure B-5: Normalised image of temperature distribution at three equivalence ratio.

B.5 Chapter Conclusion

This was an exercise in laser diagnostic technique and application of Rayleigh diagnostic technique. It was useful to understand the different aspects such as laser profile correction, image processing and result analysis and contributed towards the later work such as the laser induced incandescence in engine.